THE UNIVERSITY
of ADELAIDE

Effect of Biofuel Blending on Combustion Characteristics of Hydrogen Flames

Yilong Yin

School of Electrical and Mechanical Engineering
The University of Adelaide
South Australia 5005
Australia

Thesis submitted in fulfillment of Ph. D. in Engineering on November 17, 2023.

Ph. D. Thesis

January 30, 2024

School of Electrical and Mechanical Engineering
The University of Adelaide
South Australia 5005
Australia

Written and typeset using LaTeX.

Dedicated to my parents Yanlin Wang, Bin Yin,

my grandparents Huijun Yan, Songbai Wang, Shaomin Duan,

and in loving memory of my grandpa Jun Yin (1931–2017).

For all the love, and all the regrets.

Declarations

I certify that this work contains no material which has been accepted for the award of any other degree or diploma in my name, in any university or other tertiary institution and, to the best of my knowledge and belief, contains no material previously published or written by another person, except where due reference has been made in the text. In addition, I certify that no part of this work will, in the future, be used in a submission in my name, for any other degree or diploma in any university or other tertiary institution without the prior approval of the University of Adelaide and where applicable, any partner institution responsible for the joint-award of this degree.

I acknowledge that copyright of published works contained within this thesis resides with the copyright holder(s) of those works.

I also give permission for the digital version of my thesis to be made available on the web, via the University's digital research repository, the Library Search and also through web search engines, unless permission has been granted by the University to restrict access for a period of time.

I acknowledge the financial support through the funding from The University of Adelaide, the Australian Research Council (ARC), and the Future Fuels Cooperative Research Centre (CRC).

Yilong Yin
November 17, 2023

Acknowledgements

I am profoundly grateful for the mentorship, guidance, and support I have received throughout my Ph.D. journey from numerous individuals. I would like to first extend my deepest gratitude to my supervisors, Prof. Paul Medwell and Prof. Bassam Dally, for their insightful guidance, tireless support, and invaluable advice. Their unwavering dedication to excellence and continuous learning have greatly inspired my research.

Professor Paul Medwell has accompanied me as my principal supervisor for the majority of my Ph.D. career, especially in those difficult times and situations where he has always shown the utmost understanding and support, both academically and spiritually. His encouragement, guidance, and constructive suggestions have consistently extended my thinking and helped me to overcome various challenges, and achieve critical milestones in my work. I consider myself very fortunate to have had Prof. Paul Medwell as my supervisor throughout my Ph.D. career.

I would like to express my great appreciation to Professor Bassam Dally for offering me the opportunity to study for the Ph.D. When all other avenues to my doctoral journey seemed to be barricaded, he illuminated a glimmer of hope, leaving a window of opportunity ajar. His deep expertise, critical insights, and patient guidance have been indispensable in shaping this research.

The experimental aspects of my research have benefited immensely from the generous assistance and technical expertise of Jason Peak, Adam Gee, Dr. Douglas Proud, and Dr. Kae Ken Foo. Their invaluable contributions to the experimental work and the insightful discussions that we have had are greatly appreciated. In addition to my supervisors, Dr. Alison-Jane Hunter has helped me improve my English skills and proofread my thesis. I am deeply grateful for this.

Many of the childhood dreams of my generation revolved around the aspiration to engage in scientific research one day, and I was no exception. Having traversed a winding path filled with moments of doubt, confusion, and even lapses in motivation, I held on to the little spark; however small, however hidden. Unexpectedly, one day, the little spark turned into a blazing flame and those dreams materialised into reality. Life is fleeting: cast aside inhibitions and pursue what one truly desires, without procrastination. Regardless of the outcome, every endeavour is a unique and invaluable experience.

Mistakes are proof that you are trying, but they have burdened my family with irreparable regrets. I will always remember that cold afternoon, drenched in sunshine yet filled with regret and remorse. I only hope those regrets will transform into a perpetual reminder for the future. I owe my profound gratitude to my parents Yanlin Wang and Bin Yin, my grandparents Huijun Yan, Songbai Wang, Shaomin Duan, and Jun Yin. Their sacrifices, immense tolerance, unconditional love, and support have brought me to this point, and I am eternally grateful. Thanks to my uncle Churong Wang for the support both mentally and financially; sponsored the laptop that collected my experimental data.

I also would like to thank my dear friends Xun Luo, Yue Lan, Lei Yang, Liang Fu, Gong Zhang, and Dian Yang. Their friendship and the desire for a reunion have been a source of strength and inspiration. The COVID-19 pandemic may have separated us for the last few years, I wouldn't be where I am without them. For the colleagues and friends I met in my Ph.D. career, their willingness to listen, offer advice, and celebrate even the smallest milestones made this journey more enjoyable. For those who accompanied me in various ways throughout my Ph.D. journey, I express my heartfelt gratitude. Undoubtedly, there are many individuals whom I will deeply regret not mentioning personally in this acknowledgment. To all of them, I extend my sincere apologies in advance.

To all of you, thank you for the time, energy, and expertise you have invested in me and this work. Your contributions have been pivotal to the successful completion of this thesis, and the insights, inspiration, knowledge, and skills I have acquired through your guidance will undeniably serve me well in my future endeavours.

In closing, if given the chance, I would travel back in time to deliver this thesis to my younger self, expressing gratitude for not having given up.

Abstract

Hydrogen has gained recognition as a highly promising alternative fuel to replace fossil fuels, offering the potential of a renewable energy carrier and contributing to the mitigation of greenhouse gas emissions. One of the challenges associated with using hydrogen in combustion-based industrial processes is that such systems (e.g. furnaces and boilers) typically rely on radiative heat transfer, whereas hydrogen flames feature low radiant intensity. Adding soot-promoting additives such as biofuels, which can be renewably produced, to hydrogen flames may offer a potential approach to enhance the radiant intensity, making hydrogen more suitable for practical applications. However, neither the effectiveness of various biofuels on thermal radiation enhancement, nor the influence of biofuel addition on the combustion characteristics of biofuel/hydrogen flames were previously well understood. This research, therefore, fills this gap in the understanding of the combustion characteristics of biofuel/hydrogen flames and the influencing factors.

To evaluate the relationship between the chemistry and the effectiveness of blending hydrogen flames with biofuels on combustion characteristics, toluene, anisole, and guaiacol are chosen as aromatic surrogates for bio-oils. Eucalyptol and D-limonene are recognised as monoterpenes chosen as surrogates for essential oils. The sooting propensity of these biofuel surrogates is evaluated by assessing laminar biofuel flames using the smoke point method, showing a decreasing order of toluene $>$ anisole $>$ guaiacol $>$ D-limonene $>$ eucalyptol. The results suggest that biofuels with an aromatic structure generally exhibit higher sooting propensities than monoterpenes, which is attributed to the higher degree of unsaturation in aromatic structures that favours PAH formation. Biofuels with lower bond dissociation enthalpy tend to be more effective in radiant intensity enhancement as a weaker C-H bond promotes hydrogen abstraction through the HACA mechanism. The efficacy of oxygenated fuels (i.e. anisole and eucalyptol) in enhancing radiant heat flux

is lower compared with non-oxygenated fuels (i.e. toluene and D-limonene), as the oxygen content in oxygenated fuels aids in the oxidation of PAHs.

The is increased by 2–22% through the addition of 0.2–1 mol% prevapourised and ultrasonically atomised biofuels. Toluene and anisole exhibit higher effectiveness in radiation enhancement than D-limonene and eucalyptol. These blended hydrogen flames illustrate enhanced blue colouration due to the promoted formation of carbonaceous radicals, whilst limited soot is observed. The corresponding flame luminosity exhibits an increase of 61–293%. In comparison, adding 0.1–0.3 mol% biofuels via gas-assist atomisation alters the dominant colouration of the hydrogen flame to yellow, indicating that soot loading is significantly improved and sooting biofuel/hydrogen flames are achieved. The enhancement of flame luminosity and radiant fraction ranges from 30–500% and 2–15%, respectively. The results suggest that the method of biofuel introduction is an important influencing factor for soot formation in biofuel/hydrogen flames. The underlying mechanisms are analysed through spray characterisation using microscopic shadowgraphy. The results reveal that biofuel droplets create local fuel-rich conditions to enhance soot formation and hence radiation characteristics. Droplet size is a critical parameter in creating fuel-rich pockets as larger droplets generated by gas-assist atomisation further advance this effect.

Blending hydrogen flames with biofuels for radiant intensity enhancement leads to an increase in the emission of nitrogen oxides. The computational investigation into the mechanisms of nitric oxide (NO) reveals that the increase in global NO_x emissions is primarily ascribed to the enhanced subset of the thermal route: $OH + N \rightleftharpoons H + NO$, and the prompt route: $CH + N_2 \rightleftharpoons H + NCN$. Based on this understanding, blending sprayed biofuels to hydrogen reduces thermal NO_x because the enthalpy of vapourisation results in lower flame temperature. A larger temperature drop is observed in gas-assist atomised biofuel/hydrogen flames due to the enhanced radiative heat loss.

The findings from this research establish an understanding of the efficacy and effectiveness of blending hydrogen flames with biofuels on radiant intensity enhancement and the corresponding impact on combustion characteristics. The analyses of influencing factors and their underlying mechanisms contribute to the adaptation of hydrogen to practical applications as an alternative energy carrier to mitigate greenhouse gas emissions.

Contents

List of publications arising from this work

1. **Yilong Yin**, Paul R Medwell, Adam J Gee, Kae Ken Foo, and Bassam B Dally. "Fundamental insights into the effect of blending hydrogen flames with sooting biofuels". *Fuel* 331 (2023), p. 125618.

2. **Yilong Yin**, Paul R Medwell, and Bassam B Dally. "Hydrogen turbulent nonpremixed flames blended with spray or prevapourised biofuels". *International Journal of Hydrogen Energy* 48 (2023), pp. 25563–25580.

3. **Yilong Yin**, Paul R Medwell, and Bassam B Dally. "Radiating biofuel-blended turbulent nonpremixed hydrogen flames on a coaxial spray burner". *Fuel* (under review).

4. Adam J Gee, **Yilong Yin**, Kae Ken Foo, Alfonso Chinnici, Neil Smith, and Paul R Medwell. "Toluene addition to turbulent H_2/natural gas flames in bluff-body burners". *International Journal of Hydrogen Energy* 47(65) (2022), pp. 27733–27746.

5. **Yilong Yin**, Adam J Gee, Kae Ken Foo, Paul R Medwell, and Bassam B Dally. "Doping effect of oxygenated and non-oxygenated bio-oils on non-premixed turbulent hydrogen-based flames". *11th Saudi Arabian Section of the Combustion Institute* (2021).

6. **Yilong Yin**, Paul R Medwell, and Bassam B Dally. "The effect of blending hydrogen with bio-oils and essential oils on turbulent nonpremixed jet flames". *12th Saudi Arabian Section of the Combustion Institute* (2022).

7. Paul R Medwell, Neil Smith, Douglas B. Proud, Adam J Gee, **Yilong Yin**, and Peter J Ashman. "Hydrogen blending in domestic and industrial appliances". *Australian Hydrogen Research Conference* (2023).

List of Figures

List of Tables

Chapter 1

Introduction

1.1 Background

Reductions in greenhouse gas (GHG) emissions, which are a leading cause of climate change, have become a priority for many governments and industries around the world. At the Conference of Parties 27 (COP 27) in 2022, the Australian Government targeted a reduction of GHG emissions by 43% by the year 2030, compared with 2005 values [1, 2]. Greenhouse gases mainly comprise carbon dioxide (CO_2), methane (CH_4), and nitrous oxide (N_2O). Carbon dioxide is the predominant component of GHG and is commonly employed as the index for GHG emissions. The reports from the quarterly update of Australia's national greenhouse gas inventory, presented in Figure 1.1 reveal that even though the overall trend for GHG emissions has decreased from 157 Mt CO_2-e (million tonnes of carbon dioxide equivalent) to 123 Mt CO_2-e. The emissions from stationary energy and industrial processes sectors, where burning of fuels is directly used for energy, have increased by 30% between 2005–2022. Significant progress from the stationary sectors is yet to be made towards achieving net-zero emissions.

The combustion of fossil fuels is projected to persist into the foreseeable future as the predominant energy supply, with a concomitant increase in CO_2 emissions. In Australia, the combustion of fossil fuels in the stationary energy sector contributes 19% of the total CO_2 emissions [3]. Fossil fuels, such as coal, oil, and natural gas, provide a significant portion of the world's energy needs, owing to their high energy density, abundance, and low cost. Despite efforts to reduce CO_2 emissions through energy efficiency improvements, carbon capture, and storage technologies, the growth of the global economy and population is expected to sustain the demand for fossil fuels, leading to

a continued increase in CO_2 emissions. Figure 1.2 shows the CO_2 emissions factor of various fossil fuels measured in kilograms of CO_2 produced per megawatt-hour (MWh) of energy produced. The persistence of fossil fuels as the primary energy supply and the major source for CO_2 emissions underscores the urgency of addressing the environmental impacts of energy production and consumption, as well as the need for a transition to a sustainable and low-carbon energy system. The exploration of alternative fuels has become an imperative aspect of contemporary research efforts, driven by the desire to mitigate the adverse effects of conventional fuels on the environment and human health. As the world is pledging to achieve net-zero emissions, using potential renewable carbon-free fuels such as hydrogen to replace fossil fuels in practical applications is emerging as a promising approach to mitigate CO_2 emissions.

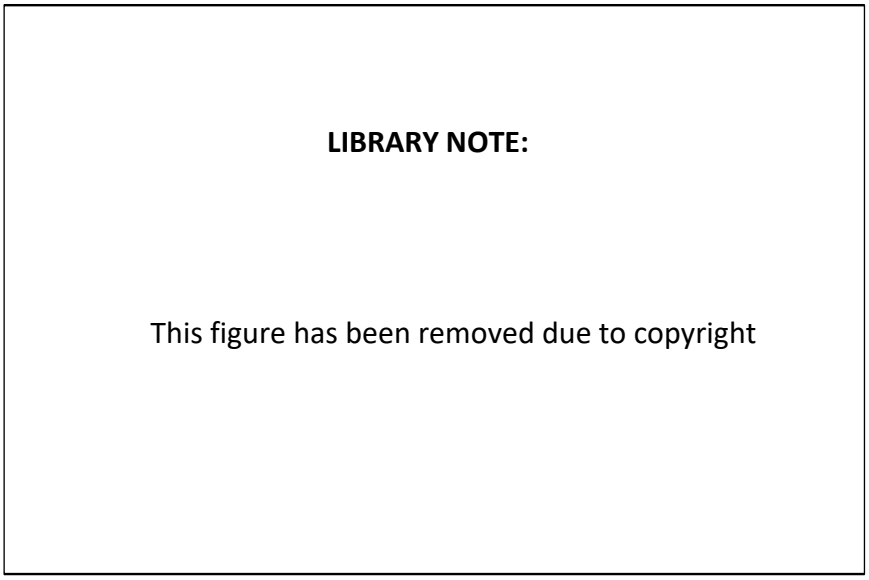

Figure 1.1: Quarterly update of Australia's national greenhouse gas inventory from all sectors and the stationary sector between 2005–2022. Adapted from Australia's National GHG Inventory [3].

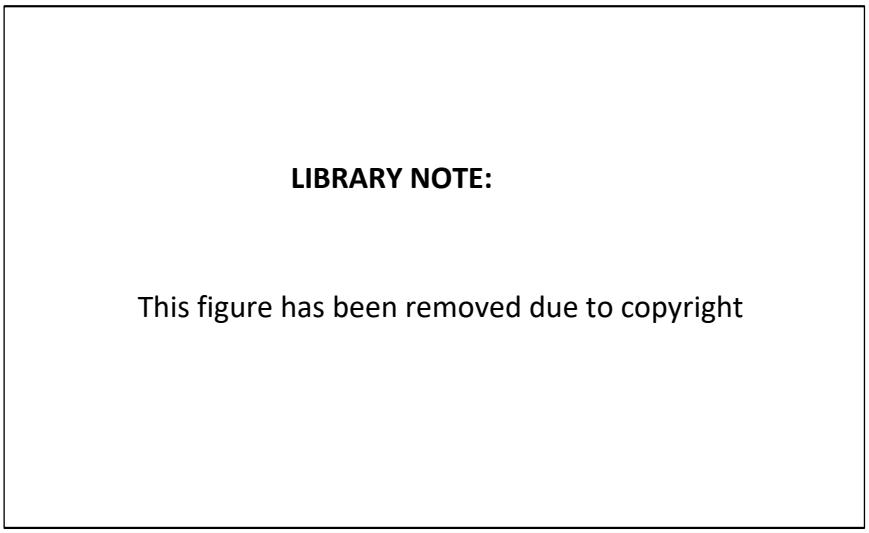

Figure 1.2: CO_2 emissions factor measured in kilograms of CO_2 produced per megawatt-hour (MWh) of energy produced from various fossil fuel sources. Adapted from Australia's National GHG Inventory [3].

1.2 Hydrogen as an alternative fuel

Hydrogen has been widely regarded as a promising substitute for fossil fuels as an energy carrier, owing to its carbon-free combustion products [4–7]. Despite the fact that steam-methane reforming or coal gasification currently accounts for over 95% of global hydrogen production, the production of green hydrogen can be achieved through water electrolysis employing renewable electricity [8]. In contrast with intermittent and geographically constrained renewable energy sources such as solar, wind, and ocean energy, hydrogen can be stored and continuously supplied as a renewable energy carrier [9–11]. Its ability to be readily mixed with other fuels has been investigated, providing a promising avenue for its integration into existing fuel infrastructures. A fraction of hydrogen can be incorporated into natural gas (NG) pipeline networks to alleviate CO_2 emissions by decreasing the carbon concentration per unit of energy supplied [11, 12]. Furthermore, hydrogen has been extensively investigated as a carbon-free additive to mitigate soot formation and particulate emissions from spray flames within internal combustion engines. Owing to its unique chemical, physical, and combustion characteristics, hydrogen has been the subject of intense research as an additive to compensate for the disadvantages of various fuels. For example, hydrogen

has been added to ammonia to improve the low flame speed of ammonia by taking advantage of the high flame speed of hydrogen [13–15]. To attain a more pronounced reduction in CO_2 emissions, the feasibility and efficacy of employing hydrogen as a primary fuel, as opposed to a mere additive, for high-temperature industrial processes necessitate a thorough understanding of hydrogen flames and innovative perspectives on their adaptation [4].

The use of hydrogen as an alternative fuel presents a range of challenges that need to be addressed in order to fully realise its potential as a sustainable energy source. Among the primary concerns are issues related to hydrogen storage, transportation, distribution, safety, cost, and operating expenditures. The low volumetric energy density of hydrogen necessitates the development of advanced storage methods that are capable of storing hydrogen at high pressures or low temperatures, in order to minimise the volume required for storage. The cost of producing and distributing hydrogen remains relatively high compared with traditional fossil fuels. Addressing this challenge requires continued advancements in hydrogen production technologies. In terms of safety concerns, the high flame speed of hydrogen, coupled with its low ignition energy and wide flammability range, makes it more susceptible to flashback than traditional hydrocarbon fuels. Therefore, the design and operation of combustion systems that use hydrogen as a fuel must incorporate measures to prevent flashback, including the use of flashback arrestors, modifications to fuel injection systems, and careful consideration of system operating parameters. Hydrogen flames have considerably lower visibility than hydrocarbon flames. Although they display a faint reddish colour due to the presence of water vapour [16], the low visibility of hydrogen flames may bring particular challenges to domestic applications. In addition to these well-known challenges, one of the main challenges of using hydrogen as a base fuel in combustion systems of industrial processes is that such combustion systems typically rely on thermal radiation as one of their primary means of heat transfer, while hydrogen flames have low radiation [17, 18]. Therefore, using hydrogen as a single-component carbon-free fuel may not be able to meet the requirements for replacing conventional fuels without other changes to the system.

The low radiant intensity of hydrogen flame is ascribed to the absence of soot particulates within the flame [19]. Soot is a complex mixture of carbonaceous particles and other organic compounds that can be formed from carbonaceous fuels during combustion processes. The emission of soot and its precursors—polycyclic aromatic hydrocarbons (PAHs)—from combustion processes can

have significant negative impacts on both the environment and human health. Inhalation of soot particles can cause respiratory and cardiovascular problems, including bronchitis, asthma, and heart disease. The International Agency for Research on Cancer (IARC) has classified many individual PAHs as Group 1 carcinogens [20]. Within the flame, soot is the major source of thermal radiation from a flame due to its high emissivity in the infrared portion of the electromagnetic spectrum. Therefore, the low radiant intensity of hydrogen flame can be enhanced by promoting the formation of soot particulates without emission from the flame. One possible solution is to blend two or more materials with complementary properties to compensate for the disadvantages of a single component fuel [21–24]. Seeding particles to the hydrogen flame as a source for improving blackbody radiation or blending sooting fuels with hydrogen to enhance radiative heat transfer by promoting soot formation in the flame are potential approaches suitable for industrial applications [17, 25].

1.3 Biofuel as a potential additive

A highly sooting hydrocarbon fuel, derived from either fossil fuels or biomass sources, can be considered a viable supplementary agent to enhance radiation in a hydrogen flame [17, 25]. Biofuel, derived from renewable biomass resources, is a preferable alternative to hydrocarbons obtained from fossil fuels [26]. The production of biofuels can be effectively integrated into existing industries to utilise by-products and waste generated during these processes, such as those from pulp and paper industries and food production plants, making it an environmentally-friendly fuel additive [27]. Incorporating biofuel as an additive, in conjunction with green hydrogen as the base fuel, has the potential to substantially reduce dependence on fossil fuels and significantly decrease carbon emissions in industrial combustion processes.

Biofuels often contain a significant proportion of aromatics, which are expected to promote the formation of polycyclic aromatic hydrocarbons (PAHs) and subsequent soot formation [28, 29]. However, other physical and chemical properties of biofuel, including oxygen and water content, boiling point, and viscosity, also influence the impact and efficacy of soot formation and oxidation [26]. The effectiveness and consequences of incorporating biofuel additives into hydrogen flames within the context of industrial combustion processes remain unclear when considering the combined effects of these various factors.

1.4 Methods of liquid fuel introduction

The approach of liquid biofuel and gaseous hydrogen blending investigated in this thesis involves two-phase flow combustion, which is directly affected by the methods of liquid fuel introduction. The characteristics of liquid fuel introduction methods can significantly influence the combustion process. The way in which fuel is introduced into the combustion process can alter the physical, chemical, and combustion properties of the system, ultimately affecting the key combustion parameters such as vapourisation rate, residence time, and flame stability.

There are various methods of liquid fuel introduction, such as direct injection, prevaporisation, and premixing [30–32]. Direct injection is commonly employed in internal combustion engines, which involves supplying the liquid fuel directly into the combustion chamber, often under high pressure [33]. In internal combustion engines, sprays aid in the control of the timing and rate of combustion, leading to precise control over engine performance [34]. The resultant spray characteristics, including breakup length, penetration length, and droplet size, were found to be critical to flame temperature, pollutant emissions, and combustion efficiency of the system [35, 36]. Sprays also play a vital role in regulating combustion processes. For instance, in gas turbines, sprays are used to control the temperature of the combustion chamber, which prevents hot spots and reduces the risk of damaging the turbine blades [37].

Prevaporisation involves preheating liquid fuels until they are vapourised before introducing them to the combustion process, while premixing involves blending the fuel with the oxidiser before entering the combustion chamber. Prevapourisation enhances the homogeneous mixing of the fuels and oxidiser, leading to lower soot and NO_x emissions [35, 36]. In addition, it avoids the energy loss in the flame from the enthalpy of vapourisation.

Previous studies have compared the effect of single- and two-phase flow combustion on burning velocity, flame stability, vapourisation rate, residence time, and pollutant emissions. At the same equivalence ratio and similar conditions for iso-octane, the burning velocity of gaseous and aerosol flames is similar [38]. Gaseous flames have a higher tendency to flame stability compared with aerosol flames. A study of nanoparticle (i.e. aluminum, iron, and boron) blended diesel in Compression Ignition (CI) engines revealed that a higher vapourisation rate leads to complete combustion, resulting in lower CO emissions, but on the other hand, the increased temperature leads to higher NO_x emissions [39]. Another study reported that adding sprayed

toluene to hydrogen flames facilitates soot formation compared with vapour toluene flames, indicating that fuel-rich regions created by liquid droplets in spray flames favour soot formation, which is expected to enhance radiant intensity [17]. However, challenges remain in evaluating the suitable methods of liquid biofuel introduction to hydrogen flames for thermal radiation enhancement and understanding their underlying mechanisms.

The effects of fuel introduction methods on combustion characteristics are complex and depend on various factors, including specific fuel properties, combustion system design, and operating conditions. Understanding the underlying mechanisms of each fuel introduction method can inform the selection of the most appropriate strategy for optimising combustion efficiency, reducing emissions, and improving combustion performance.

1.5 Thesis outline

Presented in this thesis is a combined experimental and numerical study that investigates the efficacy and effectiveness of adding biofuels with various sooting propensities to turbulent nonpremixed hydrogen flames on radiant intensity enhancement, in conjunction with the blending effect on combustion characteristics.

An in-depth review of the current understanding and findings from previous research has been carried out and presented in Chapter 2 to establish a fundamental understanding associated with the merits and challenges of using hydrogen as an alternative fuel and the soot evolution in hydrocarbon and hydrogen-based flames. A comprehensive review of the investigation of various biofuels and dominating factors of their sooting propensities has been undertaken to identify the potential biofuels as soot-enhancing additives and corresponding surrogates for analysis. The effect of the introduction methods of liquid biofuels along with the influence of the physical properties on spray characteristics has also been highlighted. Four major research gaps are identified based on the review of previous studies and corresponding scientific aims and objectives are determined.

The experimental and numerical approaches employed in this research are summarised in Chapter 3 with detailed descriptions and corresponding diagnostics used in the methodology section of each journal paper. Three different burners have been designed and used to establish various unblended and biofuel-blended flame cases for the stepped evaluation of biofuel additives

and their blending effect. Laminar flame calculations (Chemkin Pro) and a detailed chemical kinetics mechanism (CRECK Modelling Group) are used as the numerical approach in this research.

Chapters 4–7 compile the results, analyses, and findings generated in this research. The sooting propensities of five biofuel surrogates were first tested on a wick-fed burner using smoke point methods under laminar flame conditions. The results are presented in the paper shown in Chapter 4 to provide insights into the potential biofuel additives before adding to hydrogen-based flames. These biofuels are added to turbulent nonpremixed hydrogen-based flames to establish the fundamental understanding of the blending effect on radiant intensity enhancement and flame characteristics.

Chapter 5 further investigates the blending effect of biofuels, with an emphasis on the methods of additive introduction—prevapourisation and ultrasonic atomisation, additive concentration, global NO_x emissions, and dominant NO_x reaction pathways.

To analyse the influence of spray characteristics generated by gas-assist atomisation on the effect of blending biofuel additives, the coaxial needle spray burner has been first characterised by a method that utilises commercial photographic equipment. Chapter 6 presents the near-field spray characteristics of air/water and helium/water non-reacting flows along with the analysis of influencing physical properties and dominant non-dimensional parameters.

Chapter 7 exhibits the flame characteristics of radiating biofuel-blended turbulent hydrogen flames achieved on the coaxial needle spray burner.

Chapter 8 links all the results and findings in the previous chapters with stated objectives and summarises the main findings of the research.

Finally, Chapter 9 summarises the major discoveries and critical outcomes of this research, with suggestions for possible future work.

1.6 References

[1] J. Rogelj, M. Den Elzen, N. Höhne, T. Fransen, H. Fekete, H. Winkler, R. Schaeffer, F. Sha, K. Riahi, and M. Meinshausen. "Paris Agreement climate proposals need a boost to keep warming well below 2°C". *Nature* 534 (2016), pp. 631–639.

[2] N. Alayza, P. Bhandari, D. Burns, N. Cogswell, K. de Zoysa, M. Finch, T. Fransen, M. L. González, N. Krishnan, and P. Langer. "COP27: Key Takeaways and What's Next" (2022).

[3] Australian Government Department of Industry, Science, Energy and Resources. *Quarterly Update of Australia's National Greenhouse Gas Inventory: December 2022*. 2020.

[4] P. E. Dodds, I. Staffell, A. D. Hawkes, F. Li, P. Grünewald, W. McDowall, and P. Ekins. "Hydrogen and fuel cell technologies for heating: A review". *Int. J. Hydrog. Energy* 40 (2015), pp. 2065–2083.

[5] T. Kitagawa, T. Nakahara, K. Maruyama, K. Kado, A. Hayakawa, and S. Kobayashi. "Turbulent burning velocity of hydrogen-air premixed propagating flames at elevated pressures". *Int. J. Hydrog. Energy* 33 (2008), pp. 5842–5849.

[6] S. Nag, P. Sharma, A. Gupta, and A. Dhar. "Experimental study of engine performance and emissions for hydrogen diesel dual fuel engine with exhaust gas recirculation". *Int. J. Hydrog. Energy* 44 (2019), pp. 12163–12175.

[7] J. Nowotny and T. N. Veziroglu. "Impact of hydrogen on the environment". *Int. J. Hydrog. Energy* 36 (2011), pp. 13218–13224.

[8] G. Kakoulaki, I. Kougias, N. Taylor, F. Dolci, J. Moya, and A. Jäger-Waldau. "Green hydrogen in Europe-A regional assessment: Substituting existing production with electrolysis powered by renewables". *Energy Convers. Manag.* 228 (2021), p. 113649.

[9] J. Widén, N. Carpman, V. Castellucci, D. Lingfors, J. Olauson, F. Remouit, M. Bergkvist, M. Grabbe, and R. Waters. "Variability assessment and forecasting of renewables: A review for solar, wind, wave and tidal resources". *Renew. Sustain. Energy Rev.* 44 (2015), pp. 356–375.

[10] P. B. L. Neto, O. R. Saavedra, and D. Q. Oliveira. "The effect of complementarity between solar, wind and tidal energy in isolated hybrid microgrids". *Renew. Energy* 147 (2020), pp. 339–355.

[11] D. Haeseldonckx and W. D'haeseleer. "The use of the natural-gas pipeline infrastructure for hydrogen transport in a changing market structure". *Int. J. Hydrog. Energy* 32 (2007), pp. 1381–1386.

[12] M. W. Melaina, O. Antonia, and M. Penev. *Blending Hydrogen into Natural Gas Pipeline Networks: A Review of Key Issues*. Mar. 2013.

[13] A. A. Konnov, A. Mohammad, V. R. Kishore, N. I. Kim, C. Prathap, and S. Kumar. "A comprehensive review of measurements and data analysis of laminar burning velocities for various fuel/air mixtures". *Prog. Energy Combust. Sci.* 68 (2018), pp. 197–267.

[14] P. Berwal, S. Kumar, and B. Khandelwal. "A comprehensive review on synthesis, chemical kinetics, and practical application of ammonia as future fuel for combustion". *J. Energy Inst.* 99 (2021), pp. 273–298.

[15] P. Berwal, B. Khandelwal, and S. Kumar. "Effect of ammonia addition on laminar burning velocity of CH_4/H_2 premixed flames at high pressure and temperature conditions". *Int. J. Hydrog. Energy* (2023).

[16] R. W. Schefer, W. D. Kulatilaka, B. D. Patterson, and T. B. Settersten. "Visible emission of hydrogen flames". *Combust. Flame* 156 (2009), pp. 1234–1241.

[17] M. J. Evans, D. B. Proud, P. R. Medwell, H. Pitsch, and B. B. Dally. "Highly radiating hydrogen flames: effect of toluene concentration and phase". *Proc. Combust. Inst.* 38 (2021), pp. 1099–1106.

[18] A. K. Agarwal. "Biofuels (alcohols and biodiesel) applications as fuels for internal combustion engines". *Prog. Energy. Combust. Sci.* 33 (2007), pp. 233–271.

[19] D. Bäckström, R. Johansson, K. Andersson, H. Wiinikka, and C. Fredriksson. "On the use of alternative fuels in rotary kiln burners—An experimental and modelling study of the effect on the radiative heat transfer conditions". *Fuel Process. Technol.* 138 (2015), pp. 210–220.

[20] R. Baan, Y. Grosse, K. Straif, B. Secretan, F. El Ghissassi, V. Bouvard, L. Benbrahim-Tallaa, N. Guha, C. Freeman, and L. Galichet. "A review of human carcinogens—part F: chemical agents and related occupations". *The Lancet Oncology* 10 (2009), pp. 1143–1144.

[21] O. Kwon and G. Faeth. "Flame/stretch interactions of premixed hydrogen-fueled flames: measurements and predictions". *Combust. Flame* 124 (2001), pp. 590–610.

[22] A. A. Khateeb, T. F. Guiberti, X. Zhu, M. Younes, A. Jamal, and W. L. Roberts. "Stability limits and NO emissions of technically-premixed ammonia-hydrogen-nitrogen-air swirl flames". *Int. J. Hydrog. Energy* 45 (2020), pp. 22008–22018.

[23] F. Ren, H. Chu, L. Xiang, W. Han, and M. Gu. "Effect of hydrogen addition on the laminar premixed combustion characteristics the main components of natural gas". *J. Energy Inst.* 92 (2019), pp. 1178–1190.

[24] D. Maclean and H. G. Wagner. "The structure of the reaction zones of ammonia-oxygen and hydrazine-decomposition flames". *Symp. (Int.) Combust.* 11 (1967), pp. 871–878.

[25] W. Hutny and G. Lee. "Improved radiative heat transfer from hydrogen flames". *Int. J. Hydrog. Energy* 16 (1991), pp. 47–53.

[26] M. Gholizadeh, X. Hu, and Q. Liu. "A mini review of the specialties of the bio-oils produced from pyrolysis of 20 different biomasses". *Renew. Sustain. Energy Rev.* 114 (2019), p. 109313.

[27] S. Czernik and A. Bridgwater. "Overview of applications of biomass fast pyrolysis oil". *Energy & Fuels* 18 (2004), pp. 590–598.

[28] C. Zhang, L. Chen, S. Ding, H. Xu, G. Li, J.-L. Consalvi, and F. Liu. "Effects of soot inception and condensation PAH species and fuel preheating on soot formation modeling in laminar coflow CH_4/air diffusion flames doped with n-heptane/toluene mixtures". *Fuel* 253 (2019), pp. 1371–1377.

[29] M. Solikhah, F. Pratiwi, Y. Heryana, A. Wimada, F. Karuana, A. Raksodewanto, and A. Kismanto. "Characterization of bio-oil from fast pyrolysis of palm frond and empty fruit bunch". *IOP Conf. Ser.: Mater. Sci.* Vol. 349. IOP Publishing. 2018, p. 012035.

[30] E. Rostami and H. Mahdavy Moghaddam. "The velocity and viscosity impact on the annular spray atomisation of different fuels". *Combust. Theory Model.* 25 (2021), pp. 158–192.

[31] E. Lubarsky, J. R. Reichel, B. T. Zinn, and R. McAmis. "Spray in Crossflow: Dependence on Weber Number". *J. Eng. Gas Turbines Power* 132 (Oct. 2009), p. 021501.

[32] J. C. Lasheras and E. Hopfinger. "Liquid jet instability and atomization in a coaxial gas stream". *Annu. Rev. Fluid Mech.* 32 (2000), pp. 275–308.

[33] I. Ruiz-Rodriguez, R. Cracknell, M. Parkes, T. Megaritis, and L. Ganippa. "Experimental study of the effect of C8 oxygenates on sooting processes in high pressure spray flames". *Combust. Flame* 220 (2020), pp. 235–246.

[34] A. K. Agarwal, A. Dhar, J. G. Gupta, W. I. Kim, K. Choi, C. S. Lee, and S. Park. "Effect of fuel injection pressure and injection timing of Karanja biodiesel blends on fuel spray, engine performance, emissions and combustion characteristics". *Energy Convers. Manag.* 91 (2015), pp. 302–314.

[35] C. J. Mueller, A. L. Boehman, and G. C. Martin. "An experimental investigation of the origin of increased NO_x emissions when fueling a heavy-duty compression-ignition engine with soy biodiesel". *SAE Int. J. Fuels Lubr.* 2 (2009), pp. 789–816.

[36] M. D. Bohon and W. L. Roberts. "NO_x emissions from high swirl turbulent spray flames with highly oxygenated fuels". *Proc. Combust. Inst.* 34 (2013), pp. 1705–1712.

[37] I. I. Enagi, K. Al-attab, Z. Zainal, and Y. H. Teoh. "Palm biodiesel spray and combustion characteristics in a new micro gas turbine combustion chamber design". *Energy* 254 (2022), p. 124335.

[38] M. Lawes, Y. Lee, and N. Marquez. "Comparison of iso-octane burning rates between single-phase and two-phase combustion for small droplets". *Combust. Flame* 144 (2006), pp. 513–525.

[39] R. N. Mehta, M. Chakraborty, and P. A. Parikh. "Nanofuels: Combustion, engine performance and emissions". *Fuel* 120 (2014), pp. 91–97.

Chapter 2

Literature review

2.1 Hydrogen and hydrogen flames

Hydrogen has attracted significant attention due to the increasing demand for environmentally friendly energy resources with high efficiency. The overall challenges of hydrogen application regarding renewable production, cost, combustion system adjustment, supply, and storage have been outlined in §1.2. Hydrogen flames have been widely studied, including their flame visibility, flame temperature, burning velocity, and flammability limits [1–3]. In this section, the properties, flame characteristics, and potential applications of hydrogen are presented and compared with methane—a primary component of a widely used fossil fuel (natural gas) in industrial processes.

Table 2.1 shows the properties and flame characteristics of hydrogen and methane. The density of hydrogen ($0.08\,kg/m^3$) is lower than methane ($0.66\,kg/m^3$). The gross calorific value of hydrogen ($142\,MJ/kg$) is higher than that of methane ($56\,MJ/kg$) [4], indicating that compared with the fuel consumption of methane, it takes less mass of gaseous hydrogen to obtain an equivalent amount of energy. It is seen in Table 2.1 that hydrogen flames feature a higher laminar burning velocity at $2.9\,m/s$, compared with methane at $0.37\,m/s$ [1]. Increasing the flame speed improves the stability of the flame [5]. This characteristic of hydrogen has been widely utilised to increase the burning velocity of fuels with low flame speed and stabilise the flame by adding hydrogen as a complementary fuel, such as natural gas and ammonia [6–9]. The increase in flame speed can be ascribed to the facilitation of free OH radicals from hydrogen addition [10]. The OH radical is an important active oxidant that usually indicates the location of the flame front. The main

reaction pathways of OH are:

$$H + O_2 \rightleftharpoons OH + O \tag{2.1}$$

$$O + H_2 \rightleftharpoons OH + H \tag{2.2}$$

A potential issue that arises from the high flame speed of hydrogen is the risk of flashback. Flashback occurs when the flame travels at a higher speed against the gas stream, moving upstream into the burner during combustion and causing damage to the appliance. Flashback is particularly prevalent under premixed conditions. However, the risk of flashback problems from using hydrogen is of less concern as many industrial combustion systems operate under nonpremixed conditions [11].

Hydrogen flames have a higher adiabatic flame temperature than methane flames; for example, a stoichiometric mixture of fuel and air at Standard Temperature Pressure (STP), the values are 2383 K and 2223 K, respectively (refer to Table 2.1). This feature of hydrogen flames makes them advantageous in applications that demand high temperatures; however, it causes a potential issue of higher NO_x emissions from the enhanced thermal NO_x formation [12]. Nevertheless, the utilisation of hydrogen as a fuel helps avoid the production of fuel and prompt NO_x [13, 14]. The NO_x formation in hydrogen flames will be further discussed in §2.4.

Table 2.1: Properties and combustion characteristics of hydrogen and methane [1, 15–19].

Fuel	H_2	CH_4
Density (kg/m^3)	0.08	0.66
Higher heating value (HHV) (MJ/kg)	142	56
Lower heating value (LHV) (MJ/kg)	120	50
Flammability limit (by vol% in air)	4–74	5–15
Laminar burning velocity (m/s)	2.91	0.37
Adiabatic flame temperature (K)	2380	2223

Aside from the aforementioned flame behaviour, a major barrier to hydrogen application in industrial combustion systems compared with carbon-based fuels is that hydrogen flames have low radiant intensity due to the absence of soot, whereas such combustion systems rely on radiative heat transfer [20]. Practical combustion systems (e.g. a furnace schematically shown in Figure 2.1) are typically comprised of a radiant section as a primary configuration to capture thermal heat radiated from the flames [21, 22]. The radiant heat flux measured from turbulent nonpremixed natural gas and

hydrogen flames (at a constant Reynolds number of 10,000) on a bluff-body burner shows that the hydrogen flames exhibit 80% lower radiant heat flux than natural gas flames [23]. The bulk mean Reynolds number is defined in Equation 2.3:

$$Re = \frac{\rho U d_{jet}}{\mu} \tag{2.3}$$

where ρ is the density of the fluid, U is the bulk mean velocity, d_{jet} is the jet diameter of the fluid, μ is the dynamic viscosity of the fluid. Other hydrocarbon flames exhibit higher radiant heat flux than natural gas flames—the radiant faction of ethylene and propane flames are 128% and 60% higher than natural gas flame at large global flame residence time ($\tau \approx 200\,\text{ms}$) [24]. The global residence time of a flame is calculated using Equation 2.4 [24]:

$$\tau = \frac{\rho_f W_f^2 L_f f_s}{3\rho_0 d_{jet}^2 U} \tag{2.4}$$

where ρ_f, W_f, L_f are the gas density within the flame, flame width and length, f_s is the stochiometric mixture fraction, ρ_0 is the density of the fuel, d_{jet} and U are jet diameter and bulk mean exit velocity of fuel, respectively. Figure 2.2 shows photographs of natural and hydrogen flames on a jet burner (reproduced from Gee et al. [23]). The appearance of natural gas flame is dominated by bright yellow colouration as a result of high soot loading, whereas the hydrogen flame exhibits light red colouration due to the presence of water vapour. The low radiant intensity found in non-sooting hydrogen flames is because the source of radiation is mainly from gaseous species such as water vapour, which is lower than that from soot via blackbody radiation in sooting hydrocarbon flames at equivalent flame temperature [25]. Therefore, the low radiant heat flux of hydrogen flames can be enhanced by promoting soot formation within the flame or seeding particles into the flame as the provided source for blackbody radiation.

LIBRARY NOTE:

This figure has been removed due to copyright

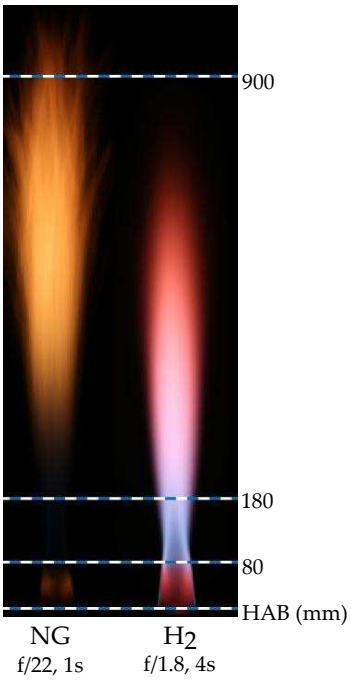

Figure 2.2: Photographs of natural gas and H_2 flames. Reproduced from Gee et al. [23].

2.2 Overview of soot

As illustrated in §2.1, soot within a flame is particularly desirable in many industrial combustion systems that rely on radiative heat transfer, such as kilns and furnaces [20]. Soot primary particles are typically 15–60 nm in diameter and have a graphite-like hexagonal structure in each stack of the layers [26–29]. When emitted from a flame, soot particles cause environmental and health problems [26, 30]. To achieve a highly radiating flame for increased heat transfer without emitting soot into the atmosphere requires a comprehensive understanding of soot formation and oxidation.

The complex process of soot formation involves chemical reactions such as fuel pyrolysis, along with physical interactions between the soot particles and fluid dynamics [29]. Soot formation is triggered by the pyrolysis-induced decomposition of the primary fuel, leading to the subsequent generation and conversion of acetylene and benzene into phenyl species, as well as the formation of polycyclic aromatic hydrocarbons (PAHs) [31]. These intermediate compounds are recognised as precursors of soot and play a significant role in the initiation of soot formation. Soot nuclei are then formed from the coalescence of PAHs, followed by surface growth. This process has been described by the hydrogen-abstraction-C_2H_2-addition (HACA) mechanism [32], which involves two steps of chemical reactions:

$$A_i + H \rightleftharpoons A_{i-} + H_2 \tag{2.5}$$

$$A_{i-} + C_2H_2 \rightarrow \text{products} \tag{2.6}$$

where A_i represents an aromatic molecule with i rings, and A_{i-} denotes its radical. The evolution of soot particles in flames is depicted in Figure 2.3 and can be generally summarised into the following five stages: (1) soot inception; (2) nucleation; (3) surface growth and coagulation; (4) agglomeration; and (5) soot oxidation [33]. The mature soot particles are typically oxidised by oxygen and OH radicals. This fundamental knowledge underpins the investigation of soot evolution in different flames and combustion regimes.

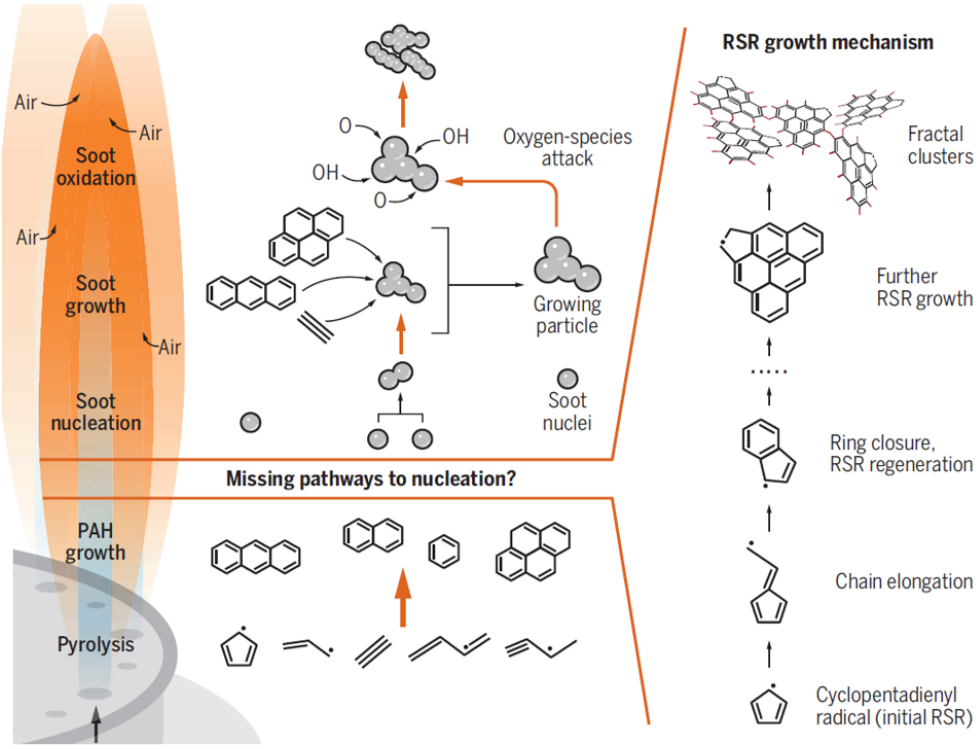

Figure 2.3: Soot evolution in a flame reproduced from Thomson and Mitra [33].

2.3 Soot evolution in hydrogen/hydrocarbon flames

Hydrogen has been widely used as a diluent to reduce carbon emissions including CO, CO_2, and soot from hydrocarbon flames, by taking advantage of its carbon-free nature [34–38]. Previous research has demonstrated a significant effect of hydrogen addition on soot reduction in sooting hydrocarbon flames. The peak soot volume fraction of an acetylene diffusion flame is reduced by 25% (from 1.5 ppm to 1.125 ppm) by adding 2.9 wt.% hydrogen, and is reduced by 51% from 1.5 ppm to 0.74 ppm by the addition of 6.2% hydrogen by mass [34]. Furthermore, the peak soot volume fraction of an ethylene flame is reduced by 13% from 7.5 ppm to 6.5 ppm by an addition of 14 vol.% hydrogen [39].

The impacts of hydrogen addition on soot production can be ascribed to three underlying mechanisms: the dilution effect, thermal effect, and chemical effect [40–42]. The dilution effect resulting from hydrogen addition reduces soot production by reducing the carbon concentration per unit volume of the fuel mixture [39, 40, 43]. As for the thermal effect, previous studies have indicated that the introduction of hydrogen into hydrocarbon flames raises the overall flame temperature, leading to reduced soot formation through the promotion of soot oxidation [10, 34, 40, 44, 45]. Moreover, the incorporation of hydrogen is associated with a tendency for smaller primary soot particle diameters at higher flame temperatures due to enhanced soot oxidation [46]. An experimental investigation focused on soot formation in acetylene laminar diffusion flames with hydrogen addition revealed a moderate increase in flame temperature by approximately 50–100 K, accompanied by a decrease in soot volume fraction with higher proportions of hydrogen [34]. The chemical inhibiting effect of hydrogen addition is complex and still under investigation. The increased concentration of hydrogen accelerates the inverse reaction of HACA (Equation (2.5)) and hence leads to the lower H-abstraction rate in PAH and particle surface growth processes [42]. Furthermore, adding hydrogen to nonpremixed ethylene/air flames chemically suppresses soot formation resulting from the lower production of C_2H_4, C_3H_8 and C_4H_{10} [40, 41]. Apart from the chemical inhibiting effect, hydrogen addition promotes the soot oxidation rate due to a higher yield of oxidising radicals [39, 43]. A numerical study showed that a 20% hydrogen addition to a laminar ethylene flame led to an increase in the OH mole fraction by 1.8% [43].

The effectiveness of the three mechanisms of hydrogen addition on soot reduction has been evaluated and compared in previous research. A fictitious

inert species i-H_2 has been used in a numerical study to isolate the chemical effects from the dilution effect, with the results showing that the dilution effect of hydrogen addition is more effective than the chemical effect on soot reduction [43]. A similar conclusion is drawn from the comparison between helium and hydrogen additions, where helium alone has a dilution effect on soot reduction [39]. Although these studies reached a consensus that adding hydrogen to hydrocarbon flames can achieve a significant soot reduction, the comparison of impact and effectiveness across these effects lacks conclusive evidence.

In comparison to utilising hydrogen as a diluent for reducing soot [47], the improvement of radiant intensity in hydrogen-based flames through hydrocarbon blending remains inadequately understood. Hydrogen flames are characterised by their inherently low radiant intensity resulting from their carbon-free composition. To enhance the radiant intensity, hydrogen fuels can be combined with hydrocarbons [48], reacting or non-reacting particles [49, 50], and small quantities of solid fuels [21, 51]. An experimental investigation [48] explored hydrogen/toluene blends with toluene concentrations ranging from 1–5 mol% (mole fraction of H_2) under turbulent nonpremixed conditions. The study revealed that increasing the additive concentration from 1–3 mol% has a significant impact on soot loading, whereas further increases in concentration exhibit diminishing effectiveness. The reacting or non-reacting particle seeding in hydrogen flames for radiation enhancement will be discussed in §2.7. These approaches have gained increasing attention in hydrogen research; however, the effect of adding a small amount of sooting hydrocarbons on the radiant intensity and other flame characteristics of hydrogen flames are insufficiently studied. Therefore, further investigating the flame features and combustion characteristics of turbulent nonpremixed hydrocarbon-blended hydrogen flames is needed to address this question.

2.4 Nitrogen oxides formation in hydrogen-based flames

In pure H_2/air combustion, one of the primary pollutant emissions is NO_x, generated due to the high flame temperature of hydrogen (refer to Table 2.1) caused by the oxidation of N_2 from the air. This contrasts with hydrocarbon combustion, where both thermal and prompt NO_x emissions are present. It has been reported that the NO_x emissions from hydrogen-enriched diesel blends were slightly higher than neat diesel in compression ignition (CI)

engine conditions, ascribed to the higher flame temperature from hydrogen addition [52]. While the smoke measured from diesel/H_2 combustion in CI engines was reduced by 20% from the implementation of hydrogen, the corresponding NO_x emissions were increased by 20% [53]. Similar conclusions were drawn from a comparison of NO_x emissions among H_2/CH_4 blends with varying H_2 concentrations that adding hydrogen to methane leads to considerable reduction in temperature levels and hence NO_x emissions. [54]. An experimental study reported that the NO_x emissions increase with hydrogen concentration in H_2/NH_3/air flames because thermal NO_x formation is enhanced by higher flame temperature in higher concentration flames [10]. Higher level of NO_x emissions is another major challenge to using hydrogen as a primary energy carrier in practical applications.

Nitrogen oxides (NO_x, comprising NO and NO_2) are part of the combustion products when hydrogen is burned under hydrogen/air conditions. Fuel NO_x, thermal NO_x, and prompt NO_x are the three types of NO_x formation. Fuel NO_x indicates that nitrogen is present in the fuel structure and chemically connected with other atoms. Utilising hydrogen as an alternative fuel avoids fuel and prompt NO_x formation but promotes thermal NO_x formation in the combustion process due to high flame temperature [13, 14]. Thermal NO_x formation is described as the direct synthesis of NO_x from oxygen and nitrogen that happens under high-temperature conditions through the decomposition of oxygen reacted with high-energy inert molecule (M) into highly active atomic oxygen [12]. It then reacts with nitrogen under high temperature, thereby NO_x is formed [55]. The pathways of elementary reactions for the thermal route, the N_2O route, and the NNH route are shown in Table 2.2.

Table 2.2: Chemical reaction equations of NO_x formation [12, 14, 56].

Thermal NO route	N_2O route	NNH route
$O + N_2 \rightleftharpoons NO + N$	$N_2 + O + M \rightleftharpoons N_2O + M$	$N_2 + H \rightleftharpoons NNH$
$N + O_2 \rightleftharpoons NO + O$	$N_2O + O \rightleftharpoons NO + NO$	$NNH + O \rightleftharpoons NO + NH$
$N + OH \rightleftharpoons NO + H$	$N_2O + H \rightleftharpoons NO + NH$	$NNH + O \rightleftharpoons N_2O + H$

The reaction $O + N_2 \rightleftharpoons NO + N$ initiates the NO formation and regulates the reaction rate, which is reliant on the flame temperature due to the high activation energy [12]. Figure 2.4 shows the temperature dependence of fuel, prompt and thermal NO_x formation pathways, reproduced from Gehrmann et al. [57]. Thermal NO_x formation increases with temperature and is more sensitive to temperature increase compared with fuel and prompt NO_x

formation pathways. Considering that hydrogen flames exhibit higher temperatures, the promotion of thermal NO formation is anticipated. Previous research has observed higher NO_x emissions from hydrogen flames compared with methane flames, which becomes one of the major concerns of hydrogen adaptation [58–60]. For example, an examination of various blends of hydrogen-doped natural gas under consistent thermal loading revealed that the amount of NO produced from pure hydrogen flames was approximately 6.5 times greater than the percentage generated in pure methane flames [59]. The NNH route, on the other hand, highlights the influence of H and O radicals in flame front and fuel-rich regions. It has been reported as an important reaction pathway, particularly in hydrogen flames [14, 61]. Experimental evidence supporting this pathway has been obtained in a low-temperature and low-pressure premixed rich hydrogen flame [62].

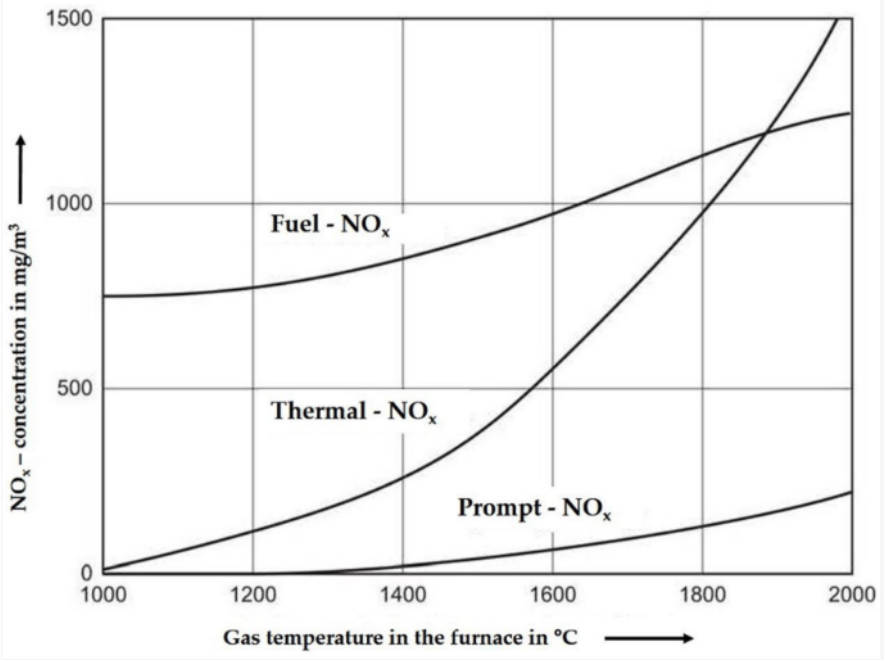

Figure 2.4: Different formation pathways of NO_x as a function of temperature. Reproduced from Gehrmann et al. [57].

While NO_x emissions and their underlying mechanisms in hydrogen flames have been well-documented, the influence of blending hydrogen flames with hydrocarbon/biofuel on NO_x formation remains poorly understood. The NO_x emissions of hydrogen-biodiesel were compared with hydrogen-diesel blends under compression ignition engine operation to evaluate the effectiveness of biodiesel addition on NO_x reduction [63, 64]. The results showed that the NO_x emission from these blends is dependent on hydrogen energy

share ratios as the NO_x emission from hydrogen-biodiesel was increased for low-hydrogen energy share ratios, in contrast to a decrease for high-hydrogen energy share ratios. Another study of NO_x emission in duel-fuel engines showed that replacing conventional diesel with rapeseed methyl ester (RME) in hydrogen blends reduced the NO_x emissions, ascribed to higher combustion temperature of biodiesel fuel [65, 66]. However, blending turbulent nonpremixed hydrogen flames with hydrocarbon/biofuel for radiation enhancement features distinct NO_x formation compared with that in internal combustion engines, as the elevated radiation loss reduces flame temperature and hence impacts the NO_x emission. It is critical to understand and document the complex interactions between biofuel addition for radiation enhancement and the corresponding effect on NO_x emission, as one of the important combustion characteristics.

2.5 Liquid biofuels

2.5.1 Overview of liquid biofuels

Identifying suitable hydrocarbons with a high sooting propensity to be used as additives is essential for radiation enhancement in hydrogen flames. Biofuels present an appealing prospect as they can be derived from renewable resources. Various forms of biofuels can be obtained, such as biochar, biogas, and bio-oil [67]. Among these, liquid biofuels, including bio-oils, biodiesel, and essential oils, are considered promising additives due to their ease of blending compared with biochar, as well as their relatively higher energy densities compared with biogas [67–69].

Biodiesel, essential oils, and bio-oils are all derived from renewable resources. The properties of each type of fuel are complex, highly diverse, and largely dependent on the feedstocks and production methods. To demonstrate these characteristics of biofuels, the properties and composition are summarised from the literature in Table 2.3 for biodiesel, Table 2.4 for essential oils, Table 2.5 for wood-derived bio-oils, and Table 2.6 for other feedstock-derived bio-oils. Since the majority of the feedstocks are plants or by-products from industrial processes, the quality, quantity, and availability of these feedstocks are highly dependent on regional natural conditions and local industries.

Table 2.3: Properties of various biodiesel from different feedstock. The viscosity of the presented biodiesel is measured at 40 °C.

Feedstock	LHV (MJ/kg)	Viscosity (mPa · s)	Carbon (wt.%)	Hydrogen (wt.%)	Oxygen (wt.%)	C/H ratio	C/O ratio	Water content (wt.%)	Ref
Diesel	43	2.0–4.5	85.9	13.3	-	6.5	-	0	[70]
Soybean biodiesel	33	3.5–5.3	77.0	12.0	11.0	6.4	7.0	5	[71, 72]
Jatropha methyl ester	40	5.9	76.6	11.9	11.4	6.4	6.7	5	[70, 72]
Cottonseed methyl ester	40	5.6	76.4	11.7	11.6	6.5	6.6	5	[70, 72]
Rubber seed oil	40	5.4	76.9	11.8	11.3	6.5	6.8	5	[70, 72]

Table 2.4: Properties of different essential oils. The viscosity of the presented essential oils is measured at 40 °C.

Feedstock	Major composition (wt.%)	LHV (MJ/kg)	Viscosity (mPa · s)	Carbon (wt.%)	Oxygen (wt.%)	C/H ratio	C/O ratio	Ref
Orange oil	Limonene (97%)	46	0.9	87.4	0.1	7.5	N/A	[73, 74]
Eucalyptus oil	Eucalyptol (90 %)	41	1.7	79.9	8.4	6.9	9.5	[73, 74]
Tea tree oil	Terpinene-4-ol (42 %)	42	1.8	82.9	5.4	7.1	15.5	[73, 74]
Red pine oil	Monoterpene (87 %)	41	1.4	85.6	2.5	7.6	33.9	[75]
White pine oil	Monoterpene (79 %)	42	1.6	85.6	3.5	8.3	24.3	[75]
Cypress oil	Monoterpene (63 %)	39	2.7	81.8	8.5	8.9	9.6	[75]

Table 2.5: Properties of bio-oils from wood. The viscosity of the presented bio-oils is measured at 40 °C unless otherwise specified.

Properties	Wood								
	Red gum	Blue gum	Eucalyptus	Mallee	Pine	Poplar	Acacia	Oak	Beech wood
Cellulose	-	-	37	-	41	47	41	35	46
Hemicellulose	-	-	10	-	30	22	24	36	32
Lignin	-	-	27	-	29	20	15	27	22
Acetic Acid	9–10	-	3	6	3	5	-	-	-
Phenolic compounds	16–21	-	7	2	1	-	2	1	2
Heating value (MJ/kg)	26	23	27	14	17	19	-	20	31
Viscosity (mPa · s)	100	85	13 (50 °C)	54	22	-	-	72 (50 °C)	70–220
Carbon (wt.%)	63.7	56.5	63.0	43.9	45.7	18–30	57–62	48.7	28.1
Hydrogen (wt.%)	6.9	7.3	6.7	7.4	7.0	6–8	5.9–8.2	6.8	11.4
Oxygen (wt.%)	24.4	22.0	30.1	48.6	47	62–72	22–36	43.8	30.1
Nitrogen (wt.%)	0.1	0.1	0	0.1	<0.1	0.7–0.9	0.1–3.1	<0.1	0.4
C/H ratio	9.2	7.7	9.4	5.9	6.5	2.1–4.3	7–11	6.9	5.1
C/O ratio	-	-	2.1	0.9	1.0	0.3–0.5	1.6–3	1.1	1.9
Water content (wt.%)	7.7	21.0	35.5	20.8	17	29.7	-	16.1	39.2
Ref	[76, 77]	[76]	[78]	[79]	[80]	[81]	[82]	[83]	[84]

Table 2.6: Properties of bio-oils from other feedstocks. The viscosity of the presented bio-oils is measured at 40 °C unless otherwise specified.

Properties	Grass			Other			
	Rice straw	Wheat straw	Napier grass	Coconut shell	Sugar cane	Tobacco waste	Algae
Cellulose	55	33	39	18	48	39	9
Hemicellulose	33	38	20	56	39	5	17
Lignin	13	9	27	26	11	7	14
Acetic Acid	1	17	-	6	8	16	-
Phenolic compounds	10	10	47	53	4	56	-
Heating Value (MJ/kg)	14	12	29	20	18	14	26
Viscosity (mPa · s)	71 (50 °C)	14	3	1	14 (50 °C)	-	-
Carbon (wt.%)	20.7	34.5	49.9	59.1	55.1	28.3	59.5
Hydrogen (wt.%)	9.4	8.2	6.8	5.5	7.7	4.9	7.2
Oxygen (wt.%)	68.9	56.5	41.3	30.8	36.7	63.6	28.5
Nitrogen (wt.%)	0.6	0.8	1.4	4.2	0.5	3.1	4.0
C/H ratio	2.2	4.2	7.4	10.8	7.1	5.7	8.3
C/O ratio	0.3	0.6	1.2	1.9	1.5	0.5	2.1
Water content (wt.%)	-	46.9	49.4	10.1	6.2	58.6	26.6
Ref	[85]	[86, 87]	[88]	[89]	[85, 90]	[91]	[92]

Biodiesel

Biodiesel, an oxygenated fuel, typically consists of alkyl esters derived from non-edible feedstocks, such as jatropha, algae, and castor oil, which are categorised as second-generation feedstocks [93–95]. The utilisation of such feedstocks helps mitigate the impacts on land use, society, and the food market associated with large-scale production. Esterification, known for its high conversion efficiency, simplicity, and ability to produce high-quality fuel products, is the most widely employed method for biodiesel production [95].

The properties of biodiesel from different feedstock are shown in Table 2.3. The presence of oxygen in biodiesel not only results in a lower heating value when compared with conventional fuels but also contributes to the promotion of thermal NO_x formation due to increased flame temperatures [71]. In addition, oxygenated fuels have been widely used to reduce soot in combustion systems such as internal combustion engines [96, 97]. Biodiesel typically contains around 10 wt.% oxygen content (refer to Table 2.3), while bio-oil contains higher oxygen content ranging from 20 to 70 wt.% (refer to Table 2.5 and Table 2.6).

Essential oils

Essential oils primarily consist of terpene-related hydrocarbons $(C_5H_8)_n$ comprising monoterpenes (C10), sesquiterpenes (C15), and diterpenes (C20), which are biosynthesised through isoprene units with five carbon atoms [75]. Table 2.4 presents the properties of different essential oils. Due to the presence of oxygen content, their heating value is observed in the range of 39 MJ/kg to 46 MJ/kg [73, 75]. The kinematic viscosity of essential oils is relatively lower than biodiesel, typically ranging from 1.4–2.7 mPa · s [75]. Similar to biodiesel, essential oils have been primarily considered as potential alternative fuels for diesel engine combustion [74, 75].

Essential oils are obtained from various plant parts such as roots, bark, leaves, and aromatic components through processes such as distillation or solvent extraction [98]. The growing demand for "therapeutic grade" essential oils has led to increased production, resulting in a significant fraction of essential oils being generated as waste products [74].

Bio-oils

Bio-oil is produced through biomass refining, which involves specific treatments to convert lignin, cellulose, and hemicellulose obtained from renewable

plant resources into fuel. Biomass refining processes enable the extraction of hemicellulose and lignin from waste and pre-treatment liquids generated by the pulp and paper industry. Furthermore, these processes can facilitate the production of high-value-added products such as carbon fibre and polymers through conversion pathways [81, 99]. The integration of biomass refining processes with the pulp and paper industry is feasible due to the substantial consumption of biomass resources by this sector. Lignocellulosic biomasses typically consist of 35–55 wt.% cellulose, 20–40 wt.% hemicellulose, 10–25 wt.% lignin, and additional extractives [100]. Although hemicellulose possesses a relatively low calorific value (14 MJ/kg) and is not well-suited for direct combustion, it can be utilised as an additive to enhance soot radiation heat transfer and enhance flame stability [101, 102]. Due to its soot-enhancing feature, the proportion of hemicellulose in bio-oil may be an important indicator for sooting propensity.

Bio-oils are commonly obtained from a thermal conversion process termed pyrolysis. As the liquid product (bio-oil) yield is highly dependent on temperature, fast pyrolysis, which is characterised by high heating rates in the range of 450–600 °C/min, is desirable for bio-oil production [79]. The bio-oil extraction rate of fast pyrolysis reaches a peak at about 75 wt.% of biomass feed basis in comparison with 50 wt.% of slow pyrolysis [103].

The properties of bio-oils derived from wood and other feedstocks are shown in Table 2.5 and Table 2.6, respectively. Bio-oils exhibit characteristics such as high viscosity, elevated water content, low volatility, acidity, significant presence of aromatics, diverse oxygenated compounds, as well as ash and other solid impurities [104]. They are complex mixtures composed of multiple components, including substantial quantities of water, organic acids, phenolic compounds, sugars, guaiacol, and furan [81]. Lignin present in the feedstock serves as an abundant source for the synthesis of phenolic chemicals [100]. The heating value of bio-oils ranges from 14 MJ/kg to 18 MJ/kg, which can be attributed to their high water content (15–30 wt.%) and significant oxygen content (35–40 wt.%) [78]. The low volatility of bio-oil is attributed to the presence of non-volatile materials, such as sugars and phenolics, in substantial amounts [67]. Furthermore, the viscosity of bio-oil surpasses that of biodiesel, typically ranging from 35–1000 mPa · s at 40 °C, and is highly dependent on the specific feedstock used [99].

2.5.2 Sooting propensities of liquid biofuels

The chart shown in Figure 2.5 illustrates the factors that affect the sooting propensity of a fuel. The influencing factors will be discussed in the following subsections.

Effect of C/H ratio

Soot is predominately carbon, indicating that fuels with a higher carbon content should produce more soot for a given amount of fuel at the same oxidation rate. Hydrogen content is involved in the reaction with O_2 to form OH, which will affect the soot oxidation rate (refer to §2.3). Therefore, the carbon to hydrogen ratio (C/H ratio) is often used as one of the factors to indicate the sooting propensity of a fuel [64, 105, 106]. The evidence, from both experimental and modelling approaches, shows that fuels with a higher C/H ratio produce more soot [107–109]. Biodiesel and essential oils have a similar C/H ratio, typically around 6.5, while bio-oils show a large variation in C/H ratio, ranging from 2.1 to 11. Fuel with a higher C/H ratio can be used as a potential additive to hydrogen flames to increase soot (refer to Table 2.3 and Table 2.4).

Further to the C/H ratio, the level of unsaturation — the presence of carbon double-bonds and carbon triple-bonds — intensifies the propensity for soot formation owing to the relatively lower bond energies. This characteristic makes them more susceptible to the formation of polycyclic aromatic hydrocarbons (PAHs) [70, 110]. It is also highlighted that the formation of acetylene species, known to be essential intermediates to soot precursor formation, is proportional to the number of carbon double bonds in methyl esters [70]. Therefore, the unsaturation degree should be combined with C/H to predict which fuel is likely to have a higher sooting propensity in hydrogen flames.

Effect of oxygenated and non-oxygenated fuel

The inclusion of oxygen content in a fuel has a significant influence on its propensity for soot formation [51, 70, 74, 111–113]. Fuels containing oxygen are commonly known as oxygenated fuels, while fuels lacking oxygen, such as conventional fossil fuels, are referred to as non-oxygenated fuels. As discussed in §2.5.1, liquid biofuels are oxygenated fuels with large differences in the amount of oxygen content, ranging from 0.1 wt.% (orange oil) to 72 wt.% (poplar oil). In a study into using biodiesel to replace diesel fuel in conventional diesel engines, experimental and computational results showed that the soot mass concentrations of jatropha methyl ester were reduced by

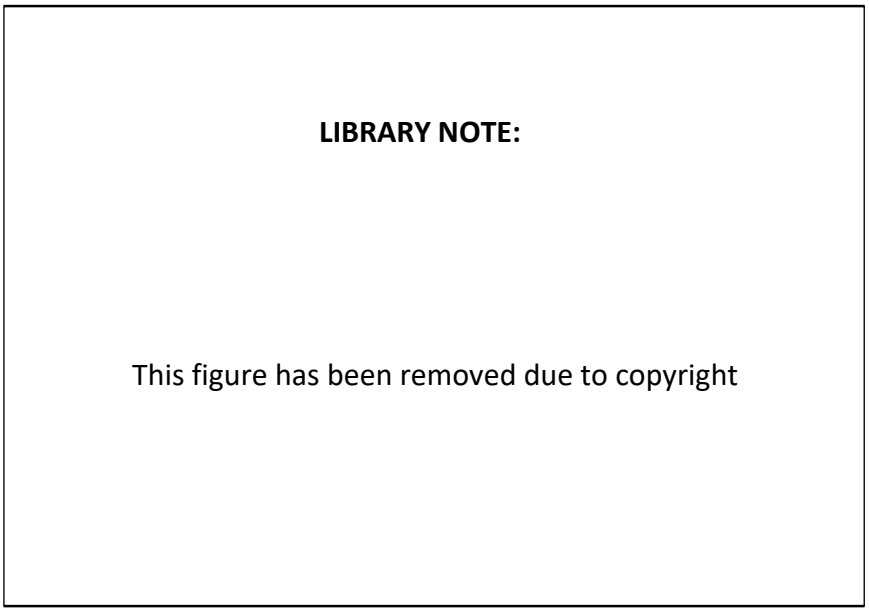
LIBRARY NOTE:
This figure has been removed due to copyright

25% and 80% at different loads because the presence of oxygen content both decreases soot formation and accelerates the soot oxidation rate [70]. The numerical simulation of adding oxygenates to diesel fuels on soot shows that oxygenated additives suppress sooting propensity by reducing the soot precursor species in fuel-rich regions due to the additional oxygen atom [114]. Similar results are found when blending different types of essential oils in diesel. The oxygen in fuel blends promotes soot oxidation, thus resulting in lower particle mass emissions. This is because the fuel-bound oxygen has a higher heat release rate and restricts the local fuel-rich zones where soot is formed [113]. Additionally, the primary particle diameter in flames with oxygenated fuel decreased by 2.8–14.3% compared with diesel fuel, due to fewer soot precursors formed in oxygenated fuels, which slows the surface growth and accelerates the oxidation process [113]. These oxygenated biofuels have also been tested in nonpremixed laminar methane/air flames to analyse their sooting propensities [51]. The results show that oxygenated fuels may produce fewer soot particles because they are already partially oxidised, which is one major difference from non-oxygenated hydrocarbons. To include oxygen content into the consideration of sooting propensity, an effective C/H ratio has been proposed, as follows [115]:

$$(C/H)_{eff} = \frac{C - \frac{1}{4}O_{-} - \frac{1}{2}O_{=}}{H} \tag{2.7}$$

where C, O, and H denote the numbers of carbon, oxygen, and hydrogen atoms, respectively. The O_{-} and $O_{=}$ subscripts denote the numbers of single- and double-bonded oxygen atoms, respectively. The effective C/H ratio indicates the equilibrium between soot formation and oxidation rate. Previous studies have focused on using oxygenated fuels to reduce soot emissions, mostly in diesel engines. How oxygenated fuel and non-oxygenated fuels will affect the soot evolution in turbulent hydrogen-based flames, where there are abundant sources to form OH, needs further investigation in the context of hydrogen blending.

Effect of water content

The presence of water content, which is higher in bio-oils than other biofuels (refer to Table 2.5 and Table 2.6), affects soot production via three mechanisms: the dilution, thermal and chemical effects [116]. Similar to hydrogen addition (refer to §2.3), the dilution effect of water content reduces soot production by decreasing the carbon flux of fuel mixtures [117]. The thermal effect of water leads to a decrease in the flame temperature, which promotes the formation of benzene and PAHs and slows the oxidation rate [118]. The

chemical effect of the water, which increases the OH concentration from the decomposition of water, accelerates the oxidation rate, and has been reported to be more significant than the thermal effect [116, 118, 119]. The increase of H_2O enhances the OH radical formation and reduction of the H radical from the reverse reaction $OH + H_2 \rightleftharpoons H + H_2O$. The subsequent decreased H-abstraction reaction slows the soot surface growth [43]. Bio-oils possess higher water content than biodiesel and essential oils due to their production method of fast pyrolysis, which needs to be considered when analysing their soot propensities [103].

Effect of chemical structure and functional group

Previous research has shown that the different chemical structures and functional groups of fuels have a major influence on sooting propensity. Five fuels with different chemical structures have been modelled to investigate the effect of functional groups on PAH formation under spray combustion conditions in diesel engines [120]. The sooting propensities of the five fuels are in the ascending order of ethanol $<$ n-butanol $<$ methyl-decanoate $<$ n-heptane $<$ 2,5-dimethylfuran. The phenol radicals are produced from the cyclic structure of 2,5-dimethylfuran, resulting in its highest sooting propensity.

It has been highlighted that fuels with a longer carbon chain have a higher sooting propensity because they tend to form more intermediate hydrocarbons such as C_3H_6 and C_2H_4 [120, 121]. The hydroxyl group (-OH) inhibits soot formation based on the observation that butane isomers produce more soot than butanol isomers [122]. Due to the presence of the hydroxyl group, butanol isomers tend to form more stable intermediates such as aldehydes and ketones.

A study has compared the particulate matter (PM) emissions between the functional group of ether in tea tree oil and the hydroxyl group in eucalyptus oil by controlling the oxygen in both blends at 2.2 wt.% [123]. The lower PM emission from tea tree oil implies that the functional group of ether has a stronger effect on soot reduction. Furthermore, the results of reaction path studies show that fuels that have ester groups in their molecular structure form fewer soot precursors due to their different consumption pathways when compared with n-alkanes [124].

The effect of the methylene group on soot formation reveals that the chemical structure of carbon double bonds in the methylene group contributes to the

highest soot production of rubber seed oil methyl esters [70]. However, there is a lack of understanding and quantitative comparison of how different functional groups in liquid biofuels, such as the methoxy, hydroxyl, and methyl groups and their combinations, will have effects on soot evolution in turbulent nonpremixed hydrogen/biofuel flames for radiation enhancement.

Efforts have been dedicated to the investigation of sooting propensities of different types of renewable hydrocarbons. Different concentrations of orange, eucalyptus and tea tree oil were blended with diesel to compare the particle emissions between essential oils and diesel fuel [73]. The results show that essential oil blends have higher particulate mass at all loadings.

The sooting propensities of C8 oxygenates were tested under high temperature, higher pressure, and spray conditions [112]. The sooting propensity of the oxygenates increases in the order of ester $<$ aldehyde $<$ alcohol $<$ ketone. A more extensive study of the sooting propensities of 275 different renewable oxygenated hydrocarbons has been conducted in nonpremixed laminar methane/air flames, which indicated that aldehydes and ketones have a similar sooting propensity [51]. The sooting propensities of ester have also been reported in increasing order: methyl and ethyl esters $<$ carboxylic acids, propyl esters $<$ butyl and pentyl esters [51]. These studies are all motivated by the demand for soot reduction in internal combustion engines under spray conditions, which are different from industrial combustion systems. In addition, the effectiveness of biofuels with different sooting propensities on radiation enhancement in turbulent hydrogen flames is unknown.

Bond dissociation enthalpy (BDE) is closely related to the effect of functional groups on sooting propensities, as it is the energy needed to break a chemical bond, separating the bonded atoms into individual atoms with unpaired electrons. It quantifies bond strength and is crucial for understanding chemical reactions and molecule stability.

As mentioned in previous sections, it has been reported that the presence of carbon double bonds in unsaturated mono-alkyl esters, methyl crotonate, and methyl esters results in a greater sooting tendency, ascribed to the weak BDE of carbon double bonds [125–127]. Chemical reactions tend to initiate at the bond with the lowest BDE. In the methoxy group, chemical reactions commonly initiate at the O-C bond with the lowest BDE ($\sim 250\,\mathrm{kJ/mol}$) [128, 129]. The BDE of the O-C bond in the methoxy group varies in different chemicals (e.g. anisole and guaiacol) due to the influence of adjacent chemical structures—the BDEs of the C-H bond in the aromatic ring in guaiacol (481–

490 kJ/mol) are significantly higher than that in anisole (471–476 kJ/mol) due to the additional hydroxyl group (-OH) in the ortho position of the methoxy group [129, 130].

The BDE of the chemicals is a critical factor in analysing the sooting propensities of the biofuel additives. Based on all the factors discussed above that may affect sooting propensity, bio-oils derived from eucalyptus, Napier grass, coconut shell, tobacco waste, together with essential oils including orange oil and eucalyptus oil, are considered to be potential additives.

2.5.3 Surrogates for liquid biofuels

The direct analysis and study of biofuels with intricate compositions pose significant challenges [78]. Instead, it is advantageous to identify suitable surrogate compounds for biofuel analysis. A fuel surrogate refers to a simplified analogue that consists of one or more well-defined hydrocarbon species. These surrogates possess known compositions and properties that allow them to replicate the chemical, physical, and combustion characteristics of complex practical fuels. This approach is commonly employed in both experimental and computational investigations of combustion processes [131, 132]. For this purpose, specific chemicals with well-established chemical mechanisms have been selected as surrogates to emulate the physical and chemical properties of corresponding biofuel additives. A summary of the surrogate properties is provided in Table 2.7.

Toluene (C_7H_8)

Toluene is a non-oxygenated aromatic hydrocarbon consisting of a methyl group attached to a phenyl group. It is known as one of the prominent components of bio-oil, and has a highly sooting propensity. Toluene has been studied as an additive for enhancing radiant intensity in turbulent nonpremixed hydrogen flames, and achieved highly radiating hydrogen flames by blending 1–5 mol% prevapourised and atomised toluene [48]. Toluene is chosen as a referencing additive in this experiment for comparison.

Eucalyptol ($C_{10}H_{18}O$)

Eucalyptol, a terpenoid oxide, has been selected as a surrogate for eucalyptus oil due to its high presence in the oil composition, accounting for approximately 90 wt.%. Eucalyptol plays a dominant role in determining the chemical and physical properties of eucalyptus oil [74]. Eucalyptus oil is an

Table 2.7: Properties of essential oil and bio-oil surrogates.

Name	Density (kg/m^3)	Molecular Wt (g/mol)	LHV (MJ/kg)	Dynamic Viscosity ($mPa \cdot s$)	Boiling Point (K)	C/H_{eff} ratio	C/O ratio	Ref
Essential Oil Surrogate								
Eucalyptol ($C_{10}H_{18}O$)	922	154	43	2.6	445	6.4	7.5	[73, 74, 133, 134]
Limonene ($C_{10}H_{16}$)	841	136	44	0.8	449	7.5	-	[74, 133, 135]
Bio-oil surrogate								
Toluene (C_7H_8)	867	92	42	0.6	384	10.5	-	[136–138]
Anisole (C_7H_8O)	995	108	33	0.9	427	10.0	5.3	[139]
Phenol (C_6H_6O)	1070	99	32	8.0	454	11.3	4.5	[140, 141]
Guaiacol ($C_7H_8O_2$)	1110	124	31	6.1	478	9.5	2.6	[141–143]

oxygenated fuel with a hydroxyl functional group, which can be presented by eucalyptol. It allows the investigation of how oxygenates and non-oxygenates, together with different functional groups, affect the soot production in hydrogen/biofuel flames. It is expected to have a highly sooting propensity due to its relatively high C/H ratio.

Limonene ($C_{10}H_{16}$)

Limonene, a terpene compound, has been identified as the surrogate for orange oil due to its predominant presence in the oil composition, accounting for approximately 97 wt.%. It is derived from citrus fruit peels and does not contain any oxygen. Therefore, it is expected to yield more soot than eucalyptol as the oxygen content facilitates the oxidation of soot. It has been reported that the particle number emissions of all essential oil blends, namely eucalyptol, limonene, and tea tree oil, are higher than that of biodiesel [74]. Limonene consists of an allylic group with the lowest BED of the C-H bond at 371 kJ/mol where chemical reactions tend to initiate [144].

Anisole (C_7H_8O)

Anisole is an organic compound characterised by a phenyl group bonded to a methoxy group, which resembles a lignin structure [129]. It is commonly employed as a simplified surrogate for bio-oil in studies concerning the formation and oxidation of methoxy phenol, a primary precursor of polycyclic aromatic hydrocarbons (PAHs) and soot in biomass combustion [145]. Reactions involving methyl radicals and anisole primarily occur through H-abstraction at the methoxy group, which exhibits significantly higher reactivity compared with attacks on the aromatic ring. Anisole features a relatively weak bond of approximately 264 kJ/mol (BDE) between the oxygen and methyl group, leading to the rapid formation of substantial quantities of the phenoxy radical [139]. It is noticed the weakest bond O-C of the methoxy group in anisole is higher than that in guaiacol at 243 kJ/mol, and is lower than the BED of the C-H bond in the allylic group of limonene. Investigating anisole can provide valuable insights into the behavior of the phenoxy radical, serving as an important surrogate for intermediates in the oxidation of other aromatic compounds.

Guaiacol ($C_7H_8O_2$)

Guaiacol is characterised by a phenyl group attached to a hydroxyl group and a methoxy group (-OCH_3). It is a prominent aromatic oxygenate compound

produced through lignin pyrolysis, demonstrating chemical structures and functional groups akin to lignin patterns. Guaiacol plays a significant role in the generation of polycyclic aromatic hydrocarbons (PAHs) and soot during the combustion of biomass and bio-oil [129]. Similarly to anisole, the reaction of guaiacol involves the O-C bond in the methoxy group, which exhibits a lower BDE at 243 kJ/mol than anisole and contributes to the formation of methyl radicals [146]. However, the presence of the hydroxyl group in the ortho position of guaiacol promotes a chain radical mechanism and higher BDE of C-H bonds from 481–490 kJ/mol, resulting in lower yields of aromatic products when compared with anisole [129].

2.6 Methods of additive introduction

2.6.1 Overview of introduction methods

Liquid fuels can be introduced either by direct spraying or by entrainment with a carrier gas. When liquid fuel droplets are introduced, they undergo a phase change from liquid to vapour before initiating decomposition. The method of introducing additives into the flame, either through prevapourisation or atomisation, can have a significant impact on the production of soot, NO_x, and CO emissions [48, 147, 148].

Promoting the prevapourisation of palm methyl ester fuel droplets has been observed to result in reduced soot production and lower NO_x emissions [147]. Under turbulent nonpremixed conditions, fuel droplet atomisation generates local fuel-rich mixtures, promoting the formation of soot [51]. A comparison between introducing toluene additives into turbulent nonpremixed hydrogen flames through the ultrasonic spray and prevapourisation methods has been conducted to investigate their influence on soot evolution [48]. It was found that ultrasonic spray flames produce significantly higher levels of polycyclic aromatic hydrocarbons, with a greater concentration of soot near the nozzle exit plane, compared with prevapourised flames.

2.6.2 Atomisation

Atomisation of liquids in the form of a spray is vital in numerous practical applications across the fields of engineering, medicine, and agriculture. Fuel spray technology is widely employed in combustion systems such as internal combustion engines, boilers, and gas turbines, as it assists in the efficient and effective combustion of liquid fuels, without introducing the complexity of prevapourisation [149–151]. Fine sprays generated from liquid fuel atom-

isation promote uniform fuel-air mixing, which is essential for stable and efficient combustion, as they break up the fuel into small droplets, increasing surface area and facilitating better mixing with the oxidiser. This contributes to the complete combustion of liquid fuels, minimising the production of harmful pollutants and improving overall combustion efficiency [149, 152, 153]. In addition, atomisation of liquid fuels affects flame characteristics such as radiant heat flux and NO_x emissions. It has been reported that spray flames generated by ultrasonic atomisation tend to have higher radiant heat flux compared with prevapourised flames, due to the enhanced soot formation from promoted fuel-rich regions [48].

In spray flames, the liquid fuel is atomised into small droplets to promote the evaporation rate by increasing the contact area between the fuel liquid droplets and air [154]. Atomisation is the essential process that determines the spray characteristics including mean droplet size, droplet size distribution, and velocity [155]. These spray characteristics are closely associated with fuel density, viscosity, and surface tension and have a marked effect on flame structure, NO_x, and soot formation. It is found that the decrease in surface tension of liquid fuel results in smaller droplet size [156]. The correlation between droplet diameter and soot formation has been reported, showing that the increase in droplet diameter suppresses local soot formation but expands the soot formation region [157]. In addition, the viscosity of these fuels has a different sensitivity to temperature, which will in turn affect the fluid dynamics within the flame.

There are various atomisers for generating sprays in practical applications using different fundamental mechanisms to atomise the liquid. Figure 2.6 schematically illustrates six types of common atomisers, namely pressure, pressure-swirl, rotary, ultrasonic, external mixing and internal mixing atomisers. They utilise different mechanisms to atomise the liquid into droplets.

Pressure and pressure swirl atomisers inject liquid at high pressure through an orifice, which are commonly employed in diesel engines. They have the advantages of simplicity in design and ease of operation, but are not suitable for producing fine droplets with viscous liquids. Considerable advancement in understanding has been made, especially in the context of internal combustion engines, aiming to achieve more homogeneous air-fuel mixing by generating fine droplets since homogeneous mixing contributes to a better charge, fewer NO_x and particulate emissions. For a certain amount of liquid

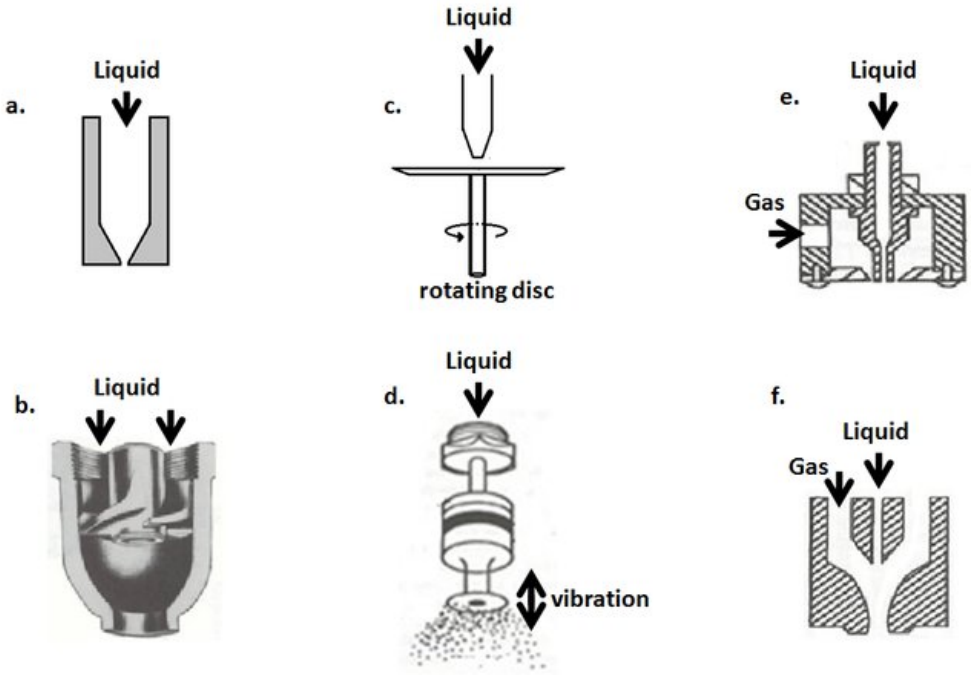

Figure 2.6: Various atomisers: (a) Pressure (b) Pressure-swirl (c) Rotary (d) Ultrasonic (e) External mixing (f) Internal mixing. Adapted from Lee et al. [158].

fuel injected into the combustion chamber, smaller droplet size (micrometre range) increases the fuel surface area for superior air-fuel interaction and mixing, leading to more complete combustion [159, 160].

Amongst the contributing factors and parameters, spray characteristics from pressure jets are subjected to fuel injection pressure, nozzle geometry, and ambient conditions [160, 161]. Diesel engines usually favour high-Weber jets with a high injection pressure and a small diameter orifice as they induce higher momentum of the droplets [162, 163]. The injection pressure was reported to have a greater influence on velocity distribution, spray tip penetration (STP), and Sauter mean diameter (SMD) than nozzle length to diameter ratio [164]. The SMD is reduced by 15% as the injection pressure is increased from 100 to 200 MPa, compared with an 8% reduction in SMD when the nozzle length to diameter ratio is changed from 4 to 8 (nozzle diameter remained constant). The Sauter mean diameter is defined in Equation 2.8 as the diameter of a sphere with the same volume-to-surface area ratio as the actual droplets in the spray [165].

$$SMD = \frac{d_v^3}{d_s^2} \tag{2.8}$$

where d_v is the volume diameter and d_s is the surface diameter, defined as:

$$d_v = (\frac{6V_p}{\pi})^{1/3} \tag{2.9}$$

$$d_s = (\frac{A_p}{\pi})^{1/2} \tag{2.10}$$

where V_p and A_p are the volume and surface area of the particle, respectively.

Ultrasonic atomisation involves the use of vibrations to create alternating high-pressure and low-pressure regions, causing the liquid to form small droplets that detach from the surface, thereby a fine mist is generated. It typically utilises a piezoelectric transducer that converts electrical energy into high-frequency mechanical vibrations. The size of the droplets generated is governed by the specific details of an ultrasonic nebuliser, such as its operating frequency. Ultrasonic atomisation may bring complexity to the configuration when designing a spray burner for establishing flames.

External mixing atomiser using the airblast effect is emphasised in this project as it is capable of atomising highly viscous liquid. Moreover, it demonstrates the potential for using gaseous fuels to atomise liquid fuel, which is desirable for the approach of biofuel/hydrogen blending. The mechanisms of gas-assist atomisation will be discussed in the following section.

2.6.3 Gas-assist atomisation

2.6.3.1 Process and mechanism of gas-assist atomisation

Gas-assist atomisation is an important method of atomisation that has been extensively employed and studied for its advantageous application in practical combustion systems. Gas-assist atomisation involves the injection of a liquid stream within a surrounding gaseous medium with velocity difference, facilitated by shear and turbulent interactions induced instabilities occurring on the interface of the two-phase flows. The dynamic motion of the interface between the liquid and gas phases induces shear effects, promoting the rapid breakup and fragmentation of the liquid flow into smaller objects.

Upon injection of the liquid flow into the gaseous medium, Kelvin-Helmholtz instabilities manifest at the interface between the two flows characterised by distinct velocities or densities [166, 167]. This, in turn, leads to an amplification of Rayleigh-Taylor instabilities. Deformations promptly emerge on the liquid interface and progressively intensify in magnitude as distance and time elapse from the nozzle exit. This phenomenon is commonly referred to

as the primary atomisation mechanism in which the dispersed phase volume fraction is typically above 10^{-3} [153].

The secondary atomisation mechanism takes place at a more distant location downstream, where the fragmented liquid undergoes interaction with aerodynamic forces. These forces contribute to the additional disintegration of the liquid fragments into smaller elements. During this phase, interactions between individual droplets become minimal. The secondary atomisation corresponds to a dilute spray regime where the dispersed phase volume fraction ranges from 10^{-6} to 10^{-3}. Secondary atomisation is quantitatively classified into different regimes based on the Weber number, namely vibrational breakup (We $\sim$ 6), bag breakup (We $<$ 10), bag/streamer breakup (We $<$ 25), stripping breakup (We $<$ 50), and catastrophic breakup (We $>$ 50) [168–170]. The exit Weber number characterises the relationship between inertial forces and the surface tension forces to study fluid dynamics, which is defined in Equation 2.11:

$$We = \frac{\rho_g (U_g - U_l)^2 D_l}{\sigma} \tag{2.11}$$

where ρ_g is the density of the gas, U_g and U_l are the bulk mean velocity of the gas and liquid, respectively, D_l is the initial liquid jet diameter, σ is the surface tension of the liquid.

The smaller elements and droplets generated from secondary atomisation are further subjected to the interactions with gas which enhances the dispersion of the droplets. The aerodynamic transport of droplets is less significant and the dispersed phase volume fraction is less than 10^{-6} such that the droplets behave almost as a gas [153]. As the finer and dispersed droplets are exposed to the gas, the increased surface area facilitates faster evaporation. Compared with dilute sprays, the dense spray behaviour is less understood due to the challenges in applying experimental diagnostics [171, 172].

2.6.3.2 Influencing factors of spray characteristics

The physical properties of the gas and liquid greatly impact the atomisation performance [168, 173]. At constant injection and ambient conditions, higher viscosity inhibits the instabilities induced by deformation and disturbance at the interface, hence delaying the atomisation. An increase in liquid density and surface tension has been found to have negative influences on the spray flow breakup. In studies of replacing conventional fuels with alternative biofuels (e.g. biodiesel) in spray regime, it was concluded that biofuels

tend to form droplets with larger SMD because biofuels usually possess higher density, surface tension, and viscosity [95, 174]. For example, rapeseed biodiesel produces a larger SMD value (29 µm) than that of coconut biodiesel (20 µm) due to its higher magnitudes of density, viscosity, and surface tension [165].

Apart from the intrinsic properties of the gas and liquid, non-dimensional parameters play an important role in the spray characteristics of gas-assist atomisation, including gas/liquid momentum flux ratio, Reynolds number ratio, Weber number, and Ohnesorge number. The gas/liquid momentum flux ratio (ψ_p) is defined in Equation 2.12 as [175]:

$$\psi_p = \frac{\rho_g U_g^2}{\rho_l U_l^2} \tag{2.12}$$

where the subscripts g and l denote gas and liquid, respectively, ρ is the density of the fluid, U is the bulk mean initial velocity.

The exit Weber number and bulk mean Reynolds number are defined in Equation 2.11 and Equation 2.3, respectively.

The Ohnesorge number (Oh) is commonly used in fluid dynamics to compare the relation between viscosity and surface tension among various types of fluids. It is defined in Equation 2.13 as:

$$Oh = \frac{\mu}{\sqrt{\rho \sigma d_{jet}}} \tag{2.13}$$

where μ, ρ, and σ are the dynamic viscosity, density, and surface tension of the fluid respectively, and d_{jet} is the jet diameter of the fluid. The Oh of water tested in this work is calculated at 0.006, indicating that the fluid behaviour is dominated by viscosity rather than surface tension. This parameter is useful for comparison amongst liquid fuels with different physical properties.

Although there is consensus on the influence of the liquid physical properties on the spray characteristics, the dominant parameter remains inconclusive. It has been identified that the relevant parameter for liquid disintegration is the Weber number. The impact of turbulence level and the fuel/air mass ratio on primary breakup length has been highlighted in addition to the turbulent Weber number [176]. The liquid jet-Reynolds number (i.e. liquid velocity) has been reported to play an important role in predicting the initiation of jet instabilities and governing the liquid flow structure [177]. Some studies emphasised that the atomisation process is mainly dependent on gas-to-liquid

velocity ratio [178–182], whereas other work has highlighted the atomisation process is primarily affected by gas-to-liquid momentum ratio [183–186]. The understanding of the dominant non-dimensional influencing parameters not only benefits the spray characterisation, but also is particularly crucial when employing hydrogen for atomising biofuel to attain stable flames with enhanced soot formation. Thus, there is a need to conduct purpose-designed experiments for parametric studies to better understand spray formation.

2.7 Particle seeding and thermal radiation

As mentioned in §2.3, aside from adding sooting liquid biofuels to hydrogen flames, another potential approach is seeding solid particles into the hydrogen flame for radiant heat flux enhancement. The seeded particles absorb heat from the flame and elevate the temperature of the particles. The seeded particles subsequently act as the source of blackbody radiation for radiant heat flux enhancement since the flame's radiated heat is proportional to the fourth power of temperature—$Q_r \propto T^4$.

Both inert and reactive particles have been seeded into flames for the purpose of radiative heat flux enhancement. It has been reported in previous research that adding 70–80 g/m^3 inert silicon carbide particles to methane/air flames by dust suspension generator leads up to a 33% increase in radiated flux, however, adding alumina and aluminum was found to reduce the radiative flux of methane/air flames. This phenomenon suggests that the alumina and aluminum particles act as heat sinks to absorb the heat of the flame. Given that the characteristic heating time of alumina and aluminum is longer than silicon carbide, the coefficient emissivity of silicon carbide is high, and the diameter of silicon carbide particles is small, hence the alumina and aluminum particles are more difficult to heat [187]. Seeding aluminum oxide (Al_2O_3) as nonreactive particles to hydrogen/air diffusion flames was found to decrease the radiative heat flux because the flame temperature is reduced via the convective heat loss to the Al_2O_3 particles, and the radiative heat blockage effects imposed by Al_2O_3 particle seeding [49, 50]. Adding magnesium oxide (MgO) has seen similar effects [50]. However, adding reactive particles to non-luminous flames displays different effects on radiant heat flux enhancement [21]. Adding reactive carbon particles at feed rates of 150 g/h and 250 g/h enhances the radiative heat flux of the hydrogen/air flame by 13% and 19%, respectively. This is due to the rise in flame temperature as well as the increase in CO_2 and soot generation from carbon particle addition [49]. The increase of 43% in average radiation flux was observed in premixed natural

gas flames by the injection of pulverised anthracite coal, in accordance with a 29 °C increase in flame temperature and the 7% improvement in flame emissivity coefficient [188]. It is also argued that the increase in flame emissivity coefficient plays a more important role in radiant heat flux enhancement than flame temperature, accounting for 17% and 83%, respectively [188].

Compared with using renewable liquid biofuels for radiation enhancement of poorly radiative flames, seeding solid particles may cause complexities and increase costs in the feeding configurations. In addition, the nonreactive particles may induce additional pollution to the environment. Therefore, this thesis focuses on using renewable liquid biofuels as soot-enhancing additives for hydrogen flames.

2.8 Research gaps

Despite the considerable research devoted to the various influencing factors for the evolution of polycyclic aromatic hydrocarbons and soot in hydrogen/hydrocarbon flames, there is a paucity of understanding regarding the efficacy and effectiveness of blending hydrogen flames with biofuels in enhancing PAH/soot formation for radiation improvement, and the corresponding impact on the combustion characteristics of turbulent non-premixed hydrogen-based flames. Based on the detailed literature review in the preceding sections, the critical research gaps in the knowledge are identified as follows:

1. Previous studies have tested and compared the sooting propensities of various hydrocarbon fuels, but essential oils are not included. In addition, it is unclear how effective these different types of prevapourised non-oxygenated additives will be on radiant intensity enhancement, global characteristics, and pollutant emissions in turbulent non-premixed hydrogen flames by promoting soot formation.
2. Oxygenated fuel has been reported to reduce soot by both inhibiting soot formation and promoting soot oxidation. There is a lack of understanding of how different prevapourised non-oxygenated and oxygenated biofuel additives affect radiation enhancement, PAH/soot evolution, and flame temperature in turbulent nonpremixed hydrogen flames.
3. Fuels with different functional groups have a marked impact on PAH/soot evolution and combustion characteristics. However, there is a

lack of qualitative and quantitative comparison between different types of liquid biofuels within the methoxy, hydroxyl, and methyl groups and their combinations on the effectiveness of radiation enhancement, soot evolution, and flame temperature in turbulent nonpremixed hydrogen flames.

4. It has previously been reported that introducing a non-oxygenated hydrocarbon additive by ultrasonic atomisation produces more polycyclic aromatic hydrocarbons than by prevapourisation. Furthermore, liquid fuels with various physical properties and atomisation mechanisms impact the spray characteristics, which in turn affects spray combustion performance. However, there is a lack of knowledge of how the biofuel additive morphology and their influencing parameters impact flame characteristics, soot formation, and the resultant radiant intensity in turbulent biofuel-blended hydrogen flames.

2.9 Aims and objectives

The overarching aim of this thesis is to establish and deepen the understanding of blending hydrogen flames with biofuels for promoting PAH/soot formation, radiation enhancement, and the corresponding impact on the combustion characteristics of turbulent nonpremixed hydrogen-based flames. To address the research gaps identified in §2.8, and achieve the thesis aims, the following objectives have been developed:

1. To establish the fundamental understanding and knowledge regarding the effect of blending turbulent nonpremixed hydrogen-based flames with prevapourised biofuels on flame characteristics, including flame appearance, flame luminosity, radiant intensity, and flame temperature.

2. To understand the influence of varying the concentration and the introduction methods of biofuel additives between prevapourisation and ultrasonic spray on global flame characteristics, with emphasis on the effectiveness of radiation enhancement and pollutant emissions in turbulent nonpremixed hydrogen-based flames.

3. To analyse the effect of adding oxygenated and non-oxygenated liquid biofuels with various functional groups (e.g. methyl, methoxy, hydroxyl and methylene groups) as additives to turbulent nonpremixed hydrogen-based flames on the effectiveness of flame appearance, flame

luminosity, radiation enhancement, pollutant emissions, and NO_x formation pathways.

4. To understand the effect of underlying mechanisms of blending hydrogen flames with biofuel additives via gas-assist atomisation on the effectiveness of radiant heat flux enhancement and the combustion characteristics of turbulent nonpremixed biofuel-blended hydrogen flames.

2.10 References

[1] H. Kobayashi, A. Hayakawa, K. K. A. Somarathne, and E. C. Okafor. "Science and technology of ammonia combustion". *Proc. Combust. Inst.* 37 (2019), pp. 109–133.

[2] G. Kakoulaki, I. Kougias, N. Taylor, F. Dolci, J. Moya, and A. Jäger-Waldau. "Green hydrogen in Europe-A regional assessment: Substituting existing production with electrolysis powered by renewables". *Energy Convers. Manag.* 228 (2021), p. 113649.

[3] S. Nag, P. Sharma, A. Gupta, and A. Dhar. "Experimental study of engine performance and emissions for hydrogen diesel dual fuel engine with exhaust gas recirculation". *Int. J. Hydrog. Energy* 44 (2019), pp. 12163–12175.

[4] R. W. Francisco Jr and A. A. M. Oliveira. "Measurement of the adiabatic flame speed and overall activation energy of a methane enriched $H_2/CO/CO_2/N_2$ low heating value mixture". *Int. J. Hydrog. Energy* 45 (2020), pp. 29533–29545.

[5] F. Verkamp, M. Hardin, and J. Williams. "Ammonia combustion properties and performance in gas-turbine burners". *Symp. (Int.) Combust.* 11 (1967), pp. 985–992.

[6] J. Armjtage and P. Gray. "Flame speeds and flammability limits in the combustion of ammonia: ternary mixtures with hydrogen, nitric oxide, nitrous oxide or oxygen". *Combust. Flame* 9 (1965), pp. 173–184.

[7] A. Ichikawa, A. Hayakawa, Y. Kitagawa, K. K. A. Somarathne, T. Kudo, and H. Kobayashi. "Laminar burning velocity and Markstein length of ammonia/hydrogen/air premixed flames at elevated pressures". *Int. J. Hydrog. Energy* 40 (2015), pp. 9570–9578.

[8] A. A. Khateeb, T. F. Guiberti, X. Zhu, M. Younes, A. Jamal, and W. L. Roberts. "Stability limits and NO emissions of technically-premixed ammonia-hydrogen-nitrogen-air swirl flames". *Int. J. Hydrog. Energy* 45 (2020), pp. 22008–22018.

[9] L. Vandebroek, F. Verplaetsen, J. Berghmans, A. Van den Aarssen, H. Winter, G. Vliegen, and E. Van't Oost. "Auto-ignition hazard of mixtures of ammonia, hydrogen, methane and air in a urea plant". *J. Hazard. Mater.* 93 (2002), pp. 123–136.

[10] J. Li, H. Huang, N. Kobayashi, Z. He, and Y. Nagai. "Study on using hydrogen and ammonia as fuels: combustion characteristics and NO_x formation". *Int. J. Energy Res.* 38 (2014), pp. 1214–1223.

[11] T. Kitagawa, T. Nakahara, K. Maruyama, K. Kado, A. Hayakawa, and S. Kobayashi. "Turbulent burning velocity of hydrogen-air premixed propagating flames at elevated pressures". *Int. J. Hydrog. Energy* 33 (2008), pp. 5842–5849.

[12] Y. Zeldvich. "The oxidation of nitrogen in combustion and explosions". *J. Acta Physicochimica* 21 (1946), p. 577.

[13] A. Frassoldati, T. Faravelli, and E. Ranzi. "A wide range modeling study of NO_x formation and nitrogen chemistry in hydrogen combustion". *Int. J. Hydrog. Energy* 31 (2006), pp. 2310–2328.

[14] M. Skottene and K. E. Rian. "A study of NO_x formation in hydrogen flames". *Int. J. Hydrog. Energy* 32 (2007), pp. 3572–3585.

[15] A. J. Reiter and S.-C. Kong. "Combustion and emissions characteristics of compression-ignition engine using dual ammonia-diesel fuel". *Fuel* 90 (2011), pp. 87–97.

[16] M. Gieras, R. Klemens, G. Rarata, and P. Wolański. "Determination of explosion parameters of methane-air mixtures in the chamber of 40 dm3 at normal and elevated temperature". *J. Loss Prev. Process Ind.* 19 (2006), pp. 263–270.

[17] H. F. Coward and G. W. Jones. *Limits of flammability of gases and vapors*. US Government Printing Office, 1952.

[18] C. Robinson and D. Smith. "The auto-ignition temperature of methane". *J. Hazard. Mater.* 8 (1984), pp. 199–203.

[19] I. Glassman, R. A. Yetter, and N. G. Glumac. *Combustion*. Academic Press, 2014.

[20] J. Marakis, C. Papapavlou, and E. Kakaras. "A parametric study of radiative heat transfer in pulverised coal furnaces". *Int. J. Heat Mass Transf.* 43 (2000), pp. 2961–2971.

[21] W. Hutny and G. Lee. "Improved radiative heat transfer from hydrogen flames". *Int. J. Hydrog. Energy* 16 (1991), pp. 47–53.

[22] L. Wu, N. Kobayashi, Z. Li, and H. Huang. "Numerical study of the effects of oxygen concentration and fuel jet velocity on thermal radiation in methane and propane turbulent diffusion flames". *Can. J. Chem. Eng.* 93 (2015), pp. 1567–1576.

[23] A. J. Gee, Y. Yin, K. K. Foo, A. Chinnici, N. Smith, and P. R. Medwell. "Toluene addition to turbulent H_2/natural gas flames in bluff-body burners". *Int. J. Hydrog. Energy* 47 (2022), pp. 27733–27746.

[24] S. R. Turns and F. H. Myhr. "Oxides of nitrogen emissions from turbulent jet flames: Part I-Fuel effects and flame radiation". *Combust. Flame* 87 (1991), pp. 319–335.

[25] K. Andersson, R. Johansson, and F. Johnsson. "Thermal radiation in oxy-fuel flames". *Int. J. Greenh. Gas Control* 5 (2011), S58–S65.

[26] P. Desgroux, X. Mercier, and K. A. Thomson. "Study of the formation of soot and its precursors in flames using optical diagnostics". *Proc. Combust. Inst.* 34 (2013), pp. 1713–1738.

[27] C. Zhang, L. Chen, S. Ding, H. Xu, G. Li, J.-L. Consalvi, and F. Liu. "Effects of soot inception and condensation PAH species and fuel preheating on soot formation modeling in laminar coflow CH_4/air diffusion flames doped with n-heptane/toluene mixtures". *Fuel* 253 (2019), pp. 1371–1377.

[28] A. Liati, B. T. Brem, L. Durdina, M. Vögtli, Y. Arroyo Rojas Dasilva, P. Dimopoulos Eggenschwiler, and J. Wang. "Electron microscopic study of soot particulate matter emissions from aircraft turbine engines". *Environ. Sci. Technol.* 48 (2014), pp. 10975–10983.

[29] A. D'Anna. "Kinetics of Soot Formation". *Reference Module in Chemistry, Molecular Sciences and Chemical Engineering*. Elsevier, 2015.

[30] T. C. Bond, S. J. Doherty, D. W. Fahey, P. M. Forster, T. Berntsen, B. J. DeAngelo, M. G. Flanner, S. Ghan, B. Kärcher, and D. Koch. "Bounding the role of black carbon in the climate system: A scientific assessment". *J. Geophys. Res. Atmos.* 118 (2013), pp. 5380–5552.

[31] Y. Wang and S. H. Chung. "Soot formation in laminar counterflow flames". *Prog. Energy. Combust. Sci.* 74 (2019), pp. 152–238.

[32] M. Frenklach and H. Wang. "Detailed modeling of soot particle nucleation and growth". *Symp. (Int.) Combust.* Vol. 23. Elsevier. 1991, pp. 1559–1566.

[33] M. Thomson and T. Mitra. "A radical approach to soot formation". *Science* 361 (2018), pp. 978–979.

[34] P. Pandey, B. Pundir, and P. Panigrahi. "Hydrogen addition to acetylene-air laminar diffusion flames: studies on soot formation under different flow arrangements". *Combust. Flame* 148 (2007), pp. 249–262.

[35] G. Lazaroiu, E. Pop, G. Negreanu, I. Pisa, L. Mihaescu, A. Bondrea, and V. Berbece. "Biomass combustion with hydrogen injection for energy applications". *Energy* 127 (2017), pp. 351–357.

[36] L. Xu, F. Yan, Y. Wang, and S. H. Chung. "Chemical effects of hydrogen addition on soot formation in counterflow diffusion flames: Dependence on fuel type and oxidizer composition". *Combust. Flame* 213 (2020), pp. 14–25.

[37] C. Yuan, C. Han, Y. Liu, Y. He, Y. Shao, and X. Jian. "Effect of hydrogen addition on the combustion and emission of a diesel free-piston engine". *Int. J. Hydrog. Energy* 43 (2018), pp. 13583–13593.

[38] J. E. Veetil, N. Kumbhakarna, S. Singh, R. K. Velamati, and S. Kumar. "Effect of hydrogen addition on the dynamics of premixed C1-C4 alkane-air flames in a microchannel with a wall temperature gradient". *Int. J. Hydrog. Energy* 47 (2022), pp. 30660–30670.

[39] Ö. Gülder, D. Snelling, and R. Sawchuk. "Influence of hydrogen addition to fuel on temperature field and soot formation in diffusion flames". *Symp. (Int.) Combust.* 26 (1996), pp. 2351–2358.

[40] F. Liu, Y. Ai, and W. Kong. "Effect of hydrogen and helium addition to fuel on soot formation in an axisymmetric coflow laminar methane/air diffusion flame". *Int. J. Hydrog. Energy* 39 (2014), pp. 3936–3946.

[41] Y. Wang, M. Gu, L. Chao, J. Wu, Y. Lin, and X. Huang. "Different chemical effect of hydrogen addition on soot formation in laminar coflow methane and ethylene diffusion flames". *Int. J. Hydrog. Energy* 46 (2021), pp. 16063–16074.

[42] H. Guo, F. Liu, G. J. Smallwood, and Ö. L. Gülder. "Numerical study on the influence of hydrogen addition on soot formation in a laminar ethylene-air diffusion flame". *Combust. Flame* 145 (2006), pp. 324–338.

[43] A. Kalbhor and J. van Oijen. "Effects of hydrogen enrichment and water vapour dilution on soot formation in laminar ethylene counterflow flames". *Int. J. Hydrog. Energy* 45 (2020), pp. 23653–23673.

[44] F. Ren, H. Chu, L. Xiang, W. Han, and M. Gu. "Effect of hydrogen addition on the laminar premixed combustion characteristics the main components of natural gas". *J. Energy Inst.* 92 (2019), pp. 1178–1190.

[45] S. H. Park, K. M. Lee, and C. H. Hwang. "Effects of hydrogen addition on soot formation and oxidation in laminar premixed C_2H_2/air flames". *Int. J. Hydrog. Energy* 36 (2011), pp. 9304–9311.

[46] D. Gu, Z. Sun, B. B. Dally, P. R. Medwell, Z. T. Alwahabi, and G. J. Nathan. "Simultaneous measurements of gas temperature, soot volume fraction and primary particle diameter in a sooting lifted turbulent ethylene/air non-premixed flame". *Combust. Flame* 179 (2017), pp. 33–50.

[47] Y. Wang, M. Gu, Y. Zhu, L. Cao, B. Zhu, J. Wu, Y. Lin, and X. Huang. "A review of the effects of hydrogen, carbon dioxide, and water vapor addition on soot formation in hydrocarbon flames". *Int. J. Hydrog. Energy* 46 (2021), pp. 31400–31427.

[48] M. J. Evans, D. B. Proud, P. R. Medwell, H. Pitsch, and B. B. Dally. "Highly radiating hydrogen flames: effect of toluene concentration and phase". *Proc. Combust. Inst.* 38 (2021), pp. 1099–1106.

[49] S. W. Baek, J. Ju Kim, H. S. Kim, and S. H. Kang. "Effects of addition of solid particles on thermal characteristics in hydrogen-air flame". *Combust. Sci. Technol.* 174 (2002), pp. 99–116.

[50] F. Steward and K. Guruz. "The effect of solid particles on radiative transfer in a cylindrical test furnace". *Symp. (Int.) Combust.* Vol. 15. Elsevier. 1975, pp. 1271–1283.

[51] C. S. McEnally and L. D. Pfefferle. "Sooting tendencies of oxygenated hydrocarbons in laboratory-scale flames". *Environ. Sci. Technol.* 45 (2011), pp. 2498–2503.

[52] P. Elumalai, N. Senthur, M. Parthasarathy, S. Dash, O. D. Samuel, M. S. Reddy, M. Murugan, P. Das, A. Sitaramamurty, and S. Anjanidevi. "Effectiveness of hydrogen and nanoparticles addition in eucalyptus biofuel for improving the performance and reduction of emission in CI engine". *Greener and Scalable E-fuels for Decarbonization of Transport*. Springer, 2021, pp. 173–191.

[53] M. S. Kumar, A. Ramesh, and B. Nagalingam. "Use of hydrogen to enhance the performance of a vegetable oil fuelled compression ignition engine". *Int. J. Hydrog. Energy* 28 (2003), pp. 1143–1154.

[54] M. Ilbas, İ. Yılmaz, and Y. Kaplan. "Investigations of hydrogen and hydrogen-hydrocarbon composite fuel combustion and NO_x emission characteristics in a model combustor". *Int. J. Hydrog. Energy* 30 (2005), pp. 1139–1147.

[55] G. Wielgosiński. "Pollutant formation in combustion processes". *Adv. Chem. Eng.* (2012), pp. 295–324.

[56] A. Konnov, G. Colson, and J. De Ruyck. "NO formation rates for hydrogen combustion in stirred reactors". *Fuel* 80 (2001), pp. 49–65.

[57] J. Gehrmann Hans, B. Jaeger, S. Wirtz, V. Scherer, K. Aleksandrov, M. Hauser, D. Stapf, G. Pollmeier, and P. Danz. "Oscillating Combustion-Primary Measure to Reduce Nitrogen Oxide in a Grate Furnace-Experiments and Simulations". *Processes* 9 (2021).

[58] P. Therkelsen, T. Werts, V. McDonell, and S. Samuelsen. "Analysis of NOx Formation in a Hydrogen-Fueled Gas Turbine Engine". *J. Eng. Gas Turbines Power* 131 (Feb. 2009), p. 031507.

[59] M. S. Cellek and A. Pınarbaşı. "Investigations on performance and emission characteristics of an industrial low swirl burner while burning natural gas, methane, hydrogen-enriched natural gas and hydrogen as fuels". *Int. J. Hydrog. Energy* 43 (2018), pp. 1194–1207.

[60] R. Tuccillo, M. C. Cameretti, R. De Robbio, F. Reale, and F. Chiariello. "Methane-Hydrogen Blends in Micro Gas Turbines: Comparison of Different Combustor Concepts". *Turbo Expo: Power for Land, Sea, and Air* 8 (June 2019), V008T26A003.

[61] J. W. Bozzelli and A. M. Dean. "O + NNH: A possible new route for NO_x formation in flames". *Int. J. Chem. Kinet.* 27 (1995), pp. 1097–1109.

[62] J. E. Harrington, G. P. Smith, P. A. Berg, A. R. Noble, J. B. Jeffries, and D. R. Crosley. "Evidence for a new NO production mechanism in flames". *Symp. (Int.) Combust.* Vol. 26. Elsevier. 1996, pp. 2133–2138.

[63] P. Dimitriou, T. Tsujimura, and Y. Suzuki. "Adopting biodiesel as an indirect way to reduce the NO_x emission of a hydrogen fumigated dual-fuel engine". *Fuel* 244 (2019), pp. 324–334.

[64] B. A. Almohammadi, P. Singh, S. Sharma, S. Kumar, and B. Khandelwal. "Experimental investigation and correlation development for engine emissions with polycyclic aromatic blended formulated fuels". *Fuel* 303 (2021), p. 121280.

[65] T. Korakianitis, A. Namasivayam, and R. Crookes. "Diesel and rapeseed methyl ester (RME) pilot fuels for hydrogen and natural gas dual-fuel combustion in compression-ignition engines". *Fuel* 90 (2011), pp. 2384–2395.

[66] H. Serin and Ş. Yıldızhan. "Hydrogen addition to tea seed oil biodiesel: Performance and emission characteristics". *Int. J. Hydrog. Energy* 43 (2018), pp. 18020–18027.

[67] A. Oasmaa and S. Czernik. "Fuel oil quality of biomass pyrolysis oils state of the art for the end users". *Energy & Fuels* 13 (1999), pp. 914–921.

[68] V. M. Reddy, P. Biswas, P. Garg, and S. Kumar. "Combustion characteristics of biodiesel fuel in high recirculation conditions". *Fuel Process. Technol.* 118 (2014), pp. 310–317.

[69] R. O. Arazo, D. A. D. Genuino, M. D. G. de Luna, and S. C. Capareda. "Bio-oil production from dry sewage sludge by fast pyrolysis in an electrically-heated fluidized bed reactor". *Sustain. Environ. Res.* 27 (2017), pp. 7–14.

[70] Z. Wang, L. Li, J. Wang, and R. D. Reitz. "Effect of biodiesel saturation on soot formation in diesel engines". *Fuel* 175 (2016), pp. 240–248.

[71] M. K. Tran, D. Dunn-Rankin, and T. K. Pham. "Characterising sooting propensity in biofuel-diesel flames". *Combust. Flame* 159 (2012), pp. 2181–2191.

[72] P. B. L. Fregolente, L. V. Fregolente, and M. R. Wolf Maciel. "Water content in biodiesel, diesel, and biodiesel-diesel blends". *J. Chem. Eng. Data.* 57 (2012), pp. 1817–1821.

[73] S. Rahman, M. Nabi, T. C. Van, K. Suara, M. Jafari, A. Dowell, M. Islam, A. J. Marchese, J. Tryner, and M. Hossain. "Performance and combustion characteristics analysis of multi-cylinder CI engine using essential oil blends". *Energies* 11 (2018), p. 738.

[74] S. A. Rahman, T. C. Van, F. Hossain, M. Jafari, A. Dowell, M. Islam, M. N. Nabi, A. Marchese, J. Tryner, and T. Rainey. "Fuel properties and emission characteristics of essential oil blends in a compression ignition engine". *Fuel* 238 (2019), pp. 440–453.

[75] S.-M. Cho, J.-H. Kim, S.-H. Kim, S.-Y. Park, J.-C. Kim, and I.-G. Choi. "A comparative study on the fuel properties of biodiesel from woody essential oil depending on terpene composition". *Fuel* 218 (2018), pp. 375–384.

[76] V. Stamatov, D. Honnery, and J. Soria. "Combustion properties of slow pyrolysis bio-oil produced from indigenous Australian species". *Renew. Energy* 31 (2006), pp. 2108–2121.

[77] C. Mulligan, L. Strezov, and V. Strezov. "Pyrolytic decomposition of red gum wood waste". *Engineering Our Future: Are We up to the Challenge?: 27-30 September 2009, Burswood Entertainment Complex* (2009), p. 110.

[78] M. Gholizadeh, X. Hu, and Q. Liu. "A mini review of the specialties of the bio-oils produced from pyrolysis of 20 different biomasses". *Renew. Sustain. Energy Rev.* 114 (2019), p. 109313.

[79] A. Bridgwater, P. Carson, and M. Coulson. "A comparison of fast and slow pyrolysis liquids from mallee". *Int. J. Glob. Energy Issues* 27 (2007), pp. 204–216.

[80] M. Garcia-Perez, J. Shen, X. S. Wang, and C.-Z. Li. "Production and fuel properties of fast pyrolysis oil/bio-diesel blends". *Fuel Process. Technol.* 91 (2010), pp. 296–305.

[81] D. Mohan, C. U. Pittman Jr, and P. H. Steele. "Pyrolysis of wood/biomass for bio-oil: a critical review". *Energy & Fuels* 20 (2006), pp. 848–889.

[82] A. Ahmed, M. S. A. Bakar, A. K. Azad, R. S. Sukri, and N. Phusunti. "Intermediate pyrolysis of Acacia cincinnata and Acacia holosericea species for bio-oil and biochar production". *Energy Convers. Manag.* 176 (2018), pp. 393–408.

[83] M. Solikhah, F. Pratiwi, Y. Heryana, A. Wimada, F. Karuana, A. Raksodewanto, and A. Kismanto. "Characterization of bio-oil from fast pyrolysis of palm frond and empty fruit bunch". *IOP Conf. Ser.: Mater. Sci.* Vol. 349. IOP Publishing. 2018, p. 012035.

[84] A. Demirbas. "Pyrolysis of ground beech wood in irregular heating rate conditions". *J. Anal. Appl. Pyrolysis* 73 (2005), pp. 39–43.

[85] W. Tsai, M. Lee, and d. Y. Chang. "Fast pyrolysis of rice straw, sugarcane bagasse and coconut shell in an induction-heating reactor". *J. Anal. Appl. Pyrolysis* 76 (2006), pp. 230–237.

[86] T. Ding, S. Li, J. Xie, W. Song, J. Yao, and W. Lin. "Rapid pyrolysis of wheat straw in a bench-scale circulating fluidized-bed downer reactor". *Chem. Eng. Technol.* 35 (2012), pp. 2170–2176.

[87] T. Mani, P. Murugan, J. Abedi, and N. Mahinpey. "Pyrolysis of wheat straw in a thermogravimetric analyzer: effect of particle size and heating rate on devolatilization and estimation of global kinetics". *Chem. Eng. Res. Des.* 88 (2010), pp. 952–958.

[88] A. Camelo, D. A. Genuino, A. L. Maglinao Jr, S. C. Capareda, J. L. Paes, and J. Owkusumsirisakul. "Pyrolysis of pearl millet and napier grass hybrid (PMN10TX15): Feasibility, byproducts, and comprehensive characterization". *Int. J. Renew. Energy Res.* 8 (2018), pp. 682–691.

[89] T. Rout, D. Pradhan, R. Singh, and N. Kumari. "Exhaustive study of products obtained from coconut shell pyrolysis". *J. Environ. Chem. Eng.* 4 (2016), pp. 3696–3705.

[90] A. K. Varma and P. Mondal. "Pyrolysis of sugarcane bagasse in semi batch reactor: effects of process parameters on product yields and characterization of products". *Ind. Crops Prod.* 95 (2017), pp. 704–717.

[91] Z. Yıldız and S. Ceylan. "Pyrolysis of tobacco factory waste biomass". *J. Therm. Anal. Calorim.* 136 (2019), pp. 783–794.

[92] T. N. Trinh, P. A. Jensen, K. Dam-Johansen, N. O. Knudsen, H. R. Sørensen, and S. Hvilsted. "Comparison of lignin, macroalgae, wood, and straw fast pyrolysis". *Energy & Fuels* 27 (2013), pp. 1399–1409.

[93] O. Herbinet, W. J. Pitz, and C. K. Westbrook. "Detailed chemical kinetic oxidation mechanism for a biodiesel surrogate". *Combust. Flame* 154 (2008), pp. 507–528.

[94] T. M. Mata, A. A. Martins, and N. S. Caetano. "Microalgae for biodiesel production and other applications: a review". *Renew. Sustain. Energy Rev.* 14 (2010), pp. 217–232.

[95] M. I. Jahirul, R. J. Brown, W. Senadeera, I. M. O'Hara, and Z. D. Ristovski. "The use of artificial neural networks for identifying sustainable biodiesel feedstocks". *Energies* 6 (2013), pp. 3764–3806.

[96] P. Singh, S. Sharma, V. K. Undavalli, B. Khandelwal, and S. Kumar. "Unregulated emissions from oxygenated fuels". *Advancement in Oxygenated Fuels for Sustainable Development*. Elsevier, 2023, pp. 221–240.

[97] P. Singh, S. Sharma, and S. Kumar. "Impact of biodiesel blended fuels on combustion engines in long term". *Adv. in Energy Tribol.* (2021), pp. 31–59.

[98] N. S. El-Mougy. "Effect of some essential oils for limiting early blight (Alternaria solani) development in potato field". *J. Plant Prot. Res.* 49 (2009).

[99] S. Czernik and A. Bridgwater. "Overview of applications of biomass fast pyrolysis oil". *Energy & Fuels* 18 (2004), pp. 590–598.

[100] R. Rana, S. Nanda, V. Meda, A. Dalai, and J. Kozinski. "A review of lignin chemistry and its biorefining conversion technologies". *J. Biochem. Eng. Bioprocess. Technol.* 1 (2018), p. 2.

[101] G. Hochman and D. Zilberman. "Algae farming and its bio-products". *Plants and BioEnergy*. Springer, 2014, pp. 49–64.

[102] P. Bajpai. "Application of enzymes in the pulp and paper industry". *Biotechnol. Prog.* 15 (1999), pp. 147–157.

[103] D. Mourant, C. Lievens, R. Gunawan, Y. Wang, X. Hu, L. Wu, S. S. A. Syed-Hassan, and C.-Z. Li. "Effects of temperature on the yields and properties of bio-oil from the fast pyrolysis of mallee bark". *Fuel* 108 (2013), pp. 400–408.

[104] J. L. Zheng and Y.-P. Kong. "Spray combustion properties of fast pyrolysis bio-oil produced from rice husk". *Energy Convers. Manag.* 51 (2010), pp. 182–188.

[105] K. Alexandrino, J. Salinas, Á. Millera, R. Bilbao, and M. U. Alzueta. "Sooting propensity of dimethyl carbonate, soot reactivity and characterization". *Fuel* 183 (2016), pp. 64–72.

[106] J. Manin, S. Skeen, L. Pickett, E. Kurtz, and J. E. Anderson. "Effects of oxygenated fuels on combustion and soot formation/oxidation processes". *SAE Int. J. Fuels Lubr.* 7 (2014), pp. 704–717.

[107] M. S. Celnik, M. Sander, A. Raj, R. H. West, and M. Kraft. "Modelling soot formation in a premixed flame using an aromatic-site soot model and an improved oxidation rate". *Proc. Combust. Inst.* 32 (2009), pp. 639–646.

[108] I. Glassman. "Soot formation in combustion processes". *Symp. (Int.) Combust.* Vol. 22. Elsevier. 1989, pp. 295–311.

[109] L. Li and P. B. Sunderland. "An improved method of smoke point normalization". *Combust. Sci. Technol.* 184 (2012), pp. 829–841.

[110] M. Salamanca, F. Mondragón, J. R. Agudelo, P. Benjumea, and A. Santamaría. "Variations in the chemical composition and morphology of soot induced by the unsaturation degree of biodiesel and a biodiesel blend". *Combust. Flame* 159 (2012), pp. 1100–1108.

[111] E. J. Barrientos, M. Lapuerta, and A. L. Boehman. "Group additivity in soot formation for the example of C-5 oxygenated hydrocarbon fuels". *Combust. Flame* 160 (2013), pp. 1484–1498.

[112] I. Ruiz-Rodriguez, R. Cracknell, M. Parkes, T. Megaritis, and L. Ganippa. "Experimental study of the effect of C8 oxygenates on sooting processes in high pressure spray flames". *Combust. Flame* 220 (2020), pp. 235–246.

[113] P. Verma, M. Jafari, S. A. Rahman, E. Pickering, S. Stevanovic, A. Dowell, R. Brown, and Z. Ristovski. "The impact of chemical composition of oxygenated fuels on morphology and nanostructure of soot particles". *Fuel* 259 (2020), p. 116167.

[114] C. K. Westbrook, W. J. Pitz, and H. J. Curran. "Chemical kinetic modeling study of the effects of oxygenated hydrocarbons on soot emissions from diesel engines". *J. Phys. Chem. A* 110 (2006), pp. 6912–6922.

[115] C. J. Mueller, A. L. Boehman, and G. C. Martin. "An experimental investigation of the origin of increased NO_x emissions when fueling a heavy-duty compression-ignition engine with soy biodiesel". *SAE Int. J. Fuels Lubr.* 2 (2009), pp. 789–816.

[116] C. E. Roberts, D. Naegeli, and C. Chadwell. "The effect of water on soot formation chemistry". *SAE trans.* (2005), pp. 1656–1672.

[117] T. Y. Kim, S. Lee, and K. Kang. "Performance and emission characteristics of a high-compression-ratio diesel engine fueled with wood pyrolysis oil-butanol blended fuels". *Energy* 93 (2015), pp. 2241–2250.

[118] Y. Wu, F. Liu, Y. Sun, and B. Zhu. "Effects of carbon dioxide and water vapor addition on benzene and PAH formation in a laminar premixed $CH_4/O_2/Ar$ flame". *Combust. Sci. Technol.* (2018).

[119] U. Trivanovic, T. A. Sipkens, M. Kazemimanesh, A. Baldelli, A. M. Jefferson, B. M. Conrad, M. R. Johnson, J. C. Corbin, J. S. Olfert, and S. N. Rogak. "Morphology and size of soot from gas flares as a function of fuel and water addition". *Fuel* 279 (2020), p. 118478.

[120] X. Liu, H. Wang, and M. Yao. "Experimental and modeling investigations on soot formation of ethanol, n-butanol, 2, 5-dimethylfuran, and biodiesel in diesel engines". *Energy & Fuels* 31 (2017), pp. 12108–12119.

[121] R. Zhang, P. X. Pham, S. Kook, and A. R. Masri. "Influence of biodiesel carbon chain length on in-cylinder soot processes in a small bore optical diesel engine". *Fuel* 235 (2019), pp. 1184–1194.

[122] P. Singh, X. Hui, and C.-J. Sung. "Soot formation in non-premixed counterflow flames of butane and butanol isomers". *Combust. Flame* 164 (2016), pp. 167–182.

[123] S. A. Rahman, T. Mahila, A. Ahmad, M. N. Nabi, M. Jafari, A. Dowell, M. A. Islam, A. Marchese, J. Tryner, and P. R. Brooks. "Effect of oxygenated functional groups in essential oils on diesel engine performance, emissions, and combustion characteristics". *Energy & Fuels* 33 (2019), pp. 9828–9834.

[124] Q. Feng, A. Jalali, A. M. Fincham, Y. L. Wang, T. T. Tsotsis, and F. N. Egolfopoulos. "Soot formation in flames of model biodiesel fuels". *Combust. Flame* 159 (2012), pp. 1876–1893.

[125] S. Sarathy, S. Gaıl, S. Syed, M. Thomson, and P. Dagaut. "A comparison of saturated and unsaturated C4 fatty acid methyl esters in an opposed flow diffusion flame and a jet stirred reactor". *Proc. Combust. Inst.* 31 (2007), pp. 1015–1022.

[126] S. Gaıl, M. J. Thomson, S. M. Sarathy, S. A. Syed, P. Dagaut, P. Diévart, A. J. Marchese, and F. L. Dryer. "A wide-ranging kinetic modeling study of methyl butanoate combustion". *Proc. Combust. Inst.* 31 (2007), pp. 305–311.

[127] S. Garner, R. Sivaramakrishnan, and K. Brezinsky. "The high-pressure pyrolysis of saturated and unsaturated C7 hydrocarbons". *Proc. Combust. Inst.* 32 (2009), pp. 461–467.

[128] Y. D. Wu and D. K. Lai. "A density functional study of substituent effects on the O- H and O- CH3 bond dissociation energies in phenol and anisole". *J. Org. Chem.* 61 (1996), pp. 7904–7910.

[129] M. Nowakowska, O. Herbinet, A. Dufour, and P.-A. Glaude. "Kinetic study of the pyrolysis and oxidation of guaiacol". *J. Phys. Chem. A* 122 (2018), pp. 7894–7909.

[130] K. Agrawal, A. M. Verma, and N. Kishore. "Thermochemical conversion of guaiacol in aqueous phase by density functional theory". *ChemistrySelect* 4 (2019), pp. 6013–6025.

[131] K. Narayanaswamy, H. Pitsch, and P. Pepiot. "A component library framework for deriving kinetic mechanisms for multi-component fuel surrogates: application for jet fuel surrogates". *Combust. Flame* 165 (2016), pp. 288–309.

[132] P. G. Szymkowicz and J. Benajes. "Development of a diesel surrogate fuel library". *Fuel* 222 (2018), pp. 21–34.

[133] F. Comelli, S. Ottani, R. Francesconi, and C. Castellari. "Densities, viscosities, and refractive indices of binary mixtures containing n-hexane+ components of pine resins and essential oils at 298.15 K". *J. Chem. Eng. Data.* 47 (2002), pp. 93–97.

[134] P. Devan and N. Mahalakshmi. "A study of the performance, emission and combustion characteristics of a compression ignition engine using methyl ester of paradise oil–eucalyptus oil blends". *Appl. Energy* 86 (2009), pp. 675–680.

[135] J. R. Ayala, G. Montero, H. E. Campbell, C. García, M. A. Coronado, J. A. León, C. A. Sagaste, and L. J. Pérez. "Extraction and characterization of orange peel essential oil from Mexico and United States of America". *J. Essent. Oil-Bear. Plants* 20 (2017), pp. 897–914.

[136] L. Cai and H. Pitsch. "Optimized chemical mechanism for combustion of gasoline surrogate fuels". *Combust. Flame* 162 (2015), pp. 1623–1637.

[137] B. Kerschgens, L. Cai, H. Pitsch, A. Janssen, M. Jakob, and S. Pischinger. "Surrogate fuels for the simulation of diesel engine combustion of novel biofuels". *Int. J. Engine Res.* 16 (2015), pp. 531–546.

[138] F. J. Santos, C. A. Nieto de Castro, J. H. Dymond, N. K. Dalaouti, M. J. Assael, and A. Nagashima. "Standard reference data for the viscosity of toluene". *J. phys. chem. ref. data* 35 (2006), pp. 1–8.

[139] S. W. Wagnon, S. Thion, E. J. Nilsson, M. Mehl, Z. Serinyel, K. Zhang, P. Dagaut, A. A. Konnov, G. Dayma, and W. J. Pitz. "Experimental and modeling studies of a biofuel surrogate compound: laminar burning velocities and jet-stirred reactor measurements of anisole". *Combust. Flame* 189 (2018), pp. 325–336.

[140] S. Namysl. "Experimental study of the formation of pollutants during the combustion of bio-oil surrogate molecules". PhD thesis. Université de Lorraine, 2019.

[141] M. Tian, R. L. McCormick, M. A. Ratcliff, J. Luecke, J. Yanowitz, P.-A. Glaude, M. Cuijpers, and M. D. Boot. "Performance of lignin derived compounds as octane boosters". *Fuel* 189 (2017), pp. 284–292.

[142] R. N. Olcese, J. Francois, M. M. Bettahar, D. Petitjean, and A. Dufour. "Hydrodeoxygenation of guaiacol, a surrogate of lignin pyrolysis vapors, over iron based catalysts: Kinetics and modeling of the lignin to aromatics integrated process". *Energy & Fuels* 27 (2013), pp. 975–984.

[143] K. V. Kovalenko and S. V. Krivokhizha. "Spectra of molecular light scattering in guaiacol". *Bull. Lebedev Phys. Inst.* 34 (2007), pp. 97–101.

[144] T. Bierkandt, M. Hoener, N. Gaiser, N. Hansen, M. Köhler, and T. Kasper. "Experimental flat flame study of monoterpenes: Insights into the combustion kinetics of α-pinene, β-pinene, and myrcene". *Proc. Combust. Inst.* 38 (2021), pp. 2431–2440.

[145] M. Nowakowska, O. Herbinet, A. Dufour, and P.-A. Glaude. "Detailed kinetic study of anisole pyrolysis and oxidation to understand tar formation during biomass combustion and gasification". *Combust. Flame* 161 (2014), pp. 1474–1488.

[146] A. M. Scheer, C. Mukarakate, D. J. Robichaud, M. R. Nimlos, and G. B. Ellison. "Thermal decomposition mechanisms of the methoxyphenols: formation of phenol, cyclopentadienone, vinylacetylene, and acetylene". *J. Phys. Chem. A* 115 (2011), pp. 13381–13389.

[147] N. Hashimoto, H. Nishida, Y. Ozawa, T. Iwatsubo, and J. Inumaru. "Influence of type of burner on NO_x emission characteristics from combustion of palm methyl ester". *Int. J. Chem. Mol. Eng.* 3 (2009), pp. 570–574.

[148] U. Potdar, A. Jamgade, P. Mahyavanshi, Y. Yoon, and S. Kumar. "Experimental investigations on stabilization mechanism of lifted kerosene spray flames". *Combust. Sci. Technol.* 189 (2017), pp. 1241–1259.

[149] Z. Petranović, M. Vujanović, and N. Duić. "Towards a more sustainable transport sector by numerically simulating fuel spray and pollutant formation in diesel engines". *J. Clean. Prod.* 88 (2015), pp. 272–279.

[150] P. Singh, R. Kumar, S. Sharma, and S. Kumar. "Effect of engine parameters on the performance of dual-fuel CI engines with producer gas—A review". *Energy & Fuels* 35 (2021), pp. 16377–16402.

[151] A. K. Agarwal. "Biofuels (alcohols and biodiesel) applications as fuels for internal combustion engines". *Prog. Energy. Combust. Sci.* 33 (2007), pp. 233–271.

[152] S. P. Lin and R. D. Reitz. "Drop and spray formation from a liquid jet". *Annual review of fluid mechanics* 30 (1998), pp. 85–105.

[153] P. Jenny, D. Roekaerts, and N. Beishuizen. "Modeling of turbulent dilute spray combustion". *Prog. Energy Combust. Sci.* 38 (2012), pp. 846–887.

[154] J.-S. Wu, Y.-J. Liu, and H.-J. Sheen. "Effects of ambient turbulence and fuel properties on the evaporation rate of single droplets". *Int. J. Heat Mass Transf.* 44 (2001), pp. 4593–4603.

[155] J. Hayashi, J. Fukui, and F. Akamatsu. "Effects of fuel droplet size distribution on soot formation in spray flames formed in a laminar counterflow". *Proc. Combust. Inst.* 34 (2013), pp. 1561–1568.

[156] S. H. Park, I. M. Youn, Y. Lim, and C. S. Lee. "Influence of the mixture of gasoline and diesel fuels on droplet atomization, combustion, and exhaust emission characteristics in a compression ignition engine". *Fuel Process. Technol.* 106 (2013), pp. 392–401.

[157] J. Hayashi, H. Watanabe, R. Kurose, and F. Akamatsu. "Effects of fuel droplet size on soot formation in spray flames formed in a laminar counterflow". *Combust. Flame* 158 (2011), pp. 2559–2568.

[158] W. Lee Seang, P. Simsoo, and D. Yasuhiro. "An experimental study of the effects of combustion systems and fuel properties on the performance of a diesel engine". *J. Automobile Eng.* 218 (2004), pp. 1317–1323.

[159] M. U. Haq, A. T. Jafry, S. Ahmad, T. A. Cheema, M. Q. Ansari, and N. Abbas. "Recent advances in fuel additives and their spray characteristics for diesel-based blends". *Energies* 15 (2022), p. 7281.

[160] A. K. Agarwal, S. Som, P. C. Shukla, H. Goyal, and D. Longman. "In-nozzle flow and spray characteristics for mineral diesel, Karanja, and Jatropha biodiesels". *Appl. Energy* 156 (2015), pp. 138–148.

[161] A. J. Hewitt. "The importance of nozzle selection and droplet size control in spray application". *Proc. of the North American Conf. on Pest. Spray Drift Manag*. Citeseer. 1998, pp. 75–85.

[162] G. J. Smallwood and O. L. Gulder. "Views on the structure of transient diesel sprays". *At. Sprays* 10 (2000).

[163] A. K. Agarwal, S. Park, A. Dhar, C. S. Lee, S. Park, T. Gupta, and N. K. Gupta. "Review of experimental and computational studies on spray, combustion, performance, and emission characteristics of biodiesel fueled engines". *J. Energy Resour. Technol.* 140 (2018).

[164] L. Geng, Y. Wang, J. Wang, Y. Wei, and C.-f. F. Lee. "Numerical simulation of the influence of fuel temperature and injection parameters on biodiesel spray characteristics". *Energy Sci. Eng.* 8 (2020), pp. 312–326.

[165] C. Ejim, B. Fleck, and A. Amirfazli. "Analytical study for atomization of biodiesels and their blends in a typical injector: surface tension and viscosity effects". *Fuel* 86 (2007), pp. 1534–1544.

[166] G. Singh, A. Kourmatzis, and A. Masri. "Volume measurement of atomizing fragments using image slicing". *Exp. Therm. Fluid Sci.* 115 (2020), p. 110102.

[167] A. Lowe, A. Kourmatzis, and A. R. Masri. "Turbulent spray flames of intermediate density: Stability and near-field structure". *Combust. Flame* 176 (2017), pp. 511–520.

[168] A. H. Lefebvre and V. G. McDonell. *At. Sprays*. CRC press, 2017.

[169] A. Wierzba. "Deformation and breakup of liquid drops in a gas stream at nearly critical Weber numbers". *Exp. Fluids* 9 (1990), pp. 59–64.

[170] F. Duronio, A. De Vita, L. Allocca, and M. Anatone. "Gasoline direct injection engines–A review of latest technologies and trends. Part 1: Spray breakup process". *Fuel* 265 (2020), p. 116948.

[171] M. Linne. "Imaging in the optically dense regions of a spray: A review of developing techniques". *Prog. Energy Combust. Sci.* 39 (2013), pp. 403–440.

[172] M. Sommerfeld and H.-H. Qiu. "Experimental studies of spray evaporation in turbulent flow". *Int. J. Heat Fluid Flow* 19 (1998), pp. 10–22.

[173] A. Kourmatzis, O. J. Jaber, G. Singh, and A. R. Masri. "Review of flow blurring atomization: advances and perspectives". *Energy & Fuels* 36 (2022), pp. 4224–4233.

[174] B. M. Simmons and A. K. Agrawal. "Drop size and velocity measurements in bio-oil sprays produced by the flow-blurring injector". *Turbo Expo: Power for Land, Sea, and Air*. Vol. 54617. 2011, pp. 701–710.

[175] A. Kourmatzis, P. X. Pham, and A. R. Masri. "Air assisted atomization and spray density characterization of ethanol and a range of biodiesels". *Fuel* 108 (2013), pp. 758–770.

[176] A. Kourmatzis and A. Masri. "Air-assisted atomization of liquid jets in varying levels of turbulence". *J. Fluid Mech.* 764 (2015), pp. 95–132.

[177] G. Singh, A. Kourmatzis, A. Gutteridge, and A. R. Masri. "Instability growth and fragment formation in air assisted atomization". *J. Fluid Mech.* 892 (2020), A29.

[178] A. Mansour and N. Chigier. "Dynamic behavior of liquid sheets". *Phys. Fluids A: Fluid Dynamics* 3 (1991), pp. 2971–2980.

[179] A. Lozano, F. Barreras, C. Siegler, and D. Löw. "The effects of sheet thickness on the oscillation of an air-blasted liquid sheet". *Exp. Fluids* 39 (2005), pp. 127–139.

[180] J. Park, K. Y. Huh, X. Li, and M. Renksizbulut. "Experimental investigation on cellular breakup of a planar liquid sheet from an air-blast nozzle". *Phys. Fluids* 16 (2004), pp. 625–632.

[181] E. Rostami and H. Mahdavy Moghaddam. "The velocity and viscosity impact on the annular spray atomisation of different fuels". *Combust. Theory Model.* 25 (2021), pp. 158–192.

[182] O. J. Jaber, A. Kourmatzis, and A. R. Masri. "Characterization of flow-focusing and flow-blurring modes of atomization". *Energy & Fuels* 35 (2020), pp. 7144–7155.

[183] C. Engelbert, Y. Hardalupas, and J. H. Whitelaw. "Breakup phenomena in coaxial airblast atomizers". *Proc. Math. Phys. Eng. Sci.* 451 (1995), pp. 189–229.

[184] Y. Hardalupas, R. Tsai, and J. Whitelaw. "Primary breakup of coaxial airblast atomizers". *Proc. Int. Conf. on Liquid Atomization and Spray Systems, Manchester, UK*. 1998, pp. 6–8.

[185] M. Chinnaraj and R. Sadanandan. "The effect of swirling air-to-liquid momentum ratio on the spray and droplet characteristics". *J. Appl. Fluid Mech.* 13 (2020), pp. 827–837.

[186] A. Sinha, R. S. Prakash, A. M. Mohan, and R. Ravikrishna. "Airblast spray in crossflow–structure, trajectory and droplet sizing". *Int. J. Multiph. Flow* 72 (2015), pp. 97–111.

[187] P. Christophe, B. M. Rim, G. Mohamed, S. Khashayar, and F. Jérôme. "Thermal radiation in dust flame propagation". *J. Loss Prev. Process Ind.* 49 (2017), pp. 896–904.

[188] S. Pourhoseini and M. Moghiman. "Effect of pulverized anthracite coal particles injection on thermal and radiative characteristics of natural gas flame: An experimental study". *Fuel* 140 (2015), pp. 44–49.

Chapter 3

Methods

3.1 Approach

This chapter summarises the methods and approaches employed in different stages of this research to achieve the aims and objectives presented in §2.9. The interconnections and underlying logic of the methodology are illustrated. A combined experimental and numerical approach was employed to investigate the effect of adding prevapourised/spray biofuel additive to turbulent nonpremixed hydrogen-based flames on combustion characteristics, including flame appearance, flame luminosity, flame temperature, radiant intensity, spray characteristics, and pollutant emissions.

Five liquid biofuel surrogates were selected based on the in-depth literature review of potential biofuels with high sooting propensities for the radiant heat flux enhancement of hydrogen-based flames. Toluene, anisole, and guaiacol are chosen as the surrogates for bio-oils, while eucalyptol and D-limonene are chosen as the surrogates for essential oils. The sooting propensities of the selected liquid biofuel surrogates were tested on a wick-fed burner under laminar flame conditions using the smoke point method to understand the chemistry of the biofuel surrogates before adding them to hydrogen-based flames. The results are presented in Chapter 4. These tests also contribute to establishing the understanding of the effect of their different functional groups on sooting propensity independent from hydrogen combustion. The sooting propensities of the tested biofuel surrogates were broadly compared with hydrocarbon fuels in the existing literature to provide insights into the potential replacement of conventional fuels with these renewable biofuels in applications that rely on radiant heat flux.

Based on the initial sooting propensities investigation, the biofuel surrogates were added to turbulent nonpremixed hydrogen-based flames at various concentrations via prevapourisation or ultrasonic spray, to allow comparisons between these two methods of additive introduction and mechanisms on radiant heat flux enhancement and flame characteristics. These experimental studies were performed on an integrated vapourised/ultrasonic spray burner. The results are presented in Chapter 5.

The results from Chapters 4 and 5 suggested the necessity for further analysis of desirable introduction methods in achieving radiating flames with greater effectiveness of radiant heat flux enhancement. Therefore, a needle spray burner that employs gas-assist atomisation for adding liquid biofuel surrogates to hydrogen-based flames was developed in Chapter 6. The working range of the spray burner was identified using both non-reacting (Chapter 6) and reacting flows (Chapter 7). The near-field spray characteristics of the burner and the corresponding non-dimensional influencing parameters were investigated using microscopic shadowgraphy imaging. The gas-assist atomised biofuel surrogates were added to turbulent nonpremixed hydrogen flames and the flame characteristics were compared with the prevapourised and ultrasonically atomised biofuel/hydrogen flames.

A series of diagnostics used to measure the aforementioned combustion characteristics and flame features are introduced with details in §3.4 and the methodology section in the papers. Numerical modelling of opposed-flow non-premixed (OPPDIF) flames was undertaken in Chemkin Pro v19.2 to estimate soot formation in the biofuel-blended hydrogen-based flames by simulating PAH formation. The numerical simulation of NO_x formation was also performed to analyse the dominant NO_x formation pathways and mechanisms in these blended flames.

3.2 Burner design and experimental setup

3.2.1 Wick burner

Three burners with complementary functions have been developed and used to investigate various flame cases at different stages of this research. A wick-fed burner was employed to evaluate the sooting propensities of the potential biofuel additives using the smoke point method before adding them to hydrogen-based flames. Pure liquid biofuel surrogate was supplied to the laminar flame via a wick. As the laminar flame's luminous length is elongated by the extension of the wick length, the smoke point is determined by the

maximum flame's luminous length before emitting smoke. The smoke point is inversely proportional to the sooting propensity of the fuel. The detailed descriptions of the burner and measurement are illustrated in Chapter 4.

3.2.2 Vapourised/spray burner

To investigate the effect of prevapourisation and ultrasonic spray as introduction methods on the combustion performance of biofuel-blended hydrogen-based flames, an integrated vapourised/ultrasonic spray burner was designed and manufactured to supply biofuel additives in droplets or vapour form. The schematic of the vapourised/ultrasonic spray burner and the experimental setup is shown in Figure 3.1.

In the ultrasonic spray flame configuration, the H_2/N_2 mixture is supplied through the carrier gas inlet and then transports the biofuel droplets generated by the ultrasonic nebuliser to the flame. The ultrasonic nebuliser consists of a piezoelectric transducer that vibrates at high frequencies, typically in the ultrasonic range (above 20 kHz). When an electric current is applied to the transducer, it undergoes rapid mechanical oscillations, creating ultrasonic waves. As the ultrasonic waves propagate, they create alternating high-pressure and low-pressure regions within the liquid. The interactions between the high-pressure and low-pressure phases of the ultrasonic cause rapid collapse of the liquid into fine droplets. The inner curve of the cover case, together with the relative position between the nebuliser droplet outlet and the central jet, ensure stable transportation of the two-phase fuel mixture.

Within the prevapourisation arrangement, the liquid biofuel undergoes prevapourisation via a controlling evaporating mixing (CEM) unit positioned prior to the burner. The CEM was heated and maintained above the boiling point of the selected biofuel surrogates. The biofuel vapour was entrained by the carrier gas into the H_2/N_2 mixture. The liquid fuel stream is blocked in this operational state. The parameters of the burner and test conditions are presented in the methodology section of Chapter 5.

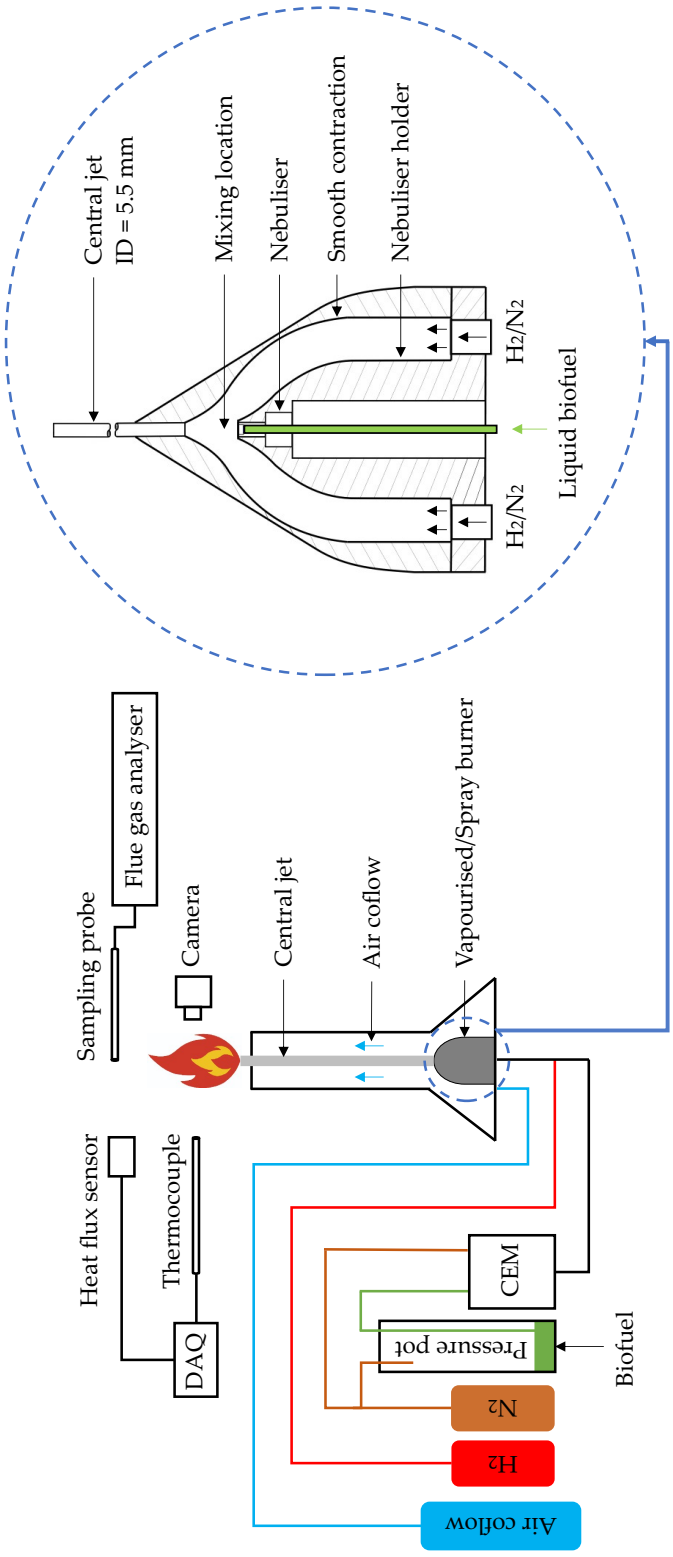

Figure 3.1: Schematic of vapourised/ultrasonic spray burner configuration. "CEM" refers to the controlled evaporating mixing unit. "DAQ" refers to the data acquisition systems.

3.2.3 Needle spray burner

The complex physical properties of biofuel play an important role in spray characteristics (e.g. droplet morphology and level of dispersion), which in turn influence the combustion characteristics. To investigate the impact of various biofuel physical properties and the non-dimensional parameters on the spray characteristics and the flame characteristics of the biofuel-blended hydrogen flames, a coaxial needle spray burner was designed to introduce the biofuel additives into the fuel mixture by gas-assist atomisation. The parameters of the needle spray burner can be found in Chapters 6 and 7. The schematic of the needle spray burner and the experimental setup is shown in Figure 3.2. This burner design is similar to the University of Sydney Needle Spray Burner (SYNSBURN^{TM}) [1, 2] that has been used in the Turbulent Combustion of Sprays (TCS) Workshop series.

Since the droplet size and morphology vary depending on the gas-assisted atomisation conditions, there is a risk of unburned liquid fuel droplets falling out of the flame envelope and causing fire. To reduce this risk, the needle spray burner is horizontally oriented and configured with a drip tray to control the potential unburned liquid fuel. Furthermore, the working range of the needle spray burner has been identified under non-reacting and reacting flow conditions to determine the safe flow cases of interest. The results of the working range identification and the spray burner characterisation are presented in §3.3 and Chapter 6, respectively.

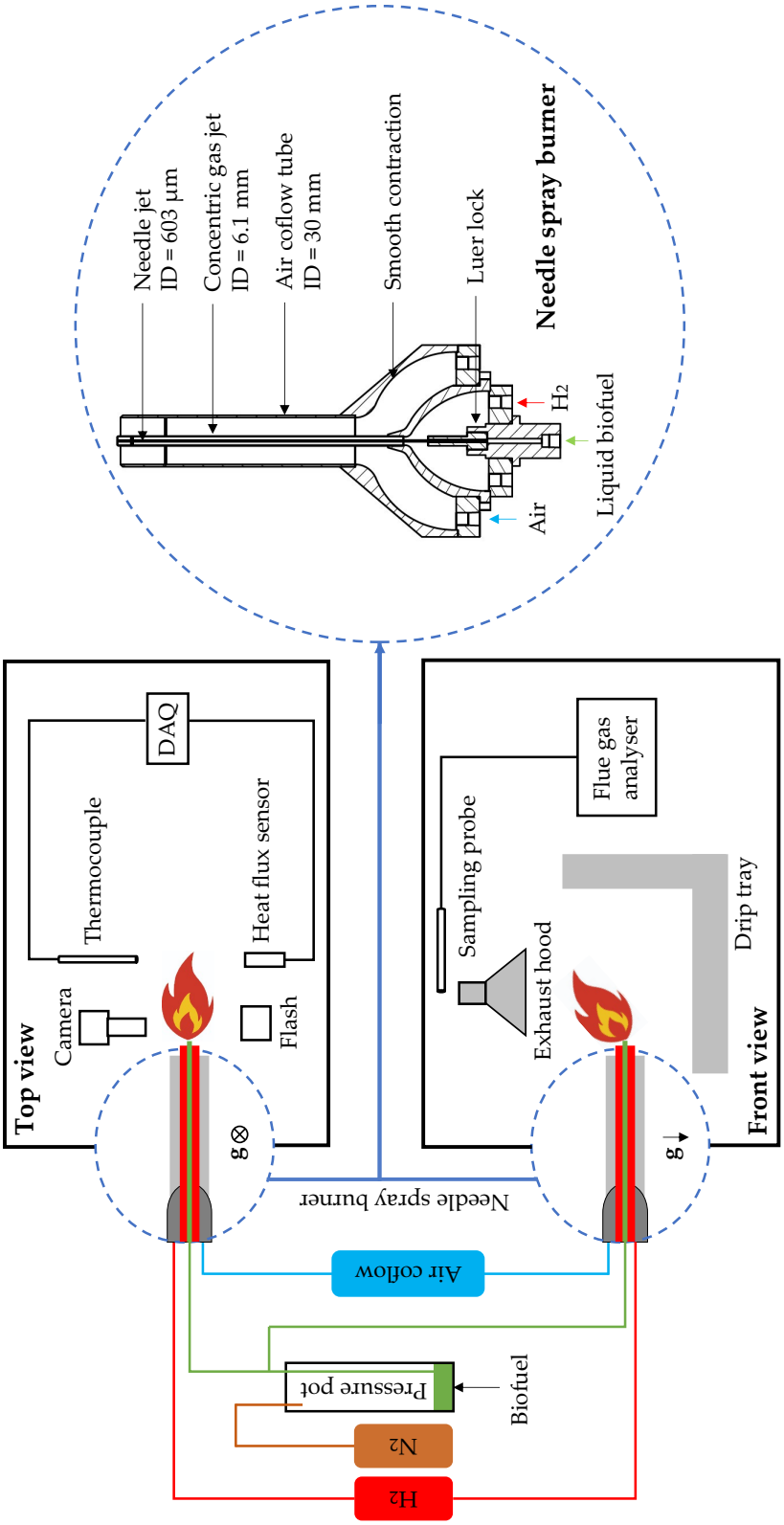

Figure 3.2: Schematic of needle spray burner configuration. "DAQ" refers to the data acquisition systems. "g" indicates the direction of gravity.

3.3 Needle spray burner characterisation

3.3.1 Working range identification—non-reacting flow

As discussed in §2.6.3, the performance of the gas-assist atomisation is controlled by various non-dimensional parameters, which in turn affects the combustion of the multi-phase fuels. A thorough and detailed identification of the working range of the spray burner is important for determining the flow cases of interest and the gas-assist spray flame analysis. Therefore, it is essential to characterise the spray burner under non-reacting conditions and understand the spray structures prior to the reacting flow tests.

In this section, the broad working range of the spray burner is identified by the observation of the spray breakup length and presented in Table 3.1 and Table 3.2, using air and helium, respectively, as the carrier gases and water as the liquid. The breakup length is defined as the axial distance before any ligament shredding or jet breakup is observed from the long-exposure photographs. The uncertainty of the measurement is $\pm$ 8%. The Weber number and gas/liquid momentum ratio are presented for each flow case in italic and bold text, respectively, using the equations presented in §2.6.3.2. The results reveal that using air or helium as the carrier gas at constant bulk mean velocity leads to distinct spray performance. This broad identification of the working range of the spray burner provides important information and evidence for further detailed investigation of spray structures and for reducing the risk of fire hazards. A detailed study of the spray characteristics of the interested flow cases along with the diagnostic—microscopic shadowgraphy imaging technology using commercial photographic equipment are presented in Chapter 6.

Table 3.1: Working range identification of spray burner using air/water. "U" denotes the bulk mean velocity (m/s); bold text in the cell (top) denotes the gas/liquid momentum flux ratio range; italic text in the cell (bottom) is the Weber number; "l" is the breakup length of the spray (mm); grey cell—no spray (l = N/A); orange cell—very coarse spray (l = 8–∞); blue cell—coarse spray (l = 3–8); yellow—fine spray (l = 1–3); and green cell—very fine spray (l < 1).

		Sprays			
Air U (m/s)	120	**108.3** *144*	**27.1** *143*	**12.0** *142*	**6.8** *141*
	110	**91.0** *121*	**22.8** *120*	**10.1** *119*	**5.7** *118*
	100	**75.2** *100*	**18.8** *99*	**8.4** *98*	**4.7** *97*
	90	**60.9** *80*	**15.2** *80*	**6.8** *80*	**3.8** *79*
	80	**48.1** *64*	**12.0** *63*	**5.3** *62*	**3.0** *62*
	70	**36.9** *48*	**9.2** *48*	**4.1** *48*	**2.3** *47*
	60	**27.1** *35*	**6.8** *35*	**3.0** *35*	**1.7** *34*
	50	**18.8** *25*	**4.7** *25*	**2.1** *25*	**1.2** *24*
	40	**12.0** *15*	**3.0** *15*	**1.3** *15*	**0.8** *15*
	30	**6.8** *9*	**1.7** *9*	**0.8** *9*	**0.4** *8*
	20	**3.0** *4*	**0.8** *4*	**0.3** *4*	**0.2** *3*
	10	**0.8** *1*	**0.2** *1*	**0.1** *1*	**0** *0.7*
Water U (m/s)		0.4	0.8	1.2	1.6

Table 3.2: Working range identification of spray burner using helium/water. "U" denotes the bulk mean velocity in m/s*; bold text in the cell (top) denotes the gas/liquid momentum flux ratio range; italic text in the cell (bottom) is the Weber number; "l" is the breakup length of the spray in* mm*; grey cell—no spray (l = N/A); orange cell—very coarse spray (l = 8–∞); blue cell—coarse spray (l = 3–8); yellow—fine spray (l = 1–3); and green cell—very fine spray (l < 1).*

		Sprays			
Helium U (m/s)	120	**15.0** *20*	**3.7** *20*	**1.7** *20*	**0.9** *20*
	110	**12.6** *17*	**3.1** *17*	**1.4** *17*	**0.8** *16*
	100	**10.4** *14*	**2.6** *14*	**1.2** *14*	**0.7** *14*
	90	**8.4** *11*	**2.1** *11*	**0.9** *11*	**0.5** *11*
	80	**6.7** *9*	**1.7** *9*	**0.7** *9*	**0.4** *9*
	70	**5.1** *7*	**1.3** *7*	**0.6** *7*	**0.3** *7*
	60	**3.7** *5*	**0.9** *5*	**0.4** *5*	**0.2** *5*
	50	**2.6** *3*	**0.7** *3*	**0.3** *3*	**0.2** *3*
	40	**1.7** *2*	**0.4** *2*	**0.2** *2*	**0.1** *2*
	30	**0.9** *1*	**0.2** *1*	**0.1** *1*	**0.1** *1*
	20	**0.4** *0.5*	**0.1** *0.5*	**0** *0.5*	**0** *0.5*
	10	**0.1** *0.1*	**0** *0.1*	**0** *0.1*	**0** *0.1*
Water U (m/s)		0.4	0.8	1.2	1.6

3.3.2 Working range identification—reacting flow

The working range identification of the spray burner under non-reacting flow conditions was presented in §3.3.1, providing initial information and evidence to establishing flames on the needle spray burner. However, whether the atomised liquid fuel droplets can be fully consumed in the flame is uncertain, which requires further investigation of the broad working range under reacting flow conditions.

In this section, the broad working range of the spray burner under reacting flow conditions is identified to provide insights into the potential flame cases for H_2/N_2/biofuel flame study while controlling the risks of fire hazards (refer to §3.2). Hydrogen was chosen as the base fuel and the carrier gas for the atomisation of liquid fuel. Ethanol was chosen as the liquid fuel due to its higher volatility and lower hazardous level compared with other biofuel surrogates. The higher volatility of ethanol makes it more likely to fully react within the hydrogen flame, while the low hazardous level of ethanol minimises the impact if spillage of unburned liquid fuel occurs. Nitrogen was added to hydrogen to adjust the momentum flux of the carrier gas because it is an inert gas of high density. The flow rate of ethanol was tested at 3, 6, 9 mL/min, equivalent to 1–3 mol% blending ratio of the gas/liquid fuel mixture. The criterion for the identification of the working range is all liquid fuel droplets can be consumed in the flame. In general, the results shown in Table 3.3 suggest that the atomised liquid droplets are fully consumed when the Weber number is greater than 80 and it is relatively insensitive to the momentum flux ratio.

Table 3.3: Working range identification of spray burner using H_2/N_2/ethanol. "V" denotes the bulk mean volumetric flow rate in L/min*; bold text in the cell (top) denotes the momentum flux ratio range; italic text in the cell (bottom) is the Weber number; orange cell—liquid droplets not fully consumed; and green cell—no unconsumed liquid droplets observed.*

		Flames				
H_2 V (L/min)	261	**15–143** *95*	**33–302** *200*	**40–368** *244*	**52–469** *310*	**70–631** *417*
	144	**5–43** *29*	**15–135** *89*	**19–176** *116*	**26–239** *158*	**38–346** *228*
	136	**4–39** *25*	**14–126** *83*	**18–165** *109*	**25–226** *149*	**36–328** *217*
	109	**2–25** *16*	**10–96** *63*	**14–129** *85*	**20–181** *120*	**30–271** *178*
	68	**1–9** *6*	**6–58** *38*	**9–82** *54*	**13–121** *80*	**21–191** *126*
N_2 V (L/min)		0	18	25	35	50

3.4 Experimental diagnostics

The blending effect of biofuel additives on the combustion characteristics of hydrogen-based flames, including flame appearance, flame luminosity, radiant intensity, flame temperature, pollutant emissions, and spray characteristics, has been experimentally investigated. The combustion characteristics and corresponding diagnostics are introduced in this section. The detailed settings and parameters of the diagnostics are adjusted accordingly to the requirements of different experiments in the methodology section of publications.

3.4.1 Flame appearance measurement

Digital single-lens-reflex (DSLR) cameras were used to capture the variations in flame appearance between unblended and biofuel-blended hydrogen flames. DSLR cameras operate by capturing light through a lens, reflecting it with a mirror and prism to the optical viewfinder, and redirecting it to the image sensor when the shutter is released. They offer superior image quality due to larger sensors, interchangeable lenses for versatility, manual controls for precise adjustments, faster performance for capturing action, and a wide range of accessories for expanded functionality. These features make DSLR cameras preferred when seeking quick assessment, high-quality images, and flexibility in measurement pursuits.

Yellow streaks were observed in hydrogen flames, showing a strong signal in spectral measurements at $\sim$589 nm. This phenomenon was attributed to the interference from sodium in the ambient air, which has been previously reported [3, 4]. A 594 nm notch filter (FWHM = 23 nm) was added in front of the camera to remove this interference from all photographs reported.

The coloured images taken by the DLSR cameras provide information on the variation in colouration between flame cases. The change in flame colouration and distribution is an indication of the dominant species such as soot particulates, water vapour, and CH^* in the flame. In addition to the direct observation provided by the images, the signal intensity of the pixels extracted from the images can be used as an indication of flame luminosity for quantitative comparison across various flame cases. The coloured images are converted to greyscale during image post-processing to acquire the signal intensity of each pixel. The signal intensity can be further processed adapting to different analyse purposes.

3.4.2 Thermocouple for temperature measurement

Temperature data of a flame is critical to the evaluation of soot evolution and NO_x emissions. Thermocouples have been extensively employed as a physical probe for time-averaged flame temperature measurements due to their reliability and low cost [5–7]. When the junction of two dissimilar metallic wires of a thermocouple is exposed to different temperatures, a proportional electrical voltage potential is generated based on the thermoelectric effect, also known as the Seebeck effect [8]. The electrical signal is then recorded and converted to temperature [7]. The insertion of a thermocouple probe into a flame can cause local and global disturbances of both an aerodynamic and chemical nature [5]. To minimise the probe-induced aerodynamic perturbations in a turbulent diffusion flame, while achieving a faster response time and higher spatial resolution, a Type-R thermocouple with 0.2 mm diameter wire size and a 0.7 mm diameter bare-bead was employed. The mean flame temperature at each measuring location was collected for 1 min at 10 Hz after a steady state was achieved. The error calculated from the obtained flame temperature data was $\pm 1\%$.

The utilisation of a thermocouple entails the measurement of temperature at the junction of the thermocouple probe, which may not inherently align with the actual temperature of the surrounding gas. As a consequence, the acquired temperature data could be notably underestimated ascribing to the inertia and energy loss. Correction for heat transfer effects is required for accurate thermocouple temperature measurements [5, 6, 9]. Radiative heat transfer of the thermocouple with its surroundings is a major concern, for example, the error can reach up to 250° C in a 1400° C flame [5]. The radiation correction equations and processes [9] for thermocouples are shown in Appendix B. The uncertainty of the mean flame temperature measurement was primarily due to the radiation correction and was estimated to be $\pm 6\%$.

3.4.3 Heat Flux Sensor for Radiant Intensity Measurement

To measure the radiant intensity emitted by the flames, a Schmidt-Boelter gauge (Medtherm Corporation) was utilised as the transducer. This heat flux sensor incorporates a thermopile as the sensing component, which is shielded by a sapphire window. The sapphire window allows the transmission of approximately 85% of the nominal thermal radiation within the range of 5–200 kW/m^2. The heat flux sensor provides a full-field angle view of 150°. Since the heat flux sensor has different angular sensitivity, a view restrictor was mounted on the heat flux sensor to reduce the view angle to 20°.

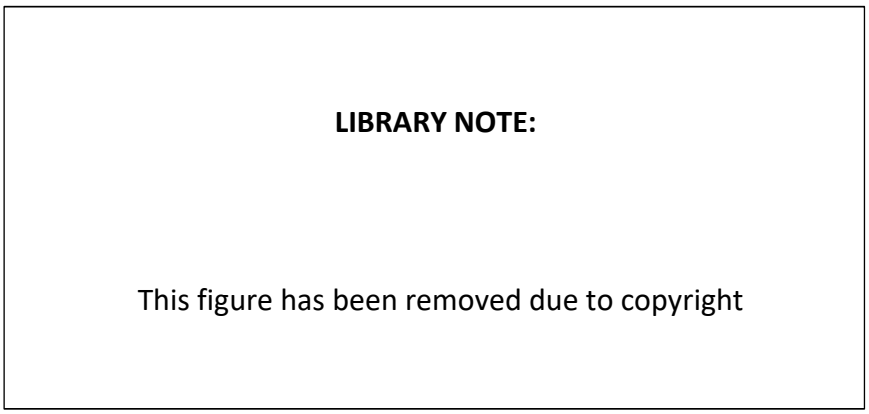

Figure 3.3: Angular sensitivity of the heat flux sensor with/without a 20° *view restrictor*

The angular sensitivity of the heat flux sensor with or without the view restrictor was assessed. A non-premixed laminar ethylene flame on a Bunsen burner was employed as the radiative heat source to investigate the angular sensitivity of the heat flux sensor (serial number 92242) from -70° to 70° (sensor to the measuring object). The Bunsen burner was placed at 380 mm radial distance from the sensor. In total, 150,000 samples were collected for 30 s at 5000 Hz, and averaged to obtain the mean radiative heat flux at each angle after the background correction. As shown in Figure 3.3, the angular sensitivity of the sensor without a view restrictor peaks at 0° and decreases as the angle increases. In comparison, the radiant heat flux signal was cut off outside of the angle range from -10° to 10° when the view restrictor was installed. This experiment provides evidence to support the multi-location measurement to locate peak radiant intensity in flames with a view restrictor. By incorporating a view restrictor, the uncertainty of the radiant heat flux measurement was reduced to $\pm 3\%$.

Radiant fraction, which is the ratio of total radiated power and the flame's output power, was employed to compare the efficiency of radiation enhancement of different biofuel dopants. The radiant fraction is defined as [10]:

$$\chi_r = \frac{\dot{Q}_r}{\dot{Q}_F} = \frac{2 \cdot \pi \cdot R \cdot \int_0^\infty q''(\dot{x}) dx}{\dot{m} \times LHV} \tag{3.1}$$

where $\dot{Q}_r$ is the total radiated power (kW), $\dot{Q}_F$ the output power of the flame (kW), R the radial distance from the centre of the jet to the heat flux sensor,

$\int_0^\infty q''(\dot{x})dx$ the total axial radiative flux (kW/m^2), $\dot{m}$ the fuel mass flow rate, and LHV the lower heating value of the fuel [10].

3.4.4 Global Emissions Measurement

Pollutant emissions including CO, CO_2, and nitrogen oxides (NO_x, comprising NO and NO_2) between different flames have been quantified and compared. Thermal NO_x is promoted due to the high flame temperature of hydrogen flames. It is essential to quantify NO_x emissions between different biofuel-doped hydrogen flames. To account for the various heat input, molecular weight, and ambient air entrainment, an emission index for NO_x (EI_{NO_x}) is employed and calculated using Equation 3.2 [10, 11]:

$$EI_{NO_x} = \frac{X_{NO_x}}{(X_{CO} + (X_{CO_2} - X_{CO_{2amb}}))} \times \frac{n_c \times MW_{NO_x}}{MW_f \times LHV_f} \tag{3.2}$$

where X is the mole concentration of NO_x, CO, CO_2 in the exhaust gases, CO_{2amb} is the concentration of CO_2 in ambient air in mole, n_c denotes the carbon concentration of fuel, MW_{NO_x} is the molecular weight of NO_x, MW_f and LHV_f denote the molecular weight and the lower heating value of the fuel mixture, respectively. Note that Equation 3.2 is not applicable to carbon-free fuel mixtures [11].

To quantify the comprehensive emissions encompassing carbon monoxide (CO), carbon dioxide (CO_2), and nitrogen oxides (NO_x), a Testo 350 XL flue gas analyser was utilised. The analyser incorporates sensors with a resolution of one parts per million (ppm) for NO, NO_2, and CO, while for CO_2 measurements, the resolution is 0.01 volume percent (vol.%). The probe was placed at the centre of the fume hood to collect samples of flue gas emitted from different biofuel-blended hydrogen flames. The flue gas samples then passed through a particle filter to the chemical cells for analysis. The flue gas analyser was calibrated by a CO, CO_2, and NO gas mixture with known concentration before use. The results from the calibration suggest a $\pm$2% uncertainty in the measurement.

3.4.5 Microscopic shadowgraphy

3.4.5.1 Optical setup

A schematic of the microscopic shadowgraphy setup is shown in Figure 3.4. Three key components for shadowgraph imaging technology are the detector, lens, and light source. A digital single-lens reflex camera (Canon EOS 50D)

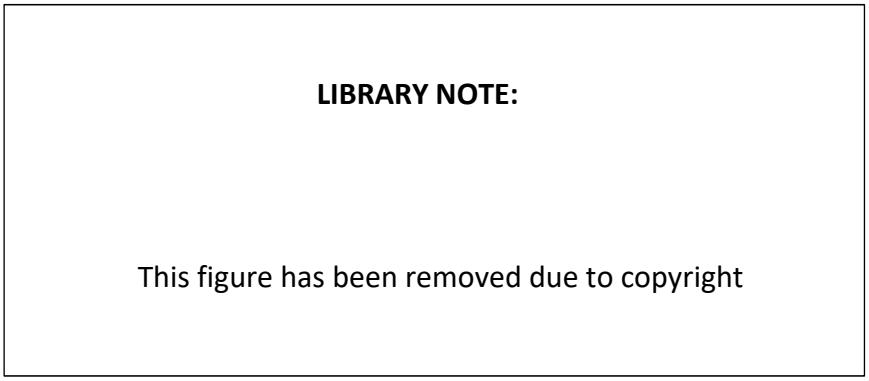

Figure 3.4: Schematic of microscopic shadowgraphy setup.

was used as the detector to capture the spray characteristics. The ISO sensitivity was adjusted to 1000 to achieve contrast between the spray and the background. A K_2 DistaMax long-distance microscope (Infinity) and a CF-2 objective were used with the DSLR camera to magnify regions of interest. An electronic flash unit (Canon EL-1) was placed opposite the microscope as the light source to back-illuminate the spray flow. The parameters of the camera, long-distance microscope, objective, and flash are reported in Table 3.4.

Table 3.4: The parameters of the camera, long-distance microscope, CF-2 objective, and electronic flash unit. The "A" refers to the adjustable aperture diaphragm. DOF is the depth of field of the image.

Parameter	Unit	Value
Canon EOS 50D		
Image resolution	pixels	4752×3168
Pixel size	µm	4.69
Sensor size	mm	22.3×14.9
ISO sensitivity	-	1000
Shutter speed	s	1/8000
Bit depth	bit	14
K_2 DistaMax with CF-2 objective		
Working distance	mm	120
Imaging area	mm	10×7
DOF (A = closed)	mm	2.95
Canon EL-1 flash		
Power output setting	-	1/8192
Flash duration (nominal)	µs	10
Flash duration (measured)	µs	15 ± 2

One of the advantages of this diagnostic configuration is the easy alignment of the camera, long-distance microscope, region of interest, and electronic flash.

Since the region of interest for shadowgraph imaging is typically the near-field spray area where PDPA is not applicable, the camera is focused on the centre of the needle jet exit. The position of the flash was adjusted to ensure the region of interest is homogeneously illuminated by the light. The use of a flash diffuser was found critical to achieve homogeneous illumination.

A key challenge for spray characterisation is the method to "freeze" the flow motion, either by the short duration time of the light source or the short exposure time of the camera. In the previously reported diagnostics, lasers functioned as the light source to achieve duration time in nanoseconds, and a scientific ICCD camera can also achieve an exposure time in nanoseconds. The shortest exposure time for Canon EOS 50D is 125 µs, several magnitudes longer than that of lasers. Therefore, the Canon EL-1 flash with the nominal duration time of 10 µs (specified by the manufacturer) was chosen to "freeze" the flow motion with a trade-off in performance that motion blur may occur when measuring small objects moving at high speed. In this case, the short duration of the flash at 10 µs ensures the caption of the flow details and the shutter speed of the camera is insignificant. The detection limit of the minimum size of a moving object without motion blur is restricted by the duration time of the flash. The power output of the camera flash is inverse to the flash duration time. To achieve the shortest flash duration, the flash power output was set to the lowest power setting (1/8192). The flash duration (FWHM) was measured to be 15 µs with inter-shot variability of ± 2 µs using an oscilloscope and a photodiode.

An advantage of using a commercial photographic camera is the higher spatial resolution can be achieved at a significantly lower cost compared with scientific cameras. The spatial detection limit of the optical setup is restricted by the diffraction-limited resolution and the in-plane spatial resolution calculated by the field of view (FOV) and the total pixels of the camera. The diffraction-limited resolution was measured at 8.8 µm using a resolution test target (Thorlabs high-frequency NBS 1963A). The field of view (FOV) of the optical setup is 10.4 mm (L) $\times$ 7.3 mm (W). The distance from the liquid jet exit is normalised by the liquid jet ID as x/D. The in-plane spatial resolution was identified from the field of view (FOV) and the total pixels of the camera as 2.3 µm. Therefore, the spatial detection limit of the optical setup is determined to be 8.8 µm. The depth of field (DOF) of the long-distance microscope-equipped camera was measured at 2.95 mm with an uncertainty of ± 0.03 mm.

3.4.5.2 Image processing and uncertainties

The flow chart shown in Figure 3.5 illustrates the steps followed in this work for image processing. All the images were corrected for dark charge. To account for vignetting, a uniformity image was taken when the light source was on and the spray flow was off. This uniformity image was used for attenuation correction. The images were subtracted by the background image, which was also corrected for dark charge and attenuation. The images were then binarised in MATLAB by applying a maximum normalised pixel threshold to distinguish the spray features and the background.

It has been systematically studied in previous research that the determination of the threshold is critical since the measurement of small objects is more sensitive to the threshold level and results in a larger discrepancy, compared with larger objects [12, 13]. For example, a 18 µm object is underestimated by 40% for a normalised threshold of 74%, whereas 5% error is found for a 145 µm object [14]. As the optical setup introduced in this chapter focused on resolving relatively larger objects than 100 µm diameter, the obtained results are less sensitive to the threshold level. In addition, the shadowgraphs were taken at the initial break-up region where few defocussed droplets were observed to interfere with the results. This is because the spray has not undergone dispersion in this region and the droplets can be captured by the relatively large DOF of 2.95 mm. In previous studies, 40–60% of the peak pixel intensity has been used as the threshold to attain an error of 10% in object size [15, 16]. A sensitivity analysis has been conducted to evaluate the threshold from 40–70% using a non-dimensional parameter area fraction (A_S/A_T), defined as the ratio of the area occupied by the spray objects (A_S) to the total area (A_T) in the FOV. The sensitivity analysis shows that for the threshold range of 40–57% and 63–70%, the uncertainty of area fraction is large from -18% to 74%. It is noted that the uncertainty is reduced within 58–62% threshold range compared with larger thresholds between 63–70%. In this study, the threshold was chosen to be 60% of the peak intensity.

Fifty (50) microscopic shadowgraphs were taken for each flow case. The non-dimensional parameter area fraction (A_S/A_T) was used to analyse the statistical significance of the data set. The area occupied by the spray objects is calculated by the total black pixels (pixel intensity = 0) in the binarised shadowgraphs, whereas the total area is indicated by the total pixels in the shadowgraphs. The results show that the accumulative average of area fraction from the data set converged to $\pm$5%. To capture the evolution of the liquid core in different flow cases, in addition to the short-exposure

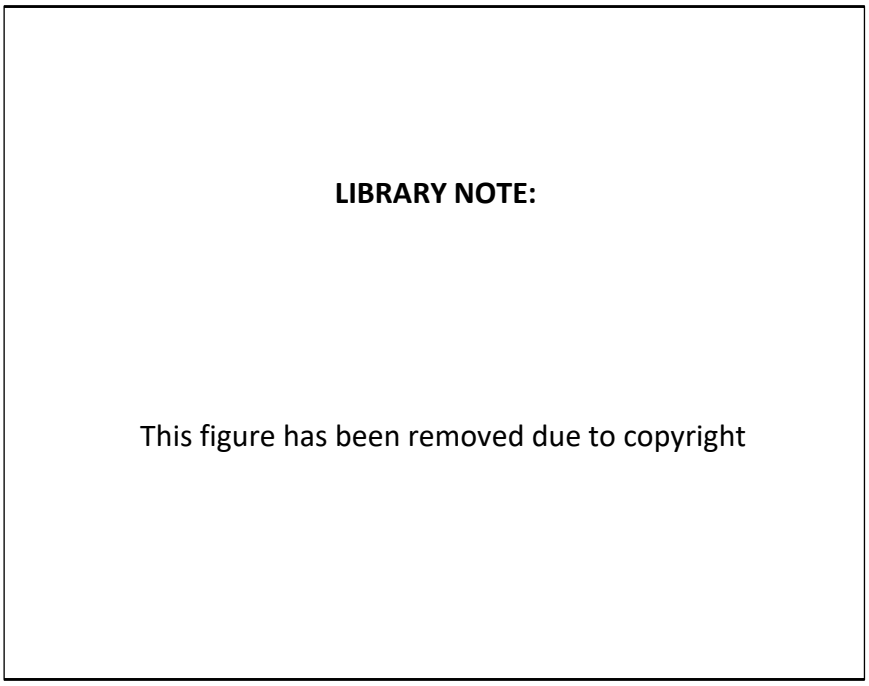

Figure 3.5: Flow chart of image processing.

shadowgraphs, five shadowgraphs with a longer exposure time of 2 s were taken for each flow case.

The extraction of spray information from the shadowgraphs for characterisation and classification could be achieved using automated algorithms [2, 13, 16] and machine learning [17], consisting of detecting dark objects on a white background and their geometric properties. The classification criterion (see §6.3.1) and uncertainties are applied in the automated algorithms for object matching [12, 14]. They could be developed in Matlab and are particularly useful for massive image post-processing. However, because the focus of this work is on introducing the optical setup and spray characterisation, applying automated algorithms or machine learning is not essential. In this work, the characteristic lengths of droplet size, wavelength, and ligaments are manually calculated based on the pixels from the microscopic shadowgraphs.

3.5 Numerical approach

Numerical simulation was employed in this research to analyse the effect of chemical structures and functional groups of biofuel surrogates on the

soot formation and pollutant emissions in biofuel-blended hydrogen flames. The chemical analysis was conducted with the opposed-flow diffusion (OPPDIF) module of Chemkin Pro v19.2 with comprehensive chemical kinetic mechanisms to model NO_x and PAHs formation.

Opposed-flow diffusion (OPPDIF) flames in Chemkin Pro are simulated using computational modelling to analyse combustion phenomena. The simulation involves defining the system geometry, specifying the fuel and oxidiser streams' characteristics, and setting the initial conditions. Conservation equations for mass, momentum, energy, and species are numerically solved to account for transport and reaction processes within the flame. The convective and diffusive transport mechanisms are considered, driven by flow velocities and molecular diffusion, respectively.

Chemical kinetic mechanisms define the reaction rates and pathways of various species, enabling the calculation of species formation and consumption rates based on local conditions. The chemical kinetics employed in this research were developed and presented by the CRECK Modelling Group for the purpose of simulating PAH formation to predict soot and dominant NO_x formation pathways in biofuel/hydrogen flames [18]. It encompasses a comprehensive network of 24501 individual reactions involving 497 distinct chemical species, spanning the combustion of hydrocarbons within the C_1 to C_{16} range. To the best of the authors' knowledge, detailed chemical kinetics mechanisms that contain toluene, anisole, and guaiacol are available; however, they are unavailable for the essential oil surrogates eucalyptol and D-limonene. With the growing interest in the potential of using bio-oils as a renewable energy carrier for combustion, more comprehensive mechanisms may become available in the future.

To predict and understand the soot evolution in biofuel-blended/H_2 flames, naphthalene ($C_{10}H_8$, henceforth denoted as A2) was chosen as the representative PAH for the Chemkin simulation. Naphthalene has been widely used in computational investigations because it is a critical intermediate in the generation of large soot precursors [19–21]. Formaldehyde (CH_2O), recognised as an abundant species in the initial oxidation reactions that is strongly linked to the biofuel concentration. It also serves as a precursor to both fuel oxidation and PAH oxidation, and a primary intermediary species in the conversion of toluene to CO_2 [19]. Therefore, formaldehyde was selected as the indicator of the PAH oxidation rate.

The NO_x formation in biofuel/hydrogen flames was conducted through numerical modelling to understand the observations of global NO_x emissions collected from the experiment. The focal point resides in the evaluation of the rate of production (ROP) of NO_x, PAHs, and the principal pathways governing their formation. The numerical results from the chemical kinetic analysis not only demonstrate the observation from experimental results, but more importantly provide understanding from a chemical perspective into the effect of biofuel addition on dominant reaction pathways for PAHs and NO_x formation which are unavailable through experiments.

3.6 References

[1] A. Lowe, A. Kourmatzis, and A. R. Masri. "Turbulent spray flames of intermediate density: Stability and near-field structure". *Combust. Flame* 176 (2017), pp. 511–520.

[2] G. Singh, A. Kourmatzis, and A. Masri. "Dense sprays with a focus on atomization and turbulent combustion". *Flow Turbul. Combust.* 106 (2021), pp. 405–417.

[3] J. Robinson and V. Smith. "Emission spectra of organic liquids in oxy-hydrogen flames". *Analytica Chimica Acta* 36 (1966), pp. 489–498.

[4] E. E. Arens, R. C. Youngquist, and S. O. Starr. "Intensity calibrated hydrogen flame spectrum". *Int. J. Hydrog. Energy* 39 (2014), pp. 9545–9551.

[5] M. Heitor and A. Moreira. "Thermocouples and sample probes for combustion studies". *Prog. Energy. Combust. Sci.* 19 (1993), pp. 259–278.

[6] N. Yilmaz, W. Gill, A. B. Donaldson, and R. E. Lucero. "Problems encountered in fluctuating flame temperature measurements by thermocouple". *Sensors* 8 (2008), pp. 7882–7893.

[7] K. Shannon and B. Butler. "A review of error associated with thermocouple temperature measurement in fire environments". *Proceedings of the 2nd International Wildland Fire Ecology and Fire Management Congress*. Citeseer. 2003, pp. 16–20.

[8] A. Van Herwaarden and P. Sarro. "Thermal sensors based on the Seebeck effect". *Sens. Actuators* 10 (1986), pp. 321–346.

[9] C. R. Shaddix. "A new method to compute the proper radiant heat transfer correction of bare-wire thermocouple measurements." *Sandia National Lab.(SNL-CA), Livermore, CA (United States)* (2017).

[10] X. Dong, G. J. Nathan, S. Mahmoud, P. J. Ashman, D. Gu, and B. B. Dally. "Global characteristics of non-premixed jet flames of hydrogen–hydrocarbon blended fuels". *Combust. Flame* 162 (2015), pp. 1326–1335.

[11] S. R. Turns and F. H. Myhr. "Oxides of nitrogen emissions from turbulent jet flames: Part I-Fuel effects and flame radiation". *Combust. Flame* 87 (1991), pp. 319–335.

[12] J. T. Kashdan, J. S. Shrimpton, and A. Whybrew. "Two-Phase Flow Characterization by Automated Digital Image Analysis. Part 2: Application of PDIA for Sizing Sprays". *Particle & Particle Systems Characterization: Measurement and Description of Particle Properties and Behavior in Powders and Other Disperse Systems* 21 (2004), pp. 15–23.

[13] A. Kourmatzis, P. X. Pham, and A. R. Masri. "Characterization of atomization and combustion in moderately dense turbulent spray flames". *Combust. Flame* 162 (2015), pp. 978–996.

[14] J. T. Kashdan, J. S. Shrimpton, and A. Whybrew. "Two-phase flow characterization by automated digital image analysis. Part 1: fundamental principles and calibration of the technique". *Particle & Particle Systems Characterization: Measurement and Description of Particle Properties and Behavior in Powders and Other Disperse Systems* 20 (2003), pp. 387–397.

[15] A. Kourmatzis, P. X. Pham, and A. R. Masri. "A two-angle far-field microscope imaging technique for spray flows". *Meas. Sci. Technol.* 28 (2017), p. 035302.

[16] G. Singh, A. Kourmatzis, and A. Masri. "Volume measurement of atomizing fragments using image slicing". *Exp. Therm. Fluid Sci.* 115 (2020), p. 110102.

[17] P. Toth, A. B. Palotas, T. A. Ring, and E. G. Eddings. "A robust method for the quantitative shadow imaging of dense reacting particulate flows". *The 8th US National Combustion Meeting, Park City, Utah*. 2013.

[18] T. Faravelli, A. Frassoldati, and E. Ranzi. "Kinetic modeling of the interactions between NO and hydrocarbons in the oxidation of hydrocarbons at low temperatures". *Combust. Flame* 132 (2003), pp. 188–207.

[19] M. J. Evans, D. B. Proud, P. R. Medwell, H. Pitsch, and B. B. Dally. "Highly radiating hydrogen flames: effect of toluene concentration and phase". *Proc. Combust. Inst.* 38 (2021), pp. 1099–1106.

[20] F. Bisetti, G. Blanquart, M. E. Mueller, and H. Pitsch. "On the formation and early evolution of soot in turbulent nonpremixed flames". *Combust. Flame* 159 (2012), pp. 317–335.

[21] A. Violi, A. D'Anna, and A. D'Alessio. "Modeling of particulate formation in combustion and pyrolysis". *Chem. Eng. Sci.* 54 (1999), pp. 3433–3442.

Chapter 4

Fundamental insights into the effect of blending hydrogen flames with sooting biofuels

Statement of Authorship

Title of Paper	Fundamental insights into the effect of blending hydrogen flames with sooting biofuels
Publication Status	☑ Published ☐ Accepted for Publication ☐ Submitted for Publication ☐ Unpublished and Unsubmitted w ork w ritten in manuscript style
Publication Details	Y. Yin, P.R. Medwell, A.J. Gee, K.K. Foo, B.B. Dally Fundamental insights into the effect of blending hydrogen flames with sooting biofuels Fuel, 331 (2023), Article 125618.

Principal Author

Name of Principal Author (Candidate)	Yilong Yin
Contribution to the Paper	1. Developed the research concept of evaluating the sooting propensities of renewable biofuels and their blending effect on the radiation enhancement of turbulent hydrogen flames. Determined the combustion characteristics of interest and their corresponding diagnostics, namely still photograph and lux meter for flame appearance and luminosity measurement, heat flux sensor for radiant heat flux, and thermocouple for flame temperature measurement. 2. Designed, organised, and conducted experimental campaigns. Selected biofuels and their surrogates for testing. Designed and built the burners for sooting propensity test of pure biofuels and for blending hydrogen with biofuels. Designed and determined the details of flame cases and test conditions. Developed required safety measures and documentation for the experiments. Prepared, tested and calibrated the equipment used in the experiments. Designed and assembled appropriate plumbing systems. 3. Designed and performed numerical modelling in Chemkin Pro for soot precursors formation and oxidation analysis to verify, interpret, and understand the observations from the experiments. Searched and revised chemical mechanisms that include soot precursors formation for the tested biofuel surrogates. 4. Collected, processed, and analysed data from the experiments and numerical simulation. Evaluated the uncertainties and reliability of the data. Initiated idea of evaluating flame luminosity using intensities extracted from the photographs. Generated and determined critical experimental and numerical results for a paper. Deepened the understanding of sooting propensities of biofuel tested in this study and the effect of prevapourised biofuel addition on combustion characteristics of hydrogen flames with the references from previous research. Identified the interactions and connections among the measured flame characteristics. Generated and determined novel findings of the study. 5. Developed and edited the manuscript. Selected the target journal of the manuscript. Submitted the manuscript and responded to reviewers' comments and recommendations as corresponding author.
Overall percentage (%)	75%
Certification:	This paper reports on original research I conducted during the period of my Higher Degree by Research candidature and is not subject to any obligations or contractual agreements with a third party that would constrain its inclusion in this thesis. I am the primary author of this paper.
Signature	2023.10.31 10:35:42 +10'30'
Date	31/10/2023

Co-Author Contributions

By signing the Statement of Authorship, each author certifies that:

i. the candidate's stated contribution to the publication is accurate (as detailed above);

ii. permission is granted for the candidate in include the publication in the thesis; and

iii. the sum of all co-author contributions is equal to 100% less the candidate's stated contribution.

Name of Co-Author	Paul R. Medwell		
Contribution to the Paper	1. Supervised the development of the research. Helped to evaluate the potential outcome and significance of the research. 2. Provided assistance with the training of experimental skills. 3. Advised on the experimental and numerical modelling details of the study. Supervised and approved the safety operation of the experiment. Advised on the calibration and setup of the experiment. 4. Advised on data processing and analysis. Evaluated the results and findings of this research. 5. Edited the manuscript. Provided suggestions for the responses to reviewers' comments.		
Signature	Paul Medwell 2023.10.31 10:46:36 +10'30'	Date	31-OCT-2023

Name of Co-Author	Adam J. Gee		
Contribution to the Paper	1. Provided assistance with the experimental setup and data collection. 2. Provided suggestions for the experimental design. 3. Helped to proofread the manuscript.		
Signature	Digitally signed by Adam Gee Date: 2023.11.02 07:34:47 +10'30'	Date	

Name of Co-Author	Kae Ken Foo		
Contribution to the Paper	1. Co-supervised the design of the experimental work, including flame cases, test conditions, and equipment calibration. 2. Provided assistance with the experimental setup and data collection. Provided suggestions for the data processing and coding. 3. Helped to proofread the manuscript.		
Signature	Digitally signed by Kae Ken Foo DN: C=AU, E=kaekenfoo@gmail.com, CN=Kae Ken Foo Date: 2023.11.01 16:09:50+10'30'	Date	1/11/2023

Name of Co-Author	Bassam B. Dally
Contribution to the Paper	1. Supervised the development of the research. Guided the direction of the research. 2. Provided assistance with the training of experimental skills. 3. Advised on the experimental and numerical approach of the study. 4. Advised on data processing and analysis. Evaluated the results and findings of this research. 5. Edited the manuscript. Provided suggestions for the responses to reviewers' comments.

Signature		Digitally signed by Bassam Dally Date: 2023.10.31 12:41:42 +03'00'	Date	

Fuel 331 (2023) 125618

Contents lists available at ScienceDirect

Fuel

journal homepage: www.elsevier.com/locate/fuel

Full length article

Fundamental insights into the effect of blending hydrogen flames with sooting biofuels

Yilong Yin [a,*], Paul R. Medwell [a], Adam J. Gee [a], Kae Ken Foo [a], Bassam B. Dally [b]

[a] School of Mechanical Engineering, University of Adelaide, Adelaide, South Australia 5005, Australia
[b] Clean Combustion Research Centre, King Abdullah University of Science and Technology, Thuwal 23955-6900, Kingdom of Saudi Arabia

ARTICLE INFO

Keywords:
Hydrogen
Biofuels
Sooting propensity
Combustion characteristics
Radiant heat flux
Oxygen content

ABSTRACT

A major challenge to using hydrogen as a carbon-free energy carrier to replace fossil fuels in high-temperature practical processes is the reduced thermal radiative transfer of hydrogen flames due to the absence of soot. To address the potential issue of low radiative heat transfer from hydrogen flames, the effect of blending highly sooting biofuels to turbulent nonpremixed hydrogen-based flames on flame luminosity and radiant heat flux enhancement is investigated in this paper. The sooting propensities of aromatic bio-oil surrogates (toluene, anisole and guaiacol) and monoterpene essential oil surrogates (eucalyptol and D-limonene) are evaluated. The Threshold Sooting Index (TSI) and Oxygen Extended Sooting Index (OESI) are calculated and compared with the data sets in the literature. The sooting propensities of the reported fuels are found to follow a decreasing order: aromatics > monoterpenes > alkenes > alkanes > aldehydes. The effect of chemical structure and functional group on sooting propensity tends to be more significant than the oxygen content and effective C/H ratio. Turbulent nonpremixed hydrogen–nitrogen (9:1 mol) jet flames are blended with 0.2 and 1 mol% (based on the molar concentration of hydrogen) vapourised biofuels. The results show that adding 0.2 and 1 mol% vapourised biofuels to the hydrogen-based flame non-linearly improves the flame luminosity and radiant fraction by 61%–253% and 2%–19%, respectively. Toluene is the most effective additive in luminosity and radiant fraction enhancement among all tested biofuels. Adding biofuels with an aromatic structure increases the radiant fraction by 10%–19%, which is more effective than cyclic monoterpenes (2%–9%). Adding non-oxygenated biofuels generally have larger increases in radiant fraction (9%–19%) than oxygenated biofuels (2%–10%).

1. Introduction

Hydrogen has long been seen as a potential alternative to fossil fuels due to its carbon-free nature [1–4]. Although over 95% of global hydrogen production still relies on steam-methane reforming or coal gasification, the production of green hydrogen is rapidly growing [5]. Unlike direct use of other renewable energy sources such as solar, wind and tidal energy, which have intermittent and geographical limitations, hydrogen can be stored and transported as a renewable energy carrier [6–8]. As a transitional step, a portion of hydrogen can be blended with natural gas (NG) in existing appliances to mitigate the CO_2 emissions by reducing the concentration of carbon per unit of energy delivered [9]. However, entire replacement of fossil fuels with pure hydrogen still requires significant advancement, not only because the current capacity of hydrogen production cannot meet the natural gas demand, but also because of the requirements of re-designing and replacing the end-use appliances. The feasibility and efficacy of using hydrogen as a base fuel for high-temperature practical processes requires a comprehensive understanding of hydrogen flames and innovative insights into their adaptation [1].

A key challenge for the direct replacement of natural gas with hydrogen is the reduced thermal radiative transfer of hydrogen flames due to their carbon-free nature, hence the absence of soot. Thermal radiation is typically one of the primary means of heat transfer in stationary energy systems, such as kilns and boilers, which is typically enhanced by the efficient blackbody radiation from soot particulates. Whilst gaseous species, such as CO_2 and H_2O also contribute to thermal radiation, these tend to be minor in comparison with the radiative heat transfer from soot [10–12]. To enhance the thermal radiation from hydrogen flames, which have considerably lower luminosity than hydrocarbon flames, one approach is to introduce additional material with complementary properties to the flames [13]. This can be in the

* Corresponding author.
E-mail address: yilong.yin@adelaide.edu.au (Y. Yin).

https://doi.org/10.1016/j.fuel.2022.125618
Received 6 July 2022; Received in revised form 6 August 2022; Accepted 11 August 2022
Available online 26 August 2022

form of non-reacting particles, or by doping the hydrogen with a small quantity of a highly sooting fuel [10,14].

To enhance the radiative heat transfer from hydrogen flames, a highly sooting hydrocarbon fuel can be chosen as a suitable additional agent [10,14,15]. Biofuels are preferable to hydrocarbons extracted from fossil fuels as they are derived from renewable biomass resources [16]. The production of biofuels can be widely combined with existing industries to utilise by-products and waste products of these production processes, such as from pulp and paper industries and food production plants, which makes it less harmful to the environment [17]. Liquid biofuels can be divided into subcategories based on their feedstocks and production methods, including bio-oils and essential oils. Bio-oils are derived from biomass refining, which mainly converts lignin, cellulose, and hemicellulose from renewable plant resources into liquid fuels through pyrolysis [18]. They often consist of a large proportion of aromatics, which is expected to promote the formation of polycyclic aromatic hydrocarbons (PAHs) and subsequently soot formation [19,20]. Essential oils are one of the renewable resources obtained from roots, bark, leaves, and aromatic parts by distillation or solvent extraction [21]. They are mainly composed of terpene-related $(C_5H_8)_n$ hydrocarbons [22]. Bio-oils and essential oils are the main focus of this study.

The sooting propensity of biofuels is indicated by various factors. Fuels with a higher carbon-to-hydrogen (C/H) ratio tend to have higher sooting propensity [23,24]. Related to this, the unsaturation degree, which is indicated by the number of carbon double-bonds and triple-bonds, increases the sooting tendency by forming polycyclic aromatic hydrocarbons (PAHs) [25,26]. In addition to the unsaturation degree and the C/H ratio, the presence of oxygen content in oxygenated fuels has been reported to reduce soot formation by promoting soot oxidation [25,27–31]. Biofuels are typically oxygenated, therefore, it is important to include the effect of oxygen content when assessing the sooting propensity of biofuels as potential add-on agents for hydrogen flames. Compared with using hydrogen as a diluent for soot reduction, improving the radiant intensity and identifying the combustion characteristics of a hydrogen-based flame by blending with hydrocarbons is poorly studied. However, a recent experimental study on hydrogen/toluene blends with 1%–5% toluene concentration (by mole of H_2) under turbulent nonpremixed conditions revealed that increasing the additive concentration from 1% to 3% has a marked effect on soot loading, but further increases in toluene concentration are less effective [10].

The smoke point (SP) has been widely employed to investigate and compare the sooting propensity of oxygenated and non-oxygenated hydrocarbons [32–34]. The smoke point is determined by the maximum luminous length of a flame without emitting soot [35]. The sooting propensity of fuels is inversely proportional to the SP. The threshold sooting index (TSI) is calculated based on the smoke point to enable correlation among different sooting propensity data sets measured in different experiments by scaling the constants of each data set [36]. The effect of molecular weight on sooting propensity is also taken into account in TSI since a higher molecular weight requires more oxygen transport into the flame and react with a unit volume of a fuel, which results in an increase in flame length [36]. To emphasise the effect of oxygen content in oxygenated hydrocarbons, the oxygen-extended sooting index (OESI) enables comparison of the sooting propensity between non-oxygenated and oxygenated hydrocarbons [37]. It has been reported in previous studies that the sooting propensities of non-oxygenated hydrocarbons follow this increasing order: alkanes < alkenes < 1-alkynes < aromatics [24]. The sooting propensities of oxygenated hydrocarbons (e.g., esters) have been reported in the increasing order: methyl and ethyl esters < carboxylic acids, propyl esters < butyl and pentyl esters [27]. However, there is a relative paucity of comparison available for the sooting propensity between oxygenated and non-oxygenated biofuels, monoterpenes and aromatics in particular — especially in the context of being additives in hydrogen flames.

The direct use of biofuels with complex compositions for data analysis and chemical mechanisms studies is challenging for fundamental-level studies [16]. Instead, it is preferable to find appropriate surrogates for biofuels. A fuel surrogate is a simple analogue created from one or more well-defined hydrocarbon species, with known compositions and properties that can emulate the chemical, physical, and combustion properties of a complex practical fuel. This approach is commonly used in both experimental and computational combustion studies [38,39]. In this study, five different biofuel surrogates are selected as potential additives. The chemical structures of the selected biofuel surrogates are shown in Fig. 1. Toluene (C_7H_8) is a non-oxygenated component of bio-oil, consisting of an aromatic structure with a methyl group attached. Anisole (C_7H_8O) is an organic compound consisting of a phenyl group attached to a methoxy group which is characteristic of a lignin structure. Anisole is one of the simplest surrogates for bio-oil for the formation and oxidation of methoxy phenol, which is the main precursor of PAH and soot in biomass combustion [40]. Guaiacol consists of a phenyl group attached to a hydroxy group and a methoxy group (-OCH_3). It is the primary aromatic oxygenate produced from lignin pyrolysis, which is more representative of a lignin pattern due to the similar chemical structures and functional groups, and is the main contribution to PAH and soot formation during biomass and bio-oil combustion [41]. Eucalyptol ($C_{10}H_{18}O$), also known as 1,8-cineole, is a cyclic monoterpenoid and surrogate for eucalyptus oil, as eucalyptus oil contains 90 wt% of eucalyptol, thus dominating the chemical and physical properties of eucalyptus oil [28]. D-limonene ($C_{10}H_{16}$) is a cyclic monoterpene compound and surrogate for orange oil, as orange oil contains 97 wt% of D-limonene. It is obtained from citrus fruit peels and has no oxygen content.

In this paper, the smoke point, luminosity and radiant heat flux of biofuels are tested on a wick-fed burner to establish the fundamental understanding of their flame characteristics and sooting propensity. In subsequent experiments, the biofuels are prevapourised and blended into turbulent nonpremixed 9:1 hydrogen/nitrogen jet flames to investigate their effects on flame appearance, flame luminosity and radiant heat flux. The addition of a small quantity of nitrogen increases the Reynolds number, so that operation in the fully turbulent regime was achieved. Qualitative and quantitative comparison amongst oxygenated and non-oxygenated biofuel additives with various chemical structures provides insights into the chemical effects on the efficacy of hydrogen/biofuel mixture thermal radiation properties and potential adaptation in practical processes.

2. Methodology

2.1. Sooting propensity measurements on a wick-fed burner

The smoke point (SP), luminosity and radiant heat flux of liquid bio-oil surrogates (toluene, anisole and guaiacol) and essential oil surrogates (eucalyptol and D-limonene) were tested under laminar non-premixed flame conditions on a wick-fed burner. Kerosene and ethanol were also tested as reference fuels. The flame length was controlled by adjusting the extended wick length above the exit plane. To measure the flame length at SP, the flame appearance was captured with a Canon 6D digital camera and a 50 mm f/1.8 lens [33,34]. The colour photos were first converted to greyscale for image post-processing. The flame contour was defined as the region in which the pixel intensity is above 75% of the peak intensity of each image [33]. The images were then binarised to determine the SP based on the flame contour. The value of SP was obtained from the pixel count between the exit plane and the flame tip. The measurement uncertainty in the SP test depends on the method for visual observation and calculation of the flame length at the SP. Obtaining the SP by pixel count from still photographs with long exposure time captured the flame length to ±3%. In addition, the measurement uncertainty of kerosene SP was also subjected to variations in its composition.

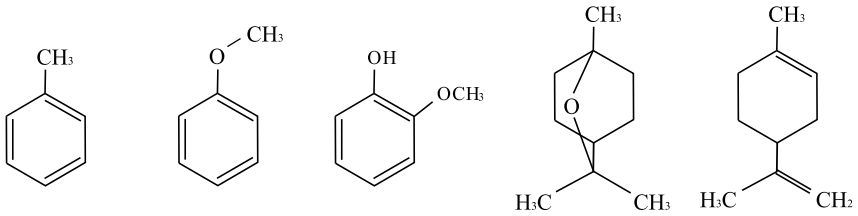

(a) Toluene (b) Anisole (c) Guaiacol (d) Eucalyptol (e) D-limonene

Fig. 1. Chemical structure of selected biofuel surrogates.

The TSI and OESI are both calculated to compare the sooting propensities of the biofuels tested in this work with fuels in the literature. The TSI is calculated from the SP as [36]:

$$TSI = a\left(\frac{MW_f}{SP}\right) + b \tag{1}$$

where a and b are constants for any given experimental setup, MW_f the molecular weight of the fuel. By adjusting the constants a and b following the procedure proposed by Calcote and Manos [36], comparison of the SP data acquired from different experiments can be achieved. The constants a and b for this test are calculated and presented in Section 3.1.1.

Among the studies that used TSI to quantify the sooting propensity, most were focussed on non-oxygenated hydrocarbons [42–44]. However, TSI is not appropriate for a comparison between oxygenated and non-oxygenated fuel as it does not account for the effect of oxygen content. Another sooting index, OESI, includes the effect of fuel-borne oxygen by including stoichiometric air requirements as a relevant parameter. The OESI is defined as [29]:

$$OESI = a'\left(\frac{n + m/4 - p/2}{SP}\right) + b' \tag{2}$$

where a' and b' are constants for a given experimental setup, and n, m and p are the number of carbon, hydrogen and oxygen, respectively. The experimental constants a' and b' of OESI can be adjusted following a similar procedure to the TSI to allow comparison of data sets obtained in different experimental setups.

In addition to the reduced radiant heat flux, hydrogen flames have considerably lower visibility than hydrocarbon flames. The approach of blending hydrogen with biofuels has potential to both enhance the luminosity and the radiant heat flux of hydrogen-based flames. In this study, the flame illuminance and radiant heat flux of laminar non-premixed biofuel flames are reported and correlated with the sooting propensities of the fuels.

The extended wick length was further adjusted to 1, 3 and 5 mm and kept consistent for all biofuels to attain stable laminar flames for luminosity and radiant heat flux measurements. In addition to the luminosity information from the photographs, flame illuminance (lumen/m^2) was measured by a Lux meter (Protech QM1584) to further investigate and quantify the visibility of the biofuel flames. The Lux meter was placed at the radial distance of 72 mm from the flame centre. A Schmidt-Boelter heat flux sensor (Medtherm Corporation model 92 241) was employed as the transducer, with a view angle restricted to 20°, to measure the radiant intensity between flames. The heat flux sensor was placed at a radial distance of 140 mm perpendicular to the vertical axis of the flame. With a 20° view angle placed at 140 mm, the heat flux sensor measured 50 mm flame length.

2.2. Experimental setup for biofuel-blended H_2/N_2 flames

Turbulent nonpremixed jet flames were stabilised on a 5.5 mm inner diameter, 300 mm length pipe, surrounded by a square (150 mm × 150 mm) uniform coflow of room-temperature air at 1 m/s. The relative distance between the flame tip and exhaust hood was kept constant at 700 mm. A 9:1 H_2/N_2 mixture (by mole) was selected as the base fuel for all flame cases with a fixed bulk mean Reynolds number 10,000 (based on the jet diameter). Vapourised biofuels at concentrations of 0.2 and 1%, based on the mole concentration of hydrogen, were added to the H_2/N_2 mixture. The H_2/N_2 flow rate and the carbon flow rates were kept constant to ensure an equivalent carbon flux in the fuel mixture. All liquid biofuels were prevapourised by heating to 190 °C and were mixed with a 9:1 mixture of H_2/N_2 gases with a controlled evaporating mixing (CEM) unit upstream of the burner. The burner was indirectly pre-heated by a hot nitrogen carrier gas flowing through the CEM (heated to 190 °C) prior to all flame case tests. To reduce heat losses between the CEM and the burner, the plumbing system was wrapped in heating coils and with thermal insulation. The jet exit temperature was measured to be 110 ± 6 °C in a non-reacting flow prior to lighting the flame. The partial pressure of the additives are below their vapour pressure at such temperatures. Condensation was not observed at the biofuel concentration used in the experiment. The vapourised biofuel/H_2/N_2 mixture flowed through symmetrically distributed holes on the base of the burner.

Table 1
Flame codes and cases of biofuel-blended H_2/N_2 flames. The total heat input is 24.6 kW ± 0.2 for 0.2 mol% case, and 28.2 kW ± 0.6 for 1 mol% case. The exit strain rate U/d (s^{-1}) is 20,400 ± 90. The Reynolds number is 10,400 ± 90 for a 0.2 mol% case, and 11,800 ± 450 for a 1 mol% case.

Flame code	Flame case
HTVx	H_2/N_2/Toluene (C_7H_8)
HEVx	H_2/N_2/Eucalyptol ($C_{10}H_{18}O$)
HLVx	H_2/N_2/D-limonene ($C_{10}H_{16}$)
HAVx	H_2/N_2/Anisole (C_7H_8O)

The exit strain rate is defined as the jet exit mean velocity (U) normalised by the jet diameter (d), i.e., U/d (s^{-1}) [45,46]. The flame conditions and corresponding flame codes are shown in Table 1 and are hereafter represented by flame codes. For example, in "HTVx", "HT" represents H_2/N_2 blended with toluene, "V" indicates the biofuels are prevapourised, and "x" represents the mole concentration of biofuel. The H_2/N_2 flame without any biofuel is hereafter referred to as "HB0".

The visual appearance of the flames was captured by a Canon 6D digital camera with a 50 mm f/1.8 lens. It was noted in preliminary experiments that yellow streaks were observed in hydrogen flames, which showed a strong signal in spectral measurements at ~589 nm. This phenomenon was attributed to the interference from sodium in the ambient air, as has been previously reported [47,48]. The use of a 594 nm notch filter (FWHM = 23 nm) in front of the camera removed this interference from all photographs reported herein.

The heat flux sensor described in Section 2.1 was placed at a radial distance of 284 mm perpendicular to the vertical axis of the flame. With a 20° view angle placed at 284 mm, the heat flux sensor measured the 100 mm flame length. The radiant heat flux data was collected at eight equi-spaced heights to measure the radiant intensity of different flames, starting from the height above burner (HAB) at 40 mm and ending at HAB 390 mm. The data points were chosen to focus on the region near the jet exit (x/L_f = 0–0.4) where the flame is mainly driven by momentum.

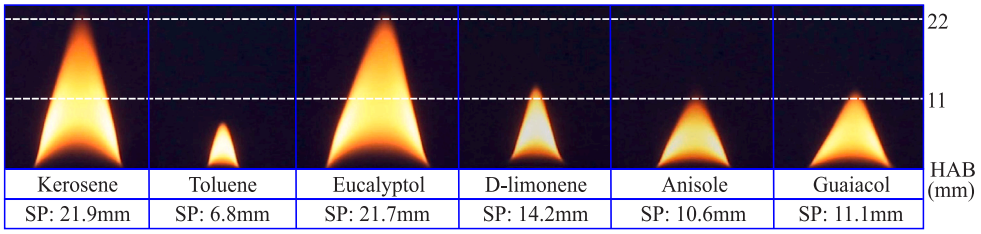

Fig. 2. Photographs of laminar nonpremixed flames on a wick-fed burner at SP. Photographs with 0.125 s exposures were taken at f/22, ISO 100. (For interpretation of the references to colour in this figure legend, the reader is referred to the web version of this article.)

The radiant fraction (χ_r), which is the ratio of total radiated power to the flame's thermal power, is employed to compare the effectiveness of radiation enhancement of different biofuels. The total radiated power ($\dot{Q}_r$) is the summation of the numerically integrated axial (z) and radial (r) radiant heat flux ($\dot{q}''$) measured in the experiment. The radiant fraction is defined as [49]:

$$\chi_r = \frac{\dot{Q}_r}{\dot{Q}_F} = \frac{2 \cdot \pi \cdot \left(\int_{R_0}^{R} r \cdot \dot{q}''(r) \cdot dr + R \cdot \int_{0}^{\infty} \dot{q}''(z) \cdot dz \right)}{\dot{m} \times LHV} \tag{3}$$

where $\dot{Q}_F$ the output power of the flame (kW), $\dot{m}$ the fuel mass flow rate, and LHV the lower heating value of the fuel, R the radial distance from the centre of the jet to the heat flux sensor, R_0 the radial distance from the centre of the jet to the flame front.

The centreline flame temperature, as an indicator of flame temperature, was measured by a Type-R thermocouple with 0.2 mm diameter wire size and a 0.7 mm diameter exposed bead. The flame temperature data points were obtained at the same locations as the radiant heat flux data. The thermocouple measurements were corrected for radiative heat losses.

2.3. Chemical kinetics modelling

To achieve a deeper understanding of the chemistry and dominating reaction pathways of PAH formation in biofuel-blended H_2/N_2 flames, numerical simulations of opposed-flow nonpremixed (OPPDIF) flames in Chemkin Pro v19.2 were employed. The OPPDIF model simulates a nonpremixed flamelet and has been widely used in conjunction with experimental approaches to investigate flame behaviours and chemical kinetics in jet flames [50,51].

The chemical kinetic mechanism used in this study was developed by the CRECK Modelling Group for soot formation modelling, with 24 501 reactions and 497 species for C_1–C_{16} hydrocarbon combustion [52]. However, the chemical kinetics modelling undertaken in this study only includes toluene and anisole. To the best of the authors' knowledge, a detailed chemical kinetics mechanism that also includes soot precursors is unavailable for the other fuels, namely guaiacol, eucalyptol and D-limonene. The concentrations of toluene and anisole were varied with a fixed H_2/N_2 concentration to simulate the experimental cases accordingly. The velocities at the fuel and oxidant inlets were adjusted to maintain a similar momentum.

To predict the soot formation and corresponding thermal radiation from the biofuel-blended H_2/N_2 flames, naphthalene ($C_{10}H_8$, hereafter referred to as A_2), was chosen for analysis in the Chemkin simulation because it is widely used in numerical studies as a key intermediate in forming large PAHs to analyse soot formation [10,53,54]. Formaldehyde (CH_2O) is a precursor to the oxidation of the fuel and the PAH, known to be (1) abundant in the initial oxidation reactions; (2) strongly correlated to the biofuel concentration; and (3) a primary intermediate species in toluene oxidation to CO_2 [10,55,56].

3. Results and discussion

3.1. Sooting propensity of biofuels

3.1.1. Flame appearance and smoke point

To compare the sooting propensities of the bio-oil surrogates with aromatic structures (toluene, anisole and guaiacol) and monoterpenes (eucalyptol and D-limonene) with non-oxygenated and oxygenated hydrocarbons, the TSI and OESI obtained in this work are correlated to the data sets from previous studies, following the procedure described in Section 2.1. Based on this comparison, the data sets of the fuels' sooting propensities are extended. It also extends knowledge of selecting suitable additives for luminosity and radiant heat flux enhancement in hydrogen-based flames.

Toluene (C_7H_8) and D-limonene ($C_{10}H_{16}$) are chosen as reference fuels to calculate the constants a, b for TSI in Eq. (1), and a', b' for OESI in Eq. (2), respectively, following the procedure described by Calcote and Manos [36]. The constants a and b are calculated to correspond to the TSI values of 44 and 24 for toluene and D-limonene, respectively [44]. The OESI values from Barrient et al. [29] (46.1 for toluene and 25 for D-limonene) are used to calculate a' and b'. The constants obtained from Eq. (1) and (2) are, $a = 5.3$ and $b = -26.86$ for TSI, $a' = 62.61$ and $b' = -36.73$ for OESI.

To include oxygen content into the consideration of sooting propensity, an effective C/H ratio has been proposed, as follows [57]:

$$(C/H)_{eff} = \frac{C - \frac{1}{4}O_{-} - \frac{1}{2}O_{=}}{H} \tag{4}$$

where C, O and H are the numbers of carbon, oxygen and hydrogen atoms, respectively. O_{-} and $O_{=}$ are the number of single- and double-bonded oxygen atoms, respectively. The effective C/H ratio represents the balance between soot formation and oxidation.

The photographs of flame appearance at SP are presented in Fig. 2. The SP for ethanol is not presented because the flame became unstable before reaching its SP. All flames except for ethanol display yellow colouration due to the presence of soot, whereas the ethanol flame is dominated by blue colouration.

The TSI and OESI of the fuels tested in this study, along with the data from the literature, are presented in Table 2. The SP, TSI and OESI of different types of hydrocarbons as a function of effective C/H ratio are plotted in Fig. 3. It is summarised from the results that the sooting propensities of the reported fuels generally follow a decreasing order of: aromatics > monoterpenes > alkenes > alkanes > aldehydes. The sooting propensity of kerosene (which is a mixture of paraffins, naphthenes and aromatic hydrocarbons) lies between non-oxygenated aromatics and alkanes. Fuels with an aromatic structure generally have a smaller value of SP and higher TSI and OESI amongst the reported fuels. This further demonstrates that aromatic fuels usually have higher sooting propensity and might be the most suitable add-on agent to be blended into hydrogen-based flames for radiation enhancement. It is noted that although the PAHs typically contain benzene rings, toluene has a higher sooting propensity than benzene. This is because the chemical bond between benzene ring and the methyl functional group in

Table 2
The Threshold Sooting Index (TSI) and Oxygen Extended Sooting Index (OESI) of oxygenated and non-oxygenated fuels. Values from previous work are from [29] unless otherwise indicated.

Compound	C/H_{eff}	TSI		OESI	
		Present	Ref [29]	Present	Ref [29]
Solvents					
Kerosene	0.46	17.9	–	16.2	–
Aromatics					
Toluene	0.88	44.0	44.0 [44]	46.1	46.1
Benzene	1.00	–	29.0	–	34.8
Anisole	0.84	27.2	–	13.5	–
Guaiacol	0.81	32.4	–	8.4	–
Monoterpenes					
Eucalyptol	0.54	10.8	–	3.7	–
D-limonene	0.63	24.0	24.0 [44]	25.0	25.0
Alkanes					
n-Hexane	0.43	–	2.6	–	3.3
n-Heptane	0.44	–	2.6	–	2.6
Alkenes					
1-Pentene	0.50	–	4.6	–	3.2
2-Heptene	0.50	–	4.7	–	4.2
Aldehydes					
1-Pentanal	0.45	–	2.9	–	0.5
Hexanal	0.46	–	5.2	–	2.2

toluene is easier to dissociate and actively participate in the hydrogen-abstraction-C_2H_2-addition (HACA) reaction. The sooting propensity of monoterpenes ranks second in the reported fuels, implying that the ring structure in eucalyptol and D-limonene might play an important role in PAH formation as their chemical structures are similar. This chemical structure in monoterpenes seems more favourable for soot formation than the chain structure in alkenes and alkanes, as the TSI and OESI of a monoterpenes are higher than that of alkenes and alkanes.

The results from the tested biofuels show that, for the same type of fuel, fuels with oxygen content (oxygenated fuels) usually have lower sooting propensities than non-oxygenated fuels, which agrees with previous studies [27,29,58]. It is seen from the comparison between OESI and TSI in Fig. 3(b) that values of OESI are similar to TSI for non-oxygenated hydrocarbons and are lower for oxygenated fuels to include the effect of fuel-borne oxygen. For example, the TSI for guaiacol (32.4) is higher than that of anisole (27.2), but the additional hydroxy group in guaiacol is known to reduce the soot formation and hence sooting propensity. This indicates that using OESI instead of TSI is more suitable for quantifying the sooting propensity of oxygenated fuels. The results also suggest that the effect of fuel-borne oxygen on sooting propensity is not as significant as chemical structures and related functional groups of the fuel. For example, although eucalyptol contains oxygen content, its OESI (3.66) is still higher than some of the non-oxygenated alkanes and alkenes with a similar effective C/H ratio. It is also noted that fuels with higher effective C/H ratio, such as aromatics (C/H_{eff} from 0.8–1), usually correlate with a higher sooting propensity. However, the sooting propensity does not always linearly increase with the C/H_{eff} ratio, implying that the chemical structure can have an effect that overwhelms the C/H_{eff} ratio.

The findings in the sooting propensity results have demonstrated the potential for lignin-derived bio-oils and waste food derived essential oils to be blended into hydrogen-based flames for radiation enhancement.

3.1.2. Flame illuminance and radiant heat flux

Figs. 4(a) and 4(b) show the liquid fuel flame illuminance and radiant heat flux, respectively, at different extended wick length. The results show that both the flame illuminance and radiant heat flux increases with the extended wick length; however, the increasing rate for different fuels is dissimilar. Anisole flames are the most sensitive to extended wick length, as their flame illuminance and radiant heat flux are increased by 70% and 26% from extended wick length 1 mm to 3 mm, respectively. Non-sooting ethanol flames display minimum increase to the change of extended wick length. They also have much lower illuminance and radiant heat flux than other tested fuels. Incorporating the observation from Section 3.1.1, the ethanol flame displays a blue colouration, indicating that its radiative heat transfer is mostly from gaseous species. Soot is known to have much stronger radiative emission than gaseous species [59]. This explains the lowest illuminance and radiant heat flux found in ethanol flames in Figs. 4(a) and 4(b).

The radiant heat flux of toluene and anisole are proportional to the TSI and OESI determined in this study. Toluene has the highest sooting propensity, which correlates with the highest flame radiant heat flux in Fig. 4(b). However, D-limonene has a higher SP (lower sooting propensity) than guaiacol, while it shows a higher radiant heat flux than guaiacol at all extended wick lengths. This observation suggests that fuels with high sooting propensities do not always directly result in high radiant heat flux from their flames. Other contributing factors, such as flame temperature, may play important roles in affecting the radiant heat flux.

Fig. 4(a) shows that eucalyptol has the highest illuminance among all tested fuels, while the flame illuminance of toluene is similar to that of anisole and D-limonene. The trend found in flame illuminance is distinct from the radiant heat flux, implying that blending eucalyptol into hydrogen-based flames may be most effective for improving flame visibility, whilst blending toluene may be the most beneficial for the hydrogen-based flame to be used in applications with high radiative heat transfer demand.

3.2. Blending H_2/N_2 with biofuels (≤ 1 mol%)

3.2.1. Flame appearance

Photographs of the turbulent nonpremixed biofuel-blended H_2/N_2 flames are presented in Fig. 5. For all cases, a long exposure time (20 s) is chosen to capture the mean characteristics of the flame. It should be noted that, although the still photographs cannot provide quantitative information about soot, they can show luminosity resulting from a soot volume fraction below the lower detection limit of laser induced incandescence (LII) [60].

The photographs show that adding biofuels at 0.2 and 1 mol% (based on the mole fraction of H_2) has moderate effects on the flame length, flame width and global flame luminosity compared with the flame without additives (HB0). All blended flames are dominated by red colouration near the flame tip, which is attributed to the presence of H_2O^* [61]. The appearance of blue colouration in the blended flames results from the presence of CH^*, C_2^*, CO_2^* and HCO^* [62], which dominate the region near the exit plane. The increase in carbon flux with the addition of biofuel promotes the formation of the aforementioned carbonaceous species and hence enhances the blue colouration. However, the increase in biofuel concentration from 0.2 to 1 mol% does not introduce a remarkable enhancement in luminosity, which may indicate that the luminosity enhancement is not linearly related to the biofuel concentration. This trend is further explored in the signal intensity analysis from the photographs.

The global signal intensity of the flames is extracted from the photographs to provide quantitative analysis for flame luminosity and is presented in Fig. 6(a). It is concluded that blending various types of biofuel at 0.2 mol% has a similar effect in luminosity enhancement. When the biofuel concentration increases to 1 mol%, vapourised toluene and anisole increase the H_2/N_2 flame luminosity by 253% and 133%, respectively. Adding 1 mol% vapourised D-limonene and eucalyptol increases the H_2/N_2 flame luminosity by 69% and 61%, respectively. The results indicate that blending biofuels with aromatic structures (toluene and anisole), is more effective in luminosity enhancement than cyclic monoterpene (D-limonene and eucalyptol). It is also concluded that non-oxygenated biofuel (toluene and D-limonene) is more effective than oxygenated biofuel (anisole and eucalyptol) in luminosity enhancement of an H_2/N_2 flame. This difference is due to the oxygen content in anisole and eucalyptol. In other words, the oxygen content creates favourable combustion conditions, which would hamper the PAH formation.

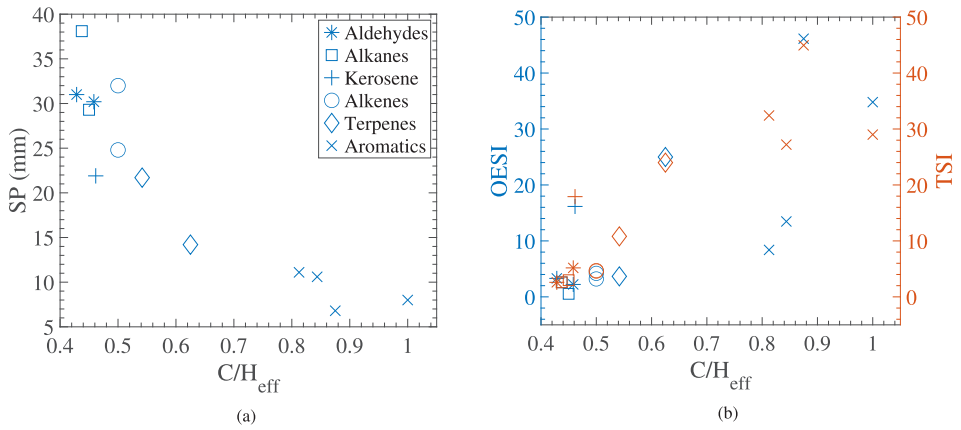

Fig. 3. (a) The SP of different types of hydrocarbons as a function of effective C/H ratio. (b) The TSI and OESI of different types of hydrocarbons as a function of effective C/H ratio.

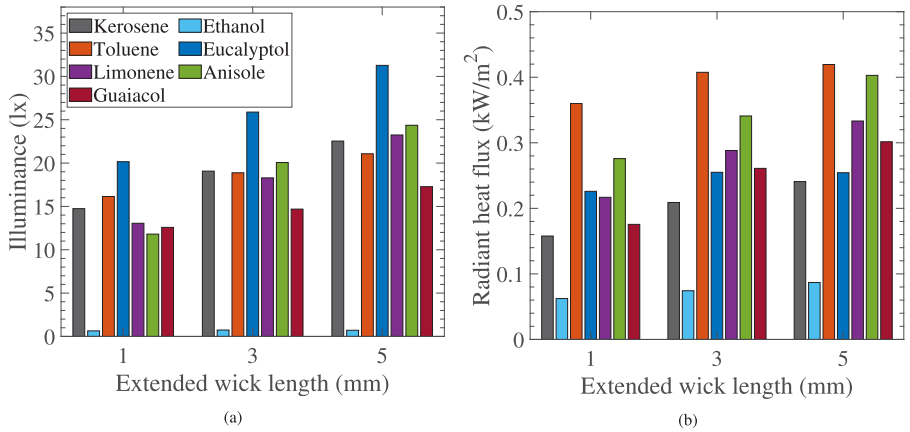

Fig. 4. Illuminance and radiant heat flux of laminar nonpremixed flames on a wick-fed burner at extended wick length 1, 3 and 5 mm. (a) Flame illuminance. (b) Flame radiant heat flux. (For interpretation of the references to colour in this figure legend, the reader is referred to the web version of this article.)

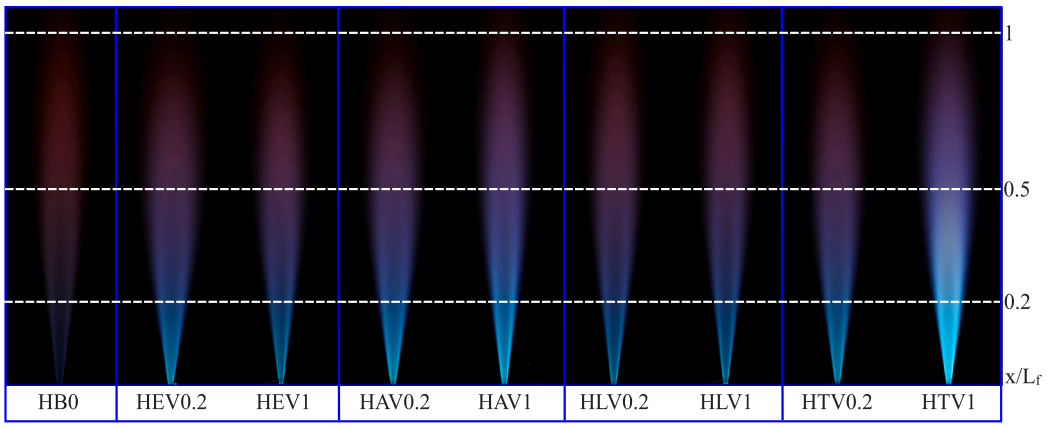

Fig. 5. Photographs of vapourised biofuel-blended H_2/N_2 flames — refer Table 1. Photographs with 20 s exposures were taken at f/22, ISO 100. (For interpretation of the references to colour in this figure legend, the reader is referred to the web version of this article.)

The peak intensity near the exit plane in vapourised toluene/anisole flames is ascribed to the presence of CH^*, C_2^*, CO_2^* and HCO^*. The prevapourised biofuels dissociate and react with OH and O radicals, hence, the aforementioned species that dominate the luminosity in the momentum driven part of the flame are enhanced.

3.2.2. Radiant heat flux

Figs. 7 and 8 present the axial distribution of the radiant fraction from the biofuel-blended H_2/N_2 flames. The results show that adding 0.2 mol% and 1 mol% biofuels has a limited effect on the radiant intensity enhancement of H_2/N_2 flames. Thermal radiation in flames can result from both soot and gaseous/vapourised species, such as H_2O and CO_2. Radiative emissions from soot are generally much stronger than gaseous species [59]. It is observed from the photographs (Fig. 5) that none of the 0.2 mol% and 1 mol% biofuel-blended flames are dominated by soot, hence the radiative emissions from these flames are mainly from gaseous species. The soot oxidation rate overwhelms

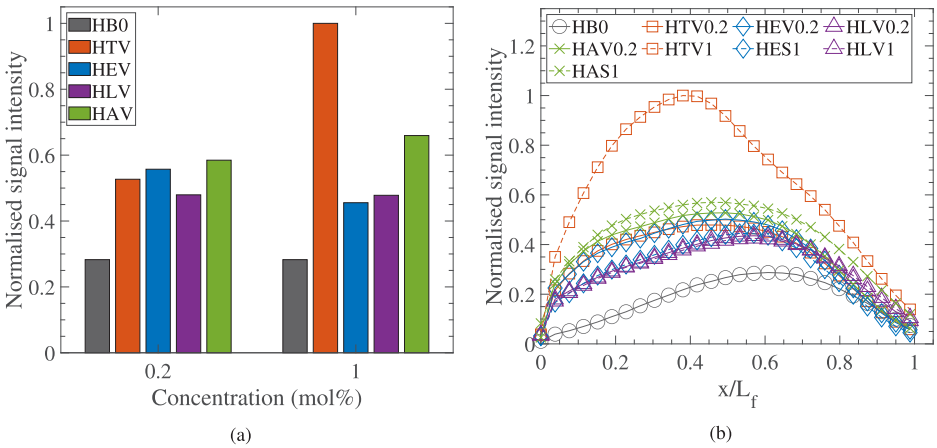

Fig. 6. Normalised signal intensity from photographs of vapourised biofuel-blended H_2/N_2 flames described in Table 1. The signal intensity is normalised to the peak signal intensity of a 1 mol% toluene vapourised flame. (a) Global signal intensity. (b) Normalised signal intensity of vapourised biofuel-blended flames as a function of flame height.

the formation rate and results in low soot loading in these turbulent biofuel-blended H_2/N_2 flames. This is ascribed to the following factors:

1. The concentration of carbon atoms (n_c) in 0.2 mol% and 1 mol% biofuel blended cases are about 0.02 and 0.07, respectively, which are still much lower than those hydrocarbon flames.
2. Abundant OH radicals available in hydrogen-based flames promote soot oxidation.
3. All flame cases possess a high exit strain rate ($U/d > 20{,}000\ s^{-1}$) and low residence time. A high strain rate and low residence time are known to have significant inhibition effects on the formation of soot and its precursors, since soot inception, nucleation, surface growth and agglomeration as the soot formation steps require sufficient time to develop [63,64].
4. The high flame temperature of a hydrogen-based flame promotes soot oxidation [65,66].

The numerical results in Fig. 9(a) show that the rate of production (ROP) of naphthalene is low at 0.2–1 mol% in toluene and anisole blended flames. This suggests that blending low concentration biofuels is unlikely to promote A_2 formation in turbulent hydrogen-based flames. In addition, the abundant availability of OH and H radicals in the flame facilitates the oxidation of toluene and anisole to CO_2 via CH_2O. The CH_2O ROP is an order of magnitude greater than the A_2 ROP, which further inhibits the PAH formation in these flames. The computational analysis also reveals that the reaction pathways of naphthalene formation in the vapourised toluene and anisole blended H_2/N_2 flames are dominated by the HACA mechanism, including $H + C_{10}H_{10} \rightleftharpoons H_2 + C_{10}H_8$ and $H + C_{10}H_8 \rightleftharpoons H_2 + C_{10}H_7$.

The radiant fraction from x/L_f = 0–0.4 in Fig. 7 shows that toluene appears to be the most effective biofuel additive in the radiant heat flux enhancement of an H_2/N_2 flame. The largest radiant heat flux enhancement is found in 1 mol% vapourised toluene-blended flames, increasing the radiant fraction of the non-blended flame by 19%. Although the effect of blending different biofuels on radiant heat flux enhancement varies at different biofuel concentrations, overall, the effectiveness of biofuels in increasing radiant heat flux follows the decreasing order of: toluene > anisole > D-limonene > eucalyptol. It is also highlighted in Fig. 7 that biofuels with an aromatic structure – toluene and anisole – are more effective in enhancing radiant heat flux than biofuels with a cyclic monoterpene structure, viz. eucalyptol and D-limonene. For example, blending 0.2 mol% vapourised toluene and anisole increases the radiant heat flux of the H_2/N_2 flame by 12% and 10%, respectively, compared with 9% and 2% for D-limonene and eucalyptol. This indicates that although eucalyptol and D-limonene consist of a cyclic six-carbon structure, the existing aromatic ring in toluene and anisole, containing a higher degree of unsaturation, favours

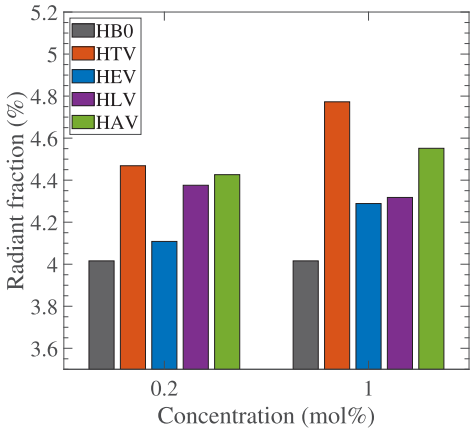

Fig. 7. Radiant fraction from x/L_f = 0–0.4.

PAH formation. One possible factor that may contribute to the higher radiant heat flux enhancement of D-limonene than eucalyptol is the weak C–H bond in the allylic group in D-limonene. The C–H bond dissociation energy in the allylic group is only 371 kJ/mol, which is lower than 438 kJ/mol for the primary C–H bond [67]. Therefore, hydrogen abstraction is more likely to take place at the allylic carbon atom level in D-limonene, which subsequently promotes the growth of PAH via the HACA mechanism.

The experimental results from Figs. 7 and 8 also reveal that blending H_2/N_2 flames with non-oxygenated biofuels (toluene and D-limonene) is more effective in radiant heat flux enhancement than oxygenated biofuels (anisole and eucalyptol). This observation agrees with the previous studies that oxygenated fuels reduce soot loading by promoting PAH and soot oxidation [25,31,68]. The fuel-bound oxygen has a higher heat release rate and restricts the local fuel-rich zones where PAH is formed. The numerical results from Fig. 9(b) show that even at low concentrations (0.2–1 mol%), the CH_2O ROP in anisole blends is more than doubled compared with the CH_2O ROP in toluene blends, implying that PAH oxidation via CH_2O is greatly enhanced in anisole blends. Another interesting point noted in Fig. 9(a) is that A_2 ROP is much higher in anisole blends than toluene blends. This is because the reaction between the methyl radicals and anisole are mainly via H-abstraction on the methoxy group, which is much faster than the attack on the aromatic ring. A particularly weak bond, approximately 264 kJ/mol, is present in anisole between the oxygen and methyl group which leads to the rapid formation of the phenoxy radical and promotes PAH growth [69]. However, the effect of oxygen content on

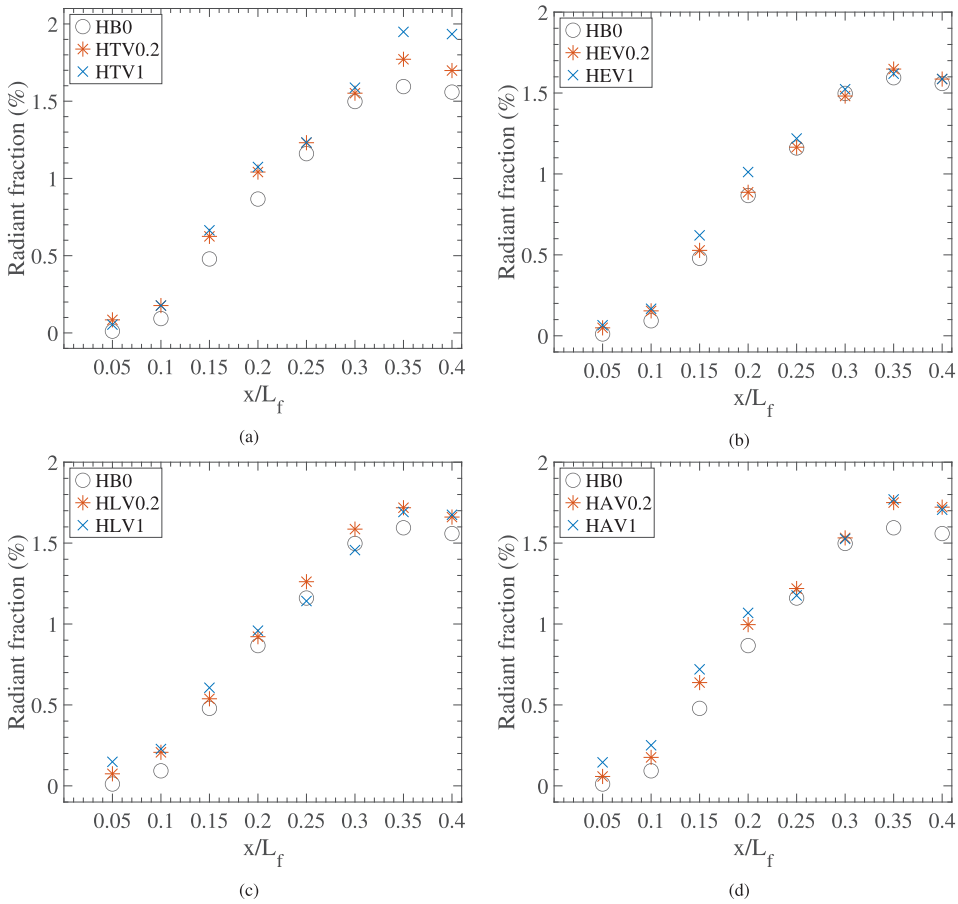

Fig. 8. Radiant fraction as a function of height of vapourised biofuel-blended H_2/N_2 flames described in Table 1: (a) Toluene blends, (b) Eucalyptol blends, (c) D-limonene blends, and (d) Anisole blends.

soot oxidation enhancement overwhelms the effect of the methoxy group on promoting soot formation — the CH_2O ROP is an order of magnitude greater than A_2 ROP. Consequently, toluene blends appear to have higher PAH loading from the numerical results and hence higher radiant heat flux from the experimental results.

Fig. 8 shows that the radiant fraction increases with flame height from x/L_f = 0–0.35 and peaks at x/L_f = 0.35 for most biofuel-blended flames. This observation agrees with the luminosity results from Fig. 6 that in most 0.2 and 1 mol% biofuel-blended flames where soot is absent, the luminosity and radiant fraction tend to peak near the jet exit. This finding further demonstrates the correlation between soot, luminosity and radiant fraction in low concentration biofuel-blended flames.

While the radiant fraction increases non-linearly with toluene and anisole concentrations from 0.2 to 1 mol%, it is interesting to note that the radiant fraction does not always increase with the biofuel concentration. For example, adding 0.2 mol% vapourised D-limonene increases the radiant fraction of the H_2/N_2 flame by 9%, but further increasing the concentration to 1 mol% only increases the radiant fraction by 7% from the H_2/N_2 flame. According to the contributing factors discussed above, soot formation is significantly inhibited in these biofuel-blended flames due to the low number of carbon atoms, the abundance of OH radicals and the high exit strain rate of the jet. It is most likely that flame temperature becomes the most sensitive contributing factor under these conditions, since radiation has a quartic relationship with temperature ($Q_r \propto T^4$). The variation of the centreline flame temperature, together with its impact on radiant heat flux, will be further discussed in Section 3.2.3.

3.2.3. Flame temperature

Fig. 10 presents the centreline flame temperature as a function of height for the vapourised biofuel-blended H_2/N_2 flames. The maximum centreline flame temperature among all flame cases is 2137 K, recorded at x/L_f = 0.35 in the non-blended H_2/N_2 flame. The results show that blending prevapourised biofuels to the H_2/N_2 flame generally increases the centreline flame temperature near the jet exit plane. The largest increase in centreline flame temperature is up to 183 K in 0.2 mol% vapourised toluene blends at x/L_f = 0.05. As the height approaches from x/L_f = 0.05–0.2, the increasing trend of centreline flame temperature tends to be smaller for all vapourised biofuel blends. From x/L_f = 0.2–0.4, adding prevapourised biofuels slightly decreases the centreline flame temperature of the H_2/N_2 flames. The largest reduction is found to be 60 K in 1 mol% vapourised D-limonene blends at x/L_f = 0.3. Apart from these two peak points, the rest of the centreline flame temperature measurements with the biofuels at various flame heights are typically within 85 K of each other.

Temperature reduction may be one of the reasons that radiant heat flux does not always increase with biofuel concentration — 1 mol% D-limonene blends has a lower radiant fraction than 0.2 mol% D-limonene blends (mentioned in Section 3.2.2). It is noted in Fig. 10(c) that 1 mol% vapourised D-limonene blends show 20–90 K temperature drops from x/L_f = 0.05–0.4 compared with 0.2 mol% case, which can be correlated with the reduced radiant heat flux in Fig. 8(c).

4. Conclusions

The SP, TSI and OESI are obtained and compared with the data sets in the literature to quantify the sooting propensities of aromatic bio-oil

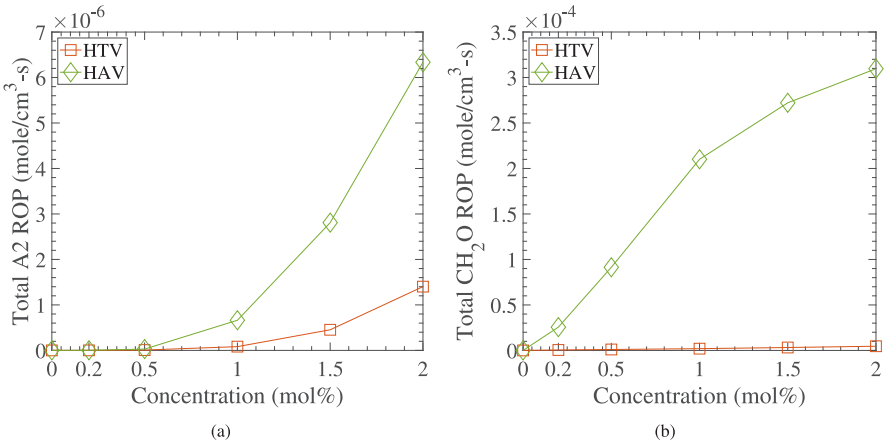

Fig. 9. Numerical results of naphthalene and CH_2O ROP from toluene and anisole blended H_2/N_2 flames. (a) Naphthalene (A_2) ROP, and (b) Formaldehyde (CH_2O) ROP.

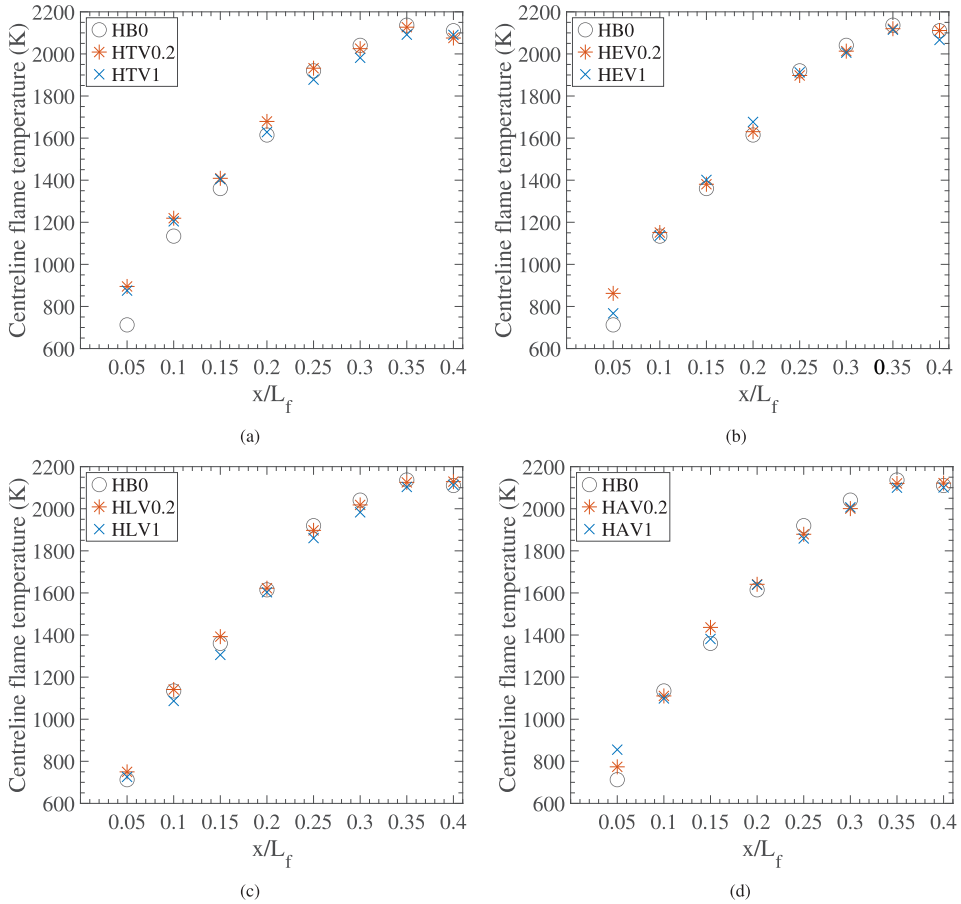

Fig. 10. Centreline flame temperature (corrected for radiative heat loss from the thermocouple) as a function of height for vapourised biofuel-blended H_2/N_2 flames described in Table 1: (a) Toluene blends. (b) Eucalyptol blends. (c) D-limonene blends. (d) Anisole blends.

surrogates (toluene, anisole and guaiacol) and monoterpene essential oil surrogates (eucalyptol and D-limonene). The flame illuminance and radiant heat flux of laminar nonpremixed biofuel flames on a wick-fed burner are investigated in conjunction with sooting propensity tests to demonstrate the potential for adding these biofuels to hydrogen-based flames for flame luminosity and radiant heat flux enhancement. The effects of adding vapourised biofuels to turbulent nonpremixed H_2/N_2 flames on flame appearance, radiant heat flux and centreline flame temperature are recorded and analysed. Laminar flame calculations are also employed to better understand the effect of blending on flame structure and soot propensity. The key findings from this study are as follows:

1. The sooting propensities of biofuels tested in this study follow the decreasing order: aromatics > monoterpenes > alkenes > alkanes > aldehydes.
2. The effect of the fuel type — chemical structure and functional group tends to be more significant than the oxygen content and effective C/H ratio on sooting propensities.

3. Adding 0.2 and 1 mol% vapourised biofuels to turbulent non-premixed H_2/N_2 flames improves the flame luminosity by 61%–253%, while the blended flames are still dominated by enhanced blue colouration due to the increase of gaseous species — CH^*, C_2^*, CO_2^* and HCO^*.
4. Adding 0.2 and 1 mol% vapourised biofuels to turbulent non-premixed H_2/N_2 flames increases the radiant fraction by 2%–19%. Limited soot formation is observed in these flames. Soot and naphthalene formation have a non-linear positive relationship with the biofuel concentration, which indicates that a threshold of ≈2 mol% might exist.
5. Biofuels with an aromatic structure (toluene and anisole) appear to form more PAH and hence are more effective than cyclic monoterpenes (D-limonene and eucalyptol) at increasing luminosity and radiation of the blended H_2/N_2 flame. Aromatic biofuels increase the radiant fraction of H_2/N_2 flames by 10%–19%, whereas monoterpenes increase the radiant fraction by 2%–9%.
6. The oxygenated fuels (anisole and eucalyptol) are less effective for radiant heat flux enhancement than non-oxygenated fuels (toluene and D-limonene). The radiant fraction of H_2/N_2 flames increases by 9%–19% and 2%–10% from blending non-oxygenated and oxygenated biofuels, respectively This is due to the presence of oxygen in oxygenated fuels, which contributes to the oxidation of PAH. The effect of promoting the PAH oxidation rate from the oxygenated fuel appears to be less significant than the effect of chemical structure on radiant heat flux enhancement.
7. The centreline flame temperature of H_2/N_2 flames increases with the 0.2 and 1 mol% biofuel addition near the jet exit plane, but it shows a decrease up to 60 K from x/L_f = 0.2–0.4.

CRediT authorship contribution statement

Yilong Yin: Conceptualization, Methodology, Software, Writing – original draft, Writing – review & editing, Formal analysis, Investigation, Data curation, Project administration. **Paul R. Medwell:** Conceptualization, Methodology, Formal analysis, Writing – review & editing, Supervision, Project administration, Funding acquisition, Resources. **Adam J. Gee:** Data curation, Writing – review & editing, Investigation. **Kae Ken Foo:** Methodology, Data curation, Supervision, Investigation. **Bassam B. Dally:** Conceptualization, Methodology, Formal analysis, Writing – review & editing, Supervision, Project administration, Funding acquisition, Resources.

Declaration of competing interest

The authors declare that they have no known competing financial interests or personal relationships that could have appeared to influence the work reported in this paper.

Data availability

Data will be made available on request.

Acknowledgements

The funding support of the Australian Research Council and the Future Fuels Cooperative Research Centre is gratefully acknowledged. Thanks go to Jason Peak and Douglas Proud for their assistance with the experimental aspects of this work.

References

[1] Dodds PE, Staffell I, Hawkes AD, Li F, Grünewald P, McDowall W, Ekins P. Hydrogen and fuel cell technologies for heating: A review. Int J Hydrogen Energy 2015;40(5):2065–83.
[2] Kitagawa T, Nakahara T, Maruyama K, Kado K, Hayakawa A, Kobayashi S. Turbulent burning velocity of hydrogen–air premixed propagating flames at elevated pressures. Int J Hydrogen Energy 2008;33(20):5842–9.
[3] Nag S, Sharma P, Gupta A, Dhar A. Experimental study of engine performance and emissions for hydrogen diesel dual fuel engine with exhaust gas recirculation. Int J Hydrogen Energy 2019;44(23):12163–75.
[4] Nowotny J, Veziroglu TN. Impact of hydrogen on the environment. Int J Hydrogen Energy 2011;36(20):13218–24.
[5] Kakoulaki G, Kougias I, Taylor N, Dolci F, Moya J, Jäger-Waldau A. Green hydrogen in Europe-A regional assessment: Substituting existing production with electrolysis powered by renewables. Energy Convers Manage 2021;228:113649.
[6] Widén J, Carpman N, Castellucci V, Lingfors D, Olauson J, Remouit F, Bergkvist M, Grabbe M, Waters R. Variability assessment and forecasting of renewables: A review for solar, wind, wave and tidal resources. Renew Sustain Energy Rev 2015;44:356–75.
[7] Neto PBL, Saavedra OR, Oliveira DQ. The effect of complementarity between solar, wind and tidal energy in isolated hybrid microgrids. Renew Energy 2020;147:339–55.
[8] Haeseldonckx D, D'haeseleer W. The use of the natural-gas pipeline infrastructure for hydrogen transport in a changing market structure. Int J Hydrogen Energy 2007;32(10–11):1381–6.
[9] Liu B, Liu X, Lu C, Godbole A, Michal G, Teng L. Decompression of hydrogen-natural gas mixtures in high-pressure pipelines: CFD modelling using different equations of state. Int J Hydrogen Energy 2019;44(14):7428–37.
[10] Evans MJ, Proud DB, Medwell PR, Pitsch H, Dally BB. Highly radiating hydrogen flames: Effect of toluene concentration and phase. Proc Combust Inst 2021;38(1):1099–106.
[11] Agarwal AK. Biofuels (alcohols and biodiesel) applications as fuels for internal combustion engines. Prog Energy Combust Sci 2007;33(3):233–71.
[12] Bäckström D, Johansson R, Andersson K, Wiinikka H, Fredriksson C. On the use of alternative fuels in rotary kiln burners—An experimental and modelling study of the effect on the radiative heat transfer conditions. Fuel Process Technol 2015;138:210–20.
[13] Schefer RW, Kulatilaka WD, Patterson BD, Settersten TB. Visible emission of hydrogen flames. Combust Flame 2009;156(6):1234–41.
[14] Hutny W, Lee G. Improved radiative heat transfer from hydrogen flames. Int J Hydrogen Energy 1991;16(1):47–53.
[15] Gee AJ, Yin Y, Foo KK, Chinnici A, Smith N, Medwell PR. Toluene addition to turbulent H_2/natural gas flames in bluff-body burners. Int J Hydrogen Energy 2022.
[16] Gholizadeh M, Hu X, Liu Q. A mini review of the specialties of the bio-oils produced from pyrolysis of 20 different biomasses. Renew Sustain Energy Rev 2019;114:109313.
[17] Czernik S, Bridgwater A. Overview of applications of biomass fast pyrolysis oil. Energy & Fuels 2004;18(2):590–8.
[18] Bridgwater A, Carson P, Coulson M. A comparison of fast and slow pyrolysis liquids from mallee. Int J Glob Energy Issues 2007;27(2):204–16.
[19] Zhang C, Chen L, Ding S, Xu H, Li G, Consalvi J-L, Liu F. Effects of soot inception and condensation PAH species and fuel preheating on soot formation modeling in laminar coflow CH_4/air diffusion flames doped with n-heptane/toluene mixtures. Fuel 2019;253:1371–7.
[20] Solikhah M, Pratiwi F, Heryana Y, Wimada A, Karuana F, Raksodewanto A, Kismanto A. Characterization of bio-oil from fast pyrolysis of palm frond and empty fruit bunch. In: IOP conference series: Materials science and engineering, Vol. 349. IOP Publishing; 2018, 012035.
[21] El-Mougy NS. Effect of some essential oils for limiting early blight (Alternaria solani) development in potato field. J Plant Prot Res 2009;49(1).
[22] Cho S-M, Kim J-H, Kim S-H, Park S-Y, Kim J-C, Choi I-G. A comparative study on the fuel properties of biodiesel from woody essential oil depending on terpene composition. Fuel 2018;218:375–84.
[23] Celnik MS, Sander M, Raj A, West RH, Kraft M. Modelling soot formation in a premixed flame using an aromatic-site soot model and an improved oxidation rate. Proc Combust Inst 2009;32(1):639–46.
[24] Li L, Sunderland PB. An improved method of smoke point normalization. Combust Sci Technol 2012;184(6):829–41.
[25] Wang Z, Li L, Wang J, Reitz RD. Effect of biodiesel saturation on soot formation in diesel engines. Fuel 2016;175:240–8.
[26] Salamanca M, Mondragón F, Agudelo JR, Benjumea P, Santamaría A. Variations in the chemical composition and morphology of soot induced by the unsaturation degree of biodiesel and a biodiesel blend. Combust Flame 2012;159(3):1100–8.
[27] McEnally CS, Pfefferle LD. Sooting tendencies of oxygenated hydrocarbons in laboratory-scale flames. Environ Sci Technol 2011;45(6):2498–503.
[28] Rahman SA, Van TC, Hossain F, Jafari M, Dowell A, Islam M, Nabi MN, Marchese A, Tryner J, Rainey T, et al. Fuel properties and emission characteristics of essential oil blends in a compression ignition engine. Fuel 2019;238:440–53.

[29] Barrientos EJ, Lapuerta M, Boehman AL. Group additivity in soot formation for the example of C-5 oxygenated hydrocarbon fuels. Combust Flame 2013;160(8):1484–98.
[30] Ruiz-Rodriguez I, Cracknell R, Parkes M, Megaritis T, Ganippa L. Experimental study of the effect of C8 oxygenates on sooting processes in high pressure spray flames. Combust Flame 2020;220:235–46.
[31] Verma P, Jafari M, Rahman SA, Pickering E, Stevanovic S, Dowell A, Brown R, Ristovski Z. The impact of chemical composition of oxygenated fuels on morphology and nanostructure of soot particles. Fuel 2020;259:116167.
[32] Donoso D, Bolonio D, Ballesteros R, Lapuerta M, Canoira L. Hydrogenated orange oil: A waste derived drop-in biojet fuel. Renew Energy 2022;188:1049–58.
[33] Corral-Gomez L, Rodriguez-Rosa D, Juarez-Perez S, Martín-Parra A, Gomez GR, Moya-Fernandez F. A novel device for automated determination of the smoke point with non-invasive adaptation of ASTM D1322 normalized lamps. Meas Sci Technol 2020;31(11):115004.
[34] Graziano B, Ottenwälder T, Manderfeld D, Pischinger S, Grünefeld G. Advanced methodology for the detection of smoke point heights in hydrocarbon flames. Energy & Fuels 2018;32(3):3908–19.
[35] Tran MK, Dunn-Rankin D, Pham TK. Characterising sooting propensity in biofuel–diesel flames. Combust Flame 2012;159(6):2181–91.
[36] Calcote H, Manos D. Effect of molecular structure on incipient soot formation. Combust Flame 1983;49(1–3):289–304.
[37] Jiao Q, Anderson JE, Wallington TJ, Kurtz EM. Smoke point measurements of diesel-range hydrocarbon–oxygenate blends using a novel approach for fuel blend selection. Energy & Fuels 2015;29(11):7641–9.
[38] Narayanaswamy K, Pitsch H, Pepiot P. A component library framework for deriving kinetic mechanisms for multi-component fuel surrogates: Application for jet fuel surrogates. Combust Flame 2016;165:288–309.
[39] Szymkowicz PG, Benajes J. Development of a diesel surrogate fuel library. Fuel 2018;222:21–34.
[40] Nowakowska M, Herbinet O, Dufour A, Glaude P-A. Detailed kinetic study of anisole pyrolysis and oxidation to understand tar formation during biomass combustion and gasification. Combust Flame 2014;161(6):1474–88.
[41] Nowakowska M, Herbinet O, Dufour A, Glaude P-A. Kinetic study of the pyrolysis and oxidation of guaiacol. J Phys Chem A 2018;122(39):7894–909.
[42] Mensch A, Santoro RJ, Litzinger TA, Lee S-Y. Sooting characteristics of surrogates for jet fuels. Combust Flame 2010;157(6):1097–105.
[43] Barrientos EJ, Boehman AL. Examination of the sooting tendency of three-ring aromatic hydrocarbons and their saturated counterparts. Energy & Fuels 2010;24(6):3479–87.
[44] Olson D, Pickens J, Gill R. The effects of molecular structure on soot formation II. Diffusion flames. Combust Flame 1985;62(1):43–60.
[45] Qamar N, Nathan G, Alwahabi Z, King K. The effect of global mixing on soot volume fraction: measurements in simple jet, precessing jet, and bluff body flames. Proc Combust Inst 2005;30(1):1493–500.
[46] Kent J, Bastin S. Parametric effects on sooting in turbulent acetylene diffusion flames. Combust Flame 1984;56(1):29–42.
[47] Robinson J, Smith V. Emission spectra of organic liquids in oxy-hydrogen flames. Anal Chim Acta 1966;36:489–98.
[48] Arens EE, Youngquist RC, Starr SO. Intensity calibrated hydrogen flame spectrum. Int J Hydrogen Energy 2014;39(17):9545–51.
[49] Buch R, Hamins A, Konishi K, Mattingly D, Kashiwagi T. Radiative emission fraction of pool fires burning silicone fluids. Combust Flame 1997;108(1–2):118–26.
[50] Glaude PA, Pitz WJ, Thomson MJ. Chemical kinetic modeling of dimethyl carbonate in an opposed-flow diffusion flame. Proc Combust Inst 2005;30(1):1111–8.
[51] Dayma G, Sarathy S, Togbé C, Yeung C, Thomson M, Dagaut P. Experimental and kinetic modeling of methyl octanoate oxidation in an opposed-flow diffusion flame and a jet-stirred reactor. Proc Combust Inst 2011;33(1):1037–43.
[52] Faravelli T, Frassoldati A, Ranzi E. Kinetic modeling of the interactions between NO and hydrocarbons in the oxidation of hydrocarbons at low temperatures. Combust Flame 2003;132(1–2):188–207.
[53] Bisetti F, Blanquart G, Mueller ME, Pitsch H. On the formation and early evolution of soot in turbulent nonpremixed flames. Combust Flame 2012;159(1):317–35.
[54] Violi A, D'Anna A, D'Alessio A. Modeling of particulate formation in combustion and pyrolysis. Chem Eng Sci 1999;54(15–16):3433–42.
[55] Skeen SA, Manin J, Pickett LM. Simultaneous formaldehyde PLIF and high-speed schlieren imaging for ignition visualization in high-pressure spray flames. Proc Combust Inst 2015;35(3):3167–74.
[56] Idicheria CA, Pickett LM. Formaldehyde visualization near lift-off location in a diesel jet. SAE Trans 2006;683–95.
[57] Mueller CJ, Boehman AL, Martin GC. An experimental investigation of the origin of increased NOx emissions when fueling a heavy-duty compression-ignition engine with soy biodiesel. SAE Int J Fuels Lubr 2009;2(1):789–816.
[58] Buchholz BA, Cheng A, Dibble R. The effect of oxygenates on diesel engine particulate matter. SP-1716, SAE; 2002, p. 01–1705.
[59] Andersson K, Johansson R, Johnsson F. Thermal radiation in oxy-fuel flames. Int J Greenh Gas Control 2011;5:S58–65.
[60] Evans MJ, Medwell PR, Sun Z, Chinnici A, Ye J, Chan QN, Dally BB. Downstream evolution of n-heptane/toluene flames in hot and vitiated coflows. Combust Flame 2019;202:78–89.
[61] Rutkowski L, Khodabakhsh A, Johansson AC, Valiev DM, Lodi L, Qu Z, Ghorbani R, Polyansky OL, Jin Y, Tennyson J, et al. Measurement of H_2O and OH in a flame by optical frequency comb spectroscopy. In: CLEO: Science and innovations. Optical Society of America; 2016, p. SW4H–8.
[62] Liu X, Wang H, Yao M. Experimental and modeling investigations on soot formation of ethanol, n-butanol, 2, 5-dimethylfuran, and biodiesel in diesel engines. Energy & Fuels 2017;31(11):12108–19.
[63] Dong X, Nathan GJ, Mahmoud S, Ashman PJ, Gu D, Dally BB. Global characteristics of nonpremixed jet flames of hydrogen–hydrocarbon blended fuels. Combust Flame 2015;162(4):1326–35.
[64] Mueller ME, Chan QN, Qamar NH, Dally BB, Pitsch H, Alwahabi ZT, Nathan GJ. Experimental and computational study of soot evolution in a turbulent nonpremixed bluff body ethylene flame. Combust Flame 2013;160(7):1298–309.
[65] Ren F, Chu H, Xiang L, Han W, Gu M. Effect of hydrogen addition on the laminar premixed combustion characteristics the main components of natural gas. J Energy Inst 2019;92(4):1178–90.
[66] Gu D, Sun Z, Dally BB, Medwell PR, Alwahabi ZT, Nathan GJ. Simultaneous measurements of gas temperature, soot volume fraction and primary particle diameter in a sooting lifted turbulent ethylene/air nonpremixed flame. Combust Flame 2017;179:33–50.
[67] Bierkandt T, Hoener M, Gaiser N, Hansen N, Köhler M, Kasper T. Experimental flat flame study of monoterpenes: Insights into the combustion kinetics of α-pinene, β-pinene, and myrcene. Proc Combust Inst 2021;38(2):2431–40.
[68] Westbrook CK, Pitz WJ, Curran HJ. Chemical kinetic modeling study of the effects of oxygenated hydrocarbons on soot emissions from diesel engines. J Phys Chem A 2006;110(21):6912–22.
[69] Wagnon SW, Thion S, Nilsson EJ, Mehl M, Serinyel Z, Zhang K, Dagaut P, Konnov AA, Dayma G, Pitz WJ. Experimental and modeling studies of a biofuel surrogate compound: laminar burning velocities and jet-stirred reactor measurements of anisole. Combust Flame 2018;189:325–36.

Chapter 5

Hydrogen turbulent nonpremixed flames blended with spray or prevapourised biofuels

Statement of Authorship

Title of Paper	Hydrogen turbulent nonpremixed flames blended with spray or prevapourised biofuels
Publication Status	☑ Published ☐ Accepted for Publication ☐ Submitted for Publication ☐ Unpublished and Unsubmitted w ork w ritten in manuscript style
Publication Details	Y. Yin, P.R. Medwell, B.B. Dally Hydrogen turbulent nonpremixed flames blended with spray or prevapourised biofuels International Journal of Hydrogen Energy 48.65 (2023), pp. 25563–25580.

Principal Author

Name of Principal Author (Candidate)	Yilong Yin
Contribution to the Paper	1. Developed the research concept of blending hydrogen with prevapourised and sprayed biofuels for radiation enhancement. Determined the combustion characteristics of interest and their corresponding diagnostics, namely still photograph for flame appearance and luminosity measurement, heat flux sensor for radiant heat flux, thermocouple for flame temperature measurement, and flue gas analyser for pollutant emission measurement. Developed systematic comparison of the flame characteristics between prevapourised and ultrasonically sprayed biofuel/hydrogen flames. 2. Designed, organised, and conducted experimental campaigns. Selected biofuels and their surrogates for testing. Designed and built an integrated spray/prevapourised burner to blend hydrogen with biofuels via prevapourisation or ultrasonic spray. Designed and determined the details of flame cases and test conditions to allow the comparison between different introduction methods. Developed required safety measures and documentation for the experiments. Prepared, tested and calibrated the equipment used in the experiments. Designed and assembled the appropriate plumbing systems. 3. Initiated, designed and performed numerical modelling in Chemkin Pro for the analysis of NO_x formation pathways to verify, interpret, and understand the observations from the experiments. Searched and revised chemical mechanisms that include NO_x formation reactions for the tested biofuel surrogates. 4. Collected, processed, and analysed data from the experiments and numerical simulation. Evaluated the uncertainties and reliability of the data. Generated and determined critical experimental and numerical results for a paper. Understood and explained the NOx emission trend as a result of biofuel addition with the support from numerical results. Deepened the understanding of dominant NOx formation pathways in biofuel-blended hydrogen flames. Compared the effect of introduction methods (i.e. prevapourisation and ultrasonic spray) on the flame characteristics of biofuel/hydrogen flames. Generated novel findings of the study. 5. Developed and edited the manuscript. Selected the target journal of the manuscript. Submitted the manuscript and responded to reviewers' comments and recommendations as corresponding author.
Overall percentage (%)	80%
Certification:	This paper reports on original research I conducted during the period of my Higher Degree by Research candidature and is not subject to any obligations or contractual agreements with a third party that would constrain its inclusion in this thesis. I am the primary author of this paper.
Signature	2023.10.31 10:37:06 +10'30'
Date	31/10/2023

Co-Author Contributions

By signing the Statement of Authorship, each author certifies that:

i. the candidate's stated contribution to the publication is accurate (as detailed above);

ii. permission is granted for the candidate in include the publication in the thesis; and

iii. the sum of all co-author contributions is equal to 100% less the candidate's stated contribution.

Name of Co-Author	Paul R. Medwell		
Contribution to the Paper	1. Supervised the development of the research. Helped to evaluate the potential outcome and significance of the research. 2. Provided assistance with the training of experimental skills. 3. Advised on the experimental and numerical modelling details of the study. Supervised and approved the safety operation of the experiment. Advised on the calibration and setup of the experiment. 4. Advised on data processing and analysis. Evaluated the results and findings of this research. 5. Edited the manuscript. Provided suggestions for the responses to reviewers' comments.		
Signature	Paul Medwell 2023.10.31 10:47:10 +10'30'	Date	31-OCT-2023

Name of Co-Author	Bassam B. Dally		
Contribution to the Paper	1. Supervised the development of the research. Guided the direction of the research. 2. Provided assistance with the training of experimental skills. 3. Advised on the experimental and numerical approach of the study. 4. Advised on data processing and analysis. Evaluated the results and findings of this research. 5. Edited the manuscript. Provided suggestions for the responses to reviewers' comments.		
Signature	Digitally signed by Bassam Dally Date: 2023.10.31 12:43:04 +03'00'	Date	

INTERNATIONAL JOURNAL OF HYDROGEN ENERGY 48 (2023) 25563–25580

Available online at www.sciencedirect.com

ScienceDirect

journal homepage: www.elsevier.com/locate/he

Hydrogen turbulent nonpremixed flames blended with spray or prevapourised biofuels

Yilong Yin [a,*], Paul R. Medwell [a], Bassam B. Dally [b]

[a] School of Mechanical Engineering, The University of Adelaide, Adelaide, South Australia 5005, Australia
[b] Clean Combustion Research Centre, King Abdullah University of Science and Technology, Thuwal 23955-6900, Kingdom of Saudi Arabia

HIGHLIGHTS

- Spray flame exhibits higher global luminosity and radiant fraction than vapour flame.
- NO_x emissions increase with biofuel addition via thermal and prompt NO formation.
- Cyclic monoterpene biofuels have higher NO_x emissions than aromatic biofuels.
- Reducing H_2 concentration leads to large increase in luminosity and radiant fraction.

GRAPHICAL ABSTRACT

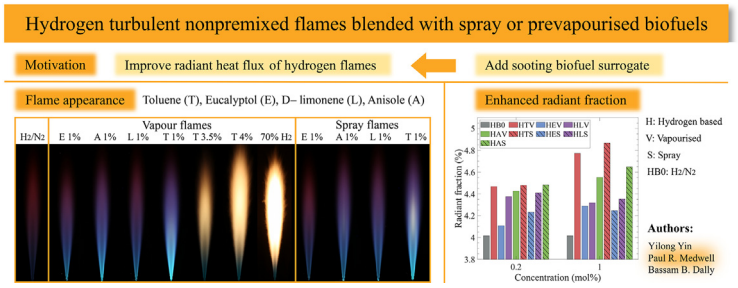

ARTICLE INFO

Article history:
Received 24 November 2022
Received in revised form
12 March 2023
Accepted 15 March 2023
Available online 6 April 2023

Keywords:
Hydrogen
Biofuel
Spray flame
Radiant heat flux
NO_x emissions

ABSTRACT

The low radiant intensity of hydrogen flames may be enhanced by adding biofuels with a high sooting propensity. This paper reports the effect of biofuel concentration and phase on the combustion characteristics of turbulent nonpremixed hydrogen-based flames. The 0.2 and 1 mol% vapourised/spray biofuel surrogates blended flames exhibit limited soot loading, except for 1 mol% spray toluene and anisole blends where soot starts to form. Spray additives benefit the formation of soot by creating localised fuel-rich conditions. Blending 3.5 and 4 mol% vapourised toluene attains a sooting flame and significantly enhances the luminosity and radiant fraction. The global NO_x emissions increase with prevapourised/spray biofuel surrogates due to the enhanced NO formation via thermal and prompt routes. Reducing the hydrogen concentration from 9:1 to 7:3 in H_2/N_2 (by mole) leads to large increases in luminosity and radiant fraction by 34 times and 135%, respectively, and a reduction in NO_x emissions by 68%.

* *Corresponding author*:
E-mail address: yilong.yin@adelaide.edu.au (Y. Yin).

https://doi.org/10.1016/j.ijhydene.2023.03.232

Nomenclature

χ_r	Radiant fraction
$\dot{m}$	Mass flow rate, kg/s
$\dot{Q}_F$	Total thermal power, kW
$\dot{Q}_r$	Radiated heat, kW
$\dot{q}''$	Radiant heat flux, kW/m^2
ρ	Density, kg/m^3
σ	Surface tension, N/m
c	Empirical constant dependent on the nebuliser type
d	Inner diameter of the jet, m
EI	Emission index
F	Ultrasound frequency of the nebuliser, Hz
L_f	Flame length, mm
MW	Molecular weight, g/mol
n_c	Carbon concentration of fuel
T	Temperature, K
U/d	Exit strain rate, s^{-1}
U	Mean velocity, m/s
CEM	Controlling evaporating mixing
CO	Carbon monoxide
CO_2	Carbon dioxide
CO_{2amb}	Mole fraction of CO_2 in ambient air
DAQ	Data acquisition systems
H_2	Hydrogen
H_2O	Water
HAB	Height above burner, mm
LHV	Lower heating value, MJ/kg
N_2	Nitrogen
NO	Nitric oxide
NO_2	Nitrogen dioxide
OPPDIF	Opposed-flow diffusion flame
PAHs	Polycyclic aromatic hydrocarbons
ROP	Rate of production
SMD	Sauter mean diameter

Introduction

As the world is shifting away from carbon-emitting processes, using hydrogen as a renewable energy carrier to replace conventional fuels, both in domestic and industrial sectors, is emerging as a promising approach [1–4]. Hydrogen has been widely studied as a diluent to reduce soot production in combustion systems such as gas turbines and internal combustion engines, by taking advantage of its carbon-free nature [5–10]. The effects of hydrogen addition on soot production can be attributed to three mechanisms: thermal effect, dilution effect, and chemical effect [11–13]. It has been reported that adding hydrogen to hydrocarbon flames increases the global flame temperature, and hence reduces soot by promoting soot oxidation via thermal effect [14,15]. The dilution effect of hydrogen addition reduces soot production by decreasing the carbon concentration per unit volume of the fuel mixture [11,16]. Previous studies have indicated that a portion of hydrogen can be blended into natural gas supply networks as a diluent to mitigate CO_2 emissions [17]. There is an increasing demand for achieving a more complete replacement of fossil fuels in a broader range of applications, as countries and companies are pledging to attain net zero emissions. Therefore, the work in this study is dedicated to identifying the challenges of using hydrogen as a primary energy source in practical applications and evaluating potential solutions.

A major challenge for replacing conventional fuels with hydrogen in high-temperature practical applications is the low thermal radiation from hydrogen flames due to the absence of soot. Thermal radiation is the transfer of heat energy through electromagnetic radiation and is a significant mode of heat transfer in many practical combustion systems (e.g., furnaces and boilers). The low radiant heat flux of hydrogen flames makes it difficult to effectively transfer heat from the flame to surrounding materials, reducing the efficiency of these systems [18–21]. One possible approach to compensate for this disadvantage of hydrogen flames in practical applications is to blend hydrogen with highly sooting additives to promote soot formation in the flame. Hence, the radiant intensity of the flame can be enhanced via efficient blackbody radiation from soot particulates [19,22,23].

Biofuels with high sooting propensities can be chosen as suitable additives since they are generally comprised of abundant aromatics, which favour the formation of soot precursors — polycyclic aromatic hydrocarbons (PAHs). In addition, the raw materials for their production can be harvested from the by-products and waste products from the existing industries, such as pulp industries and food production plants [24,25]. Bio-oils and essential oils are the two types of biofuels focused in this paper for their abundant aromatics, sooting propensity, and accessibility. Bio-oils are obtained from fast pyrolysis of lignin and cellulose multicomponent mixtures chemically comprised of substantial amounts of phenolic compounds, toluene, anisole and furan [26]. Lignin in their feedstock is the source for the synthesis of phenolic chemicals [27]. Essential oils are mainly comprised of terpenes $(C_5H_8)_n$, including monoterpenes (C10), sesquiterpenes (C15) and diterpenes (C20), which are biosynthesised via five-carbon isoprene units [28].

Efforts have been dedicated to evaluating the efficacy of adding sooting hydrocarbons to hydrogen-based flames on radiative heat transfer enhancement. Adding pulverised bituminous coal could improve the radiative properties of a hydrogen-coal flame because the heavy hydrocarbons (tar) produced from coal pyrolysis promote soot formation [22]. Highly radiating hydrogen-based flames were previously achieved by adding 1–5 mol% toluene [19]. Adding toluene as a soot-generating additive has significantly increased soot volume fraction in a hydrogen-nitrogen (1:1 vol) jet flame with a bulk mean Reynolds number of 5000. Gee et al. [23] further investigated the effect of toluene addition to pure hydrogen flames at 10,000 Reynolds number on a bluff-body burner. By comparing the thermal radiation of natural gas flame established on the same burner, approximately 4% vapourised toluene is required for H_2 flames to attain an equivalent radiant heat flux of a natural gas flame. These studies provided a preliminary assessment of the efficacy of this approach. However, the additives tested in these studies are

limited by heavy hydrocarbons and toluene. As discussed in the previous paragraph, biofuels, including bio-oils and essential oils, can be used as suitable additives to enhance the radiant heat flux of hydrogen flames. Yin et al. [29] investigated the sooting propensity of biofuel surrogates (eucalyptol, limonene, and anisole) on a wick-fed burner and demonstrated their potential to be used as soot-enhancing additives for hydrogen-based flames through combined experimental and numerical methods. The findings indicated that, although these biofuel surrogates have less sooting propensity than toluene, they enhance the radiant fraction of the H_2/N_2 flame by 2–19%. However, there is still a lack of quantitative measurements of the radiant heat flux enhancement. In addition, the influencing factors of the radiation enhancement, such as the chemical structure of additives, concentration, Reynolds number and exit strain rate are largely unavailable.

In addition to the issues around low radiation from the absence of soot, another challenge associated with hydrogen adaptation into practical applications is the increased NO_x emissions. The higher flame temperature of hydrogen promotes the formation of thermal NO_x by providing the required high activation energy of the NO route: $O + N_2 \rightleftharpoons NO + N$, which initiates the NO formation [30]. However, fuel and prompt NO_x are avoided when using hydrogen as the fuel [31,32]. Although hydrogen flames are often associated with higher NO_x emissions, the impact of biofuel blending (e.g., through the lower flame temperature due to increased heat radiation) is not well understood. None of the studies reported the efficacy of blending additives to hydrogen flames on radiant intensity enhancement along with the potential challenge of NO_x emissions.

To introduce additives to hydrogen flames in practical applications, liquid fuels could be sprayed directly into the flame or entrained by the gaseous fuel. Whether the additives are introduced in the gaseous or liquid phase — by prevapourisation or atomisation, respectively — may have a significant impact on soot production, NO_x and CO emissions [19,33]. Reduced soot production and NO_x emissions were observed in nonpremixed flames established on a burner that promotes prevapourisation of palm methyl ester fuel droplets [33]. Under turbulent nonpremixed conditions, the local fuel-rich mixture generated by fuel droplets from atomisation promotes the formation of aromatics and ultimately soot [34]. A more detailed comparison between spray and prevapourisation for introducing toluene into turbulent nonpremixed hydrogen flames was conducted to study their influence on soot evolution [19]. Substantially more polycyclic aromatic hydrocarbons and soot are formed near the nozzle exit plane in spray flames than prevapourised flames [19]. Investigation of these two methods using liquid biofuels with different properties can provide valuable knowledge for future applications.

Since biofuels are usually comprised of complex compositions and various properties ascribed to the different feedstocks and production methods, directly using biofuels inevitably introduces challenges for fundamental-level studies of the chemical effects [24]. Therefore, surrogates that can emulate the various properties of complex fuels are widely employed in experimental and numerical research [35,36]. Four different surrogates (see chemical structures in Fig. 1) are chosen in this study to emulate the combustion properties of bio-oils and essential oils. Toluene (C_7H_8), together with other aromatics, are the main components in bio-oils [19]. Anisole (C_7H_8O) is the characteristic of lignin structures and is recognised as the main source in forming aromatics during the production of bio-oils [37]. In addition, anisole is usually used to emulate the evolution of methoxy phenol, a key precursor of PAH and soot in biomass combustion [37]. Cyclic monoterpenes — eucalyptol ($C_{10}H_{18}O$) and D-limonene ($C_{10}H_{16}$) — are the primary components in eucalyptus oil and orange oil, accounting for 90 wt% and 97 wt%, respectively [38].

The efficacy of adding sooting hydrocarbons to enhance the low radiant heat flux of hydrogen flames for practical systems has been established. However, previous studies that focussed on this approach either only achieved a Reynolds number of 5000 [19], tested only a limited variety of additives [19,23], or did not consider the potential challenge of NO_x emissions [29]. Furthermore, the influencing factors such as hydrogen concentration, bulk mean exit strain rate, and their correlation to the flame characteristics are not well understood. In this paper, the combustion characteristics, including flame appearance, radiant heat flux, flame temperature, and NO_x emissions of turbulent nonpremixed hydrogen-nitrogen flames, blended with four different prevapourised or sprayed biofuel surrogates, are investigated. Qualitative and quantitative evaluation of introduction methods, biofuel surrogates' concentrations, and hydrogen concentrations deepen the understanding of dominating factors in achieving radiating hydrogen flames, along with the aforementioned flame characteristics. In particular, the experimental and numerical investigations of NO_x formation in these blended hydrogen flames provide insights into the potential challenge of this approach. Future experimental work using laser-based diagnostic techniques to measure the instantaneous flame temperature, OH^*, distribution of liquid droplets, soot volume fraction, and soot sizing can yield a better understanding of soot evolution in these blended flames.

Methodology

Burner configuration

An integrated vapourised/spray jet flame burner, shown in Fig. 2a, supplied biofuels as either droplets or vapour. An ultrasonic nebuliser was installed in a holder with an exterior smooth contraction, which was in turn inserted in a housing with an internal smooth contraction. A 5.5-mm-internal-diameter jet was located at the top of the housing and axially aligned with the nebuliser exit. In the prevapourisation configuration, liquid biofuel surrogate was prevapourised by a controlling evaporating mixing (CEM) unit heated to 190 °C upstream of the burner and mixed with a 9:1 mixture of H_2/N_2 gases. The liquid fuel inlet was blocked in this configuration.

In the spray flame configuration, the H_2/N_2 mixture was supplied as a carrier gas through the gas inlet of the burner and transported the biofuel-surrogate droplets generated by the ultrasonic nebuliser with minimal initial momentum to the flame. The gas and liquid flow rates were controlled by

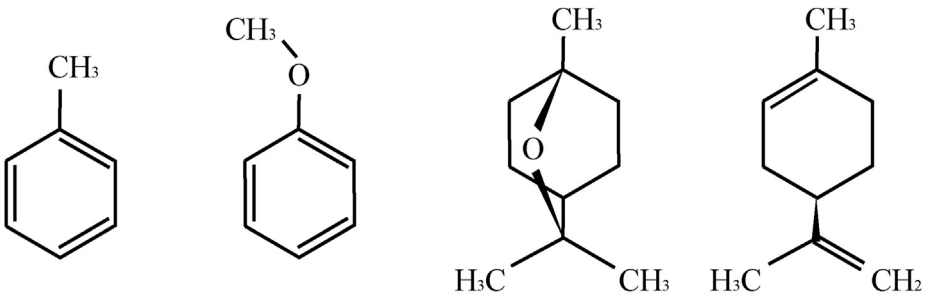

(a) Toluene (b) Anisole (c) Eucalyptol (d) D-limonene

Fig. 1 – Chemical structure of biofuel surrogates.

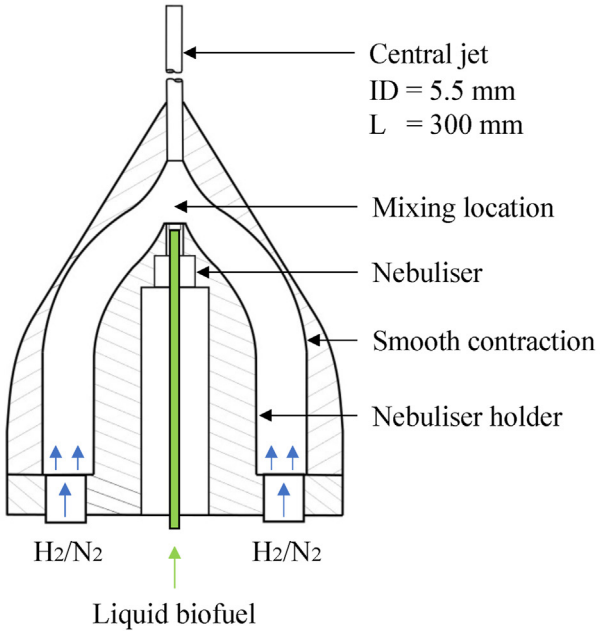

(a) Integrated vapourised/spray burner.

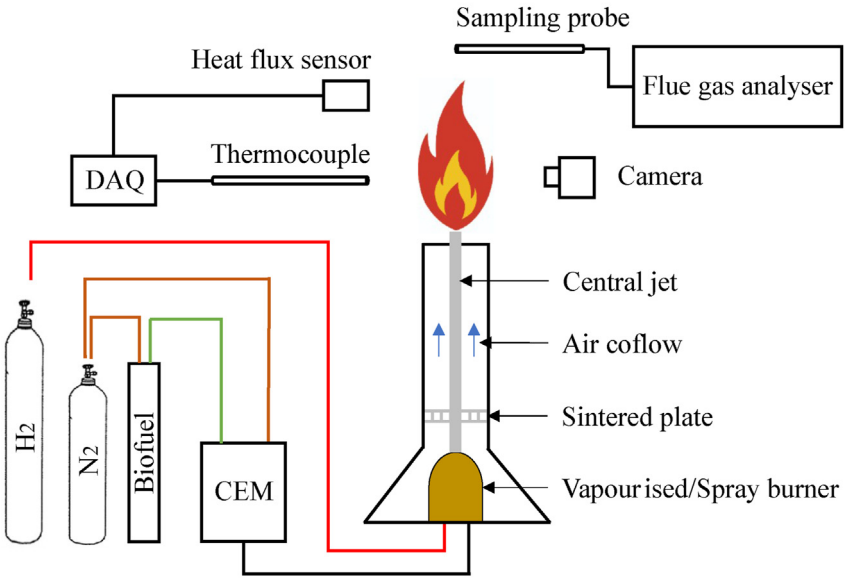

(b) Schematic of the experimental setup.

Fig. 2 – Schematic of the vapourised/spray burner (2a) and the experimental setup (2b).

mass flow controllers (Alicat) with the manufacturer-specified uncertainty of ±0.5% of reading and ±0.2% of full scale. The Sauter mean diameter (SMD) of the biofuel droplets is estimated to be 30 μm at the ultrasonic nebuliser exit based on the data provided by the manufacturer (Sonotek). The SMD of the droplets is calculated from the commonly used equation for ultrasound-induced atomisation [39]:

$$d_{SMD} = c\left(\frac{8\pi\sigma}{\rho F^2}\right)^{\frac{1}{3}} \quad (1)$$

where c is an empirical constant dependent on the nebuliser type, σ is the surface tension, ρ is the density of the liquid, and F is the ultrasound frequency of the nebuliser.

The burner was pre-heated in both vapourised and spray configurations before lighting the flame. A nitrogen carrier gas was heated to 190 °C by the CEM and supplied to the jet. The temperature at the jet exit was measured and maintained at 110±6 °C. At the biofuel surrogate concentrations tested in this work, the partial pressure of the prevapourised biofuel surrogates is lower than their vapour pressure at such temperatures.

Experimental setup

Turbulent nonpremixed flames were stabilised on the vapourised/spray burner. A uniform coflow at 1.0 m/s of room-temperature flowed through a 150 mm × 150 mm square contractor. An exhaust hood was placed at a constant vertical distance (700 mm) above the flame tip. A H_2/N_2 mixture (9:1 by mole) was selected as the non-blended flame case, with a fixed bulk mean Reynolds number of 10,000. Nitrogen was blended with hydrogen to increase the bulk mean Reynolds number of the flames to 10,000. As highly radiating H_2/N_2 (1:1 vol) flames with a Reynolds number of 5000 were achieved previously by blending 1–5% toluene [19], there is a need to investigate the effect of blending biofuels at lower concentrations and compared with higher concentrations. Therefore, the H_2/N_2 mixture was blended with 0.2 and 1% biofuel surrogate (based on the mole concentration of H_2) by prevapourisation and spray. Prevapourised toluene was further tested at 3.5 and 4% as higher concentration cases for comparison. The carbon flow rates between different biofuel/H_2/N_2 mixtures were kept constant for each biofuel surrogate concentration to ensure an equivalent carbon flux. To investigate the effect of lower hydrogen concentration on flame characteristics, a 7:3 H_2/N_2 mixture (by mole) blended by 3.5 mol% vapourised toluene with bulk mean Reynolds number above 10,000 and reduced bulk mean exit velocity was also tested on the same jet. From the 9:1 H_2/N_2 to 7:3 H_2/N_2 mixture, the H_2 flow rate was reduced by half and the N_2 flow rate was increased to maintain a constant bulk mean Reynolds number of 10,000.

Table 2 – Test conditions.

Test parameter	Unit	Result
Ambient temperature	°C	25
Ambient pressure	atm	1
Temperature at the jet exit	°C	110±6
Air coflow	m/s	1
H_2 flow rate	L/min	144
N_2 flow rate	L/min	15
H_2 flow rate (LHTV)	L/min	72
N_2 flow rate (LHTV)	L/min	26

The detailed flame cases are presented along with flame codes in Table 1. The test conditions are shown in Table 2. Due to various chemical and physical properties of biofuel surrogates, the total heat input and Reynolds number of flame cases at the same blending ratio change less than 1%. The non-blended flame is hereafter referred to as "HB0". The blended flame cases, for example, in "HEV/Sx", "HE" indicates that the H_2/N_2 mixture is blended with eucalyptol, "V/S" represents the introduction method — prevapourisation or spray, "x" is the biofuel surrogate concentration used in the case in mol%. In "LHTV", "L" indicates the lower hydrogen concentration. The exit strain rate (U/d) is the ratio between the mean velocity at the jet exit and the inner diameter of the jet [40,41]. The flame length of the non-blended H_2/N_2 flame (HB0) is denoted as L_f in this paper.

Experimental diagnostics

Fig. 2b shows the schematic of the experimental setup. To analyse the effect of biofuel surrogate addition on the appearance of the flames, a digital commercial single-lens reflex camera — Canon 6D with a 50 mm focal length and f/1.8 lens was used. The colour still photographs were converted to grayscale in image post-processing to analyse the luminosity of the flames.

To measure the radiative heat transfer from the flames, two heat flux sensors (Medtherm Corporation model 92241/2) were placed at a radial distance of 284 mm from the centre of the jet. The angular sensitivity of the heat flux sensor was measured prior to the experiment. To minimise the effect of

Table 1 – Flame details and codes of the turbulent nonpremixed non-blended and biofuel surrogate/H_2/N_2 flames. The flame cases and corresponding flames codes are as follows: H_2/N_2/Toluene - HTV/Sx; H_2/N_2/Eucalyptol - HEV/Sx; H_2/N_2/D-limonene - HLV/Sx; H_2/N_2/Anisole - HAV/Sx.

mol%	Heat input	Exit strain rate	Re_{jet}	Flame code
x	(kW)	U/d (s^{-1})	(–)	x = mol%
0.2	24.6	20,300	10,400	HTV/Sx, HEV/Sx, HLV/Sx, HAV/Sx
1.0	28.2	20,500	11,800	HTV/Sx, HEV/Sx, HLV/Sx, HAV/Sx
3.5	37.2	20,900	17,500	HTV
3.5	18.6	12,800	13,200	LHTV
4.0	39.2	21,000	18,600	HTV

angular sensitivity, a 20° view restrictor was used. The uncertainty of the radiant heat flux measurement was reduced to ±3%. The heat flux sensor equipped with a 20° view restrictor measured heat flux from a portion of the flame 100 mm tall at a radial distance of 284 mm. In comparison to measuring the global heat flux of the flame, heat flux data measured at different flame heights can be correlated to the flame temperature data collected at the same flame height to evaluate the potential interferences between these parameters. To compare the effect of different introduction methods — sprayed or prevapourised — on the combustion characteristics between blended flames, the measuring points are designed to focus on the momentum-driven region near the jet exit between height above burner (HAB) 40 mm − 390 mm (i.e., $x/L_f = 0 - 0.4$), with eight equi-spaced measuring points. The heat flux data at each measuring location was recorded for 1 min at 2500 Hz. The error calculated from the data was within ±2%.

To correlate the mean centreline flame temperature to the radiant heat flux and flame appearance, a Type-R thermocouple with a 0.2 mm diameter wire size and a 0.7 mm diameter bare-bead was employed to measure the mean centreline flame temperature between flame cases at the same measuring points as radiant intensity data. The thermocouple flame temperature measurements were corrected for radiation losses. Soot deposition on the thermocouple bead was not observed in the experiment; however, emissivity temperature dependence was considered. The mean centreline flame temperature was recorded after a steady state was achieved. The uncertainty of the mean centreline flame temperature measurement was mainly ascribed to the radiation correction and was estimated to be ±6%. The mean centreline flame temperature at each measuring location was collected for 1 min at 10 Hz after a steady state was achieved. The error calculated from the obtained flame temperature data was ±1%.

A Testo 350 XL flue gas analyser was used to measure and compare the global emissions including CO, CO_2 and NO_x (NO, NO_2) across various flame cases. The resolution of NO, NO_2, CO sensors is 1 ppm, and that of CO_2 measurement is 0.01 vol %. To achieve consistency with sampling across different flame cases, a probe was placed at the centreline of flames with a constant relative distance of 100 mm to collect flue gas samples emitted from the flames. The emission index of NO_x is independent of ambient air dilution because of the normalisation based on carbonaceous species using equation (3). The flue gas analyser was calibrated daily using a gas mixture with a known percentage. In accordance with the manufacturer' specification, the uncertainty of the global emission measurement was within ±2%.

Chemical analysis

To analyse the chemistry (i.e., reaction pathways and chemical mechanisms) contributing to NO_x emissions in the blended H_2/N_2 flames, opposed-flow diffusion (OPPDIF) flames in Chemkin Pro v19.2 was used along with a comprehensive chemical kinetic mechanism for NO_x formation modelling. The chemical kinetic mechanism was developed by CRECK Modelling Group for $C_1 - C_{16}$ hydrocarbon combustion, which comprised 24,501 reactions and 497 species [42]. The results from OPPDIF modelling have been widely coupled with experimental measurements to evaluate the chemistry in jet flames [43,44]. To the best of the authors' knowledge, a chemical kinetics mechanism for comprehensive NO_x formation is not available for all biofuels tested in this work — eucalyptol and D-limonene excluded. Therefore, only toluene and anisole blends were analysed for NO_x formation. The numerical simulations of NO_x formation were undertaken to analyse the global NO_x emissions collected from the flue gas. The strain rate was set to 100 s^{-1} in the Chemkin simulations. Although Chemkin simulation is under laminar conditions, this work focuses on the kinetic impact of the additives. It is noteworthy that the bulk flow field is consistent amongst the flame cases since the additive in the fuel mixture accounts for a small portion. The rate of production (ROP) of NO_x and its primary reaction pathways are the focus. The computational analysis provides qualitative information and insights from a chemistry aspect into the interpretation and understanding of the experimental observations.

Results and discussion

The effect of blending lower concentration biofuel surrogates ($\leq$ 1 mol%)

Flame luminosity

The appearance and the luminosity of the turbulent non-premixed biofuel surrogate/H_2/N_2 flames are shown in Fig. 3. The mean characteristics of the flames are captured with a long exposure time of 20 s. For the 1% vapourised and sprayed toluene flames, a shorter exposure time (250 μs) is also shown to illustrate the fluctuating nature of the turbulent flames.

Fig. 3a and b shows the flame appearance of vapourised and sprayed biofuel surrogates blended H_2/N_2 flames, respectively. In Fig. 3a, a moderate effect was found on the flame volume and flame appearance of the H_2/N_2 flame from blending vapourised biofuel surrogates at 0.2 and 1 mol%. However, a clear enhancement of blue colouration was observed in the vicinity of $x/L_f = 0 - 0.5$, due to the promoted formation of CH^*, C_2^*, CO_2^* and HCO^* from blending biofuel surrogates [45,46]. In comparison to the vapourised biofuel surrogate blended flames, it is seen in Fig. 3b that changing the additives' introduction method from prevapourisation to spray solely does not achieve a highly sooting blended flame. Similar to the vapourised flames, introducing 0.2 and 1 mol% biofuel surrogates by spray has slight impacts on the flame length, width, and luminosity in comparison to the non-blended flame. It is highlighted that blending 1 mol% toluene and anisole by dilute spray (Fig. 3b) exhibits a distinct flame appearance compared with the vapourised flames (Fig. 3a). A transition of flame appearance from blue to yellow starts to take place in the 1 mol% toluene and anisole spray cases due to the soot formation. Liquid droplets in the spray flame generate local fuel-rich regions which promote soot formation, and the energy loss from the phase change in turn reduces soot oxidation. It is seen from the photographs with 20 s exposures and 1/4000 s that the soot clusters in the

vicinity of the fuel-rich region from $x/L_f = 0.4 - 0.8$. The other flame cases do not feature such a transition. Another noteworthy observation is that the spray flames display less enhancement in blue colouration near the jet exit plane between $x/L_f = 0$ and 0.4, compared with vapourised flames. This observation will be further discussed in conjunction with the signal intensity in the following paragraph.

The global signal intensity extracted from the still photographs is used to compare the luminosity of various biofuel surrogate blended flames. Fig. 4a reports the global flame luminosity extracted from the photographs, for the various fuels and introduction methods, at blending ratios of 0.2 and 1 mol%. For the 0.2 mol% blending case, it is seen that the vapourised flames display higher luminosity than the spray flames and that this is consistent for all the biofuel surrogates reported. Fig. 4b exhibits the luminosity of toluene and anisole blends as a function of flame height. It is observed in Fig. 4b that spray flames tend to have higher peak signal intensity (18% and 8% for toluene and anisole blends, respectively) than vapourised flames. The peak signal intensity appears closer to the flame tip in spray flames compared with the vapourised flames. The enhanced formation of carbon-based gaseous species accounts for the peak signal intensity observed near the jet exit in vapourised toluene and anisole flames, whereas the peak intensity in spray flames is resulting from the presence of soot. Figs. 4c and 4d show the mean flame luminosity of the vapourised/spray biofuel surrogate blended flames at $x/L_f = 0.2$ and 0.6, respectively. Vapourised biofuel surrogate blended flames show higher luminosity than spray flames at the blending ratios of 0.2 and 1 mol%, which further underpins the observation from the photographs that introducing biofuel surrogate by prevapourisation tends to have higher luminosity near the jet exit than spray. On the other hand, it is seen in Figs. 3 and 4d that as the biofuel surrogate concentration increases to 1 mol%, the luminosity of spray flames overwhelms vapourised flames at $x/L_f = 0.6$ due to the enhanced soot radiation. This luminosity difference between vapourised flames and spray flames tends to be more significant at $x/L_f = 0.2$ and less evident downstream ($x/L_f = 0.6$). The reason for the aforementioned phenomenons is that, compared with spray flames, introducing biofuel surrogates by prevapourisation facilitates the mixing between hydrogen and biofuels as phase change is avoided in such regime and the reactants actively participate in chemical reactions. Consequently, the species that contribute to the luminosity in the blue region of the flame are enhanced than in sprayed biofuel cases, as enthalpy of vapourisation is prevented.

It has been reported that prevapourised aromatic fuels are more effective than monoterpenes, and prevapourised non-oxygenated fuels are more effective than oxygenated fuels in enhancing global flame luminosity [29]. It is seen in Fig. 3a that altering the introduction method from prevapourisation to spray follows a similar trend. Sprayed aromatic biofuel surrogates (toluene and anisole) are more effective than terpene-related hydrocarbons (eucalyptol and D-limonene) in improving flame luminosity, which is consistent with the trend in vapourised flames. It is seen in Fig. 4a that blending 1 mol% toluene/anisole by spray increases the flame luminosity of the non-blended flame by 293% and 126%,

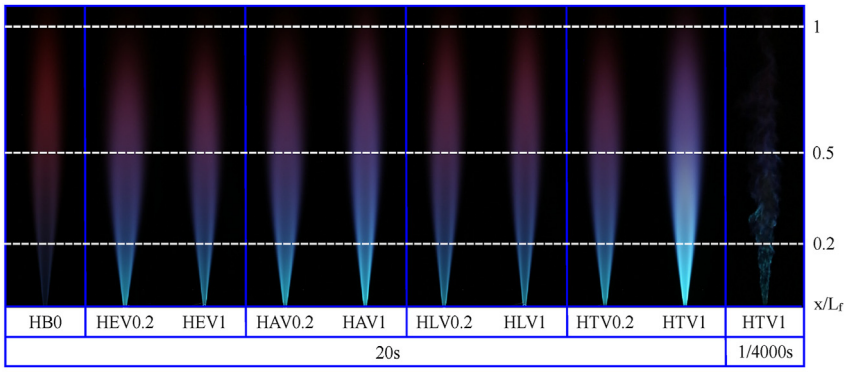

(a) Flame appearance of vapourised flames

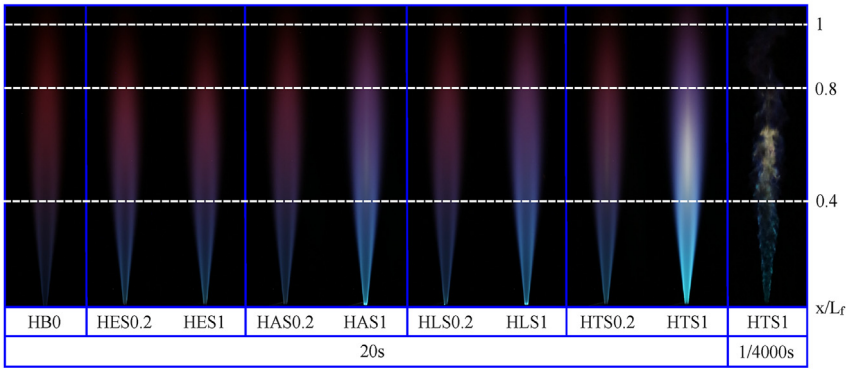

(b) Flame appearance of spray flames

Fig. 3 – Flame appearance of lower concentration (0.2 and 1 mol%) vapourised (3a) and spray (3b) biofuel surrogate/H_2/N_2 flames.

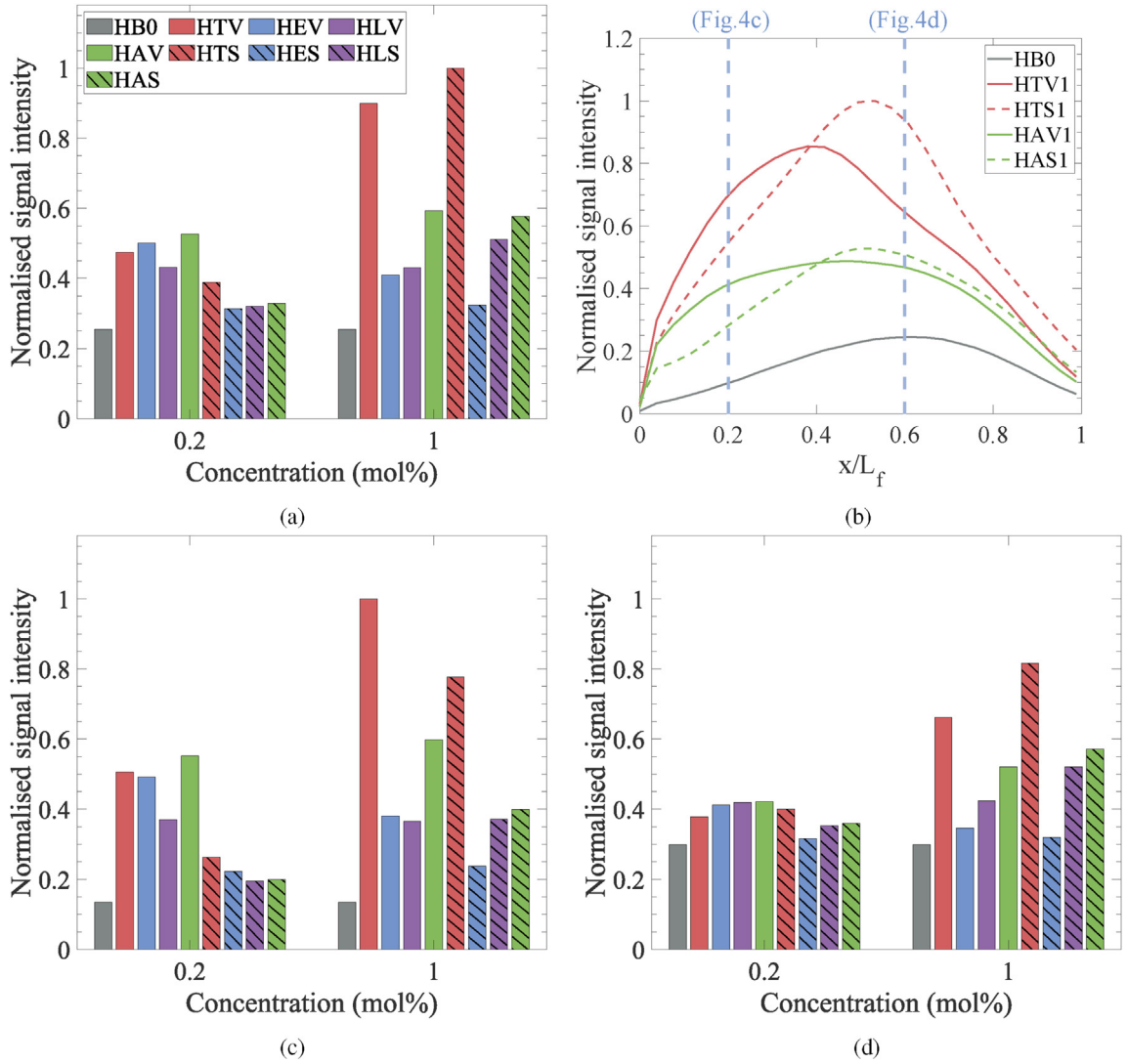

Fig. 4 – Flame luminosity of the vapourised/spray biofuel surrogate blended H_2/N_2 flames indicated by the signal intensity extracted from photographs. The signal intensity is normalised to the peak signal intensity of 1 mol% toluene spray flame. (4a) Global mean flame luminosity. (4b) Flame luminosity of toluene/anisole blends as a function of flame height. (4c) Mean flame luminosity at $x/L_f = 0.2$. (4d) Mean flame luminosity at $x/L_f = 0.6$.

respectively. Introducing 1 mol% prevapourised D-limonene and eucalyptol increases the non-blended flame by 101% and 28%, respectively. Similarly, sprayed non-oxygenated biofuel surrogates are more effective than sprayed oxygenated biofuel surrogates due to the improved soot oxidation rate from the presence of oxygen content [29]. This is also the reason for less soot being observed in the 1 mol% spray anisole flame compared with the 1 mol% toluene spray flame.

Radiant heat flux

To compare the radiant heat flux enhancement of different biofuels, the radiant fraction (χ_r) defined in Equation (2) is employed [47].

$$\chi_r = \frac{\dot{Q}_r}{\dot{Q}_F} = \frac{2\cdot\pi\cdot\left(\int_{R_0}^{R} r\cdot\dot{q}''(r)\cdot dr + R\cdot\int_{0}^{\infty}\dot{q}''(z)\cdot dz\right)}{\dot{m}\times LHV} \quad (2)$$

where χ_r is the radiant fraction, $\dot{Q}_r$ is the radiated heat (kW), and $\dot{Q}_F$ is the total thermal power (kW) of the flame. The radiated heat ($\dot{Q}_r$) in Eq. (2) is the summation of the axial (z) and radial (r) radiant heat flux ($\dot{q}''$) obtained by the heat flux transducer, R and R_0 denote the radial distance from the heat flux transducer to the centre of the nozzle exit and the flame front, respectively, $\dot{m}$ is the mass flow rate of the fuel, and LHV is the lower heating value of the fuel.

Figs. 5 and 6 show the global and axial radiant fraction, respectively, measured from non-blended and prevapourised or spray biofuel surrogate/H_2/N_2 flames. It is concluded from the results that introducing 0.2 and 1 mol% biofuel surrogate by spray is more effective than by prevapourisation in radiant intensity enhancement of H_2/N_2 flames, but the difference is not evident at lower concentration blended flames. For example, adding 1 mol% toluene by prevapourisation and

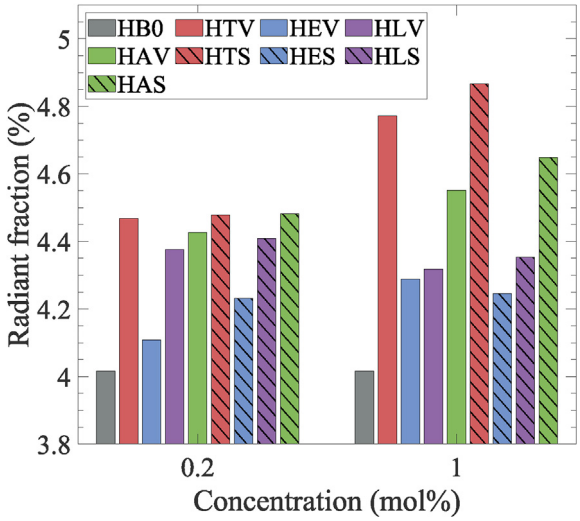

Fig. 5 – Global radiant fraction of lower concentration (0.2 and 1 mol%) vapourised/spray biofuel surrogate/H_2/N_2 flames from $x/L_f = 0 - 0.4$.

spray increases the radiant fraction (χ_r) of the HB0 flame by 18% and 22%, respectively. Adding 1 mol% anisole by prevapourisation increases the radiant fraction of the HB0 flame by 13%, compared with a 16% increase from the spray. It is also found that introducing the additives by spray instead of prevapourisation has a larger impact on the radiant fraction enhancement of the 1 mol% toluene and anisole blends than other biofuel surrogate blended flames. This phenomenon can be correlated to the observation in Section Flame luminosity that soot formation is promoted in these two flame cases directly as a result of changing the introduction method.

The results from Figs. 5 and 6 indicate that blending lower concentration biofuel surrogates to a H_2/N_2 flame by spray has a limited impact on radiant heat flux enhancement. It was concluded in Section Flame luminosity that changing the introduction method from prevapourisation to spray does not attain a highly sooting flame at 0.2 and 1 mol% additive concentration, therefore, the source of radiative heat transfer from these lower concentration biofuel blended flames is still from gaseous species (e.g., CO, CO_2, and H_2O). It is known that gaseous species have much less radiant heat flux than soot at

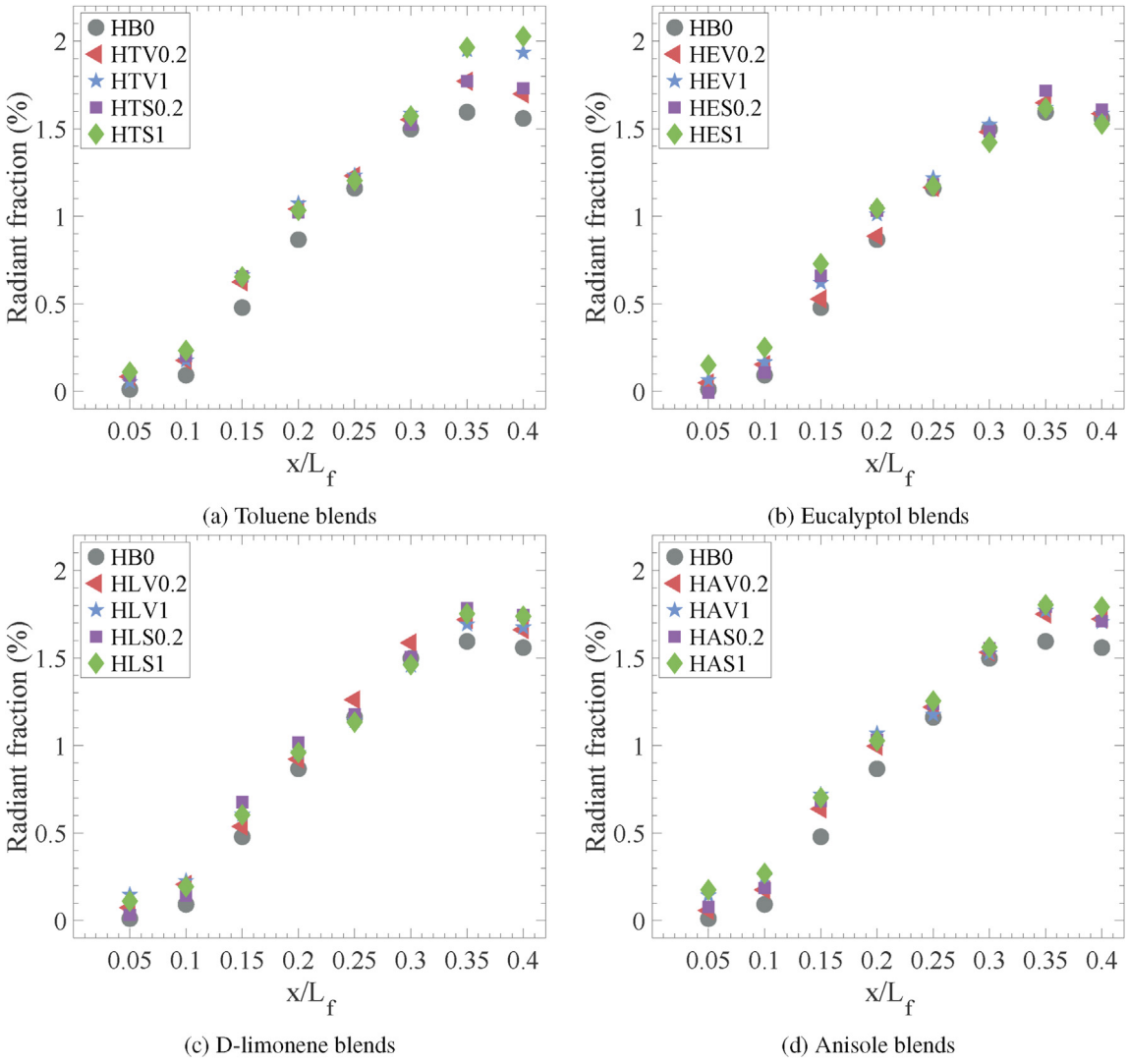

Fig. 6 – Axial radiant fraction of lower concentration (0.2 and 1 mol%) vapourised/spray biofuel surrogate/H_2/N_2 flames described in Table 1.

equivalent temperature [48]. Another factor that contributes to the limited radiant intensity enhancement observed in the 9:1 mol H_2/N_2 flame is that such flame with high hydrogen concentration has abundant OH radicals and high flame temperature, leading to a high oxidation rate that hampers sooting formation from the relatively low carbon flux (note that the concentration of carbon atoms in lower concentration biofuel blended flames are about 0.02 – 0.07, much lower than conventional hydrocarbon fuels). Therefore, an additional flame case with lower hydrogen concentration was tested to evaluate the effect of hydrogen concentration on the flame characteristics of biofuel surrogate blended H_2/N_2 flames. The results will be further discussed in Section The effect of blending higher concentration vapourised toluene (≥ 3.5mol %).

It is observed in Fig. 6 that the radiant fraction of spray toluene and anisole blended flames reach the peak value at $x/L_f = 0.4$ between $x/L_f = 0 - 0.4$, which is dissimilar to the trend in other vapourised/spray biofuel-blended cases — reaches the peak radiant fraction at $x/L_f = 0.35$. In the flames without soot (i.e., all flame cases except for 1 mol% spray toluene/anisole flames), the flame luminosity and radiant fraction reach their peaks closer to the jet exit as a result of enhanced formation of gaseous species. On the other hand, in the 1 mol % spray toluene and anisole blended flames where soot formation becomes evident from $x/L_f = 0.4$, soot loading is the major contributing factor to the radiant intensity enhancement. This finding is consistent with the observations in Fig. 4.

Another noteworthy finding in Fig. 5 is that the global radiant fraction from $x/L_f = 0 - 0.4$ of the spray D-limonene blended flame case shows a decreasing trend with the increase in additive concentration, indicating that other factors may play important roles in radiant intensity enhancement in addition to carbon flux. Introducing 0.2 mol% D-limonene as a spray enhances the radiant fraction of the HB0 flame by 10%, but adding 1 mol% spray D-limonene enhances the radiant fraction by 8%. It was reported that flame temperature is one of the contributing factors to the radiant heat flux as the flame's radiated heat is proportional to the fourth power of temperature — $Q_r \propto T^4$ [29]. The impact is more evident in spray flames The spray flame temperature results presented in Section 3.1.3 further support this finding.

Flame temperature

Fig. 7 reports the mean axial flame temperature along the centreline for both the vapourised and spray biofuel surrogate blended H_2/N_2 flames. The results show that introducing prevapourised biofuel surrogates increases the mean centreline flame temperature of the non-blended H_2/N_2 flame near the jet exit plane while decreasing the flame temperature at the region further into the momentum-driven part. Compared with vapourised flames, adding biofuel surrogates to HB0 flames by spray evidently decreases centreline flame temperature. The most significant reduction is recorded to be 213 K in 1 mol% spray D-limonene blends at $x/L_f = 0.05$. Dissimilar to the trend of all vapourised flame cases, reductions in mean centreline flame temperature are observed throughout the flame from $x/L_f = 0.05 - 0.4$ in spray flames.

It is seen in Fig. 7 that spray flames generally have lower mean centreline flame temperature than vapourised or non-blended flame, particularly near the exit plane. The enthalpy of vapourisation leads to a reduction in the temperature of the spray flames. The temperature difference tends to be less downstream, where the rate of vapourisation decreases. The prevapourised biofuel surrogates and hydrogen mixture actively participate in the reactions mixed with oxidant when they leave the jet exit, while sprayed biofuel surrogates first require energy for phase change. Therefore, a faster and more homogeneous mixing is achieved in vapourised flames and subsequently results in higher flame temperature. It was discussed in Sections Flame luminosity and Radiant heat flux that in these lower concentration biofuel surrogate blended flames, where thermal radiation is primarily from gaseous species, higher flame temperature and higher heat release rate lead to higher flame luminosity and radiant intensity. The mean flame temperature results further provide evidence to explain why all vapourised flames display higher flame luminosity at $x/L_f = 0.2$ in Fig. 4b and reach their peak luminosity closer to the jet exit plane in Fig. 4d, compared with spray flames. Temperature reduction is the reason that radiant fraction decreases with the increase in biofuel concentration (i.e., carbon flux). The largest temperature reduction (ie., 213 K in 1 mol% spray D-limonene) is correlated to the lower radiant fraction in 1 mol% spray D-limonene blends, compared with 0.2 mol% spray D-limonene blends (discussed in section Radiant heat flux).

Large mean centreline flame temperature drops are also observed in 1 mol% spray toluene and anisole blends (Figs. 7a and d), however, exhibiting an opposite trend to D-limonene blends regarding radiant heat flux. Soot formation becomes evident in the 1 mol% spray toluene and anisole blended flame, hence the source of the radiative heat transfer in these flames gradually shifts from gaseous species to a stronger source — soot. It is known that lower temperature favours soot formation since the soot oxidation rate is reduced [15,49]. Therefore, the reduced mean flame temperature in the 1 mol% spray toluene blends and anisole blends contributes to soot formation and subsequently results in laser radiant fraction increases. It is also observed in Fig. 7a that 1 mol% spray toluene blends and anisole blends see larger mean temperature drops in the vicinity of $x/L_f = 0.3$ compared with D-limonene and eucalyptol. In addition to the enthalpy of vapourisation of liquid droplets in spray flames, it is also ascribed to the elevated radiative heat loss from the soot, which is consistent with the observation in spray flame photographs (Fig. 3b) that soot loading becomes evident in 1 mol% spray anisole and toluene-blended flames. This phenomenon will be further demonstrated in Section The effect of blending higher concentration vapourised toluene (≥ 3.5mol%).

NO_x emissions

The emission index for NO_x (EI_{NO_x}) is calculated using Eq. (3) [50,51]:

$$EI_{NO_x} = \frac{X_{NO_x}}{(X_{CO} + (X_{CO_2} - X_{CO_{2amb}}))} \times \frac{n_c \times MW_{NO_x}}{MW_f \times LHV_f} \quad (3)$$

where X denotes the mole concentration of NO_x, CO, CO_2 in the flue gases, CO_{2amb} is the mole fraction of CO_2 in ambient air, n_c is the carbon concentration of fuel, MW_{NO_x} is the

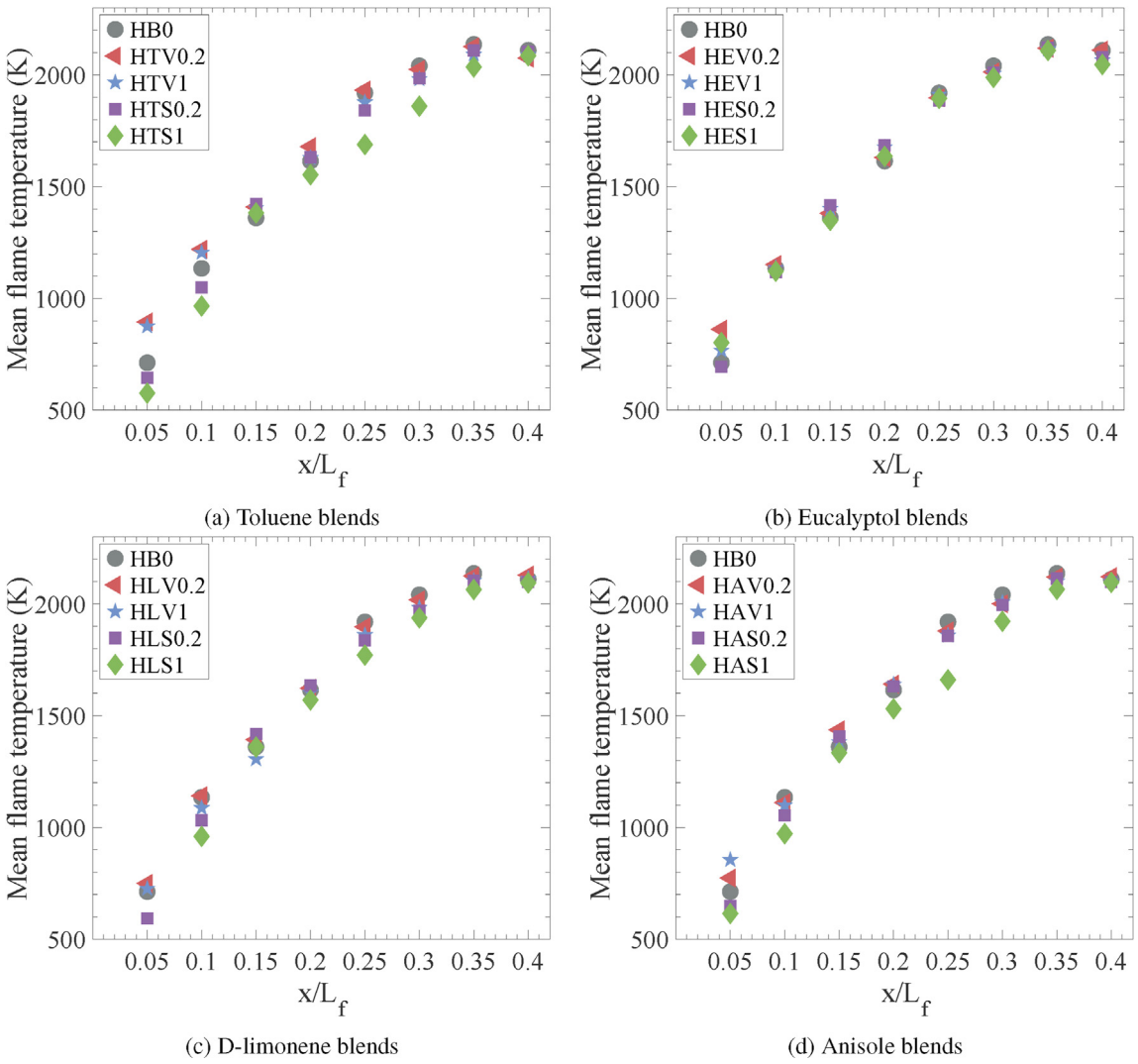

Fig. 7 – Mean axial flame temperature along the centreline of lower concentration (0.2 and 1 mol%) vapourised/spray biofuel surrogate/H_2/N_2 flames described in Table 1. The results are corrected for radiative heat loss from the thermocouple.

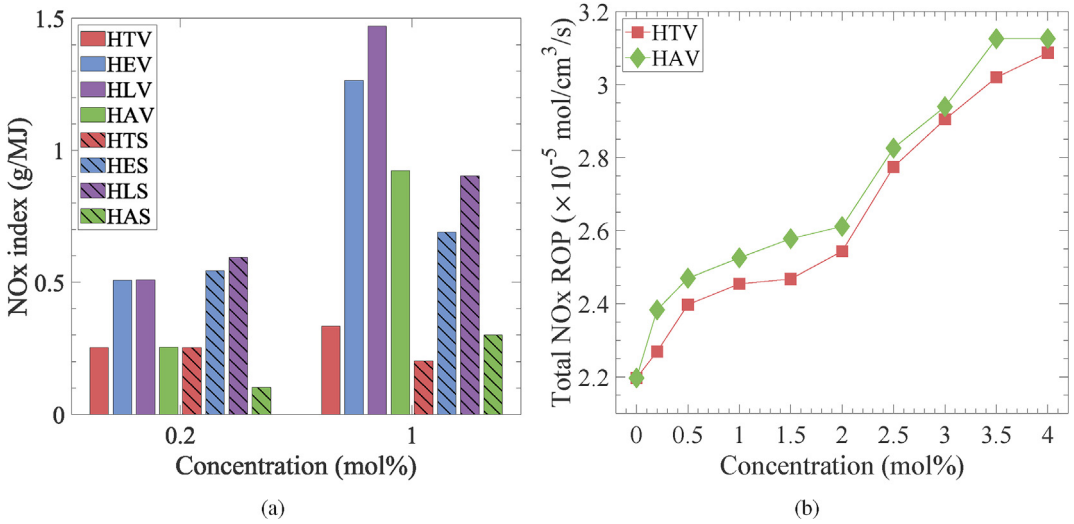

Fig. 8 – Global NO_x emissions measured in the experiment and numerical simulation of NO of lower concentration (0.2 and 1 mol%) vapourised/spray biofuel surrogate/H_2/N_2 flames described in Table 1. (8a) Emission index for NO_x measured in the experiment. (8b) ROP of NO in toluene and anisole blends from numerical simulation.

molecular weight of NO_x, MW_f and LHV_f denote the molecular weight and the lower heating value of the fuel mixture, respectively. Note that Eq. (3) is not applicable to carbon-free fuel mixtures [51].

The EI_{NO_x} (g/MJ) from measurements in both the spray and vapourised biofuel surrogate blended H_2/N_2 flames is plotted as a function of biofuel concentration in Fig. 8a. Fig. 8b presents the total ROP of NO_x in toluene and anisole blends as a function of concentration from numerical modelling. The results show that introducing 1 mol% additives into the H_2/N_2 flames by spray results in lower EI_{NO_x} than introducing prevapourised biofuel surrogates. Introducing 0.2 and 1 mol% anisole by spray decreases the EI_{NO_x} by 60% and 67%, respectively, compared with introducing 0.2 and 1 mol% anisole by prevapourisation. This is mainly because the lower centreline flame temperature (Fig. 7) measured in spray flames reduces NO_x formation via the thermal route. Thermal NO_x was previously reported as the dominant NO_x formation route in hydrogen-based flames [52,53].

It is highlighted in Fig. 8 that as the biofuel surrogate concentration increases from 0.2 mol% to 1 mol%, the EI_{NO_x} increases. However, the centreline flame temperature shown in Fig. 7 does not exhibit a positive correlation with biofuel surrogate concentration in vapourised flames. Furthermore, the numerical results from the OPPDIF simulation in Fig. 9 show that as the biofuel surrogate concentration increases, the peak adiabatic flame temperature of vapourised toluene and anisole blended flames decreases from 2302 K to 2238 K, while the total NO_x ROP in Fig. 8b displays an increasing trend. These observations imply that other NO_x formation pathways in addition to the thermal route may enhance NO_x formation in biofuel surrogate blended flames. Therefore, a detailed modelling of NO_x formation reaction pathways was conducted.

Nitrogen oxides (NO_x) is predominantly comprised of nitric oxide (NO) with a minor proportion of nitrogen dioxide (NO_2). It is found in the simulation that the ROP of NO_2 is two orders of magnitude smaller than that of NO. Thus, the computational analysis is focused on the reaction pathways of NO. Fig. 10 presents the ROP for four primary reaction pathways of NO — three NO formation pathways and one consumption

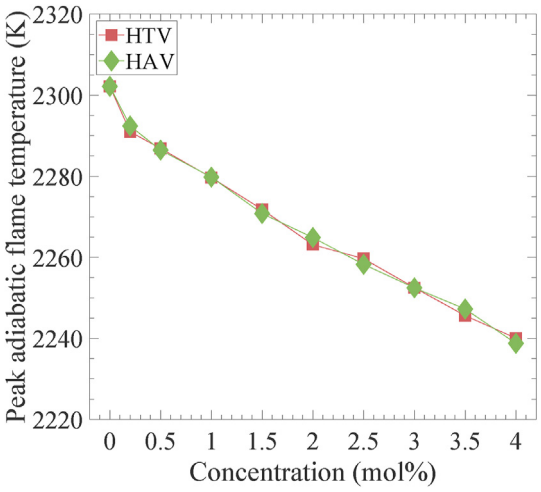

Fig. 9 – Peak adiabatic flame temperature of toluene and anisole blends from numerical simulation.

pathway. It is seen from Fig. 10a that the ROP of NO via the $OH + N \rightleftharpoons H + NO$ reaction increases with the vapourised toluene and anisole addition. This reaction pathway is known as one of the subsets in the thermal NO formation route [30]; however, it does not mean this reaction is driven by the flame temperature. It is the first reaction in the thermal route: $O + N_2 \rightleftharpoons NO + N$ that requires high energy from the flame temperature and initiates the NO formation. This reaction also controls the reaction rate via the thermal route [30]. Based on this understanding, the acceleration of NO formation via the $OH + N \rightleftharpoons H + NO$ reaction in these biofuel surrogate blended H_2/N_2 flames likely results from the OH and N radical increase. The OH radicals are expected to be abundant in hydrogen-based flames. The N radicals, on the other hand, are usually created from CH_i radicals attacking the triple bond in N_2 [54]. Therefore, as the concentration of CH_i radicals increases with the biofuel surrogate addition, the production of N radicals is subsequently promoted and hence leads to the increase in NO formation. The CH_i radicals are also involved with the reaction pathways associated with prompt NO formation, which will be discussed in the following paragraph.

The prompt route is another reaction pathway that is expected to have a major effect on the NO formation. The prompt route is initiated by $CH + N_2 \rightleftharpoons H + NCN$ and then the NCN radical forms HCN via the $NCN + H \rightleftharpoons HCN + N$ reaction. The HCN radical subsequently reacts with O to eventually form NO. It is noted in Fig. 10b that the prompt NO_x formation route is of less importance in lower concentration (0.2 and 1 mol%) vapourised biofuel surrogate blended flames, which is an order of magnitude smaller than the $OH + N \rightleftharpoons H + NO$ route.

Fig. 10c indicates that HNO plays an important role in NO formation via the $H + HNO \rightleftharpoons H_2 + NO$ reaction, which is known as the HNO-intermediate route [55]. The ROP of NO via this route tends to decrease with the increase in biofuel surrogate concentration. To investigate the reason behind this trend, the reaction chain of HNO needs to be understood. HNO is generally formed from NH through $NH + OH \rightleftharpoons HNO + H$ reaction, and the formation of NH is related to the subset of NNH route: $NNH + O \rightleftharpoons NO + NH$. The NNH route emphasises the influence of H and O radicals at flame fronts and rich regions, especially in hydrogen flames [52]. The oxygen content in anisole actively participates in the $NNH + O \rightleftharpoons NO + NH$ reaction and hence results in a slower decrease in NO formation via the HNO-intermediate route than toluene.

The process of NO consumption to a relatively steady state N_2 is another important consideration. Fig. 10d shows the ROP of NO consumed to N_2 via the $NO + N \rightleftharpoons N_2 + O$. Higher ROP is observed in the H_2/N_2 flame without biofuel surrogate, which in turn results in more NO formation in biofuel-blended flames. Combined with the ROP of other major reaction pathways, the overall ROP of NO tends to increase with the biofuel surrogate addition, which agrees with the experimental results in Fig. 8a.

Another noteworthy observation from both experimental and numerical results is that vapourised anisole tends to produce more NO_x than vapourised toluene at low concentrations. It is seen from Figs. 8 and 10 that the differences of NO ROP along with the NO consumption rate between anisole

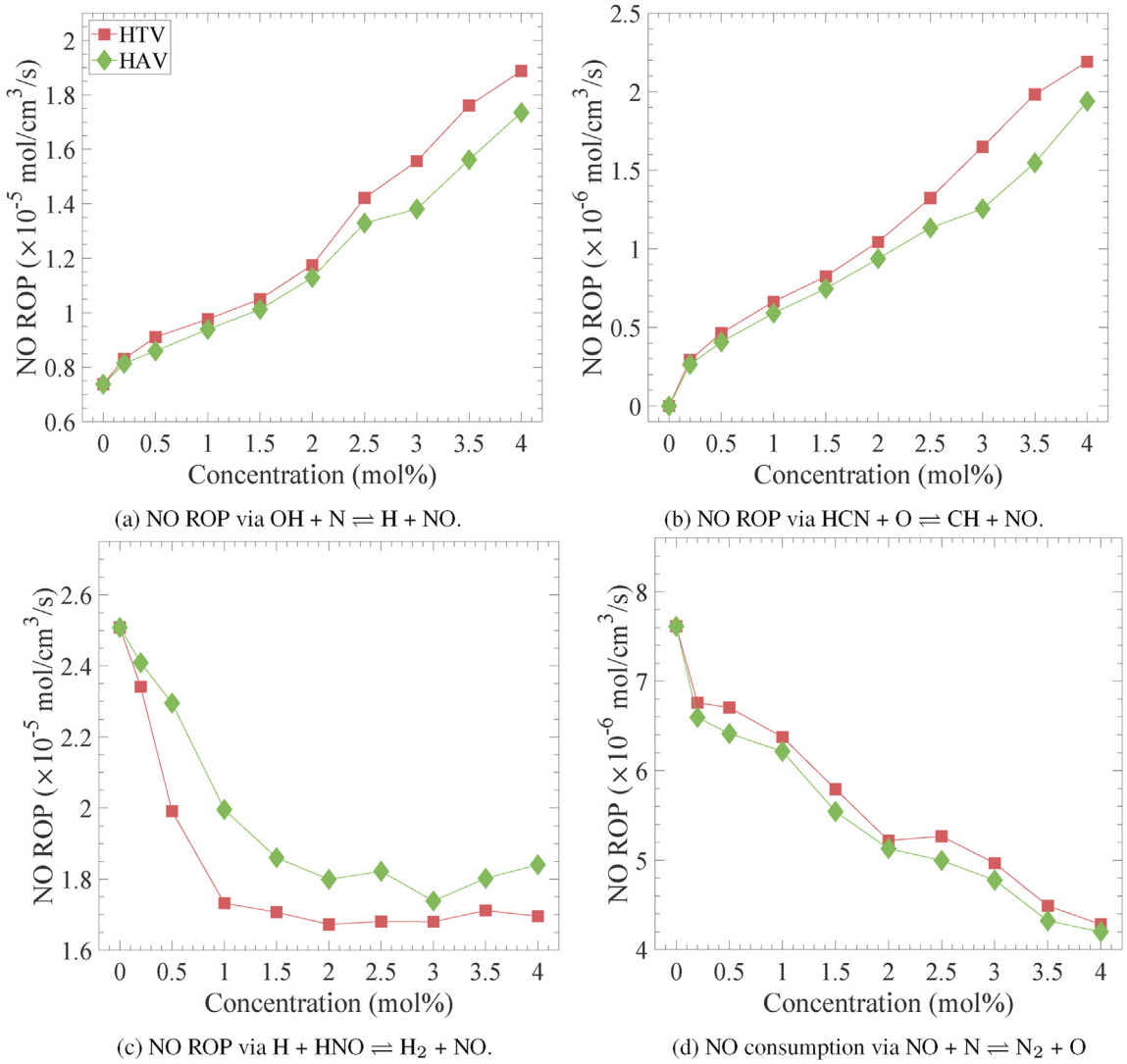

Fig. 10 – Reaction pathways of NO in toluene and anisole blends from numerical modelling.

and toluene via the OH + N ⇌ H + NO, NO + N ⇌ N_2 + O, and HCN + O ⇌ CH + NO routes are minor compared with the most distinct difference via the HNO-intermediate route: H + HNO ⇌ H_2 + NO. This is because the weak chemical bond in anisole chemical structure, which connects the oxygen atom and aromatic ring, is easily broken to form free oxygen atoms which then actively participate in the NNH route through NNH + O ⇌ NO + NH reaction to form NH and hence HNO [56].

It is seen in Fig. 8a that cyclic monoterpene biofuels (eucalyptol and D-limonene) generally have higher EI_{NO_x} compared with toluene and anisole. Furthermore, the EI_{NO_x} of 0.2 and 1 mol% D-limonene blends is higher than that of eucalyptol-blended flames, either by spray or prevapourisation. D-limonene is a non-oxygenated fuel that is comprised of a C=C double bond, while eucalyptol is an oxygenated fuel without C=C double bonds. Previous studies show that the presence of C=C double bond and oxygen content in the chemical structure of a fuel increase the flame temperature and lead to higher NO_x emissions [57,58]. The EI_{NO_x} comparison between D-limonene and eucalyptol may imply that the effect of unsaturation degree on NO_x emissions is more significant than the oxygen content in these biofuel surrogate blended H_2/N_2 flames.

The effect of blending higher concentration vapourised toluene ($\geq$ 3.5 *mol%*)

Higher concentrations (3.5 and 4 mol%) of vapourised toluene are blended in H_2/N_2 flames to investigate the combustion characteristics and compare them with the lower concentration cases. As discussed in Section The effect of blending lower concentration biofuel surrogates ($\leq$ 1 mol%), high hydrogen concentration can be a major factor that hampers soot formation. Therefore, an additional 3.5 mol% vapourised toluene-blended H_2/N_2 (7:3 by mole) flame case (LHTV3.5) with U/d = 12,800 s^{-1} was tested. In this section, the flame appearance, radiant fraction, centreline flame temperature, and NO_x emission of the LHTV3.5 flame are presented to evaluate the effect of lower exit strain rate, H_2 and N_2 concentration on flame characteristics.

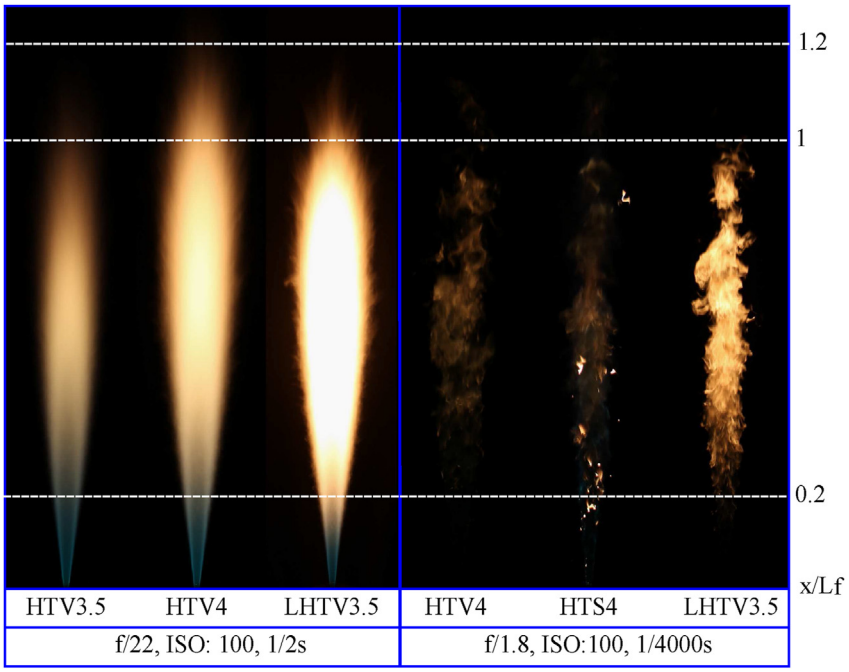

Fig. 11 – Photographs of 3.5 and 4 mol% vapourised toluene-blended H_2/N_2 flames (HTV3.5 and HTV4) and the 3.5 mol% vapourised toluene-blended H_2/N_2 flame with lower hydrogen concentration (LHTV3.5) described in Table 1.

Fig. 11 presents photographs of the flame appearance with longer (0.5 s) and shorter exposure times (250 μs). There is a clear transition from blue to yellow colouration as the vapourised toluene concentration increases from 0.2 to 3.5 mol%, which indicates that soot is markedly promoted. The blue colouration, which represents the gaseous species as discussed in Section Flame luminosity, is distributed near the exit plane ($x/L_f \leq 0.2$), but the length of this region becomes shorter as the toluene concentration further increases. The photographs with shorter exposure times (250 μs) capture the instantaneous distribution of soot in flames. Soot is predominantly distributed between $x/L_f = 0.2 - 0.8$ and its chaotic state is because of flame turbulence. The photograph of the 4 mol% spray toluene blended flame is presented to show the visual observation of toluene droplets burning in the flame. The local fuel-rich condition created by toluene droplets significantly enhances soot formation near that region. This characteristic of spray flame is distinct from the vapourised flame and it is the major contributing factor to the difference between 1 mol% vapourised/spray toluene and anisole flames in Fig. 3. Fig. 12a provides signal intensity extracted from the photograph to demonstrate the luminosity enhancement of 3.5 mol% toluene. The signal intensity of the 3.5 mol% toluene flame is 34 times greater than the 1 mol% toluene flame, and this value is more than doubled at 4 mol% (70 times).

Fig. 12b shows the radiant fraction measured from the 0, 3.5, and 4 mol% vapourised toluene blends. Unlike lower concentration biofuel-blended flames, blending high concentration toluene to H_2/N_2 flame tends to have a larger non-linear increase in radiant fraction starting from $x/L_f = 0.35$. At $x/L_f = 0.4$, increasing the vapourised toluene concentration to 4 mol% leads to a 33% increase in the radiant fraction of the HB0 flame, compared with 21% increase by blending 1 mol% vapourised toluene. The radiant fraction of the 4 mol vapourised toluene is increased by 52% compared with the non-blended H_2/N_2 flame. The previously reported numerical results of naphthalene ROP have further underpinned the experimental observation [29]. The formation of naphthalene in lower concentration (0 – 2 mol%) toluene and anisole blends is moderate, followed by a large non-linear increase as the biofuel concentration rises from 2 to 4 mol%. This further supports the finding that blending lower concentrations of biofuels has limited impact on the flame appearance and radiant fraction of a H_2/N_2 flame, but a clear transition in flame appearance and the radiant fraction is observed when blending higher concentration biofuels.

Fig. 12c shows the mean axial flame temperature along the centreline of higher concentration toluene blended H_2/N_2 flames. It is seen from Fig. 12c that the overall trend of mean centreline flame temperature variation in higher concentration vapourised toluene blends is dissimilar to the lower concentration vapourised cases — the mean centreline flame temperature displays a decreasing trend starting from $x/L_f = 0.25$, which is not seen in the lower concentration vapourised biofuel surrogate blended flames, but only in spray flames. It was discussed in Section Flame temperature that the reduced mean centreline flame temperature in spray flames is due to the enthalpy of vapourisation of liquid droplets, which does not occur in the prevapourised flames. In conjunction with the radiant fraction results in Fig. 12b, the reduced mean centreline flame temperature found in the higher concentration vapourised toluene blended flame (HTV3.5 and 4) is due to the increased radiative heat loss from the soot enhancement. The reduced mean flame temperature in these flames leads to a lower soot oxidation rate, which further promotes the soot production in the flame.

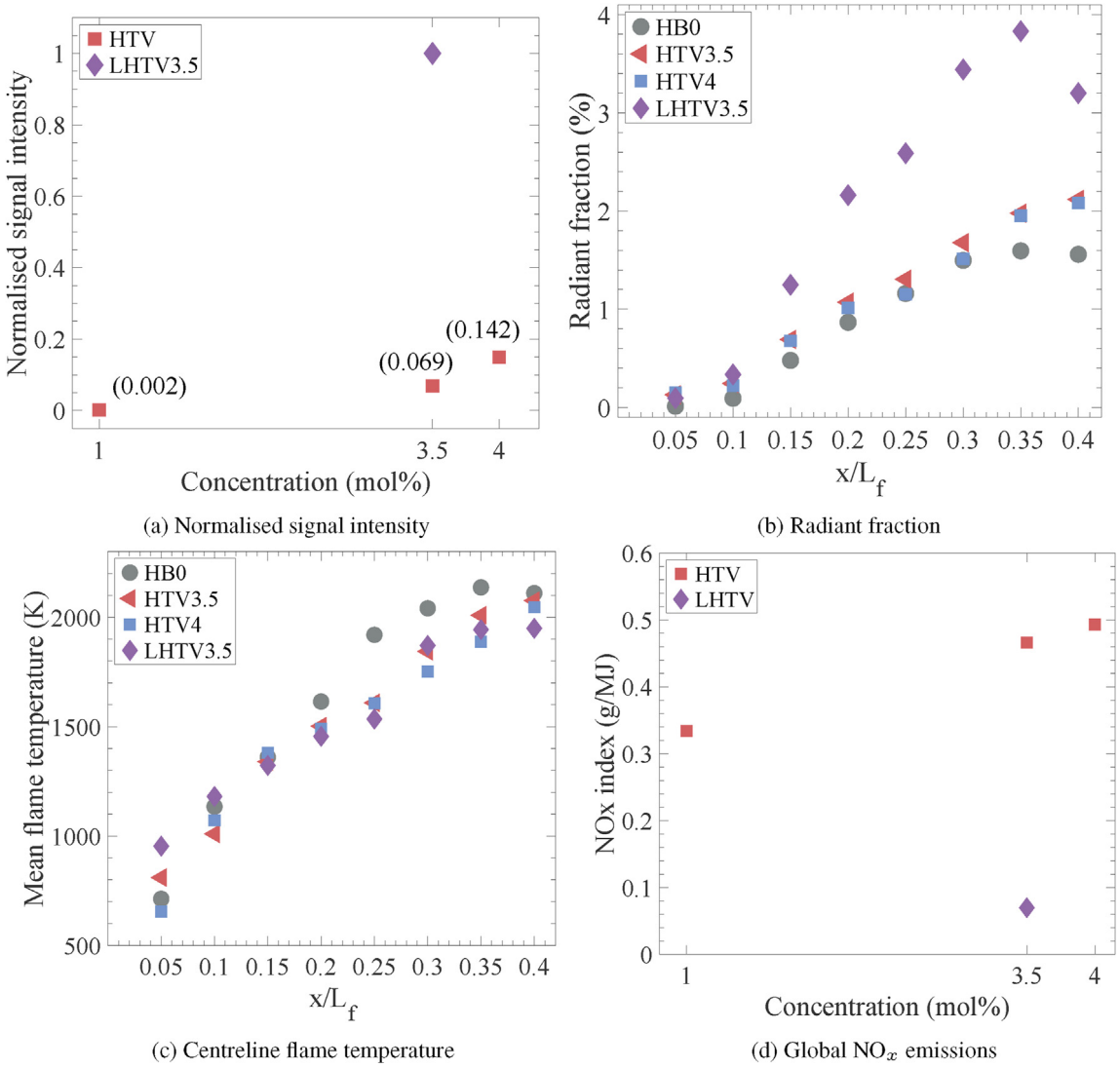

Fig. 12 – Flame characteristics of vapourised toluene-blended H_2/N_2 flames (HTV1, HTV3.5 and HTV4) and the 3.5 mol% vapourised toluene-blended H_2/N_2 flame with lower hydrogen concentration (LHTV3.5) described in Table 1. (12a) Normalised signal intensity from photographs. The signal intensity is normalised to the peak signal intensity among the vapourised toluene flames. (12b) Radiant fraction from $x/L_f = 0.05 - 0.4$. (12c) Mean axial flame temperature along the centreline of the flames. The results are corrected for radiative heat loss from the thermocouple. (12d) Global NO_x emissions.

Fig. 12d reports the global EI_{NO_x} of higher concentration vapourised toluene-blended H_2/N_2 flames. The emission index for NO_x increases by 40% from 1 to 3.5 mol% vapourised toluene blends, and further increases by 6% from 3.5 to 4 mol%. The increasing trend of EI_{NO_x} in higher concentration vapourised toluene blends is consistent with the lower concentration cases discussed in Section NOx emissions. As is shown in Fig. 8, the kinetic mechanism and dominating reaction pathways of NO formation in 3.5 and 4 mol% vapourised toluene blends are not dissimilar to the lower concentration cases, with one distinct exception that the ROP of NO formation through prompt route: $HCN + O \rightleftharpoons CH + NO$ reaction in 4 mol% toluene blends is 7 times greater than that in 0.2 mol% toluene blends. This implies that as the toluene concentration increases to 4 mol%, HCN radicals formed from CH and NCN routes are enhanced. Hence, NO formation through the prompt route has gradually become one of the primary reaction pathways in higher concentration toluene-blended H_2/N_2 flames.

As discussed in Section Introduction, adding hydrogen to hydrocarbon fuels reduces soot loading of the flame via three mechanisms: thermal effect, dilution effect, and chemical effect [11–13,16,59]. Therefore, an additional 7:3 H_2/N_2 flame case with lower hydrogen concentration, blended with 3.5 mol % vapourised toluene (LHTV3.5) was tested (see flame details in Table 1). It is also noted that the exit strain rate of the higher hydrogen concentration flame cases is above 20,000 s^{-1}, whereas the lower hydrogen flame case is only 12,800 s^{-1}. A high exit strain rate (low residence time) is known to inhibit soot formation as the key soot formation processes — surface growth and agglomeration require time [60]. The flame luminosity, radiant fraction, centreline flame temperature, and NO_x emission of the lower H_2 concentration flame (LHTV3.5) are presented in the figures along with the higher H_2

concentration flame (HTV3.5) for comparison. The signal intensity which indicated the flame luminosity in Fig. 11 shows that the 3.5% vapourised toluene-blended flame with low hydrogen concentration (LHTV3.5) is 15 times greater than the 3.5 mol% vapourised toluene blends with higher hydrogen concentration (HTV3.5). For radiant fraction enhancement, it is seen in Fig. 12b that the radiant fraction of the 3.5 mol% vapourised toluene blends with lower hydrogen concentration (LHTV3.5) increases the radiant fraction of the HB0 flame by 135% at $x/L_f = 0.35$. The results demonstrate the significant enhancement of flame luminosity and radiant intensity of the non-blended H_2/N_2 flame from reducing the hydrogen concentration with constant bulk mean Reynolds number and toluene concentration. Additionally, the global NO_x emissions (Fig. 12d) decrease by 68% compared with the high hydrogen concentration 3.5% toluene blends. The reduced temperature inhibits the NO formation via the thermal route and the reduced H_2 concentration results in lesser H and OH radicals, which in turn inhibits the reaction pathways via the $OH + N \rightleftharpoons H + NO$ and $H + HNO \rightleftharpoons H_2 + NO$ routes.

Conclusions

The effect of biofuel blending with H_2/N_2 turbulent nonpremixed jet flames was investigated in this study. Both vapourised and sprayed biofuel surrogates are used and the flames' appearance, flame luminosity, radiant intensity, centreline flame temperature, and NO_x emissions are investigated through combined experimental and numerical methods. Based on experimental observations and numerical results, the following conclusions are made:

1. Soot starts to form in the 1 mol% spray toluene and anisole blends between $x/L_f = 0.4 - 0.8$. Blending higher concentrations (3.5 and 4 mol%) vapourised toluene to H_2/N_2 flames results in a clear transition into a sooting flame. The flame luminosity of the 3.5 mol% toluene flame is 34 times greater than the 1 mol% toluene flame. The radiant fraction of the 4 mol% vapourised toluene flame at $x/L_f = 0.4$ is increased by 33% compared with the 1 mol% toluene flame.
2. Introducing biofuel surrogates in liquid droplets to H_2/N_2 flames has demonstrated its advantages in promoting soot formation by creating a local fuel-rich condition. Vapourised flames are more luminous and display a higher radiant fraction near the jet exit as the vapourised biofuels facilitate the mixing with H_2 and actively participate in the oxidation reactions, while sprayed biofuel surrogates first require energy for phase change. The centreline flame temperature in spray flames is lower due to the enthalpy of vapourisation, which in turn favours the formation of soot precursors. The NO_x emission from 1 mol% spray biofuel surrogate blended flames is lower than vapourised flames since the lower temperature in spray flames reduces thermal NO_x formation.
3. Both experimental and numerical results show that the global NO_x emissions from the turbulent nonpremixed H_2/N_2 flame increase with biofuel surrogate addition. The numerical simulation shows that the primary NO formation reaction pathways are the subset of the thermal route: $OH + N \rightleftharpoons H + NO$ and prompt route: $CH + N_2 \rightleftharpoons H + NCN$, with HNO-intermediate route: $H + HNO \rightleftharpoons H_2 + NO$ also contributing. The addition of biofuel surrogates mainly enhances NO_x formation via thermal and prompt routes, leading to the increase in global NO_x emission.
4. High hydrogen concentration of the turbulent nonpremixed hydrogen-based flames has a major inhibition effect on soot formation and corresponding radiative heat flux. As the hydrogen concentration decreases from 90% to 70% in the H_2/N_2 mixture, while Reynolds number (10,000) and toluene concentration (3.5 mol%) are kept constant, the radiant fraction of the LHTV3.5 flame is increased by 115% at $x/L_f = 0.35$, compared with the HTV3.5 flame. The global NO_x emissions of the LHTV3.5 flame case decrease by 68% compared with the HTV3.5 flame case. The global NO_x emissions from both the LHTV3.5 and HTV3.5 flame cases are lower than the non-blended H_2/N_2 (HB0) flame case. The elevated radiative heat loss reduces the flame temperature in the LHTV3.5 flame case, which in turn inhibits the NO formation via the thermal route.

The key findings in this paper further contribute to the understanding of biofuel-blended hydrogen flames, revealing that hydrogen concentration in the fuel mixture and exit strain rate may be dominating in enhancing flame luminosity and radiant heat flux, compared with other factors (e.g., the chemical structure of additive). It is also highlighted that the NO_x emissions increase with biofuel addition via the subset of the thermal route and prompt route, which is another potential challenge in evaluating the feasibility of biofuel-blended hydrogen flames.

Declaration of competing interest

The authors declare that they have no known competing financial interests or personal relationships that could have appeared to influence the work reported in this paper.

Acknowledgements

The research reported in this publication was supported by funding from the University of Adelaide, the Australian Research Council (ARC), and the Future Fuels Cooperative Research Centre (CRC). The assistance with the experimental work from Jason Peak, Kae Ken Foo, Adam John Gee, and Douglas Proud is acknowledged.

REFERENCES

[1] Dodds PE, Staffell I, Hawkes AD, Li F, Grünewald P, McDowall W, et al. Hydrogen and fuel cell technologies for heating: a review. Int J Hydrogen Energy 2015;40:2065–83.
[2] Kitagawa T, Nakahara T, Maruyama K, Kado K, Hayakawa A, Kobayashi S. Turbulent burning velocity of hydrogen–air premixed propagating flames at elevated pressures. Int J Hydrogen Energy 2008;33:5842–9.

[3] Nag S, Sharma P, Gupta A, Dhar A. Experimental study of engine performance and emissions for hydrogen diesel dual fuel engine with exhaust gas recirculation. Int J Hydrogen Energy 2019;44:12163–75.
[4] Nowotny J, Veziroglu TN. Impact of hydrogen on the environment. Int J Hydrogen Energy 2011;36:13218–24.
[5] Yuan C, Han C, Liu Y, He Y, Shao Y, Jian X. Effect of hydrogen addition on the combustion and emission of a diesel free-piston engine. Int J Hydrogen Energy 2018;43:13583–93.
[6] Akal D, Öztuna S, Büyükakın MK. A review of hydrogen usage in internal combustion engines (gasoline-Lpg-diesel) from combustion performance aspect. Int J Hydrogen Energy 2020;45:35257–68.
[7] Kanth S, Debbarma S, Das B. Experimental investigations on the effect of fuel injection parameters on diesel engine fuelled with biodiesel blend in diesel with hydrogen enrichment. Int J Hydrogen Energy 2022;47:35468–83.
[8] Gürbüz H. Analysis of the effects of multiple injection strategies with hydrogen on engine performance and emissions in diesel engine. Int J Hydrogen Energy 2020;45:27969–78.
[9] Shadidi B, Najafi G, Yusaf T. A review of hydrogen as a fuel in internal combustion engines. Energies 2021;14:6209.
[10] Wang Y, Gu M, Zhu Y, Cao L, Zhu B, Wu J, et al. A review of the effects of hydrogen, carbon dioxide, and water vapor addition on soot formation in hydrocarbon flames. Int J Hydrogen Energy 2021;46:31400–27.
[11] Liu F, Ai Y, Kong W. Effect of hydrogen and helium addition to fuel on soot formation in an axisymmetric coflow laminar methane/air diffusion flame. Int J Hydrogen Energy 2014;39:3936–46.
[12] Wang Y, Gu M, Chao L, Wu J, Lin Y, Huang X. Different chemical effect of hydrogen addition on soot formation in laminar coflow methane and ethylene diffusion flames. Int J Hydrogen Energy 2021;46:16063–74.
[13] Guo H, Liu F, Smallwood GJ, Gülder ÖL. Numerical study on the influence of hydrogen addition on soot formation in a laminar ethylene–air diffusion flame. Combust Flame 2006;145:324–38.
[14] Ren F, Chu H, Xiang L, Han W, Gu M. Effect of hydrogen addition on the laminar premixed combustion characteristics the main components of natural gas. J Energy Inst 2019;92:1178–90.
[15] Li J, Huang H, Kobayashi N, He Z, Nagai Y. Study on using hydrogen and ammonia as fuels: combustion characteristics and NO_x formation. Int J Energy Res 2014;38:1214–23.
[16] Kalbhor A, van Oijen J. Effects of hydrogen enrichment and water vapour dilution on soot formation in laminar ethylene counterflow flames. Int J Hydrogen Energy 2020;45:23653–73.
[17] Liu B, Liu X, Lu C, Godbole A, Michal G, Teng L. Decompression of hydrogen-natural gas mixtures in high-pressure pipelines: CFD modelling using different equations of state. Int J Hydrogen Energy 2019;44:7428–37.
[18] Clarke MC. Can the hydrogen economy concept be the solution to the future energy crisis? J. Multidiscip. Eng 2022;18:70–84.
[19] Evans MJ, Proud DB, Medwell PR, Pitsch H, Dally BB. Highly radiating hydrogen flames: effect of toluene concentration and phase. Proc Combust Inst 2021;38:1099–106.
[20] Agarwal AK. Biofuels (alcohols and biodiesel) applications as fuels for internal combustion engines. Prog Energy Combust Sci 2007;33:233–71.
[21] Bäckström D, Johansson R, Andersson K, Wiinikka H, Fredriksson C. On the use of alternative fuels in rotary kiln burners—an experimental and modelling study of the effect on the radiative heat transfer conditions. Fuel Process Technol 2015;138:210–20.
[22] Hutny W, Lee G. Improved radiative heat transfer from hydrogen flames. Int J Hydrogen Energy 1991;16:47–53.
[23] Gee AJ, Yin Y, Foo KK, Chinnici A, Smith N, Medwell PR. Toluene addition to turbulent H_2/natural gas flames in bluff-body burners. Int J Hydrogen Energy 2022;47:27733–46.
[24] Gholizadeh M, Hu X, Liu Q. A mini review of the specialties of the bio-oils produced from pyrolysis of 20 different biomasses. Renew Sustain Energy Rev 2019;114:109313.
[25] Czernik S, Bridgwater A. Overview of applications of biomass fast pyrolysis oil. Energy Fuels 2004;18:590–8.
[26] Mohan D, Pittman Jr CU, Steele PH. Pyrolysis of wood/biomass for bio-oil: a critical review. Energy Fuels 2006;20:848–89.
[27] Rana R, Nanda S, Meda V, Dalai A, Kozinski J. A review of lignin chemistry and its biorefining conversion technologies. J. Biochem. Eng. Bioprocess. Technol. 2018;1:2.
[28] Cho S-M, Kim J-H, Kim S-H, Park S-Y, Kim J-C, Choi I-G. A comparative study on the fuel properties of biodiesel from woody essential oil depending on terpene composition. Fuel 2018;218:375–84.
[29] Yin Y, Medwell PR, Gee AJ, Foo KK, Dally BB. Fundamental insights into the effect of blending hydrogen flames with sooting biofuels. Fuel 2023;331:125618.
[30] Zeldvich Y. The oxidation of nitrogen in combustion and explosions. J. Acta Physicochimica 1946;21:577.
[31] Frassoldati A, Faravelli T, Ranzi E. A wide range modeling study of nox formation and nitrogen chemistry in hydrogen combustion. Int J Hydrogen Energy 2006;31:2310–28.
[32] Skottene M, Rian KE. A study of NO_x formation in hydrogen flames. Int J Hydrogen Energy 2007;32:3572–85.
[33] Hashimoto N, Nishida H, Ozawa Y, Iwatsubo T, Inumaru J. Influence of type of burner on NO_x emission characteristics from combustion of palm methyl ester. Int. J. Chem. Mol. Eng. 2009;3:570–4.
[34] McEnally CS, Pfefferle LD. Sooting tendencies of oxygenated hydrocarbons in laboratory-scale flames. Environ Sci Technol 2011;45:2498–503.
[35] Narayanaswamy K, Pitsch H, Pepiot P. A component library framework for deriving kinetic mechanisms for multi-component fuel surrogates: application for jet fuel surrogates, Combust. Flame 2016;165:288–309.
[36] Szymkowicz PG, Benajes J. Development of a diesel surrogate fuel library. Fuel 2018;222:21–34.
[37] Nowakowska M, Herbinet O, Dufour A, Glaude P-A. Detailed kinetic study of anisole pyrolysis and oxidation to understand tar formation during biomass combustion and gasification. Combust Flame 2014;161:1474–88.
[38] Rahman SA, Van TC, Hossain F, Jafari M, Dowell A, Islam M, et al. Fuel properties and emission characteristics of essential oil blends in a compression ignition engine. Fuel 2019;238:440–53.
[39] Lang RJ. Ultrasonic atomization of liquids. J Acoust Soc Am 1962;34:6–8.
[40] Qamar N, Nathan G, Alwahabi Z, King K. The effect of global mixing on soot volume fraction: measurements in simple jet, precessing jet, and bluff body flames. Proc Combust Inst 2005;30:1493–500.
[41] Kent J, Bastin S. Parametric effects on sooting in turbulent acetylene diffusion flames. Combust Flame 1984;56:29–42.
[42] Faravelli T, Frassoldati A, Ranzi E. Kinetic modeling of the interactions between NO and hydrocarbons in the oxidation of hydrocarbons at low temperatures. Combust Flame 2003;132:188–207.

[43] Glaude PA, Pitz WJ, Thomson MJ. Chemical kinetic modeling of dimethyl carbonate in an opposed-flow diffusion flame. Proc Combust Inst 2005;30:1111–8.
[44] Dayma G, Sarathy S, Togbé C, Yeung C, Thomson M, Dagaut P. Experimental and kinetic modeling of methyl octanoate oxidation in an opposed-flow diffusion flame and a jet-stirred reactor. Proc Combust Inst 2011;33:1037–43.
[45] Liu X, Wang H, Yao M. Experimental and modeling investigations on soot formation of ethanol, n-butanol, 2, 5-dimethylfuran, and biodiesel in diesel engines. Energy Fuels 2017;31:12108–19.
[46] Rutkowski L, Khodabakhsh A, Johansson AC, Valiev DM, Lodi L, Qu Z, et al. Measurement of H_2O and OH in a flame by optical frequency comb spectroscopy. CLEO: Sci Innovat 2016:SW4H.8.
[47] Buch R, Hamins A, Konishi K, Mattingly D, Kashiwagi T. Radiative emission fraction of pool fires burning silicone fluids. Combust Flame 1997;108:118–26.
[48] Andersson K, Johansson R, Johnsson F. Thermal radiation in oxy-fuel flames. Int J Greenh Gas Control 2011;5:S58–65.
[49] Park SH, Lee KM, Hwang CH. Effects of hydrogen addition on soot formation and oxidation in laminar premixed C_2H_2/air flames. Int J Hydrogen Energy 2011;36:9304–11.
[50] Dong X, Nathan GJ, Mahmoud S, Ashman PJ, Gu D, Dally BB. Global characteristics of non-premixed jet flames of hydrogen–hydrocarbon blended fuels. Combust Flame 2015;162:1326–35.
[51] Turns SR, Myhr FH. Oxides of nitrogen emissions from turbulent jet flames: Part I—fuel effects and flame radiation. Combust Flame 1991;87:319–35.
[52] Bozzelli JW, Dean AM. O + NNH: A possible new route for NO_x formation in flames. Int J Chem Kinet 1995;27:1097–109.
[53] Wielgosiński G. Pollutant formation in combustion processes. Adv Chem Eng 2012:295–324.
[54] Glarborg P, Miller JA, Ruscic B, Klippenstein SJ. Modeling nitrogen chemistry in combustion. Prog Energy Combust Sci 2018;67:31–68.
[55] Chen C-H, Li Y-H. Role of N_2O and equivalence ratio on NO_x formation of methane/nitrous oxide premixed flames. Combust Flame 2021;223:42–54.
[56] Wagnon SW, Thion S, Nilsson EJ, Mehl M, Serinyel Z, Zhang K, et al. Experimental and modeling studies of a biofuel surrogate compound: laminar burning velocities and jet-stirred reactor measurements of anisole. Combust Flame 2018;189:325–36.
[57] Fu X, Aggarwal SK. Fuel unsaturation effects on NO_x and PAH formation in spray flames. Fuel 2015;160:1–15.
[58] Rahman SA, Mahila T, Ahmad A, Nabi MN, Jafari M, Dowell A, et al. Effect of oxygenated functional groups in essential oils on diesel engine performance, emissions, and combustion characteristics. Energy Fuels 2019;33:9828–34.
[59] Gülder Ö, Snelling D, Sawchuk R. Influence of hydrogen addition to fuel on temperature field and soot formation in diffusion flames. Symp. (Int.) Combust. 1996;26:2351–8.
[60] Mueller ME, Chan QN, Qamar NH, Dally BB, Pitsch H, Alwahabi ZT, et al. Experimental and computational study of soot evolution in a turbulent nonpremixed bluff body ethylene flame. Combust Flame 2013;160:1298–309.

Chapter 6

Needle spray burner imaging and characterisation using commercial photographic equipment

6.1 Introduction

6.1.1 Motivation of spray burner characterisation

As presented in Chapters 4 and 5, introducing 0.2–1 mol% liquid biofuels to hydrogen-based flames by prevapourisation and ultrasonic spray has a moderate impact on the radiant heat flux and luminosity enhancement of hydrogen flames. Therefore, a needle spray burner has been developed to analyse the effect of adding gas-assist atomised biofuels to hydrogen flames on combustion characteristics.

It is essential to characterise the spray burner under non-reacting flow conditions as it not only contributes to the understanding of the breakup mechanisms and resultant spray morphology, but also to the analysis of their impact on the combustion characteristics (e.g. flame appearance and radiant intensity) of biofuel/hydrogen flames. In addition, spray burner characterisation under non-reacting flow conditions also benefits the safe operation of establishing biofuel/hydrogen flames on the burner. The working range of the spray burner has been identified and presented in §3.3.1 and the non-reacting flow cases of interest are chosen for further evaluation using microscopic shadowgraphy imaging in this chapter.

6.1.2 Overview of spray characteristics and influencing factors

The macroscopic and microscopic characteristics of spray flows have been widely studied, including the breakup length of the liquid core, dispersed phase area fraction, droplet size, and spray pattern. These spray characteristics are affected by a series of contributing factors and influencing parameters, namely the velocity differential between the fluid medium and the ambient gas, the physical properties of the liquid (e.g. surface tension, viscosity, and density), physical properties of the surrounding gas [1–4].

Various non-dimensional parameters such as Weber number, gas-to-liquid (GLR) momentum flux ratio, Reynolds number, and velocity ratio have been employed to describe and predict the spray characteristics. The liquid jet velocity (i.e. liquid jet-Reynolds number) impact on the spray structures of acetone and ethanol has been conducted in a coaxial needle spray burner. The results show that the initiation of surface instabilities and their wavelength are greatly influenced by the liquid jet velocity [5]. The dependence of droplet size on Weber number has been investigated in a pressurised chamber (4 bar) with a preheated air coflow, showing that droplet diameter decreases from 100–200 µm to 15–30 µm as the Weber number increases [4].

Previous studies have highlighted that an increase in gas-to-liquid mass flow ratio leads to a decrease in droplet size. The results from air-assist atomised water spray on twin-fluid atomisers suggest that the Sauter mean diameter (SMD) of droplets decreases from 130 µm to 50 µm as the GLR mass flow ratio increases from 2.5% to 5% [1]. Similarly, the decrease of SMD (from 100 µm to 20 µm) with the increase of GLR mass flow ratio (from 0.25 to 1) was observed in air-assist water atomisation on a counterflow nozzle [6]. A comprehensive review of the influencing parameters on spray structures from both experimental and numerical studies presented an inverse correlation between the gas/liquid momentum flux ratio and the liquid core length, and a higher Weber number and Reynolds number led to finner sprays [7]. Though these studies have reported the impact of non-dimensional parameters on spray performance, the dominant non-dimensional parameters of specific spray characteristics are not well understood due to the lack of comprehensive comparisons among the effect of various non-dimensional parameters on spray characteristics.

The properties of the carrier gas play an important role in gas-assist atomisation. A comparison of using air, nitrogen, argon, and carbon dioxide as the carrier gas for gas-assist atomisation on a swirl burner at constant mass

and momentum flux control reveals that gases with smaller density (i.e. air and nitrogen) generate smaller droplets and higher number density than denser gases (i.e. argon and carbon dioxide) [8, 9]. However, most studies focused on using air as the carrier gas for various liquid atomisation. There is a lack of understanding regarding the influence of using different gases, particularly very light gases such as helium and hydrogen, as carrier gases with varying parameters on spray characteristics.

6.1.3 Spray diagnostics

To investigate the spray characteristics with minimum disturbance of the multi-phase flow, various types of non-intrusive optical diagnostics with high temporal and spatial resolutions are demanded. Benefiting from the development of laser technology, laser Doppler velocimetry (LDV) and phase Doppler particle anemometry (PDPA) have been prevalent in the measurement of droplet velocities and sizes. However, a known limitation of LDV/PDPA is the measurement of non-spherical droplets—large ligaments and irregular objects in low Weber number ($We < 20$) spray regions where the liquid jet core is still largely intact [10, 11]. This limitation can be compensated by using the shadowgraph imaging technique, which has been widely employed to visualise spray features (e.g. shock waves, flow patterns, and density gradients) at different regions due to the relative simplicity [11–14].

In the shadowgraph setup, a light source illuminates the flow from one side. The light interacts with the spray, such that an image of the flow structure is captured on the opposite side of the source by a detector. Lasers and high-speed cameras are commonly used as the incident light source and the detector, respectively. Microscopes can be equipped to magnify the microscopic characteristics of near-field spray structures. The early shadowgraph setup employed an electronic circuit with a short duration to "freeze" the motion of the flow and a camera to capture the interacted light with limited reports on the details regarding the resolution and limitations [15]. The light source was then replaced by lasers and the detector was replaced by high-speed scientific-grade cameras to achieve shorter exposure time for motion blur reduction and time-resolved images [16].

The optical setup involving the use of lasers may increase the cost, the safety risks (e.g. eye and skin injuries), and the complexity of experimental setup and alignment. With the development of digital single-lens-reflex (DSLR) cameras and electronic flash technologies, a digital photographic camera available commercially is usually cost-effective and has better resolution than

similarly priced scientific-grade cameras. An electronic flash is used to set up and align with the DSLR camera to "freeze" the motion of the flow. This optical setup has advantages in cost, spatial resolution, simplicity, and lower safety risks, while minimising the trade-off in performance.

6.1.4 Chapter outline

In this chapter, a microscopic shadowgraph imaging technology using a commercial camera and electronic flash is explored to characterise multi-phase non-reacting spray flows on a concentric needle spray burner. Helium is chosen as a low-density carrier gas to compare with air for the gas-assist atomisation of water in order to evaluate the impact of different carrier gases on spray characteristics. The macroscopic and microscopic characteristics of the air/water and helium/water spray flows are presented, including the breakup lengths of the liquid core, the characteristic major length of droplets and ligaments, the area fraction, and the wavelength of the wave structure. The non-dimensional parameters, namely the liquid-to-gas velocity ratio, momentum flux ratio, mass flow ratio, volumetric flow ratio, Reynolds number ratio, and Weber number are correlated with the measured spray characteristics to analyse the dominant influencing non-dimensional parameters of specific spray characteristics. The advantages, limitations, and uncertainties of this diagnostic configuration are evaluated and reported. The findings in this chapter contribute to the understanding of the effect of using different carrier gases for gas-assist atomisation and the appropriate influencing non-dimensional parameters for the prediction and description of gas-assist spray performance.

6.2 Methodology

6.2.1 Burner configuration

A concentric needle spray burner, shown schematically in Figure 6.1, utilises the airblast effect to atomise liquid flow. There are three streams designed for this burner—a liquid fuel stream, a gaseous fuel stream, and a coflow stream. The liquid flow is issued from a central dispensing needle (L = 300 mm, ID = 603 µm, OD = 908 µm), which is concentrically inserted in a jet with a 6.1 mm internal diameter to supply gaseous fuel. The outermost stainless tube with 30 mm ID serves as a coflow. The dispensing needle is connected to the liquid stream inlet via a Luer lock connection.

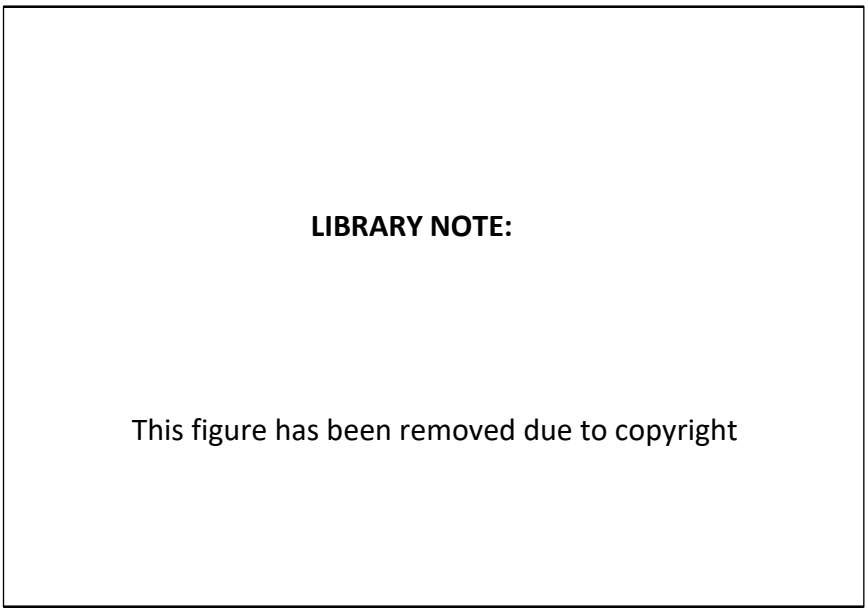

6.2.2 Flow cases

Turbulent non-reacting spray flows were established on the needle spray burner. In the gas-assist atomisation process, air and helium were used separately to atomise water ejected from the needle. The carrier gas bulk mean velocities for air and helium were investigated across the range from 30 m/s to 110 m/s, in 10 m/s increments. The air velocity was chosen to start from 30 m/s as a reference gas case to attain a Reynolds number of 10,000, hence the gas flow was in turbulent conditions. The bulk mean velocity was kept constant for helium for comparison. The flow cases with 10 m/s increments in bulk mean velocity are presented because clearer changes in spray characteristics were observed. The water bulk mean velocities were tested at 0.4 m/s, 0.8 m/s, and 1.2 m/s. In total, the microscopic shadowgraphs of 60 different flow cases were collected. The water flow rate was controlled by a rotameter (ABB), with the manufacturer-specified total error within 8% for the flow rates tested in this work. Mass flow controllers (Alicat) were employed to control the air and helium flow rate, with a manufacturer-specified uncertainty of $\pm$0.5% of reading and $\pm$0.2% of full scale. The mass flow controllers and the rotameter were calibrated prior to the experiment. The test conditions of 60 reported cases are shown in Table 6.1. The velocity, Reynolds number, Weber number, momentum flux, mass flow, and volumetric flow reported in this chapter are all bulk mean values. The calculation of these parameters is described in §6.3.3.

Table 6.1: Test conditions for the cases studied, including air or helium bulk mean velocity (U_g m/s), water bulk mean velocity (U_l m/s), bulk mean Reynolds number for carrier gas—air (Re_A), carrier gas—helium (Re_H), gas/liquid velocity ratio (ψ_U), air/liquid momentum flux ratio (ψ_{p_A}), helium/liquid momentum flux ratio (ψ_{p_H}), exit Weber number (We) for air/water and helium/water flows.

Cases	U_g	U_l	Re_A	Re_H	ψ_U	ψ_{p_A}	ψ_{p_H}	We_A	We_H
W0.4(A/H)030	30	0.4	10000	1300	75	6.8	0.9	9	1
W0.4(A/H)040	40	0.4	13400	1800	100	12.0	1.7	15	2
W0.4(A/H)050	50	0.4	16700	2200	125	18.8	2.6	25	3
W0.4(A/H)060	60	0.4	20100	2600	150	27.1	3.7	35	5
W0.4(A/H)070	70	0.4	23400	3100	175	36.9	5.1	48	7
W0.4(A/H)090	90	0.4	30100	4000	225	60.9	8.4	80	11
W0.4(A/H)110	110	0.4	36800	4800	275	91.0	12.6	120	17
W0.8(A/H)030	30	0.8	10000	1300	38	1.7	0.2	9	1
W0.8(A/H)040	40	0.8	13400	1800	50	3.0	0.4	15	2
W0.8(A/H)050	50	0.8	16700	2200	63	4.7	0.7	25	3
W0.8(A/H)060	60	0.8	20100	2600	75	6.8	0.9	35	5
W0.8(A/H)070	70	0.8	23400	3100	88	9.2	1.3	48	7
W0.8(A/H)090	90	0.8	30100	4000	113	15.2	2.1	80	11
W0.8(A/H)110	110	0.8	36800	4800	138	22.8	3.1	120	17
W1.2(A/H)030	30	1.2	10000	1300	25	0.8	0.1	9	1
W1.2(A/H)040	40	1.2	16700	1800	33	1.3	0.2	15	2
W1.2(A/H)050	50	1.2	16700	2200	42	2.1	0.3	25	3
W1.2(A/H)060	60	1.2	20100	2600	50	3.0	0.4	35	5
W1.2(A/H)070	70	1.2	23400	3100	58	4.1	0.6	48	7
W1.2(A/H)090	90	1.2	30100	4000	75	6.8	0.9	80	11
W1.2(A/H)110	110	1.2	36800	4800	92	10.1	1.4	120	17

6.2.3 Diagnostics

Microscopic shadowgraphy using commercial equipment was employed to investigate the spray characteristics of the coaxial needle spray burner. The optical setup is illustrated in §3.4.5.1.

6.2.4 Spatial detection limit of moving objects

In addition to the uncertainties described in the image processing section in §3.4.5.2, there is a minimum exposure time required to measure moving objects with a certain size without motion blur. Since the minimum exposure time of the current optical setup is limited by the electronic flash at 15 ± 2 µs and can not be further reduced, the spatial detection limit of this optical setup varies when measuring moving objects at various velocities without motion blur. The velocity-dependent spatial detection limit for the worst-case scenario is calculated and presented in Table 6.2. The objects are assumed to move at the same velocity as the bulk mean carrier gas velocity. The percentage of motion blur in the flow cases was calculated based on the measured droplet

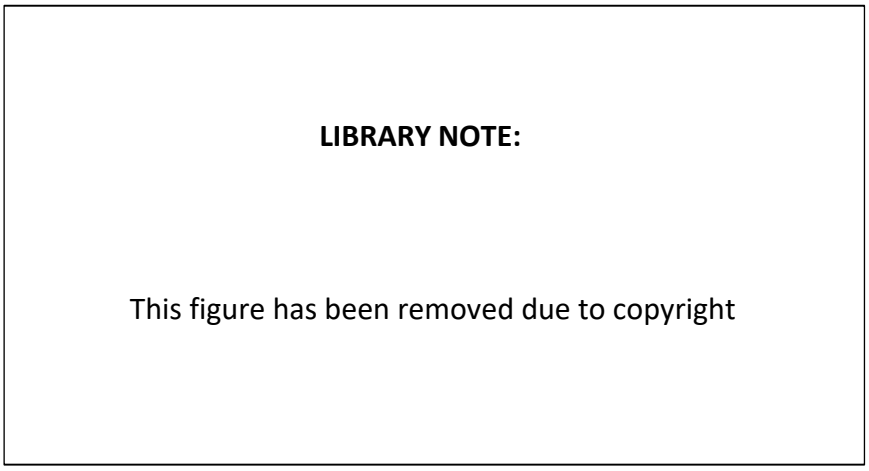

Figure 6.2: Motion blur percentage as a function of bulk mean velocity of measured flow cases described in Table 6.1.

characteristic length (ℓ_{max}) and corresponding spatial detection limit, and presented in Figure 6.2. The motion blur percentage increases as smaller objects move at higher U_g. The influence of motion blur on larger objects of interest is moderate in the current optical setup.

Table 6.2: The spatial detection limit of the optical setup at tested gas bulk mean velocities (U_g).

U_g m/s	Spatial detection limit mm
30	0.15
40	0.20
50	0.25
60	0.30
70	0.35
90	0.45
110	0.55

6.3 Results and discussion

6.3.1 Near-field spray structure classification

Microscopic backlit shadowgraphy is used to identify five typical characteristics, namely: (**A**) liquid core, (**B**) wave structure, (**C**) irregular object, (**D**) ligament, and (**E**) droplet. Features **A** and **B** describe the liquid stream as it is issued from the jet exit. Subsequently, fragments are formed (**C**–**E**), which

may be classified based on their aspect ratio (AR), characteristic major length (ℓ_{max}), and the initial liquid jet diameter (D_l) [10, 11, 17–20], as follows:

- Droplets ($\ell_{max} < D_l$ and AR < 3).
- Ligaments (AR > 3).
- Irregular objects (AR > 3, $\ell_{max} > D_l$).

The representative binarised shadowgraphs of flow cases W1.2H110 and W0.8A090 are shown in Figure 6.3 to present the five typical spray structures captured by microscopic shadowgraphy imaging. The W1.2H100 was chosen for its clear presentation of a liquid core and a wave-like structure, while other spray structures—irregular objects, ligaments, and droplets can be found in W0.8A090 which are typical representatives of the result of primary and secondary breakups. The liquid core (**A**) appears at the ejection of liquid flow and is attached to the jet exit ($x/D = 0$). The spray flow is subjected to Kelvin-Helmholtz instabilities and Rayleigh-Taylor instabilities as soon as it is injected into the gas flow with bulk mean velocity difference $U_g \gg U_l$; however, the liquid jet remains intact for a certain amount of time and distance due to liquid surface tension. The length of the intact liquid stream, i.e., liquid core (**A**) and wave structure (**B**), is usually termed breakup length as a major indicator of spray performance [21–23]. The wave structure (**B**) appears after the liquid core and before the primary breakup region as a result of deformation and disturbance developing on the liquid jet surface. The resultant oscillations form wave structures. The amplitude and frequency of the waves acquired from the shadowgraphs can be used for quantitative analysis of the liquid jet atomisation. As soon as the surface tension can no longer ensure the cohesion of the liquid jet, primary breakups occur and the liquid jet is disintegrated to form irregular objects (**C**), ligaments (**D**), and droplets (**E**). These elements are continuously subjected to aerodynamic forces and consequently break into self-stabilised small droplets—where the surface tension maintains the cohesion of the droplets. This process is referred to as the secondary breakup. The presence of a long-length liquid core and wave structure with the absence of ligaments and droplets generally indicates that the atomisation process is at an early stage or a pre-primary breakup stage. It may become coarse sprays or remain as liquid streams further downstream in the far-field region. The presence of a short-length liquid core, ligaments, and droplets in the near-field region, on the other hand, is an indication

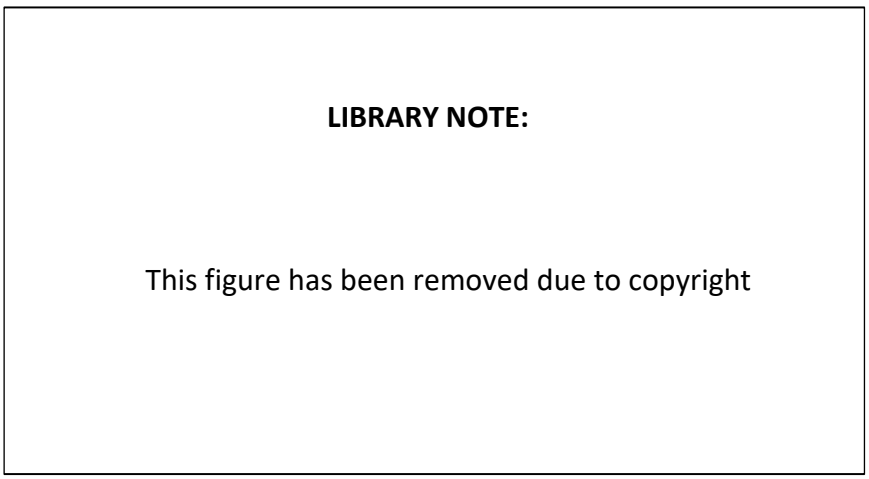

Figure 6.3: Representative binarised shadowgraphs of gas-assist water spray structure classification. A: Liquid core. B: Wave structure. C: Irregular object. D: Ligament. E: Droplet.

of primary and secondary breakup occurrence, generally leading to a finer spray in the far-field region.

It is observed in Figure 6.3 that not all five spray structures appear in the two different flow cases W1.2H110 and W0.8A090. For example, only the liquid core and wave structure are observed in the W1.2H110 case without any of the subsequent secondary breakup appearing within the field of view. One of the reasons is that the disintegration region of the liquid jet falls out of the FOV detected by the current microscopic shadowgraphy. Similarly, although the wave structure (**B**) of W0.8A090 is shorter than that of W1.2H110 and only has one complete cycle, the occurrence of the wave structure is ascribed to the same mechanism—oscillation.

6.3.2 Characterisation of near-field spray

The microscopic shadowgraphs of air/water and helium/water flow cases are presented in Figure 6.4 and Figure 6.5, respectively. One image that is the most representative of the typical spray characteristics for each flow case has been selected. The direct visualisation of the spray structures from Figure 6.4 indicates that, as the bulk mean air velocity increases while the liquid velocity remains constant, the liquid flow tends to break up into smaller fragments, thus a finer spray. In the low air velocity cases (i.e. W0.8A030 and W1.2A030), the liquid jet remains intact and a mild wave structure appears as a result of instabilities on the interface. As the air/water velocity ratio increases, the

breakup length is reduced and the liquid jet is elongated to form ligaments of large AR and large droplets (e.g. W0.4A030, W0.4A040, and W0.8A050). With the further increase in air/water velocity ratio, the AR of the ligaments and the droplet diameter are decreased but the number of smaller droplets is increased.

Helium was also tested as the carrier gas at the same gas/liquid bulk mean velocity ratio as the air/water flow cases. The microscopic shadowgraphs of helium/water flow cases shown in Figure 6.5 exhibit distinct near-field spray characteristics compared with air/water at the same velocity ratio. Unlike for air, there are no fragments observed in the flow cases where water velocities equal to 0.8 and 1.2 m/s with helium velocities varying from 30 to 110 m/s. The liquid jet in most of these flow cases remains in the shape of an undisturbed continuous liquid stream, except for W10.8H090, W0.8H110, and W1.2H110 where mild wave-like structures are observed, which implies that the velocity difference-induced influences on the interface are minimum. In addition, it is inferred from the oversized droplets ($\ell_{max} \gg D_l$) in W0.4H030, W0.4H040, and W0.4H050 that the liquid may be dripping from the needle exit because of the relatively low flow rate between the liquid and the ambient gas environment. According to Table 6.1, the bulk mean gas/liquid velocity ratio (ψ_U) is the same for air/water and helium/water flow cases, ranging from 25 to 138. However, the spray structures observed in helium/water flow cases indicate that the performance of gas-assist atomisation is weaker than that in air/water flow cases, even though the bulk mean gas/liquid velocity ratio is identical. This finding reveals that considering velocity ratio as the controlling parameter in gas-assist atomisation, which has been reported in some previous research, is not in itself appropriate without considering other parameters.

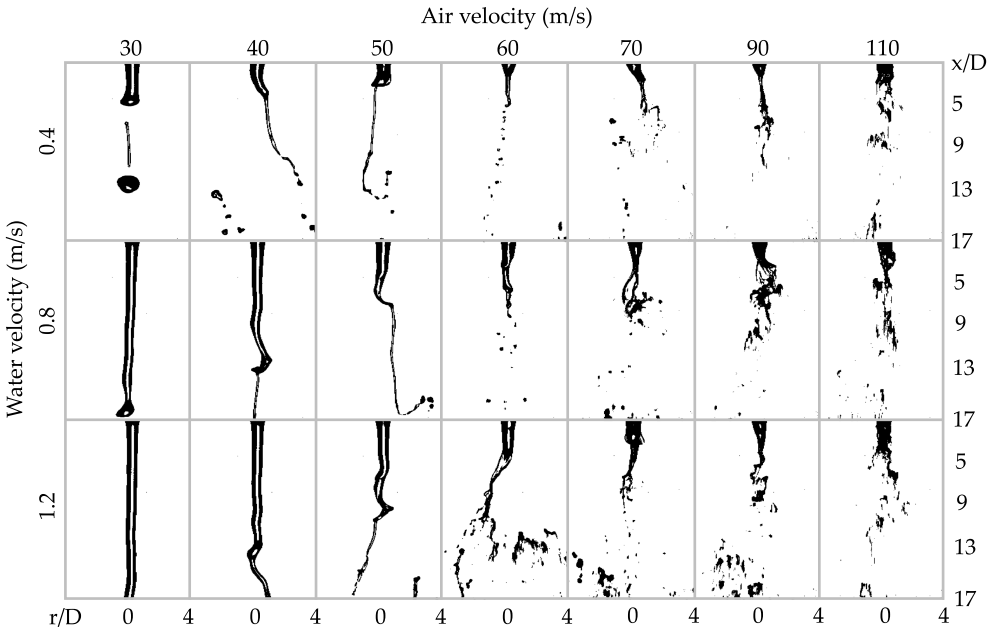

Figure 6.4: Representative microscopic shadowgraphs for the near-field (x/D = 0–17) spray characteristics of air/water flow cases described in Table 6.1.

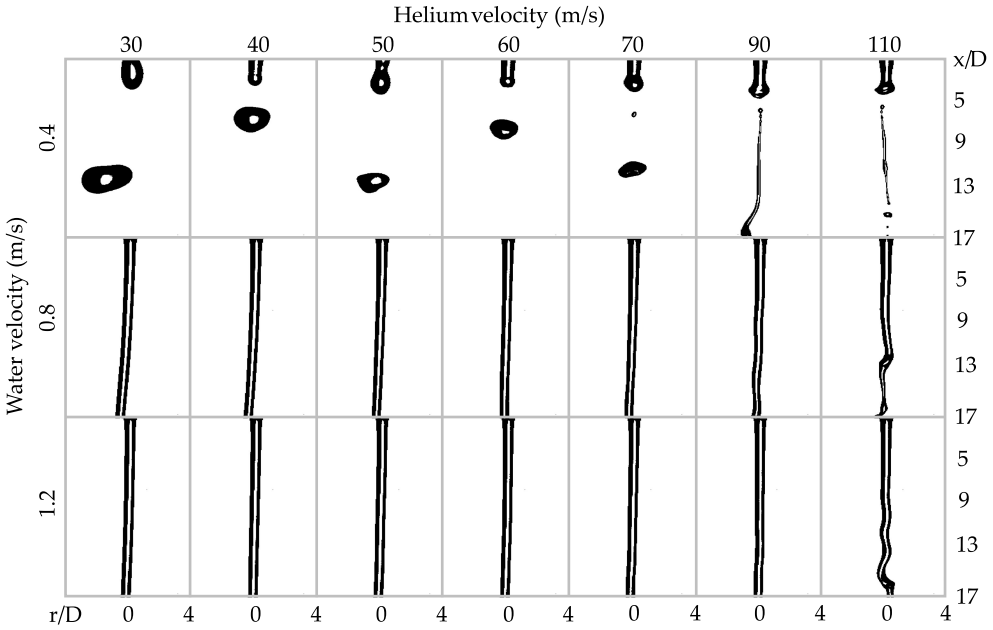

Figure 6.5: Representative microscopic shadowgraphs for the near-field (x/D = 0–17) spray characteristics of helium/water flow cases described in Table 6.1.

6.3.3 Influencing parameters for spray atomisation

The major non-dimensional influencing parameters for spray atomisation that have been studied in this research include gas/liquid bulk mean velocity ratio (ψ_U), gas/liquid momentum flux ratio (ψ_p), exit Weber number (We), gas/liquid bulk mean Reynolds number ratio (ψ_{Re}), gas/liquid mass flow ratio ($\dot{m}_g/\dot{m}_l$), gas/liquid volumetric flow ratio ($\dot{V}_g/\dot{V}_l$), and Ohnesorge number (Oh). The definitions and equations for these non-dimensional parameters are shown in §2.6.3.2.

To evaluate the influencing parameters for gas-assist liquid atomisation, key features of the spray characteristics are extracted from the microscopic shadowgraphs, including breakup length, the characteristic major length (ℓ_{max}) of droplets and ligaments, and the area fraction (A_S/A_T) of the spray objects occupied area to the total area (FOV).

6.3.3.1 Evolution of liquid core

The evolution of the liquid core morphology in various flow cases is captured in Figure 6.4 and Figure 6.5. From direct visualisation, the breakup length shortens with the increase in slip velocity for the same type of gas/liquid flows. The liquid jet is subjected to oscillation from the high-speed gas stream, hence the liquid core is turned into a wave-like structure. In some flow cases, e.g., W0.4A040, W0.4A060, and W0.4A090, the liquid core is further elongated and forms a tapered shape. The occurrence of the tapered shape is a transition from the liquid core to the formation of ligaments with larger AR.

The breakup length is commonly used as an indicator of the performance of liquid atomisation—a shorter breakup length usually indicates a finer spray, whereas a longer breakup length indicates a coarse spray [24]. The breakup length of different flow cases is extracted from long-exposure (2 s) shadowgraphs. The breakup length of various flow cases as a function of non-dimensional parameters is presented in Figure 6.6, including bulk mean gas/liquid velocity ratio, gas/liquid momentum flux ratio, exit Weber number, Reynolds number ratio, gas/liquid mass flow ratio, and volumetric flow ratio. The results show that the breakup lengths of air/water sprays increase from 0.42 mm to larger than the longitudinal field of view (>10.4 mm) as the gas/liquid momentum flux ratio decreases from 91 to 3. The breakup lengths of helium/water sprays exceed the detection limit of the setup (>10.4 mm) when the gas/liquid momentum flux ratio is below 3. The flow cases that show intact liquid core within the field of view visually seem to maintain

a liquid stream into the far-field region and unsuccessful gas-assist liquid atomisation. The decrease in the breakup lengths becomes insensitive to the gas/liquid momentum flux ratio as the gas/liquid momentum flux ratio reaches 27, given that the breakup length only decreases from 0.54 mm to 0.42 mm as the gas/liquid momentum flux ratio increases from 27 to 91.

The results shown in Figure 6.6 further underpin the observation concluded from the direct visualisation of the shadowgraphs that the gas/liquid bulk mean velocity ratio (ψ_U) may not be an appropriate non-dimensional parameter for the prediction and characterisation of atomisation performance, particularly among different types of carrier gas. For example, at the same ψ_U value of 50, the breakup length of W1.2A060 (2.3 mm) is distinct from W0.8A040 (4.5 mm) where the air is used as the carrier gas in both flow cases. Furthermore, replacing air with helium for gas-assist atomisation at a constant ψ_U value of 50, the breakup length of W0.8H040 exceeds the measurement limit, indicating poor atomisation performance compared with the air-assist flow cases. Among the reported non-dimensional parameters, it is evident that the gas/liquid momentum flux ratio (ψ_p) is the dictating factor to describe the breakup length of the spray, as for a constant value of ψ_p, the gas-assist atomisation tends to form similar breakup length across different flow conditions and gas types. One of the major differences between using helium or air as the carrier gas is the large density difference—the density of air (1.2 kg/m^3) is approximately seven times greater than helium (0.17 kg/m^3) at normal temperature and pressure (NTP). As the air is replaced by helium, the resultant increase in the liquid-to-gas density ratio leads to a lower level of turbulence persisting within the liquid core in the near-field region [25]. The momentum flux ratio includes this difference in its calculation and hence reflects its influence on the breakup length. There are eleven flow cases that displayed breakup lengths exceeding the measurement limit, namely W1.2A030, W0.8H030–W0.8H070, and W1.2H030–W1.2H070. Their ψ_U values are within the lowest range of tested flow cases, typically below 1.0 according to Table 6.1. It is also noted that the breakup length for the different flow cases follows a more consistent trend when plotted as a function of exit Weber number (We) and the bulk mean Reynolds number ratio (ψ_{Re}). In contrast, the mass and volumetric flow ratio show more variability.

A consistent trend is observed in Figure 6.6 that at a constant liquid momentum flux, the breakup length decreases with the increase in gas/liquid momentum flux ratio. For example, in W0.4A040 and W0.4A050, the breakup

length decreases by 30% (from 1 mm to 0.7 mm) as the air/water momentum flux ratio increases by 58% (from 12 to 19). The decreasing rate of the breakup length becomes lower as the air/water momentum flux ratio approaches a higher level—as the air/water momentum flux ratio increases from 61 to 91 (i.e. by 50%), the breakup length decreases from 0.44 mm to 0.42 mm (5% decrease). The asymptotic relationship is attributed to the liquid jet immediately breaking up when injected into the gas flow, such that the breakup length in high ψ_p multi-phase flows converges to a value at a certain momentum flux ratio.

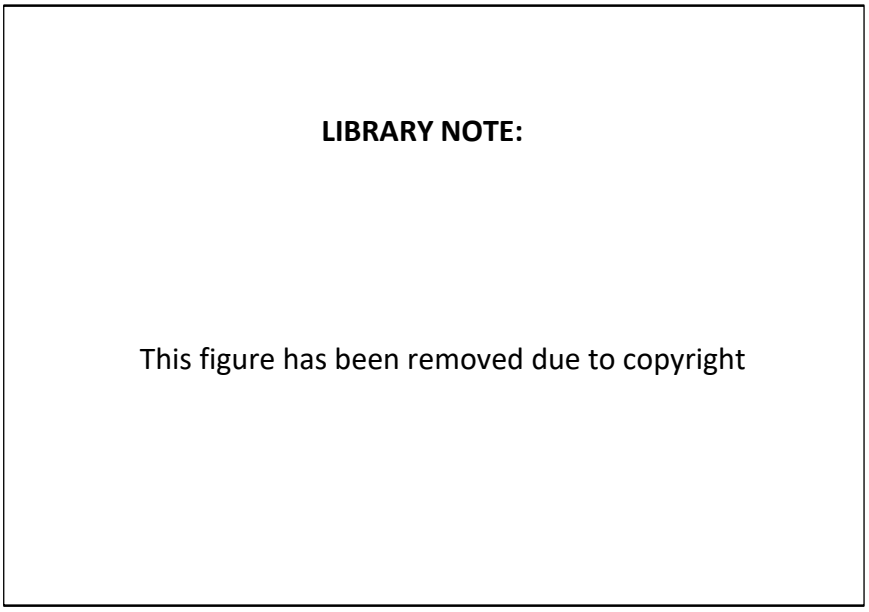

Figure 6.6: Breakup length as a function of non-dimensional parameters extracted from the long-exposure microscopic shadowgraphs of various flow cases described in Table 6.1. The non-dimensional parameters include bulk mean gas/liquid velocity ratio (ψ_U), gas/liquid momentum flux ratio (ψ_p), exit Weber number (We), gas/liquid Reynolds number ratio (ψ_{Re}), gas/liquid mass flow ratio ($\dot{m}_g/\dot{m}_l$), and gas/liquid volumetric flow ratio ($\dot{V}_g/\dot{V}_l$).

6.3.3.2 Droplet evolution

The characteristic major length (ℓ_{max}) is used to indicate the size of the droplets identified in the microscopic shadowgraphs of various flow cases, following the criterion described in §6.3.1. The obtained mean ℓ_{max} of droplets as a function of ψ_U, ψ_p, We, ψ_{Re}, $\dot{m}_g/\dot{m}_l$, and $\dot{V}_g/\dot{V}_l$ is presented in Figure 6.7. It is concluded both from the qualitative visualisation in Figure 6.4 and Figure 6.5, and quantitative analysis in Figure 6.7 that the ℓ_{max} of droplets is decreased with the increase in the value of ψ_U, ψ_p, We, ψ_{Re}, $\dot{m}_g/\dot{m}_l$, and $\dot{V}_g/\dot{V}_l$. The ℓ_{max} of droplets ranges from 60 µm to 590 µm (less than the initial liquid jet diameter D_l). There are no droplets generated in W0.8A030, W0.8A040, W1.2A030, W1.2A040, and most of the helium/water flow cases. Although a large droplet with $\ell_{max} = 2.94\,\text{mm} \gg D_l$ is observed in Figure 6.5 flow case W0.4H030, the large droplet is formed by liquid dripping from the needle exit and not via atomisation. When emerging in a still/low-velocity gas stream, capillary Plateau-Rayleigh instability occurs on the liquid jet which eventually breaks the liquid jet into droplets [26]. As the velocity of the gas stream increases, axisymmetric instability is induced and eventually overcomes the Plateau-Rayleigh instability. This physical phenomenon has been previously reported [26] and further supports the criterion for classifying spray structures that the droplets with $\ell_{max} > D_l$ should be filtered out.

It is interesting to note that the momentum flux ratio is not the most appropriate non-dimensional parameter for droplet diameter prediction, although it still appears to achieve more consistent droplet size across different flow cases than the velocity ratio. The results show that the exit Weber number (We) is the dominant influencing parameter for determining and estimating droplet generation in gas-assist atomisation, as similar ℓ_{max} values of droplets are obtained at similar We, in comparison to other parameters. For example, flow cases W0.4A090, W0.8A090, and W1.2A090 have the We value of 80, the droplet ℓ_{max} obtained in these flow cases are 120 µm, 160 µm, and 140 µm, respectively. However, at the same gas/liquid ψ_{Re} value of 54, flow cases W0.4A030, W0.8A060, and W1.2A090 form droplets with dispersed ℓ_{max} value of 1310 µm, 290 µm, and 140 µm, respectively. This observation is consistent with previously reported findings that the Weber number is the appropriate parameter to describe the droplets formed according to the secondary breakup mechanism [27].

Stokes number is used to estimate the behaviour of droplets whose size is below the spatial detection limit of the introduced optical setup—8.8 µm. The

Stokes number is widely used in scenarios that involve multi-phase flows (e.g. particle image velocimetry) to indicate the level of responsiveness of droplets to the turbulent fluctuation in the ambient gas environment [11]. The Stokes number is the ratio of droplet relaxation time (τ_d) to the turbulent time scale (τ_t) calculated by a series of Equations 6.1, 6.2, 6.3, and 6.4 as follows [11, 28–30]:

$$\tau_d = \frac{4}{3}\frac{\rho_l}{\rho_g}\frac{d}{C_d|U_s|} \tag{6.1}$$

$$C_d = \frac{24}{Re_p}\left(1 + 0.15Re_p^{0.687}\right) \tag{6.2}$$

$$Re_p = \frac{dU_s}{v_g} \tag{6.3}$$

$$\tau_t = \frac{0.65R_{1/2}}{u'} \tag{6.4}$$

where C_d denotes the drag coefficient, Re_d is the droplet Reynolds number, $R_{1/2}$ is the half radius of the gas phase velocity profile, u' is the fluctuating gas phase velocity, taken on the jet centerline, $|U_s|$ is the absolute value of the mean slip velocity of a particular droplet size, and d is the droplet diameter. Since the local velocity is not measured in this experiment, a series of assumptions are made. The droplet is assumed to be located at x/D = 17 with an approximate local velocity equivalent to the bulk mean exit velocity. The actual local velocity of the droplet is well below the bulk mean exit velocity. Based on these assumptions, the Stokes number of droplets whose size is below the detection limit of 8.8 µm is less than unity, indicating that these very fine droplets fluctuate with the gas flow and are of minor importance in spray characterisation and will follow the gas flow.

It should be noted that the microscopic shadowgraphy introduced in this chapter is a two-dimensional line-of-sight measurement of the droplets, sufficient for the order of magnitude estimation of droplet size; however, the volume-to-surface area ratio is not available to estimate Sauter mean diameter (SMD). The microscopic shadowgraphy setup introduced in this chapter is more suitable for estimating droplets with relatively large diameters or moving in a low-velocity flow field. The evaluation of Stokes number of flow cases further demonstrates the potential for the optical setup to resolve the key spray characteristics of importance.

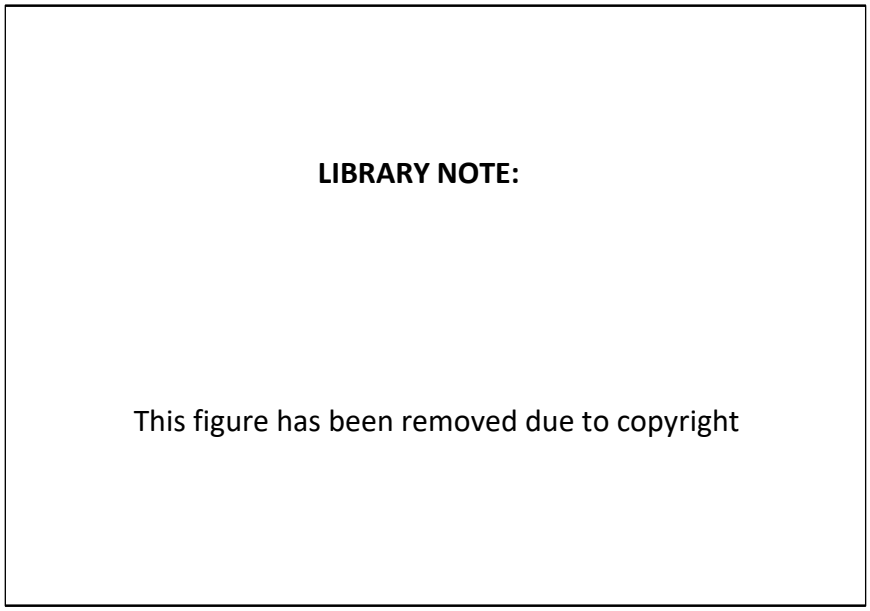

Figure 6.7: Characteristic major length (ℓ_{max}) of droplets as a function of non-dimensional parameters extracted from the short-exposure microscopic shadowgraphs of various flow cases described in Table 6.1. The non-dimensional parameters include bulk mean gas/liquid velocity ratio (ψ_U), gas/liquid momentum flux ratio (ψ_p), exit Weber number (We), gas/liquid Reynolds number ratio (ψ_{Re}), gas/liquid mass flow ratio ($\dot{m}_g/\dot{m}_l$), and gas/liquid volumetric flow ratio ($\dot{V}_g/\dot{V}_l$).

6.3.3.3 Evolution of area fraction

The area fraction of spray is a critical parameter to denote the level of atomisation by describing the dispersed spray objects, which has been area fraction (A_S/A_T %) is commonly used in two-dimensional line-of-sight shadowgraphy. The definition of area fraction was presented in §3.4.5.2. Figure 6.8 shows the area fraction extracted from the 50 binarised shadowgraphs for each flow case as a function of the non-dimensional parameters described in §6.3.3. The FOV-based A_S/A_T ranges from 1.7% to 6.5% across the tested flow cases. In general, the A_S/A_T decreases with the increase in gas/liquid non-dimensional parameters reported, in agreement with the trend revealed in previous research [31]. It has been reported that the area fraction decreases from 14% to 9% as the fuel/air mass flow ratio is increased given that a two-dimensional estimate of volume fraction is measured [32]. The area fraction decreases as ligaments and irregular shapes break up into droplets and disperse radially [11].

It is seen in Figure 6.8 that the gas/liquid momentum ratio (ψ_p) is more consistent across flow cases, particularly in those that use different gases (air/helium) as the carrier gas, indicating it may be a controlling parameter. The flow cases W0.8A110 and W0.8H110 show distinct A_S/A_T at 2.6% and 5.5%, respectively, even though they have the same $\dot{m}_g/\dot{m}_l$ value of 13.8. The exit Weber number, although the most appropriate to characterise droplet ℓ_{max} (refer to §6.3.3.2), is not suitable for the estimate of the area fraction of sprays. The flow cases W0.4A090, W0.8A090, and W1.2A090 have a $\dot{m}_g/\dot{m}_l$ value of 80 yet exhibit A_S/A_T at 1.8%, 3%, 3.9%, respectively. It is noticed that the A_S/A_T of flow cases W0.4H(030–110) seem not to follow the same decreasing trend with the increase in ψ_p, due to the liquid dripping phenomenon observed in the experiment as a result of low ψ_p at a low liquid flow rate. The liquid dripping creates large droplets with $\ell_{max} > D_l$, which decreases in size with the increase in ψ_p and results in a lower A_S/A_T.

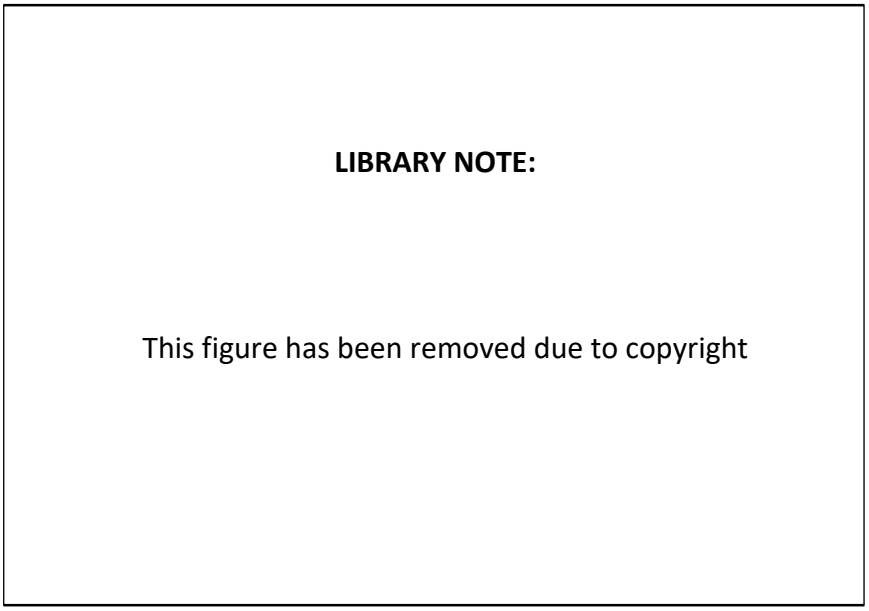

Figure 6.8: Area fraction (A_S / A_T %) as a function of non-dimensional parameters extracted from the short-exposure microscopic shadowgraphs of various flow cases described in Table 6.1. The non-dimensional parameters include bulk mean gas/liquid velocity ratio (ψ_U), gas/liquid momentum flux ratio (ψ_p), exit Weber number (We), gas/liquid Reynolds number ratio (ψ_{Re}), gas/liquid mass flow ratio ($\dot{m}_g/\dot{m}_l$), and gas/liquid volumetric flow ratio ($\dot{V}_g/\dot{V}_l$).

6.3.3.4 Evolution of ligament and wave structure

Ligaments are formed either in the transition of wave-like liquid jets breaking up into droplets, or large droplets becoming elongated ellipsoids. Ligaments eventually break up into smaller droplets. Similar to the droplet characterisation employed in this work, the characteristic major length ℓ_{max} is used to describe the ligament measured in the microscopic shadowgraphs of flow cases, following the classification criterion mentioned in §6.3.1. The mean ℓ_{max} of ligaments is plotted in Figure 6.9 for the non-dimensional parameters considered (refer to §6.3.3). It is concluded both from the qualitative visualisation in Figure 6.4, Figure 6.5, and quantitative data in Figure 6.9 that the ligaments are less likely formed in the low ψ_p and We flow cases and the ligament ℓ_{max} decreases with the increase in ψ_p and We. Similar to the droplet ℓ_{max}, the exit Weber number may be the appropriate non-dimensional parameter to describe the evolution of ligament, but the varying trend in ligament ℓ_{max} is less consistent compared with the droplets.

The wave structure is another important characteristic in the transition from an intact liquid core to ligaments, irregular objects, and droplets. The ligament size is found to be dictated by the primary wavelength [32]. The formation of the wave structure is mainly subjected to oscillation on the interface and an accelerated mechanism of destabilisation based on the amplified Rayleigh-Taylor instabilities. The resultant shear instability imposes significant accelerations perpendicular to the surfaces of the liquid flow [33].

The wavelength of the wave structure acquired from the shadowgraphs for the tested cases is plotted as a function of ψ_U, ψ_p, We, ψ_{Re}, $\dot{m}_g/\dot{m}_l$, and $\dot{V}_g/\dot{V}_l$, in Figure 6.10. In the flow cases that have an undisturbed liquid jet, e.g. W0.8H(030–070) and W1.2H(030–070), the wavelength is considered infinite. In the high ψ_p and We flow cases where the liquid jet immediately breaks up into smaller objects, the wavelength is considered zero. Apart from those cases, the wavelength of the wave structure varies from 0.7 mm to 3.8 mm as the We ranges within 15–80. In general, with a constant water mass flow rate, the wavelength shows a decreasing trend as the exit Weber number is increased. The results are consistent with the findings reported previously [33]. Amongst all the non-dimensional parameters presented, the exit Weber number appears to be the most appropriate to describe the wavelength of the wave structure. The change in wavelength follows a similar decreasing trend with the increase in We for W0.4H(070–110) flow cases.

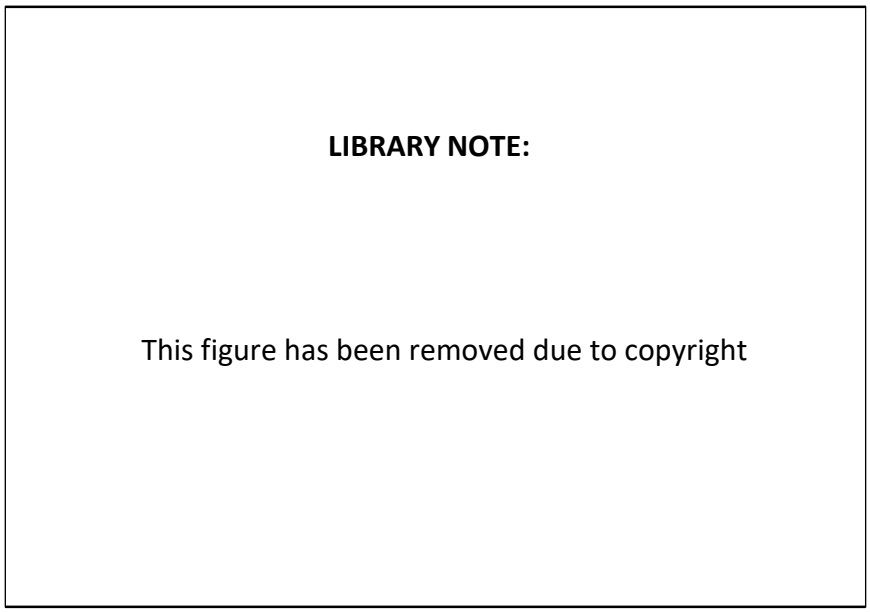

Figure 6.9: Characteristic major length (ℓ_{max}) of ligaments as a function of non-dimensional parameters extracted from the short-exposure microscopic shadowgraphs of various flow cases described in Table 6.1. The non-dimensional parameters include bulk mean gas/liquid velocity ratio (ψ_U), gas/liquid momentum flux ratio (ψ_p), exit Weber number (We), gas/liquid Reynolds number ratio (ψ_{Re}), gas/liquid mass flow ratio ($\dot{m}_g/\dot{m}_l$), and gas/liquid volumetric flow ratio ($\dot{V}_g/\dot{V}_l$).

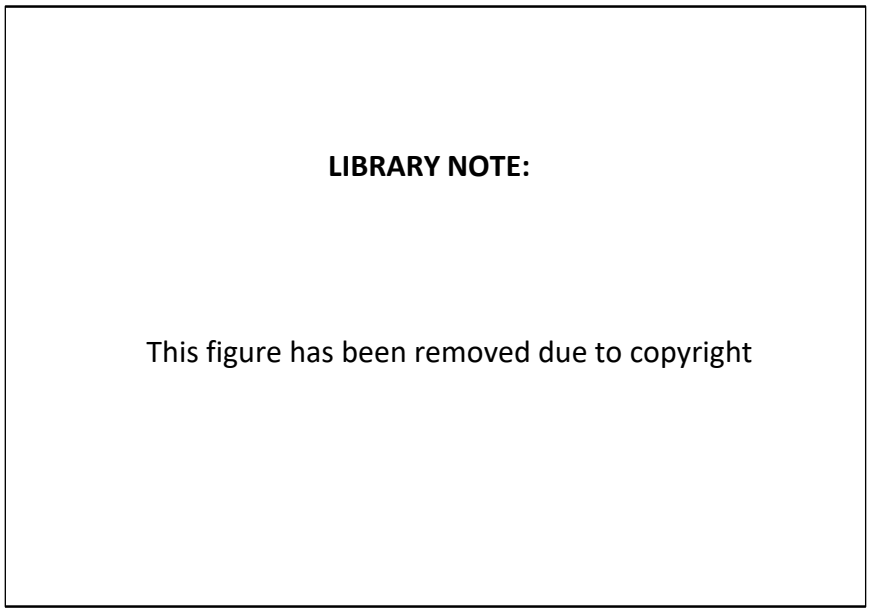

Figure 6.10: Wavelength of the wave structures as a function of non-dimensional parameters extracted from the short-exposure microscopic shadowgraphs of various flow cases described in Table 6.1. The non-dimensional parameters include bulk mean gas/liquid velocity ratio (ψ_U), gas/liquid momentum flux ratio (ψ_p), exit Weber number (We), gas/liquid Reynolds number ratio (ψ_{Re}), gas/liquid mass flow ratio ($\dot{m}_g/\dot{m}_l$), and gas/liquid volumetric flow ratio ($\dot{V}_g/\dot{V}_l$).

6.3.4 non-dimensional parameters and spray characterisation

The analysis of influencing parameters for near-field dense spray characterisation concludes that the momentum flux ratio and Weber number are more appropriate in describing and predicting spray characteristics, whereas the gas/liquid bulk mean velocity ratio is not appropriate to predict and describe the gas-assist atomisation performance across the tested flow cases. This is because as the type of carrier gas changes, the physical properties of the carrier gas play an important role in gas-assist atomisation, which has not been reflected in previous studies that focus on the airblast effect. In this work, the comparison between air-assist and helium-assist atomisation at constant gas/liquid bulk mean velocity ratio clearly demonstrated their distinct performance. For a similar reason, the gas/liquid mass and volumetric flow ratio which have not taken the physical properties of carrier gas into consideration, although widely employed in previous studies as key parameters for gas-assist atomisation analysis, are demonstrated as not being the most appropriate either.

The comparison between momentum flux ratio and Weber number for the appropriate non-dimensional parameter in atomisation has been recently reported [34]. The individual assessment of these two parameters confirms the effect of momentum flux ratio—high momentum flux ratio cases tend to have early completion of atomisation and more dispersed flow in the near field. It also has been highlighted that at a constant momentum ratio, the atomisation rate reduces with the Weber number due to increased liquid loading. Also, the atomisation completes at a similar axial location, which indicates that the variation in Weber number has a minor effect compared with the momentum flux ratio [34]. The consistent findings in this work may indicate that the Weber number is more suitable to describe the microscopic characteristics of the spray (e.g. droplet size), as it reflects the relationship between inertial forces and the surface tension forces in fluid dynamics. The surface tension is a key force to resist the instabilities on the interface of liquid and gas flows, therefore preventing the liquid stream from breaking up. In contrast, the momentum flux ratio is more suitable to describe the macroscopic characteristics of the spray since it emphasises the effect of density and velocity difference between the liquid and carrier gas.

It is highlighted that the wavelength and amplitude of the liquid jet are subjected to instabilities induced by different physical mechanisms. At high Weber numbers where the surface tension has mild influences on atomisation, the instability growth on the liquid jet is governed by slip velocity. At

low Weber numbers, as mentioned in §6.3.3.2, the surface tension becomes dominant, and capillary Plateau-Rayleigh instability grows on the liquid jet [26].

The bulk mean Reynolds number of carrier gases in Table 6.1 shows that the Re_A ranges from 10,000 to 36,800, indicating that the air-assist atomisation cases all attain turbulent gas flow condition, whereas the Re_H of helium-assist cases is lower (1,300–4,800). The lower level of turbulence in the ambient gas condition explains the lower atomisation performance observed in the helium/water flow cases due to less intense instabilities induced by turbulence. The presence of eddies in turbulent conditions facilitates the interactions between liquid and gas streams and thus contributes to the breakup process. The effect of turbulence on primary breakup length, wavelength, and ligaments has been previously reported [5, 26, 32]. It has been highlighted that using a single exit Weber number to predict spray characteristics is insufficient. This is because the addition of local turbulence leads to instantaneous Weber numbers which affect the breakup regimes of flows [32].

Table 6.3 summarises the previous discussion and findings, and lists the most appropriate influencing parameters for partly predicting spray characteristic.

Table 6.3: Appropriate influencing parameters for partly predicting spray characteristics.

Spray characteristics	Appropriate parameter
Breakup length	Momentum flux ratio (ψ_p)
Droplet ℓ_{max}	Exit Weber number (We)
Area fraction	Momentum flux ratio (ψ_p)
Ligament ℓ_{max}	Exit Weber number (We)
Wavelength of the wave structure	Exit Weber number (We)

6.4 Conclusions

The gas-assist atomisation performance of coaxial multi-phase air/water and helium/water flows from a needle spray burner was investigated by backlit microscopic shadowgraphy using commercial equipment. The key findings of this chapter are summarised as follows:

1. The introduced experimental method is suitable for identifying the main features and objects in sprays where LDV and PDPA are not applicable (e.g. large ligaments and irregular objects), while reducing the hazards and complexity of a setup using lasers.

2. Five key structures that represent the performance of gas-assist atomisation in the near-field region were identified and analysed. The results reveal that different types of carrier gas with various physical properties greatly influence the performance of atomisation. Using helium as the carrier gas leads to longer breakup lengths of the liquid core, larger droplet size, and longer ligament lengths, compared with air under the same liquid flow conditions. The coarser water spray generated by helium is ascribed to its low density.

3. The evaluation of influencing non-dimensional parameters on spray characterisations demonstrates that the momentum flux ratio is appropriate to describe and predict the macroscopic characteristics of spray—breakup length and area fraction. The exit Weber number (We) is more suitable for the characterisation of microscopic features—characteristic major length ℓ_{max} of droplet and ligaments and the wavelength of the wave structure, whereas the bulk mean velocity ratio is not an appropriate parameter to predict and determine spray characteristics.

4. The breakup lengths of the air/water sprays decrease from 9.7 mm to 0.4 mm as the gas/liquid momentum flux ratio increases from 1.3 to 37. As the gas/liquid momentum flux ratio exceeds 27, the decrease in the breakup lengths is insensitive to the gas/liquid momentum flux ratio. The liquid core of the helium/water sprays stays intact at the gas/liquid momentum flux ratio < 3.

5. The exit Weber number of the air/helium water sprays tested in this study (11–120) generates characteristic major length ℓ_{max} of droplets from 60 µm to 590 µm. Liquid dripping or intact liquid core was observed at the exit Weber number less than 9.

6.5 References

[1] M. Mlkvik and B. Knizat. "On the spray pulsations of the effervescent atomizers". *EPJ Web of Conferences*. Vol. 180. EDP Sciences. 2018, p. 02069.

[2] E. Rostami and H. Mahdavy Moghaddam. "The velocity and viscosity impact on the annular spray atomisation of different fuels". *Combust. Theory Model.* 25 (2021), pp. 158–192.

[3] M. A. Khan, H. Gadgil, and S. Kumar. "Influence of liquid properties on atomization characteristics of flow-blurring injector at ultra-low flow rates". *Energy* 171 (2019), pp. 1–13.

[4] E. Lubarsky, J. R. Reichel, B. T. Zinn, and R. McAmis. "Spray in Crossflow: Dependence on Weber Number". *J. Eng. Gas Turbines Power* 132 (Oct. 2009), p. 021501.

[5] G. Singh, A. Kourmatzis, A. Gutteridge, and A. R. Masri. "Instability growth and fragment formation in air assisted atomization". *J. Fluid Mech.* 892 (2020), A29.

[6] R. Rangarajan, H. Zhang, P. J. Strykowski, A. Hoxie, S. Yang, and V. Srinivasan. "Atomization of high viscosity liquids using a two-fluid counterflow nozzle: Experiments and modeling". *Turbo Expo: Power for Land, Sea, and Air*. Vol. 84133. American Society of Mechanical Engineers. 2020, V04BT04A022.

[7] J. C. Lasheras and E. Hopfinger. "Liquid jet instability and atomization in a coaxial gas stream". *Annu. Rev. Fluid Mech.* 32 (2000), pp. 275–308.

[8] R. Aftel. "Effect of atomization gas properties on droplet atomization in an air-assist atomizer". PhD thesis. Virginia Polytechnic Institute and State University, 1996.

[9] A. E. S. E. T. Alajmi, N. M. Adam, A. A. Hairuddin, and L. C. Abdullah. "Fuel atomization in gas turbines: A review of novel technology". *Int. J. Energy Res.* 43 (2019), pp. 3166–3181.

[10] G. Singh, A. Kourmatzis, and A. Masri. "Volume measurement of atomizing fragments using image slicing". *Exp. Therm. Fluid Sci.* 115 (2020), p. 110102.

[11] A. Lowe, A. Kourmatzis, and A. R. Masri. "Turbulent spray flames of intermediate density: Stability and near-field structure". *Combust. Flame* 176 (2017), pp. 511–520.

[12] S. Wu, M. Xu, D. L. Hung, and H. Pan. "In-nozzle flow investigation of flash boiling fuel sprays". *Appl. Therm. Eng.* 117 (2017), pp. 644–651.

[13] P. Aleiferis, J. Serras-Pereira, A. Augoye, T. Davies, R. Cracknell, and D. Richardson. "Effect of fuel temperature on in-nozzle cavitation and spray formation of liquid hydrocarbons and alcohols from a real-size optical injector for direct-injection spark-ignition engines". *Int. J. Heat Mass Transf.* 53 (2010), pp. 4588–4606.

[14] M. Wei, Y. Gao, F. Yan, L. Chen, L. Feng, G. Li, and C. Zhang. "Experimental study of cavitation formation and primary breakup for a biodiesel surrogate fuel (methyl butanoate) using transparent nozzle". *Fuel* 203 (2017), pp. 690–699.

[15] D. W. Lee and R. C. Spencer. *Photomicrographic studies of fuel sprays*. US Government Printing Office, 1933.

[16] M. Linne. "Imaging in the optically dense regions of a spray: A review of developing techniques". *Prog. Energy Combust. Sci.* 39 (2013), pp. 403–440.

[17] S. Ghaemi, P. Rahimi, and D. S. Nobes. "Assessment of parameters for distinguishing droplet shape in a spray field using image-based techniques". *At. Sprays* 19 (2009), pp. 809–831.

[18] S. Horiashchenko, K. Horiashchenko, and J. Musial. "Methodology of measuring spraying the droplet flow of polymers from nozzle". *Mechanics* 26 (2020), pp. 82–86.

[19] G. Singh, A. Kourmatzis, and A. Masri. "Dense sprays with a focus on atomization and turbulent combustion". *Flow Turbul. Combust.* 106 (2021), pp. 405–417.

[20] A. Kourmatzis, P. X. Pham, and A. R. Masri. "A two-angle far-field microscope imaging technique for spray flows". *Meas. Sci. Technol.* 28 (2017), p. 035302.

[21] M. Shimizu, M. Arai, and H. Hiroyasu. "Measurements of breakup length in high speed jet". *Bulletin of JSME* 27 (1984), pp. 1709–1715.

[22] G. Laryea and S. No. "Spray angle and breakup length of charge-injected electrostatic pressure-swirl nozzle". *J. Electrost.* 60 (2004), pp. 37–47.

[23] S. Rezaei, F. Vashahi, G. Ryu, and J. Lee. "On the correlation of the primary breakup length with fuel temperature in pressure swirl nozzle". *Fuel* 258 (2019), p. 116094.

[24] G. Charalampous, C. Hadjiyiannis, and Y. Hardalupas. "Comparative measurement of the breakup length of liquid jets in airblast atomisers using optical connectivity, electrical connectivity and shadowgraphy". *Measurement* 89 (2016), pp. 288–299.

[25] N. Beheshti, A. A. Burluka, and M. Fairweather. "Assessment of $\Sigma - Y_{liq}$ model predictions for air-assisted atomisation". *Theor. Comput. Fluid Dyn.* 21 (2007), pp. 381–397.

[26] P. Marmottant and E. Villermaux. "On spray formation". *J. Fluid Mech.* 498 (2004), pp. 73–111.

[27] C. Lee and R. D. Reitz. "An experimental study of the effect of gas density on the distortion and breakup mechanism of drops in high speed gas stream". *Int. J. Multiph. Flow* 26 (2000), pp. 229–244.

[28] R. Antonia and R. W. Bilger. "An experimental investigation of an axisymmetric jet in a co-flowing air stream". *J. Fluid Mech.* 61 (1973), pp. 805–822.

[29] J. D. Gounder, A. Kourmatzis, and A. R. Masri. "Turbulent piloted dilute spray flames: Flow fields and droplet dynamics". *Combust. Flame* 159 (2012), pp. 3372–3397.

[30] S. H. Stårner, J. Gounder, and A. R. Masri. "Effects of turbulence and carrier fluid on simple, turbulent spray jet flames". *Combust. Flame* 143 (2005), pp. 420–432.

[31] A. Kourmatzis, P. X. Pham, and A. R. Masri. "Characterization of atomization and combustion in moderately dense turbulent spray flames". *Combust. Flame* 162 (2015), pp. 978–996.

[32] A. Kourmatzis and A. Masri. "Air-assisted atomization of liquid jets in varying levels of turbulence". *J. Fluid Mech.* 764 (2015), pp. 95–132.

[33] C. M. Varga, J. C. Lasheras, and E. J. Hopfinger. "Initial breakup of a small-diameter liquid jet by a high-speed gas stream". *J. Fluid Mech.* 497 (2003), pp. 405–434.

[34] G. Singh, K. Jayanandan, A. Kourmatzis, and A. Masri. "Spray atomization and links to flame stability over a range of Weber numbers and pressure ratios". *Energy & Fuels* 35 (2021), pp. 16115–16127.

Chapter 7

Radiating biofuel-blended hydrogen flames on a coaxial spray burner

Statement of Authorship

Title of Paper	Radiating biofuel-blended turbulent nonpremixed hydrogen flames on a coaxial spray burner
Publication Status	☐ Published ☐ Accepted for Publication ☑ Submitted for Publication ☐ Unpublished and Unsubmitted w ork w ritten in manuscript style
Publication Details	Y. Yin, P.R. Medwell, B.B. Dally Radiating biofuel-blended turbulent nonpremixed hydrogen flames on a coaxial spray burner, Fuel, (under review).

Principal Author

Name of Principal Author (Candidate)	Yilong Yin
Contribution to the Paper	1. Developed the research concept of introducing biofuels to hydrogen flames by gas-assist atomisation for soot and radiant heat flux enhancement. Determined the combustion characteristics of interest and their corresponding diagnostics, namely still photograph for flame appearance and luminosity measurement, heat flux sensor for radiant heat flux, microscopic shadowgraphy for spray characterisation, thermocouple for flame temperature measurement, and flue gas analyser for pollutant emission measurement. 2. Designed, organised, and conducted experimental campaigns. Selected biofuels and their surrogates for testing. Designed and built a needle spray burner to blend hydrogen with liquid biofuels by gas-assist atomisation. Designed and determined the details of flame cases and test conditions to allow the comparison between different introduction methods. Developed required safety measures and documentation for the experiments. Prepared, tested and calibrated the equipment used in the experiments. Designed and assembled the appropriate plumbing systems. Conducted a series of preliminary tests to ensure the safe operation of the experiments and to determine the flame cases of interest. Evaluated the results and adjusted the experimental approach accordingly. 3. Initiated, designed and performed numerical modelling in Chemkin Pro for the analysis of PAH formation pathways to verify, interpret, and understand the observations from the experiments. Searched and revised chemical mechanisms that include PAH formation reactions for the tested biofuel surrogates. 4. Collected, processed, and analysed data from the experiments and numerical simulation. Evaluated the uncertainties and reliability of the data. Generated and determined critical experimental and numerical results for a paper. Understood and explained the PAH formation and corresponding radiant heat flux enhancement among the biofuel surrogates tested with the support from numerical results. Analysed the effect of liquid biofuel properties and corresponding spray characteristics on soot formation and radiant heat flux of biofuel/hydrogen flames. Compared the effect of introduction methods, i.e. prevapourisation, ultrasonic spray, and gas-assist atomisation, on the flame characteristics of biofuel/hydrogen flames. Generated novel findings of the study. 5. Developed and edited the manuscript. Selected the target journal of the manuscript. Submitted the manuscript as corresponding author.
Overall percentage (%)	80%
Certification:	This paper reports on original research I conducted during the period of my Higher Degree by Research candidature and is not subject to any obligations or contractual agreements with a third party that would constrain its inclusion in this thesis. I am the primary author of this paper.
Signature	:023.10.31 0:37:57 +10'30'
Date	31/10/2023

Co-Author Contributions

By signing the Statement of Authorship, each author certifies that:

i. the candidate's stated contribution to the publication is accurate (as detailed above);

ii. permission is granted for the candidate in include the publication in the thesis; and

iii. the sum of all co-author contributions is equal to 100% less the candidate's stated contribution.

Name of Co-Author	Paul R. Medwell		
Contribution to the Paper	1. Supervised the development of the research. Helped to evaluate the potential outcome and significance of the research. 2. Provided assistance with the training of experimental skills. 3. Advised on the experimental and numerical modelling details of the study. Supervised and approved the safety operation of the experiment. Advised on the calibration and setup of the experiment. 4. Advised on data processing and analysis. Evaluated the results and findings of this research. 5. Edited the manuscript. Provided suggestions for the responses to reviewers' comments.		
Signature	Paul Medwell 2023.10.31 10:47:39 +10'30'	Date	31-OCT-2023

Name of Co-Author	Bassam B. Dally		
Contribution to the Paper	1. Supervised the development of the research. Guided the direction of the research. 2. Provided assistance with the training of experimental skills. 3. Advised on the experimental and numerical approach of the study. 4. Advised on data processing and analysis. Evaluated the results and findings of this research. 5. Edited the manuscript. Provided suggestions for the responses to reviewers' comments.		
Signature	Digitally signed by Bassam Dally Date: 2023.10.31 12:44:06 +03'00'	Date	

Radiating biofuel-blended turbulent nonpremixed hydrogen flames on a coaxial spray burner

Yilong Yin[a,*], Paul R. Medwell[a], Bassam B. Dally[b]

[a] *School of Electrical and Mechanical Engineering, The University of Adelaide, Adelaide, South Australia 5005, Australia*

[b] *Clean Combustion Research Centre, King Abdullah University of Science and Technology, Thuwal 23955-6900, Kingdom of Saudi Arabia*

Abstract

The low radiant intensity and luminosity of hydrogen flames can be enhanced by the addition of a small portion of sooting biofuels. To achieve higher effectiveness, the impact of blending turbulent nonpremixed hydrogen flames with liquid biofuels, by gas-assist atomisation, is investigated and compared with the introduction methods of prevapourisation and ultrasonic spray. The flame appearance, luminosity, radiant fraction, centreline temperature, and the near-field spray characteristics of four biofuel surrogates (eucalyptol, D-limonene, guaiacol, and anisole) blended into hydrogen flames are measured experimentally. Radiating biofuel/hydrogen flames are achieved on a coaxial needle spray burner by the addition of 0.1–0.3 mol% biofuel surrogates. Compared with the unblended hydrogen flame, the luminosity and radiant fraction are enhanced by 30–500% and 2–15%, respectively, with the addition of biofuel surrogates. The results show that adding the biofuel surrogates by gas-assist atomisation is more effective than prevapourisation and

*Corresponding author
URL: yilong.yin@adelaide.edu.au (Yilong Yin)

ultrasonic atomisation in luminosity and radiant fraction enhancement. It is found that the local fuel-rich conditions, which are beneficial for soot formation, are further facilitated by the larger droplets and spray objects generated by gas-assist atomisation. Of the additives tested, anisole is the most effective for luminosity and radiant fraction enhancement of a hydrogen flame while exhibiting the largest flame temperature drop due to the enthalpy of vapourisation and the radiative loss from the promoted soot formation. The viscosity and surface tension greatly influence the spray characteristics which in turn impacts the flame characteristics. Guaiacol, the representative of lignin, appears to have the lowest effectiveness in radiant fraction enhancement due to the presence of a hydroxy group, a higher bond dissociation enthalpy, and a coarser spray ascribed to higher viscosity and surface tension.
Keywords: Hydrogen flame, Biofuel surrogate, Needle spray burner, Radiative heat flux, Gas-assist atomisation

---

1. Introduction

In recent years, hydrogen has been increasingly recognised as a promising energy carrier capable of replacing fossil fuels in industrial processes, driven by the urgent need to mitigate greenhouse gas emissions. This burgeoning interest in hydrogen arises from its potential to offer a clean and sustainable energy alternative, owing to its ability to produce only water vapour when consumed. However, this carbon-free nature of hydrogen flames gives rise to a noteworthy challenge for practical applications—their diminished radiant intensity renders hydrogen flames inadequate for many industrial combustion systems, which typically depend on radiative heat transfer as a primary means of heat transfer. To address the diminished radiant intensity exhibited by hydrogen flames, a viable strategy involves incorporating a small fraction of sooting biofuels into the hydrogen blend [1, 2].

This intentional blending serves to augment the radiative heat flux by facilitating the formation of soot particles [3–7].

The effectiveness of promoting soot formation and the consequent radiant intensity is subject to the influence of numerous factors. These factors encompass a wide range of parameters that can impact the process, including but not limited to residence time, flame temperature, and the properties of additives [8–17]. It has been reported that blending turbulent hydrogen flames with various biofuels at less than 1 mol% (based on the mole concentration of H_2) by prevapourisation and ultrasonic atomisation does not achieve sooting flames and the largest radiant fraction enhancement was found at 19% in toluene/hydrogen blends [6, 7]. Further increasing the concentration of toluene in the hydrogen blends to 4 mol% greatly promotes soot formation and alters the flame appearance from blue to yellow colouration [7]. The radiant fraction increases by 33% compared with the non-blended hydrogen flame. Amongst the various biofuels studied, non-oxygenated biofuels with aromatic structures tend to favour soot formation compared with oxygenated fuels and monoterpenes [4–7, 18].

Apart from influencing factors of additives' chemical properties and concentrations, the method of introducing additives to the hydrogen flame affects the phase and morphology of the additive, therefore impacting soot formation and radiant intensity enhancement due to altered mixing mechanisms. Spray additives produce more soot compared with prevapourised additives because fuel-rich regions created by a spray favour soot formation [4]. However, changing the introduction method from prevapourisation to ultrasonic spray has a moderate effect on the radiant intensity enhancement of biofuel-blended hydrogen flames [7]. The liquid droplets generated by ultrasonic atomisation are fine, at about 30 µm diameter [4, 7, 19]. It is hypothesised that larger liquid fuel droplets may be

needed to further enhance the local fuel-rich conditions for promoting soot formation. In addition, the use of ultrasonic nebuliser for atomisation induces complexity to application and limits the liquid fuel additives since it is sensitive to purity and physical properties of the fuel. Therefore, investigating an introduction method of the additive with the potential for further enhancing soot formation while maintaining the spray flame stability becomes the motivation of this investigation.

Amongst various methods of liquid fuel atomisation, gas-assist atomisation driven by the airblast effect has the most potential as the liquid droplet size can be controlled by atomisation conditions, hence capable of forming larger droplets. In addition, the simplicity of the gas-assist atomisation configuration and the insensitivity to liquid with various physical properties benefit its application in liquid fuel combustion. Gas-assist atomisation can be described as the process of dispersing individual liquid droplets within a gaseous medium, wherein these droplets undergo progressive evolution facilitated by the interactions of turbulent dispersed two-phase flow phenomena [20, 21]. When a liquid flow is introduced into a gaseous medium, the interface between the two flows, characterised by varying velocities or densities, gives rise to Kelvin-Helmholtz instabilities. These instabilities promote the amplification of Rayleigh-Taylor instabilities. Immediately upon exiting the nozzle, deformations emerge on the liquid interface, which subsequently evolve in size and magnitude over both distance and time. The presence of deformations and disturbances on the liquid flow surface initiates oscillations characterized by dilation and wave structures. These oscillations lead to the fragmentation of the liquid flow into ligaments, large droplets, and irregular objects, constituting the primary breakup mechanism. This primary breakup predominantly occurs in the vicinity of the nozzle exit, representing a region of dense spray regime, wherein the dynamics are primarily governed by fragment coalescence and collision. Subsequently, as the liquid fragments progress downstream,

they encounter aerodynamic forces that trigger a secondary breakup mechanism. In this mechanism, the fragments experience further disintegration into smaller elements, with minimal droplet-to-droplet interactions occurring [22, 23].

Dual concentric jets burners are commonly employed to perform gas-assist atomisation and establishing gas/liquid blended flames. The spray characterisation involves using techniques such as laser Doppler velocimetry (LDV), phase Doppler particle anemometry (PDPA), and microscopic shadowgraph imaging to investigate the break-up morphology of liquid streams under various gas/liquid conditions, including breakup length, ligaments, and droplets. In comparison to spray characterisation, multi-phase reacting flows are relatively poorly understood due to the challenge of stabilising the flame. There is a risk of unconsumed atomised liquid fuel droplets escaping from the flame when excessively large droplets are formed in coarse sprays as a result of the inappropriate design of atomisation conditions (e.g. nondimensional parameters such as gas/liquid momentum flux ratio). The physical properties of the liquid fuel play an important role in gas-assist atomisation, including viscosity, surface tension, and density, which in turn affect flame stability. In addition, the combustion properties of the liquid fuel are also the critical factors contributing to flame stability, namely flammability and volatility. The blow-off limit and the corresponding flame stability have been investigated on dual concentric jet burners using highly flammable gaseous fuels and liquid fuels (e.g. acetone and ethanol) with a piloted flame [23]. There is a lack of research that has reported on utilising the gas-assist atomisation of liquid biofuels for enhancing the radiant intensity of hydrogen flames. As mentioned, soot formation favours larger liquid droplets for creating fuel-rich conditions, which raises challenges of balancing the form of larger liquid droplets in a coarse spray for the effectiveness of radiant intensity enhancement, and the impact of larger liquid droplets on flame stability.

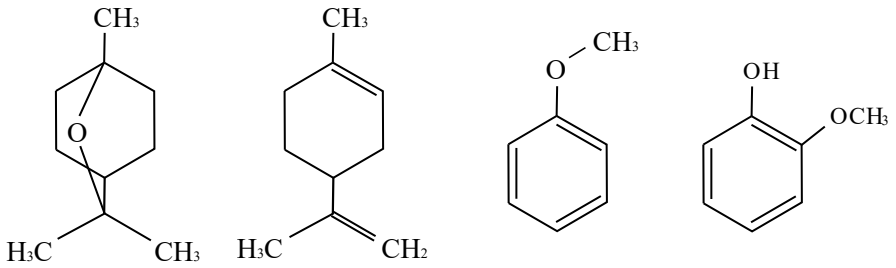

(a) Eucalyptol (b) D-limonene (c) Anisole (d) Guaiacol

Figure 1: Chemical structure of biofuel surrogates

Liquid biofuels are suitable soot-enhancing additives as they are biomass-derived renewable fuels with high sooting propensities. Bio-oil and essential oil are two major categories of biofuels which commonly comprise aromatics and terpene, respectively. Since bio-oil and essential oil contain complex compounds, surrogates are needed to emulate the chemical, physical, and combustion properties of the biofuels for chemical analysis [24–26]. Four biofuel surrogates are selected in this paper, with their chemical structures shown in Figure 1. Anisole (C_7H_8O) and guaiacol ($C_7H_8O_2$) are chosen as the surrogates for bio-oil since their chemical structures and functional groups are representative of the lignin patterns [27]. They both are oxygenated fuels containing a methoxy group (-OCH_3) which is a typical functional group of bio-oil derived by fast pyrolysis. The additional hydroxyl group in guaiacol compared with anisole allows the investigation of its effect on soot formation. Eucalyptol ($C_{10}H_{18}O$) and D-limonene ($C_{10}H_{16}$) are selected as the surrogates for essential oils as they are the primary component of eucalyptus oil and orange oil, respectively [28, 29]. The effectiveness of blending these monoterpenes on soot formation can be compared with aromatics to deepen the understanding of the potential application of biofuels.

The fundamental understanding of the sooting propensities of the potential biofuel additives and their effect of phase and concentration on the biofuel-blended hydrogen flames have

been established. However, the influence on flame characteristics and radiant intensity enhancement is limited. The gaps in understanding various biofuel surrogates, and how the introduction method and mixing mechanism will have impacts on the blending effect still remain. In this paper, the efficacy and effectiveness of blending turbulent pure hydrogen flames with four biofuel surrogates are tested on a coaxial needle spray burner. The flame appearance, flame luminosity, radiant heat flux, flame temperature, and spray characteristics of these biofuel/hydrogen flames are investigated by an experimental approach. The results and findings in this research further expand the understanding of critical influencing factors in soot formation and the radiant intensity enhancement of hydrogen flames.

2. Methodology

2.1. Burner configuration

A coaxial needle spray burner was used to utilise the gas-assist atomisation for biofuel surrogates addition to the hydrogen-based flame. A dispensing needle with L = 300 mm, ID = 603 μm, OD = 908 μm is located in the central to supply the liquid biofuel surrogates. Hydrogen is issued from a concentrically mounted gas jet with ID = 6.1 mm as the carrier gas for gas-assist atomisation. The liquid and gaseous fuel jets are inserted in a stainless steel jet which supplies an air coflow. The schematic of the needle spray burner is shown in Figure 2.

2.2. Flame cases

One of the major challenges for the gas-assist atomisation of biofuel additives is ensuring the ambient gas condition is able to generate sprays that can be completely consumed within

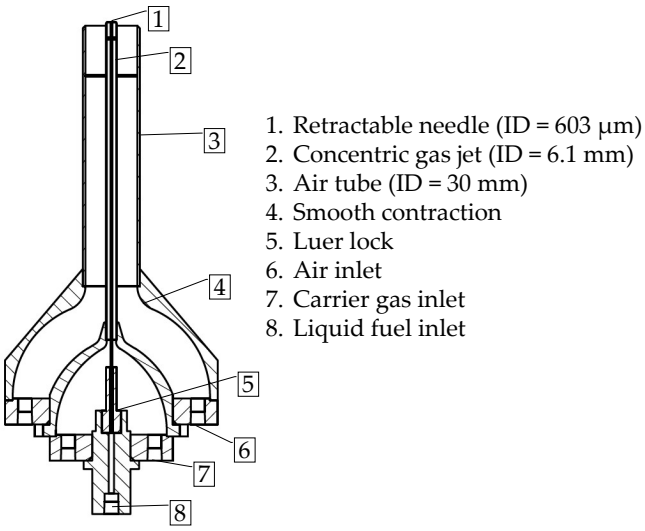

Figure 2: Schematic of coaxial needle spray burner

the flame, while maximising the fuel-rich condition for soot formation. The hydrogen flow rate was chosen to attain a bulk mean Reynolds number of 10,000, ensuring a turbulent flow regime in all flow cases. The details of the flame cases and the corresponding flame codes are shown in Table 1. Turbulent nonpremixed hydrogen-based flames were blended with liquid biofuel surrogates by gas-assist atomisation with different concentrations. The flow rates of the four biofuel surrogates were kept constant across the flame cases with a concentration equivalent to 0%, 0.1%, 0.2%, and 0.3% based on the mole concentration of H_2, respectively. In addition, the carbon flow rate across different biofuel surrogates at the same concentration was kept constant to achieve an equivalent carbon flux.

Table 1: Details of flame cases and flame codes of the turbulent nonpremixed biofuel surrogates blended hydrogen flames, including mole fraction of additives based on the mole fraction of hydrogen (mol%), total heat input (Q), gas/liquid momentum flux ratio (ψ_{p_A}), bulk mean Weber number (We), bulk mean Reynolds number (Re), and Ohnesorge number (Oh). The flame codes and corresponding flame cases are as follows: "HU0" - unblended pure hydrogen flame; "HE" - H_2/Eucalyptol; "HL" - H_2/D-limonene; "HA" - H_2/Anisole; and "HG" - H_2/Guaiacol.

Flame code	mol%	Q (kW)	ψ_{p_A}	We	Re	Oh
HU0	0.0	43.0	N/A	N/A	10,000	N/A
HL0.1	0.1	44.1	439	81	10,300	0.0073
HL0.2	0.2	45.1	110	81	10,700	0.0073
HL0.3	0.3	46.1	49	81	11,000	0.0073
HE0.1	0.1	44.2	375	34	10,400	0.0138
HE0.2	0.2	45.3	94	34	10,900	0.0138
HE0.3	0.3	46.5	42	34	11,000	0.0138
HG0.1	0.1	44.0	342	56	10,400	0.0385
HG0.2	0.2	44.9	85	56	11,000	0.0385
HG0.3	0.3	45.9	38	56	11,500	0.0385
HA0.1	0.1	43.9	404	60	10,300	0.0068
HA0.2	0.2	44.8	101	60	10,800	0.0068
HA0.3	0.3	45.7	45	60	11,000	0.0068

2.3. Experimental setup

As mentioned in Section 1, the risk of fire hazard may increase if the liquid droplets cannot react completely within the flame. Therefore, the coaxial needle spray burner was oriented horizontally in conjunction with a metal drip tray to control the potential escaped liquid droplets. For the selected flames, no escaped liquid droplet from the flame was observed in the experiment.

To capture the flame appearance and the resultant changes in the appearance due to the biofuel surrogate addition, a digital single-lens-reflex (DSLR) camera (Canon 6D) with a 50 mm focal length was used. The in-plane spatial resolution is 0.6 mm. The field of

view (FOV) of the cropped image is 1411 mm $\times$ 644 mm (length $\times$ width). In the image post-processing, the photographs were transformed into greyscale to extract signal intensity from each pixel for quantitative flame luminosity analysis. The greyscale images were then binarised to obtain the flame area by counting the white pixels in the FOV of the cropped image.

To measure the global radiant heat flux of various biofuel surrogate-blended hydrogen flames, a heat flux sensor (Schmidt-Boelter gauge, Medtherm Corporation) was employed. The heat flux sensor is able to measure nominal radiation over the range of 5–200 $\mathrm{kW/m^2}$, with a full-field angle view of 150°. The heat flux sensor was located at the radial distance of 284 mm perpendicular to the centreline of the jet. The uncertainty calculated from the mean radiative heat flux data was within $\pm 2\%$.

Soot formation and corresponding radiant heat flux have a close relationship with flame temperature [7]. In addition, the enthalpy of vapourisation in spray flames decreases the flame temperature, which in turn has an impact on the soot formation process. A Type R thermocouple with 0.2 mm diameter wire size and a 0.7 mm diameter bare-bead was employed to collect the mean flame temperature at the distance of 150 mm from the jet exit, focusing on the momentum-driven part of the flame and near-field of gas-assist atomisation. While a full axial profile of the temperature would have been useful, it was not practicable due to the horizontal nature of the flames. Nonetheless, the temperature data at $x = 150\,\mathrm{mm}$ serves the purpose of relating the drop in gaseous temperature with the increase in thermal radiation from the flames and the enthalpy of vaporisation. The conclusions drawn from these measurements are carefully made to account for the fact that the measurements are made at one point in all flames. The flame temperature measurements were corrected for radiative heat loss from the thermocouple. The uncertainty of the mean flame temperature

measurement was estimated to be $\pm 6\%$.

To investigate the influence of spray characteristics of various biofuel surrogates generated by gas-assist atomisation, back-lit microscopic shadowgraph imaging was employed. This technique uses a light source to back-illuminate the objects from one side, and a detector to capture the light on the opposite side to the source. In this study, a DSLR camera (Canon 50D) was used as the detector to capture the light from the objects. A long-distance microscope (K_2 DistaMax Infinity) and a CF-2 objective were equipped with the DSLR camera for the magnification of the near-field spray structure. An electronic flash (Canon EL-1) was used as the illumination light source with a nominal flash duration of 10 µs to "freeze" the motion of the spray objects. The FOV and the depth of field (DOF) of the optical setup were 10 mm × 9 mm (length × width) and 3 mm, respectively. The in-plane spatial resolution was determined from the FOV divided by the image resolution (i.e. total pixels of the camera) as 3 µm.

The major nondimensional influencing parameters for spray atomisation are calculated to investigate the spray characteristics of the biofuel surrogate/hydrogen flames. The gas/liquid (g/l) momentum flux ratio (ψ_p), exit Weber number (We), gas/liquid bulk mean Reynolds number ratio (ψ_{Re}), and Ohnesorge number (Oh) are defined in Equations 1, 2, 3, and 4, respectively [30].

$$\psi_p = \frac{\rho_g U_g^2}{\rho_l U_l^2} \tag{1}$$

$$We = \frac{\rho_g (U_g - U_l)^2 D_l}{\sigma} \tag{2}$$

$$Re = \frac{\rho U L}{\mu} \tag{3}$$

$$Oh = \frac{\mu}{\sqrt{\rho \sigma L}} \tag{4}$$

where ρ denotes the density of the fluid, U is the bulk mean velocity, σ is the surface tension of the liquid, μ is the dynamic viscosity of the fluid, D_l is the initial liquid jet diameter, and L is the jet diameter of the fluid.

2.4. Chemical analysis

In this study, numerical simulations were utilised to gain a deeper comprehension of the chemistry involved and the dominant reaction pathways responsible for polycyclic aromatic hydrocarbon (PAH) formation in biofuel-blended hydrogen flames. The simulations were conducted using the opposed-flow non-premixed (OPPDIF) flame model in Chemkin Pro v19.2. The OPPDIF model, commonly combined with experimental methods, allows for an investigation of flame behaviour and chemical kinetics in jet flames [31, 32].

The chemical kinetic mechanism employed in this research was developed by the CRECK Modelling Group specifically for modeling soot formation [33, 34]. It consists of 24,501 reactions and 497 species related to the combustion of hydrocarbons ranging from C_1 to C_{16}. However, the current study only considered the presence of anisole and guaiacol in the chemical kinetics modeling. To the best of the authors' knowledge, a comprehensive chemical kinetics mechanism that includes soot precursors is not available for essential oil surrogates—eucalyptol and D-limonene. The concentrations of guaiacol and anisole were varied while keeping the H_2 concentration fixed to simulate different experimental

cases. The fuel and oxidant inlet velocities were adjusted to maintain similar momentum conditions. To predict soot formation and the corresponding thermal radiation in the biofuel-blended hydrogen flames, the Chemkin simulation focused on analysing naphthalene ($C_{10}H_8$, hereafter referred to as A_2). Naphthalene is commonly employed in numerical studies as a key intermediate in the formation of large PAHs to investigate soot formation [4, 35, 36].

3. Results and discussion

3.1. Flame appearance

The flame appearance of the spray biofuel surrogate blended hydrogen flames is compared with the unblended hydrogen flame, shown in Figure 3. The spray essential oil surrogates (i.e. D-limonene and eucalyptol) and bio-oil surrogates (i.e. guaiacol and anisole) blended hydrogen flames are presented in Figure 3a and Figure 3b, respectively. The long-exposure (10 s) photographs illustrate the mean characteristics of the biofuel surrogate blended hydrogen flames. Additional short-exposure photographs (2 ms) of eucalyptol and anisole blended hydrogen flames capture the instantaneous soot distribution in the flame envelope.

The unblended hydrogen flame (HU0) is dominated by red colouration due to the presence of water vapour as the major combustion product of hydrogen. It is the least luminous flame presented in Figure 3. With the addition of 0.1–0.3% biofuel surrogates, the visibility of the unblended hydrogen flame is improved. As the biofuel surrogates are added to the flame, enhanced blue colouration appears near the jet exit (axial distance x = 0–180 mm from the jet exit) in contrast to the nearly invisible region in the unblended hydrogen flame. The enhanced blue colouration is ascribed to the formation of carbonaceous radicals—

HCO^*, C_2^*, CH^*, and CO_2^* by the biofuel blending [4]. The red colouration from the middle to the tip of the unblended hydrogen flame is transformed to yellow, which is a typical indication of soot formation, as the 0.1, 0.2, and 0.3 mol% biofuel surrogates are added. A clear shift to yellow colouration is achieved by the gas-assist atomisation of the biofuel additives. In contrast, it has been reported that adding 0.2–1 mol% biofuel surrogates by prevapourisation or ultrasonic atomisation enhances the blue colouration due to promoted formation of carbonaceous radicals, but the transition to yellow colouration was not observed [7]. The dominant source of flame luminosity is shifted from gaseous species to soot particulates in these sooting gas-assist atomised biofuel surrogate/hydrogen flames. The promoted soot loading in the gas-assist atomised biofuel surrogate/hydrogen flames indicates that the alternation of the introduction method benefits the soot formation. From the direct observation of the photographs, the yellow colouration transformation is the most intensive in anisole/hydrogen flames. The region near the jet exit is occupied by yellow colouration, indicating an early formation of soot particulates in anisole/hydrogen flames. The eucalyptol/hydrogen flame illustrates the least enhancement in luminosity and soot formation among all biofuel surrogates.

The short-exposure photograph of anisole/hydrogen shows that soot particulates evidently cluster from the jet exit to the flame tip, whereas the soot can be barely seen in eucalyptol/hydrogen flames at the same camera settings. The soot clusters in anisole/hydrogen flames are ascribed to the local fuel-rich region created by large liquid fuel droplets from gas-assist atomisation, which will be further demonstrated by microscopic shadowgraphs in Section 3.4. The larger droplets generated from gas-assist atomisation benefit soot formation and corresponding luminosity enhancement by creating more intensive local fuel-rich conditions.

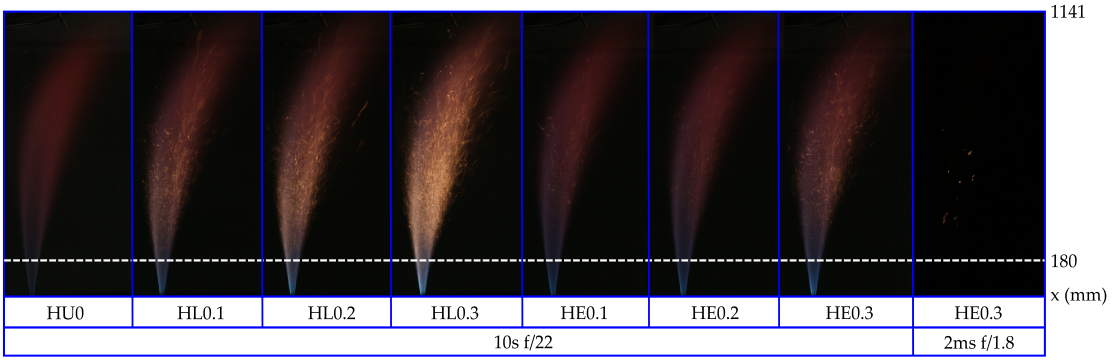

(a) Flame appearance of spray essential oil surrogates blended hydrogen flames

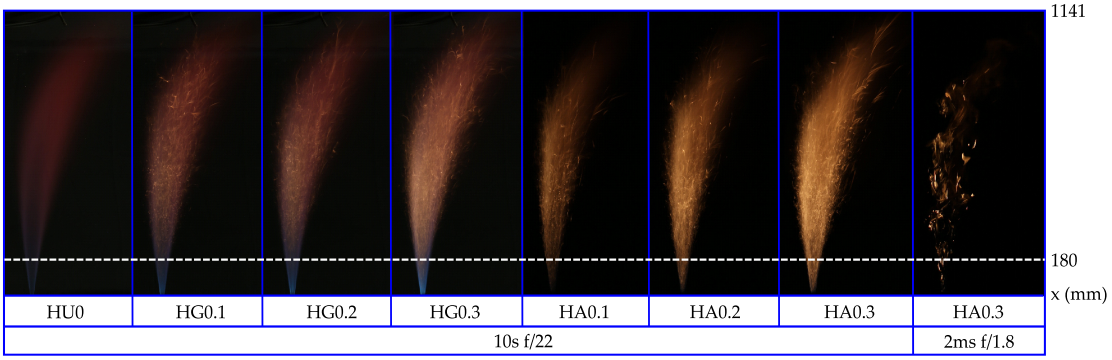

(b) Flame appearance of spray bio-oil surrogates blended hydrogen flames

Figure 3: Flame appearance of spray essential oil surrogates blended (3a) and bio-oil surrogates blended (3b) hydrogen flames. The flames were established on the horizontally oriented needle spray burner described in Section 2.1. "g" indicates the direction of gravity relative to the flame. The long-exposure (10 s) and short-exposure (2 ms) photographs were taken at ISO-100.

The average signal intensity extracted from the photographs shown in Figure 4 can present quantitative information on the luminosity of the flames. The average signal intensity is calculated by the summation of each pixel signal intensity in the FOV of the cropped image and the flame area obtained from the binarised image. The average signal intensity is normalised to the average signal intensity of 0.3 mol% anisole/hydrogen flame. The average signal intensity increases with the addition of gas-assist atomised biofuel surrogates, indicating that the flame luminosity of the hydrogen-based flame is enhanced by the addition of biofuel surrogates. The highest luminosity is found in the 0.3 mol% spray anisole/hydrogen flame, which is five times more luminous than the unblended hydrogen flame. The smallest luminosity increase of the unblended hydrogen flame is also 30% from blending 0.1 mol% spray eucalyptol/hydrogen flame. The luminosity enhancement of the unblended hydrogen flame is enhanced by 400% by the addition of 0.2 mol% gas-assist atomised anisole, whereas the 0.2 mol% prevapourised and ultrasonically atomised anisole only increases the luminosity by 200% [7]. The effectiveness of biofuel surrogates in hydrogen flame luminosity enhancement follows the trend as anisole $>$ D-limonene $>$ guaiacol $>$ eucalyptol. The luminosity of these sooting gas-assist atomised biofuel/hydrogen flames is primarily contributed by the incandescence from soot particulates formed in the flame. Anisole produces the most soot among the biofuel surrogates, thus it has the most luminosity enhancement. The effect of functional groups will be discussed together with the radiant fraction results in Section 3.3. The average signal intensity extracted from the photographs further provides quantitative evidence to support the effectiveness of luminosity enhancement of biofuel blending, in addition to the direct observation of the photographs.

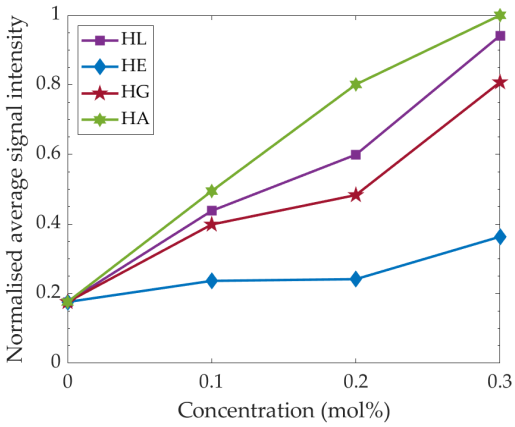

Figure 4: Flame luminosity indicated by the average signal intensity from photographs of spray biofuel surrogate blended H_2 flames described in Table 1. The average signal intensity is calculated by the summation of each pixel signal intensity and the flame area obtained from the binarised image. The average signal intensity is normalised to the peak signal intensity of 0.3 mol% anisole-blended H_2 flame.

3.2. Flame temperature

The flame temperature measured at x = 150 mm (axial distance from the jet exit on centre-line) of the gas-assist atomised biofuel surrogate/hydrogen flame as a function of additive's concentration is presented in Figure 5. The flame temperature shows a decreasing trend with the addition of biofuel additives. The unblended hydrogen flame has a flame temperature of 945°C. The 0.3 mol% anisole/hydrogen flame exhibits the lowest flame temperature at 850°C. The flame temperature drop as a result of spray biofuel addition is up to 95°C. The flame temperature of biofuel surrogate blended hydrogen flames follows the trend from high to low as eucalyptol $>$ guaiacol $>$ limonene $>$ anisole. The phenomenon of flame temperature drop with the spray biofuel addition is ascribed to the following factors: 1) the lower flame temperature of the biofuel surrogates; 2) the enthalpy of vapourisation; and 3) the radiative heat loss from the promoted soot loading in the blended flames. The larger droplets formed by the gas-assist atomisation lead to a greater enthalpy of vapourisation.

It is observed from Figures 3, 4 and 5 that the luminosity enhancement of the biofuel surrogates shows a reverse trend to the flame temperature drop. Anisole blends exhibit the largest luminosity enhancement while displaying the most significant flame temperature drop. This phenomenon implies that the radiative heat loss becomes a major factor of the flame temperature drop in these sooting blended hydrogen flames. As discussed in Section 3.1, sooting biofuel surrogate/hydrogen flames are achieved by the gas-assist atomisation such that the presence of the soot particulates is the major contribution to flame luminosity enhancement. As the soot formation is promoted with the biofuel surrogate addition, the fraction of radiative heat transfer is increased in the total heat output of the fuel mixture correspondingly, leading to the flame temperature decreases. Therefore, the biofuel surrogate that produces more soot particulates tends to have a larger flame temperature drop. It is also observed that the centreline temperature drop in these sooting gas-assist atomised biofuel surrogate/hydrogen flames is more significant than that in non-sooting ultrasonically atomised biofuel surrogate/hydrogen flames [6, 7]. Despite the factor of the enthalpy of vapourisation in both flames, the additional radiative heat loss from sooting gas-assist atomised biofuel/hydrogen flames may cause the larger flame temperature drop. The radiant fraction presented in the following Section 3.3 will further support this hypothesis.

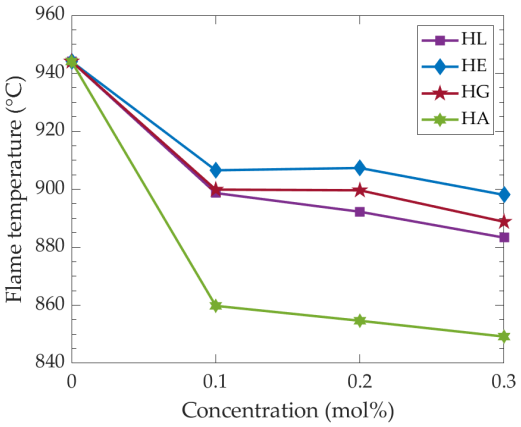

Figure 5: Flame temperature of spray biofuel surrogate blended H_2 flames measured at axial distance x = 150 mm from the jet exit on centreline. The flame temperature is corrected for radiative heat loss from the thermocouple.

3.3. Radiant heat flux

To investigate the radiant heat flux enhancement by the addition of gas-assist atomised biofuel surrogates, a radiant fraction is calculated based on the global radiant heat flux data measured by the heat flux sensor. The radiant fraction is calculated using Equation 5 [37]:

$$\chi_r = \frac{\dot{Q}_r}{\dot{Q}_F} = \frac{2 \cdot \pi \cdot \left(\int_{R_0}^{R} r \cdot \dot{q}''(r) \cdot dr + R \cdot \int_0^{\infty} \dot{q}''(z) \cdot dz \right)}{\dot{m} \times LHV} \tag{5}$$

where χ_r denotes the radiant fraction as the fraction of radiated heat $\dot{Q}_r$ (kW) normalised by the total heat input $\dot{Q}_F$ (kW) of the flame. The radiated heat ($\dot{Q}_r$) is acquired by the heat flux transducer, which is the summation of the axial (z) and radial (r) radiant heat flux ($\dot{q}''$). The radial distance between the heat flux sensor and the centre of the jet exit R and the flame front R_0 are considered in this equation. LHV and $\dot{m}$ denote the lower heating value and the mass flow rate of the fuel, respectively.

Figure 6a presents the global radiant fraction of the unblended and gas-assist atomised biofuel surrogate/hydrogen flames as a function of the biofuel surrogates' concentration. All global radiant fractions of the blended hydrogen flame increase with the addition of the biofuel surrogates. The effectiveness of the biofuel surrogates in radiant fraction enhancement ranks from significant to mild as: anisole > limonene > eucalyptol > guaiacol. The largest radiant fraction enhancement of an unblended hydrogen flame is from the addition of 0.3 mol% anisole by 15%. The smallest increase in the radiant fraction of an unblended hydrogen flame is 2%, from the addition of 0.1% guaiacol. Both anisole and guaiacol have a methoxy group (-OCH_3) while guaiacol possesses an additional hydroxyl group (-OH) in the ortho position of the methoxy function. The decomposition of anisole and guaiacol initiates at the weakest O-C chemical bond in the methoxy group

with bond dissociation enthalpy (BDE) of 243 kJ/mol (guaiacol) and 264 kJ/mol (anisole), respectively [27, 38]. The loss of methyl group followed by ipso-additions on guaiacol forms pyrocatechol as the primary product of the guaiacol reaction. Pyrocatechol is comprised of two hydroxyl groups which are more readily accessible to react with soot and PAHs to promote soot oxidation [39]. In addition, the BDEs of the C-H bond in the aromatic ring of guaiacol (481–490 kJ/mol) are higher than that in anisole (471–476 kJ/mol), making the aromatic ring in guaiacol less reactive [27, 40]. The formation of naphthalene—a critical intermediate in soot formation, has been detected in both pyrolysis and oxidation of anisole but only detected in the oxidation of guaiacol [27]. Compared with bio-oil surrogates, D-limonene, and eucalyptol are less effective than anisole on radiant fraction enhancement due to the higher unsaturation degree of aromatic structures, and the lowest BDE of the C-H bond in the allylic group of D-limonene (371 kJ/mol) is still much higher than that in anisole [41]. The minor effectiveness of guaiacol on radiant fraction enhancement compared with the essential oil surrogates may imply that the effect of the additional hydroxyl group in guaiacol on promoting PAH oxidation overwhelms the advantages of aromatic structures in PAH formation, resulting in a lower global radiant fraction.

The rate of production (ROP) of naphthalene (A_2) from the numerical simulation of guaiacol and anisole blended hydrogen flames, shown in Figure 6b, further supports the observation from the experimental results that anisole tends to have higher A_2 ROP than guaiacol hence larger radiant fraction enhancement. The A_2 ROP in the 0.3 mol% anisole-blended hydrogen flame is up to seven times greater than that in 0.3 mol% guaiacol-blended hydrogen flame. Figures 7a and 7b illustrate six dominant chemical reaction pathways of A_2 formation in anisole/hydrogen and guaiacol/hydrogen flames, respectively. The results show that $H_2 + C_{10}H_7 \rightleftharpoons H + A_2$ is the most dominant chemical reaction in forming A_2

in both anisole/hydrogen and guaiacol/hydrogen flames, followed by the reverse reactions of $H_2 + A_2 \rightleftharpoons H + C_{10}H_7$, and $H + A_2 \rightleftharpoons 0.5 \cdot C_{10}H_7 + 0.5 \cdot$Tetralin. The similar dominant chemical reaction pathways of A_2 formation found in anisole and guaiacol suggest similar pyrolysis and reaction processes. The reaction initiates at the weakest O-C bond of the methoxy group in both anisole and guaiacol. The PAH formation in these two aromatic fuels is mainly attributed to H-abstractions, which is consistent with the kinetic studies in the literature [27, 42]. Since guaiacol has a more stable aromatic structure with higher BDEs due to the presence of the additional hydroxyl group compared with anisole, although the dominant reactions are similar, the ROP of A_2 formation is significantly lower.

It has been reported that adding prevapourised and ultrasonically atomised 0.2 mol% anisole enhanced the radiant fraction of unblended hydrogen flame by 9% and 10%, respectively, less effective than 13% enhancement of radiant fraction from adding 0.2 mol% anisole by gas-assist atomisation [6, 7]. This is because in these sooting biofuel surrogate blended hydrogen flames, the radiant heat flux is primarily due to the blackbody radiation from soot particulates in the flame with minor contributions from the gaseous species such as CO_2 and water vapour. In contrast, the primary source of the radiant heat flux in prevapourised biofuel blended hydrogen flames is dominated by gaseous species. Given that radiant heat flux from soot particulates is much stronger than gaseous species, adding biofuel surrogates by gas-assist atomisation is more effective than the methods of prevapourisation and ultrasonic atomisation [43]. This trend agrees with the luminosity enhancement discussed in Section 3.1.

Soot formation, flame temperature, and radiant heat flux have complex interactions with each other. For a constant soot loading, higher flame temperature results in higher radiant heat flux because blackbody radiation has a quartic relationship with the temperature

($Q_r \propto T^4$). Hence, mild variation in flame temperature has a significant influence on the radiant heat flux. However, the higher temperature provides energy for soot oxidation and facilitates the soot oxidation rate, leading to a reduction in soot particulate which is the essential source of the blackbody radiation.

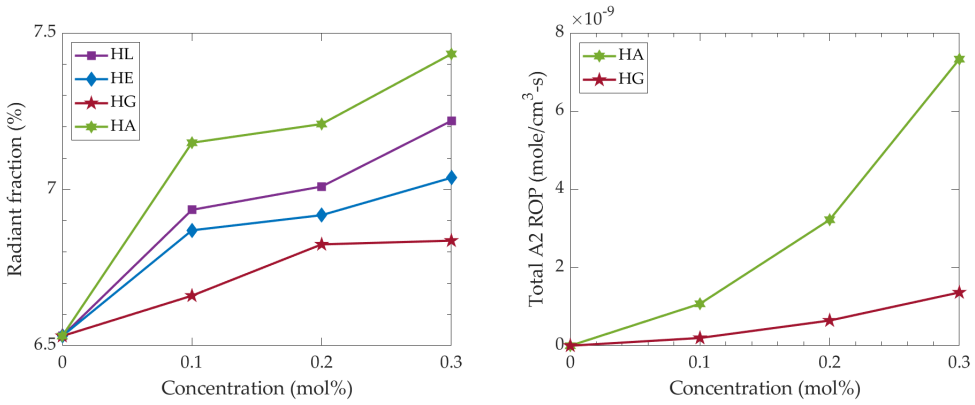

Figure 6: (6a) Global radiant fraction measured from spray biofuel surrogate blended H_2 flames described in Table 1. (6b) The rate of production (ROP) of naphthalene (A_2) from numerical simulation of guaiacol and anisole blended H_2 flames.

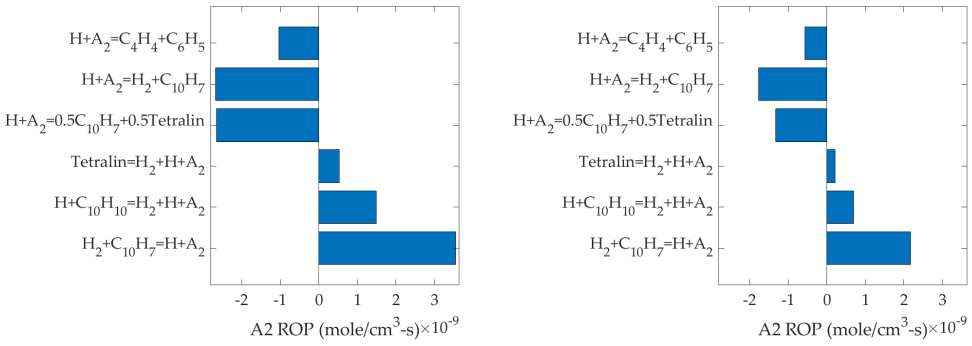

Figure 7: Dominant chemical reaction pathways of naphthalene (A_2) formation in anisole/hydrogen (7a) and guaiacol/hydrogen (7b) flames described in Table 1.

3.4. Microscopic shadowgraphy

The near-field spray characteristics are identified by the microscopic shadowgraph imaging as five major structures: (**A**) liquid core, (**B**) wave structure, (**C**) irregular object, (**D**) ligament, and (**E**) droplet. The liquid core (**A**) and wave structure (**B**) characterise the intact liquid stream as it is ejected from the jet. The subsequent formation of fragments **C**, **D**, and **E** may be classified by their aspect ratio (AR), characteristic major length (ℓ_{max}), and initial liquid jet diameter (D_l) as follows [23, 44–48]:

- Droplets ($\ell_{max} < D_l$ and AR < 3).
- Ligaments (AR > 3).
- Irregular objects (AR > 3, $\ell_{max} > D_l$).

where AR is the aspect ratio, ℓ_{max} is the characteristic major length, and D_l is the initial liquid jet diameter.

The representative microscopic shadowgraphs of the near-field spray characteristics of the biofuel surrogate/hydrogen flames are shown in Figure 8. From the direct observation from the shadowgraphs, guaiacol, and eucalyptol sprays appear to display different overall spray characteristics compared with D-limonene and anisole sprays. Guaiacol and eucalyptol sprays exhibit more dispersed spray than D-limonene and anisole sprays, indicating a finer spray. A relatively larger number of droplets are present in the near-field region of the spray in D-limonene and anisole flames in contrast to very limited droplets generated in eucalyptol and guaiacol sprays. The liquid core of the eucalyptol spray is evidently more elongated than the D-limonene and anisole sprays. The extent of the liquid core elongation is even more significant in guaiacol sprays. These observations are ascribed to

the different physical properties of eucalyptol and guaiacol that they have higher viscosity and surface tension than D-limonene and anisole, which in turn have a significant impact on the spray characteristics. The dynamic viscosity of eucalyptol is 2.6 mPa·s whereas the dynamic viscosity of D-limonene and anisole is less than 1 mPa·s [18, 49, 50]. Guaiacol, the representative pattern of lignin, has a dynamic viscosity of 6.1 mPa·s, more than six times greater than D-limonene and anisole [51, 52]. Similar to the viscosity difference, the surface tensions of guaiacol 37 mN/m and eucalyptol 62 mN/m are higher than D-limonene (26 mN/m) and anisole (35 mN/m) [53–55].

The distinct physical properties of the liquid fuel lead to a large difference in exit Weber number and Ohnesorge number, which are critical nondimensional influencing parameters for spray characteristics. The Weber number indicates the relationship between the disruptive hydrodynamic force—inertia force and the stablising force—surface tension in fluid dynamics. The Ohnesorge number reflects the effect of viscosity on the tendency of the droplet breakup. A larger Ohnesorge number requires a larger critical Weber number for liquid stream breakup which is defined as the value at which droplet breakup occurs. It is seen in Table 1 that the exit Weber number and Ohnesorge number of the biofuel surrogate blended flames are insensitive to the liquid fuel concentration because the liquid flow rate is very low compared with the gas flow rate. Since the density of the liquid fuel is similar (840–1100 kg/m^3), the difference in these two parameters is mainly from their viscosity and surface tension. The exit Weber number of D-limonene and anisole are larger than guaiacol and eucalyptol, indicating that the inertia force tends to overcome the cohesion force more easily in these fluids hence resulting in more intensive liquid stream breakup. The Oh of guaiacol (0.0385) is the largest followed by eucalyptol (0.0138), whereas D-limonene and anisole have similar smaller values of $Oh \approx 0.007$. A larger value of Oh implies that the effect of viscosity has a greater impact on the dispersion of droplets that

they tend to cluster together. These analyses of the physical properties and influencing parameters explain the direct observations from the microscopic shadowgraphs.

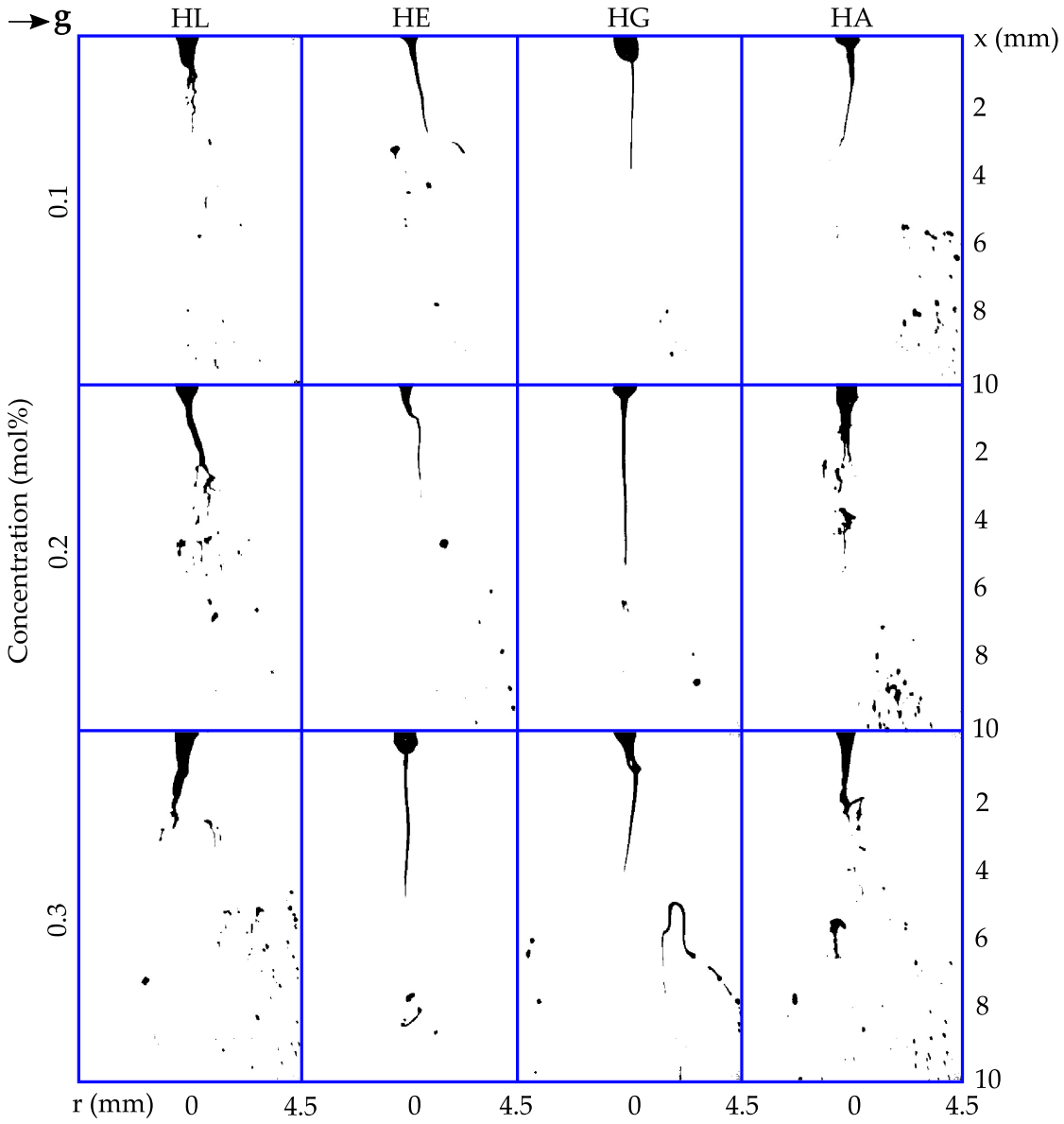

Figure 8: Representative microscopic shadowgraphs for the near-field (x = 0–10 mm) spray characteristics of biofuel surrogate blended H_2 flames described in Table 1. "g" indicates the direction of gravity relative to the flame.

The key spray characteristics including breakup length, the characteristic major length (ℓ_{max}) of droplets, and the area fraction (A_S/A_T) of the spray objects occupied area to the total area (FOV) are extracted from the microscopic shadowgraphs to study the sprays of different biofuel surrogates. The breakup length, the characteristic major length (ℓ_{max}) of droplets and ligaments, and the area fraction (A_S/A_T) of the biofuel surrogate sprays as a function of biofuel surrogate concentration, gas/liquid momentum flux ratio (ψ_p), gas/liquid Reynolds number ratio (ψ_{Re}), and exit Weber number (We) are presented in Figures 9, 10, and 11, respectively.

Figure 9 shows that for the same biofuel surrogate, the breakup length of the gas-assist biofuel spray increases with the liquid loading and decreases with the gas/liquid momentum flux ratio (ψ_p). Larger ψ_p and ψ_{Re} values induce a higher level of instabilities on the gas/liquid interface and turbulence of the flows, leading to a more intense primary breakup of the liquid stream. A larger breakup length value is an indication of a coarser spray. It is observed that the gas/liquid momentum flux ratio (ψ_p) is not suitable for predicting breakup length across various liquid fuels since the breakup length varies across different liquid fuels at the same ψ_p. This means that other factors such as viscosity and surface tension may play a non-negligible role in the variation of breakup length. Guaiacol sprays display the largest breakup length followed by eucalyptol sprays. The breakup lengths of D-limonene and anisole are similar and smaller than eucalyptol sprays. This trend of breakup length is consistent with the order of the fuel viscosity—guaiacol $>$ eucalyptol $>$ D-limonene $\approx$ anisole, implying that the viscosity of the liquid fuel may have a significant impact on the breakup length of the gas-assist spray. In the guaiacol and eucalyptol sprays, the liquid cores are elongated as a result of higher viscosity and surface tension acting against the disruptive force from the instabilities on the surface. The resistance of the higher viscosity to the motion of the flow keeps the liquid stream propagating in the direction of the initial

momentum rather than spreading into a wide angle of direction. The elongated liquid core eventually breaks at a weak point into ligaments with large characteristic major lengths and aspect ratios rather than directly into droplets. Hence more ligament structures with larger ℓ_{max} are observed in guaiacol and eucalyptol sprays in contrast to D-limonene and anisole sprays.

The characteristic major length of droplets, shown in Figure 10, increases with the liquid loading and decreases with ψ_p, ψ_{Re}, and We. The characteristic major length of droplets in the gas-assist spray flames ranges from 0.08–0.34 mm. Dissimilar to the breakup length trend, eucalyptol sprays generate the largest droplets followed by guaiacol sprays, anisole sprays, and D-limonene sprays. The order of the droplets ℓ_{max} is the reverse order of the We in Table 1 as eucalyptol $>$ guaiacol $>$ anisole $>$ D-limonene, indicating that We is the dominant parameter for predicting the droplet size in gas-assist sprays. In conjunction with the observations of the breakup length, the liquid streams of D-limonene and anisole break up early into droplets while the liquid stream undergoes an elongation and then breaks up into ligaments. The number of droplets in D-limonene and anisole sprays is more than that in guaiacol and eucalyptol sprays. The dispersion of the spray objects can be further investigated by the area fraction results.

Figure 11 displays the area fraction of the biofuel surrogate spray flames. The area fraction is calculated by the area occupied by the spray objects and the FOV. For the same type of biofuel surrogate, the area fraction increases with the liquid loading and decreases with ψ_p and ψ_{Re}. It is interesting that the ψ_{Re} appears to dominate in describing the area fraction. The area fraction of these biofuel spray flames is mainly influenced by two factors: (i) surface area growth as a result of the primary and secondary breakup; and (ii) evapouration rate of the liquid in the spray flame. The guaiacol spray has the lowest

area fraction among all biofuel surrogates, which agrees with the observations of breakup length and droplet size results, appearing to be the most coarse spray. The area fractions of the biofuel surrogates follow the order from low to high as guaiacol $<$ eucalyptol $<$ anisole $<$ D-limonene, which is the opposite order of the Ohnesorge number. The area fraction analysis provides evidence to further support that liquid fuel with higher viscosity and surface tension tends to have lower dispersion and coarser sprays than that with lower viscosity and surface tension.

The results of spray characteristics provide evidence to analyse the more effective flame luminosity and radiant fraction enhancement found in gas-assist atomised biofuel/hydrogen flames, compared with prevapourised and ultrasonically atomised biofuel/hydrogen flames. The droplet size formed by gas-assist atomisation is found between 0.15–0.34 mm, much larger than the droplet size generated by ultrasonic atomisation at 0.03 mm (specified by the manufacturer) [7]. The presence of larger droplets in gas-assist atomised biofuel/hydrogen flames creates even more extreme fuel-rich conditions which further favours soot formation. In addition, the ultrasonically atomised droplets are entrained by hydrogen upstream of the jet exit and have an earlier and more homogeneous mixing with gaseous fuels, compared with less dispersion of liquid droplets and later mixing downstream of the jet exit in gas-assist atomisation. Therefore, the mixing of liquid fuel droplets and the local OH radicals from the reaction of hydrogen in gas-assist atomised biofuel/hydrogen flames is less homogeneous, again resulting in localised fuel-rich conditions.

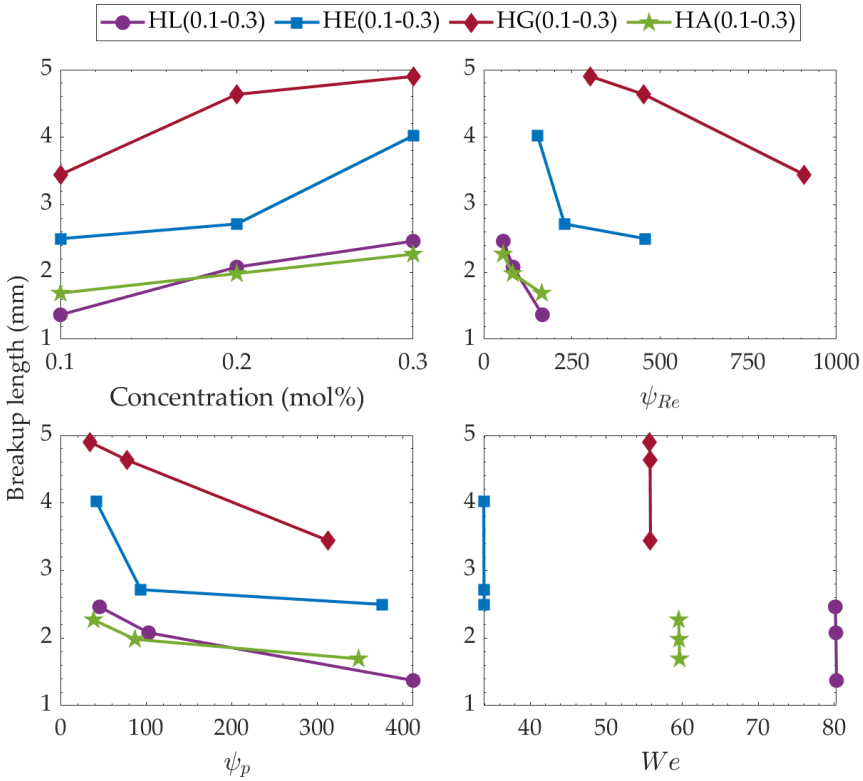

Figure 9: Breakup length of the gas-assist biofuel surrogate sprays as a function of biofuel concentration, gas/liquid momentum flux ratio (ψ_p), gas/liquid Reynolds number ratio (ψ_{Re}), and exit Weber number (We).

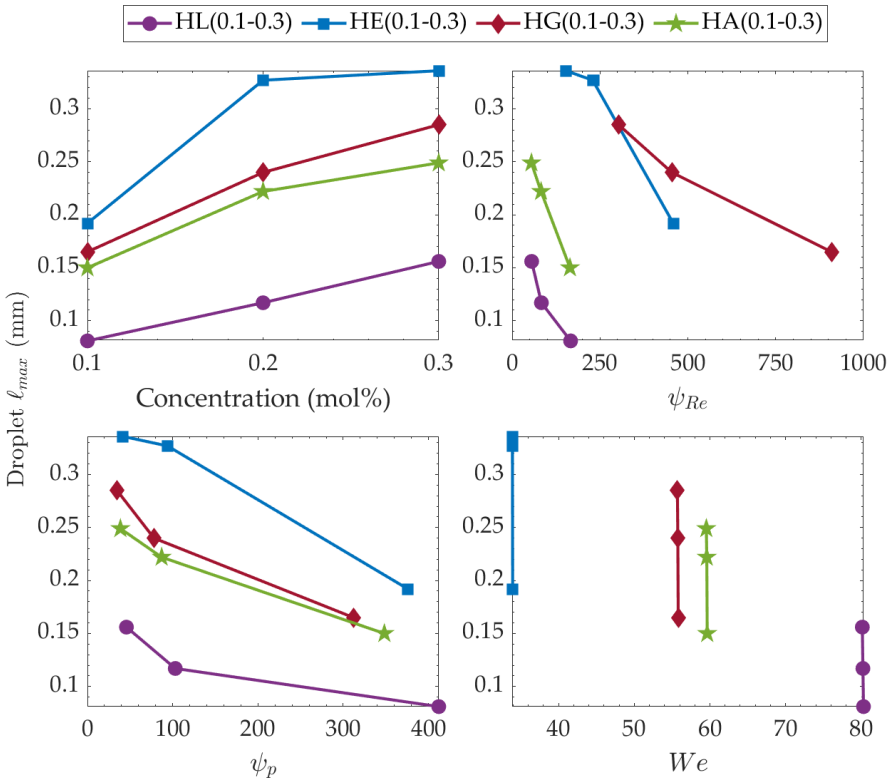

Figure 10: Droplet characteristic major length (ℓ_{max}) of the gas-assist biofuel surrogate sprays as a function of biofuel concentration, gas/liquid momentum flux ratio (ψ_p), gas/liquid Reynolds number ratio (ψ_{Re}), and exit Weber number (We).

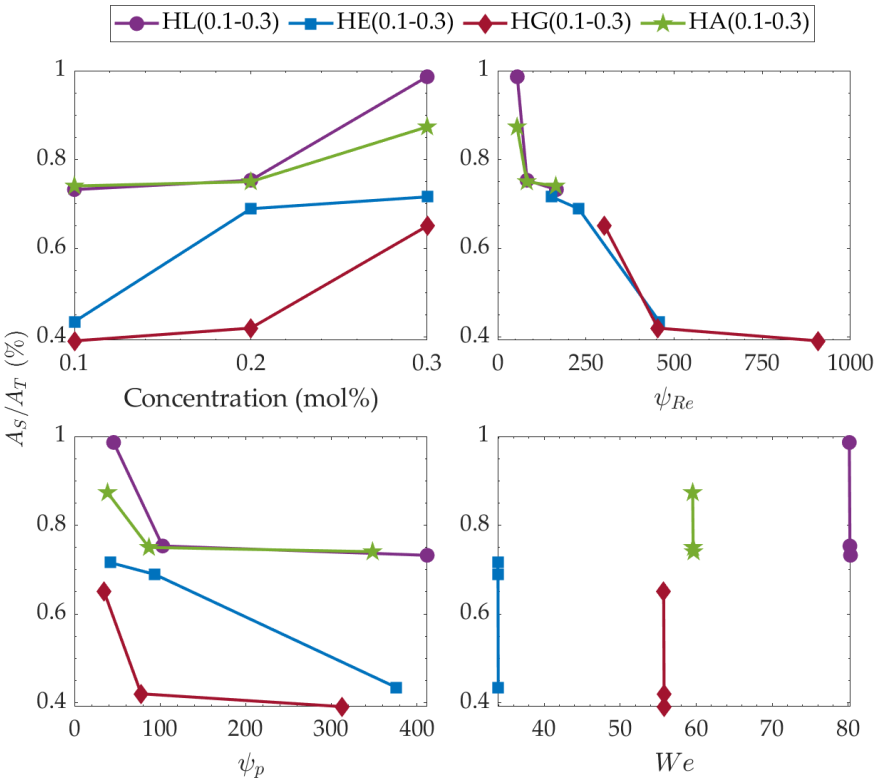

Figure 11: Area fraction (A_S/A_T %) of the gas-assist biofuel surrogate sprays as a function of biofuel concentration, gas/liquid momentum flux ratio (ψ_p), gas/liquid Reynolds number ratio (ψ_{Re}), and exit Weber number (We).

4. Conclusions

The effect of adding biofuel surrogates to turbulent nonpremixed pure hydrogen flames by gas-assist atomisation on the flame characteristics was investigated. The flame appearance, flame luminosity, flame temperature, radiant fraction, and near-field spray characteristics of essential oil surrogates (eucalyptol and D-limonene) and bio-oil surrogates (guaiacol and anisole) blended hydrogen flames were measured by experimental approaches. The key findings of this study are summarised as follows:

1. Thermal radiation of hydrogen flames was increased by blending biofuel surrogates in a coaxial spray burner by taking advantage of the gas-assist atomisation. A clear transition of flame colouration from blue/red to yellow was observed with the addition of 0.1–0.3 mol% biofuel surrogates.
2. The flame luminosity and the radiant fraction of the unblended hydrogen flame were increased by 30–500% and 2–15%, respectively, from the addition of 0.1–0.3 mol% biofuel surrogates, demonstrating that blending the biofuel surrogates by gas-assist atomisation is more effective than prevapourisation and ultrasonic atomisation.
3. The flame temperature measured at $x = 150\,\text{mm}$ on the centre axis of the gas-assist atomised biofuel surrogate/hydrogen flames dropped evidently due to the enthalpy of vapourisation and the promoted radiative heat loss from the enhanced soot formation.
4. The viscosity and surface tension of the liquid biofuel surrogates and the resultant variation in Weber number and Ohnesorge number impact the near-field spray characteristics. The droplets' characteristic major length of biofuel surrogate sprays is dominated by exit Weber number, following the reverse order of We as eucalyptol $>$ guaiacol $>$ anisole $>$ D-limonene. The area fraction of the biofuel surrogate sprays from low to high follows the order of guaiacol $<$ eucalyptol $<$ anisole $<$ D-limonene,

which is the reverse order of the Ohnesorge number. Guaiacol and eucalyptol sprays, which have higher viscosity and surface tension tend to generate coarser sprays than D-limonene and anisole.

5. Guaiacol, as a representative of the lignin pattern, is less effective than anisole, D-limonene, and eucalyptol in radiant fraction enhancement due to (i) the hydroxyl group promotes PAH oxidation; (ii) higher BDE of the aromatic ring makes guaiacol less reactive; and (iii) a coarser spay, i.e. larger breakup length, droplet size, ligament size, and less dispersed spray objects generated by the gas-assist atomisation compared with other biofuel surrogates tested.

Declaration of competing interest

The authors declare that they have no known competing financial interests or personal relationships that could have appeared to influence the work reported in this paper.

Acknowledgements

The research reported in this publication was supported by funding from The University of Adelaide, the Australian Research Council (ARC), and the Future Fuels Cooperative Research Centre (CRC).

References

[1] V. M. Reddy, P. Biswas, P. Garg, S. Kumar, Combustion characteristics of biodiesel fuel in high recirculation conditions, Fuel Process. Technol. 118 (2014) 310–317.

[2] W. Hutny, G. Lee, Improved radiative heat transfer from hydrogen flames, Int. J. Hydrog. Energy 16 (1991) 47–53.

[3] C. S. McEnally, L. D. Pfefferle, Sooting tendencies of oxygenated hydrocarbons in laboratory-scale flames, Environ. Sci. Technol. 45 (2011) 2498–2503.

[4] M. J. Evans, D. B. Proud, P. R. Medwell, H. Pitsch, B. B. Dally, Highly radiating hydrogen flames: effect of toluene concentration and phase, Proc. Combust. Inst. 38 (2021) 1099–1106.

[5] A. J. Gee, Y. Yin, K. K. Foo, A. Chinnici, N. Smith, P. R. Medwell, Toluene addition to turbulent h_2/natural gas flames in bluff-body burners, Int. J. Hydrog. Energy 47 (2022) 27733–27746.

[6] Y. Yin, P. R. Medwell, A. J. Gee, K. K. Foo, B. B. Dally, Fundamental insights into the effect of blending hydrogen flames with sooting biofuels, Fuel 331 (2023) 125618.

[7] Y. Yin, P. R. Medwell, B. B. Dally, Hydrogen turbulent nonpremixed flames blended with spray or prevapourised biofuels, Int. J. Hydrog. Energy 48 (2023) 25563–25580.

[8] P. Pandey, B. Pundir, P. Panigrahi, Hydrogen addition to acetylene–air laminar diffusion flames: studies on soot formation under different flow arrangements, Combust. Flame 148 (2007) 249–262.

[9] F. Ren, H. Chu, L. Xiang, W. Han, M. Gu, Effect of hydrogen addition on the laminar premixed combustion characteristics the main components of natural gas, J. Energy Inst. 92 (2019) 1178–1190.

[10] F. Liu, Y. Ai, W. Kong, Effect of hydrogen and helium addition to fuel on soot formation in an axisymmetric coflow laminar methane/air diffusion flame, Int. J. Hydrog. Energy 39 (2014) 3936–3946.

[11] J. Li, H. Huang, N. Kobayashi, Z. He, Y. Nagai, Study on using hydrogen and ammonia as fuels: combustion characteristics and NO_x formation, Int. J. Energy Res. 38 (2014) 1214–1223.

[12] S. H. Park, K. M. Lee, C. H. Hwang, Effects of hydrogen addition on soot formation and oxidation in laminar premixed C_2H_2/air flames, Int. J. Hydrog. Energy 36 (2011) 9304–9311.

[13] D. Gu, Z. Sun, B. B. Dally, P. R. Medwell, Z. T. Alwahabi, G. J. Nathan, Simultaneous measurements of gas temperature, soot volume fraction and primary particle diameter in a sooting lifted turbulent ethylene/air non-premixed flame, Combust. Flame 179 (2017) 33–50.

[14] M. S. Celnik, M. Sander, A. Raj, R. H. West, M. Kraft, Modelling soot formation in a premixed flame using an aromatic-site soot model and an improved oxidation rate, Proc. Combust. Inst. 32 (2009) 639–646.

[15] I. Glassman, Soot formation in combustion processes, in: Symp. (Int.) Combust., volume 22, Elsevier, pp. 295–311.

[16] L. Li, P. B. Sunderland, An improved method of smoke point normalization, Combust. Sci. Technol. 184 (2012) 829–841.

[17] M. E. Mueller, Q. N. Chan, N. H. Qamar, B. B. Dally, H. Pitsch, Z. T. Alwahabi, G. J. Nathan, Experimental and computational study of soot evolution in a turbulent nonpremixed bluff body ethylene flame, Combust. Flame 160 (2013) 1298–1309.

[18] S. W. Wagnon, S. Thion, E. J. Nilsson, M. Mehl, Z. Serinyel, K. Zhang, P. Dagaut, A. A. Konnov, G. Dayma, W. J. Pitz, Experimental and modeling studies of a biofuel surrogate compound: laminar burning velocities and jet-stirred reactor measurements of anisole, Combust. Flame 189 (2018) 325–336.

[19] D. B. Proud, M. J. Evans, P. R. Medwell, Q. N. Chan, Experimental investigation of the flame structure of dilute sprays issuing into a hot and low-oxygen coflow, Combust. Flame 230 (2021) 111439.

[20] C. Dumouchel, On the experimental investigation on primary atomization of liquid streams, Exp. Fluids 45 (2008) 371–422.

[21] P. Jenny, D. Roekaerts, N. Beishuizen, Modeling of turbulent dilute spray combustion, Prog. Energy Combust. Sci. 38 (2012) 846–887.

[22] A. Kourmatzis, P. X. Pham, A. R. Masri, Characterization of atomization and combustion in moderately dense turbulent spray flames, Combust. Flame 162 (2015) 978–996.

[23] A. Lowe, A. Kourmatzis, A. R. Masri, Turbulent spray flames of intermediate density: Stability and near-field structure, Combust. Flame 176 (2017) 511–520.

[24] J. L. Zheng, Y.-P. Kong, Spray combustion properties of fast pyrolysis bio-oil produced from rice husk, Energy Convers. Manag. 51 (2010) 182–188.

[25] K. Narayanaswamy, H. Pitsch, P. Pepiot, A component library framework for deriving kinetic mechanisms for multi-component fuel surrogates: application for jet fuel surrogates, Combust. Flame 165 (2016) 288–309.

[26] P. G. Szymkowicz, J. Benajes, Development of a diesel surrogate fuel library, Fuel 222 (2018) 21–34.

[27] M. Nowakowska, O. Herbinet, A. Dufour, P.-A. Glaude, Kinetic study of the pyrolysis and oxidation of guaiacol, J. Phys. Chem. A 122 (2018) 7894–7909.

[28] S. A. Rahman, T. C. Van, F. Hossain, M. Jafari, A. Dowell, M. Islam, M. N. Nabi, A. Marchese, J. Tryner, T. Rainey, et al., Fuel properties and emission characteristics of essential oil blends in a compression ignition engine, Fuel 238 (2019) 440–453.

[29] S. Rahman, M. Nabi, T. C. Van, K. Suara, M. Jafari, A. Dowell, M. Islam, A. J. Marchese, J. Tryner, M. Hossain, et al., Performance and combustion characteristics analysis of multi-cylinder ci engine using essential oil blends, Energies 11 (2018) 738.

[30] A. Kourmatzis, P. X. Pham, A. R. Masri, Air assisted atomization and spray density characterization of ethanol and a range of biodiesels, Fuel 108 (2013) 758–770.

[31] P. A. Glaude, W. J. Pitz, M. J. Thomson, Chemical kinetic modeling of dimethyl carbonate in an opposed-flow diffusion flame, Proc. Combust. Inst. 30 (2005) 1111–1118.

[32] G. Dayma, S. Sarathy, C. Togbé, C. Yeung, M. Thomson, P. Dagaut, Experimental and kinetic modeling of methyl octanoate oxidation in an opposed-flow diffusion flame and a jet-stirred reactor, Proc. Combust. Inst. 33 (2011) 1037–1043.

[33] W. Pejpichestakul, A. Cuoci, A. Frassoldati, M. Pelucchi, A. Parente, T. Faravelli, Buoyancy effect in sooting laminar premixed ethylene flame, Combust. Flame 205 (2019) 135–146.

[34] T. Faravelli, A. Frassoldati, E. Ranzi, Kinetic modeling of the interactions between NO and hydrocarbons in the oxidation of hydrocarbons at low temperatures, Combust. Flame 132 (2003) 188–207.

[35] F. Bisetti, G. Blanquart, M. E. Mueller, H. Pitsch, On the formation and early evolution of soot in turbulent nonpremixed flames, Combust. Flame 159 (2012) 317–335.

[36] A. Violi, A. D'Anna, A. D'Alessio, Modeling of particulate formation in combustion and pyrolysis, Chem. Eng. Sci. 54 (1999) 3433–3442.

[37] R. Buch, A. Hamins, K. Konishi, D. Mattingly, T. Kashiwagi, Radiative emission fraction of pool fires burning silicone fluids, Combust. Flame 108 (1997) 118–126.

[38] Y. D. Wu, D. K. Lai, A density functional study of substituent effects on the o- h and o- ch3 bond dissociation energies in phenol and anisole, J. Org. Chem. 61 (1996) 7904–7910.

[39] B. Graziano, P. Burkardt, M. Neumann, H. Pitsch, S. Pischinger, Development of a modified joback–reid group contribution method to predict the sooting tendency of oxygenated fuels, Energy & Fuels 35 (2021) 13144–13158.

[40] K. Agrawal, A. M. Verma, N. Kishore, Thermochemical conversion of guaiacol in aqueous phase by density functional theory, ChemistrySelect 4 (2019) 6013–6025.

[41] T. Bierkandt, M. Hoener, N. Gaiser, N. Hansen, M. Köhler, T. Kasper, Experimental flat flame study of monoterpenes: Insights into the combustion kinetics of α-pinene, β-pinene, and myrcene, Proc. Combust. Inst. 38 (2021) 2431–2440.

[42] M. Nowakowska, O. Herbinet, A. Dufour, P.-A. Glaude, Detailed kinetic study of anisole pyrolysis and oxidation to understand tar formation during biomass combustion and gasification, Combust. Flame 161 (2014) 1474–1488.

[43] K. Andersson, R. Johansson, F. Johnsson, Thermal radiation in oxy-fuel flames, Int. J. Greenh. Gas Control 5 (2011) S58–S65.

[44] S. Ghaemi, P. Rahimi, D. S. Nobes, Assessment of parameters for distinguishing droplet shape in a spray field using image-based techniques, At. Sprays 19 (2009) 809–831.

[45] S. Horiashchenko, K. Horiashchenko, J. Musial, Methodology of measuring spraying the droplet flow of polymers from nozzle, Mechanics 26 (2020) 82–86.

[46] G. Singh, A. Kourmatzis, A. Masri, Volume measurement of atomizing fragments using image slicing, Exp. Therm. Fluid Sci. 115 (2020) 110102.

[47] G. Singh, A. Kourmatzis, A. Masri, Dense sprays with a focus on atomization and turbulent combustion, Flow Turbul. Combust. 106 (2021) 405–417.

[48] A. Kourmatzis, P. X. Pham, A. R. Masri, A two-angle far-field microscope imaging technique for spray flows, Meas. Sci. Technol. 28 (2017) 035302.

[49] F. Comelli, S. Ottani, R. Francesconi, C. Castellari, Densities, viscosities, and refractive indices of binary mixtures containing n-hexane+ components of pine resins and essential oils at 298.15 k, J. Chem. Eng. Data. 47 (2002) 93–97.

[50] J. R. Ayala, G. Montero, H. E. Campbell, C. García, M. A. Coronado, J. A. León, C. A. Sagaste, L. J. Pérez, Extraction and characterization of orange peel essential oil from mexico and united states of america, J. Essent. Oil-Bear. Plants 20 (2017) 897–914.

[51] R. N. Olcese, J. François, M. Bettahar, D. Petitjean, A. Dufour, Hydrodeoxygenation of guaiacol, a surrogate of lignin pyrolysis vapors, over iron based catalysts: Kinetics and modeling of the lignin to aromatics integrated process, Energy & fuels 27 (2013) 975–984.

[52] M. Tian, R. L. McCormick, M. A. Ratcliff, J. Luecke, J. Yanowitz, P.-A. Glaude, M. Cuijpers, M. D. Boot, Performance of lignin derived compounds as octane boosters, Fuel 189 (2017) 284–292.

[53] J. J. Jasper, The surface tension of pure liquid compounds, J. phys. chem. ref. data 1 (1972) 841–1010.

[54] G. Vazquez, E. Alvarez, J. M. Navaza, Surface tension of alcohol water+ water from 20 to 50. degree. c, J. Chem. Eng. 40 (1995) 611–614.

[55] P. F. Onyekere, D. O. Nnamani, C. O. Peculiar-Onyekere, P. F. Uzor, Limonene, in: Green Sustainable Process for Chemical and Environmental Engineering and Science, Elsevier, 2021, pp. 219–227.

Chapter 8

Discussion

8.1 Radiant heat flux of biofuel/hydrogen and hydrocarbon flames

This chapter illustrates the internal connections within the research project and integrates the content and results contained in the individual articles to arrive at synthesised findings. The fundamental motivation of this research project is establishing and advancing the understanding of adding sooting renewable biofuels to enhance the radiant intensity of hydrogen flames for the replacement of fossil fuels in practical applications. In previous chapters, the radiant heat flux of biofuel/hydrogen flames has been compared with unblended hydrogen flames to analyse the effectiveness of adding biofuel on thermal radiation enhancement. To complement the results of the hydrogen-based flames, it is also insightful to compare the radiant heat flux of biofuel/hydrogen flames with commonly used fossil fuel flames in practical systems—natural gas flames.

It has been reported that the radiant fraction of pure hydrogen flames ($Re \approx 7,600$) is about 40% lower than H_2/natural gas (20:80 vol%) flames on a simple jet burner [1]. The results shown in Appendix A indicate that the thermal radiation of turbulent hydrogen flames ($Re > 10,000$) is 80% lower than that of natural gas flames on a bluff-body burner. The radiant fraction of hydrogen flames was found to be 55% lower than H_2/natural gas (80:20 vol%) flames at a constant Reynolds number of 150 on a circular fuel burner [2]. Given that thermal radiation differs between various burners, to enable a direct comparison, it is necessary to establish natural gas and unblended hydrogen flames on the needle spray burner described in §6.2.1.

Due to the blow-off limit of natural gas flames, fully turbulent ($Re > 10,000$) natural gas flames could not be stabilised on the burner. Therefore, a natural gas flame at $Re = 5,000$ was established on the needle spray burner as a reference flame to compare its radiant flux with unblended hydrogen flame at an equivalent heat input of the natural gas flame. The details of the natural gas and hydrogen flames are shown in Table 8.1. Through this comparison, the radiant heat flux of the biofuel/H_2 flames could be linked to natural gas flames to better understand the effectiveness of biofuel addition on thermal radiation enhancement.

Table 8.1: Details of the natural gas and unblended hydrogen flames established on the needle spray burner described in §6.2.1.

Parameter/Fuel	Natural gas	Hydrogen
Flow rate (L/min)	21	68
Exit velocity (m/s)	16	54
Heat input (kW)	11.2	11.2
Reynolds number	5,000	2,600

Figure 8.1 shows the radiant fraction comparison between the natural gas and hydrogen flames established on the needle spray burner described in §6.2.1. The radiant heat flux of the flames was measured by the heat flux sensor at the radial distance of 284 mm perpendicular to the jet centreline. The radiant fraction is calculated by Equation 3.1. The results show that the radiant fraction of the pure hydrogen flame is 40% less than the pure natural gas flame. This finding is similar to the radiant fraction difference reported in the literature—the radiant fraction of pure hydrogen flames ($Re \approx 7,600$) is about 40% lower than H_2/natural gas (20:80 vol%) flames on a jet burner [1]. These results provided background for the thermal radiation enhancement of hydrogen flames via biofuel addition in achieving equivalent thermal radiation of natural gas flames.

The amount of additives required to compensate for the thermal radiation difference between hydrogen and natural gas flames is critical for the adaptation of hydrogen flame in practical systems. It has been reported in Chapter 5 that the radiant fraction of unblended hydrogen flame was enhanced by 33% from the addition of 4 mol% prevapourised toluene. In other words, adding 4 mol% prevapourised toluene to hydrogen jet flames is close to compensating for the thermal radiation difference of NG jet flames. Similarly, the results from Appendix A show that 4 mol% prevapourised toluene addition is required for a hydrogen flame to attain equivalent radiant heat flux to a natural gas flame on a bluff-body burner. Given that hydrogen is a low

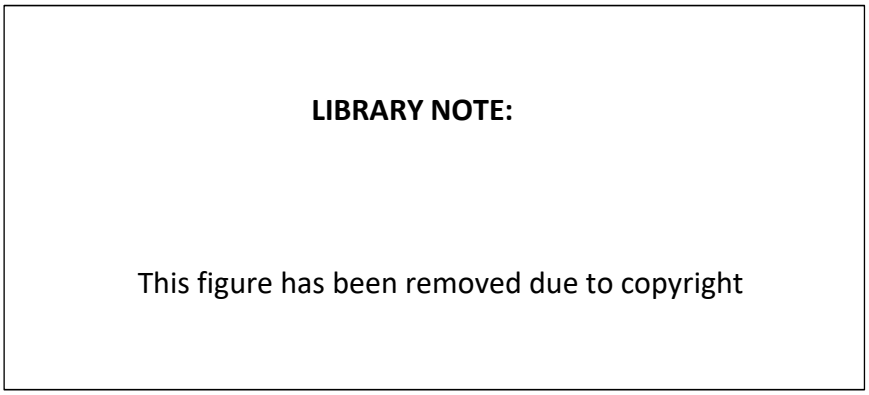

Figure 8.1: Comparison of the radiant fraction between natural gas and unblended hydrogen flames established on the needle spray burner described in §6.2.1. The natural gas flame has a Reynolds number of 5,000. The unblended hydrogen flame is at the equivalent heat input of the natural gas flame.

density fuel, although the molar fraction and the heat input of the amount of toluene required to achieve equivalent radiant heat flux to a natural gas flame are relatively low, the mass fraction of the 4 mol% toluene reaches 40 wt%.

Although the thermal radiation difference between hydrogen and NG jet flames measured in this study has provided backgrounds for the thermal radiation compensation from biofuel addition, the amount of biofuel needed for this purpose cannot be linearly predicted. This is because the biofuel concentration in hydrogen-based flames shows a non-linear correlation to radiant heat flux enhancement. Figure 8.2a and Figure 8.2b present the numerical results of PAHs (i.e. naphthalene) and CH_2O formation in toluene, anisole, and guaiacol blended hydrogen flames, respectively. The results are reproduced from data in Chapter 5 and 7. Figure 8.2a shows that the rate of production (ROP) of PAHs is low at 0.2–0.5 mol%, followed by a rapid increase from 0.5 mol% concentrations, which indicates a non-linear correlation between the biofuel concentration and PAH formation. This finding is consistent with the results reported by previous studies that adding 5 mol% or more toluene tends to have a larger increase in radiant heat flux compared with the toluene concentration from 1–5 mol% [3].

The results from Figure 8.2a show that toluene has a lower ROP of A2 than anisole and guaiacol. It is hypothesised that the weak bond in the methoxy groups of anisole and guaiacol more easily breaks and subsequently participates in the early stages of PAH formation [4, 5]; however, toluene

was reported to be the most effective for radiant fraction enhancement from the previous Chapters 4 and 5. This is because the ROP of CH_2O (i.e. the indicator of the PAH oxidation rate shown in Figure 8.2b) in toluene blends is a magnitude lower than that in anisole and guaiacol blends. Anisole and guaiacol are known as oxygenated fuels and the oxygen in these fuels promotes the PAH oxidation rate. The numerical results suggest that the oxidation rate of PAHs, rather than the production rate of PAHs, dominates the PAH/soot loading and resultant radiant intensity in these biofuel-blended hydrogen flames. Since toluene is the most effective of the biofuel surrogates tested for radiant fraction enhancement, it is worth noting that although other biofuel additives were not tested at 4 mol% or higher concentrations in this study, it can be predicted that more than 4 mol% of anisole, eucalyptol, D-limonene, and guaiacol is required to attain an equivalent radiant heat flux of a natural gas flame.

(b)

Figure 8.2: Numerical results of naphthalene (A2) and formaldehyde (CH_2O) ROP from anisole, guaiacol, and toluene blended H_2/N_2 flames adapted from Chapters 4 and 7. (a) Naphthalene (A2) ROP, and (b) Formaldehyde (CH_2O) ROP.

8.2 Comparison of introduction methods

8.2.1 Overview of introduction method impact

In Chapters 4 and 5, the sooting propensities of biofuel surrogates, the blending effect of prevapourisation/ultrasonic spray and concentration on the combustion characteristics of hydrogen flames have been understood to achieve Objectives 1 and 2. The influences of chemical structures and functional groups of biofuels on combustion characteristics of biofuel/hydrogen flames have been included in Chapters 4, 5, and 7 to address Objective 3. In accordance with Objective 4, the findings from needle spray burner characterisation using non-reacting flows (refer to Chapter 6) is coupled with gas-assist atomised biofuel surrogate/hydrogen flames (refer to Chapter 7), showing distinct flame characteristics including flame appearance, flame luminosity, flame temperature, and radiant fraction, compared with the additives introduced to the hydrogen flame by prevapourisation and ultrasonic atomisation discussed in Chapters 4, 5, and Appendix A. The impact of these three introduction methods on the combustion characteristics of biofuel/H_2 flames along with the influencing mechanisms are presented in this section.

8.2.2 Impact of introduction method on combustion characteristics

Flame appearance

Photographs of prevapourised, ultrasonic atomised, and gas-assist atomised biofuel-blended hydrogen-based flames are reproduced from Chapters 4, 5, and 7, shown in Figure 8.3 and Figure 8.4 for the comparison of the effect of introduction methods on flame appearance. Sooting turbulent hydrogen flames were achieved by adding 0.1–0.3 mol% gas-assist atomised biofuel surrogate (Figure 8.4), whereas the 0.2–1 mol% prevapourised (Figure 8.3a) and ultrasonic atomised (Figure 8.3b) biofuel surrogate blended hydrogen-based flames are still non-sooting. They are dominated by blue colouration due to the presence of gaseous species. In the short-exposure photographs, large amounts of soot are present in the anisole/hydrogen flames, which are not observed in the 0.2–1 mol% prevapourised and ultrasonically atomised biofuel/hydrogen flames at similar additive concentrations. A large amount of soot starts to appear in prevapourisation and ultrasonic spray blends when 4 mol% toluene is added and toluene has a higher sooting propensity than the biofuel surrogates tested in this study.

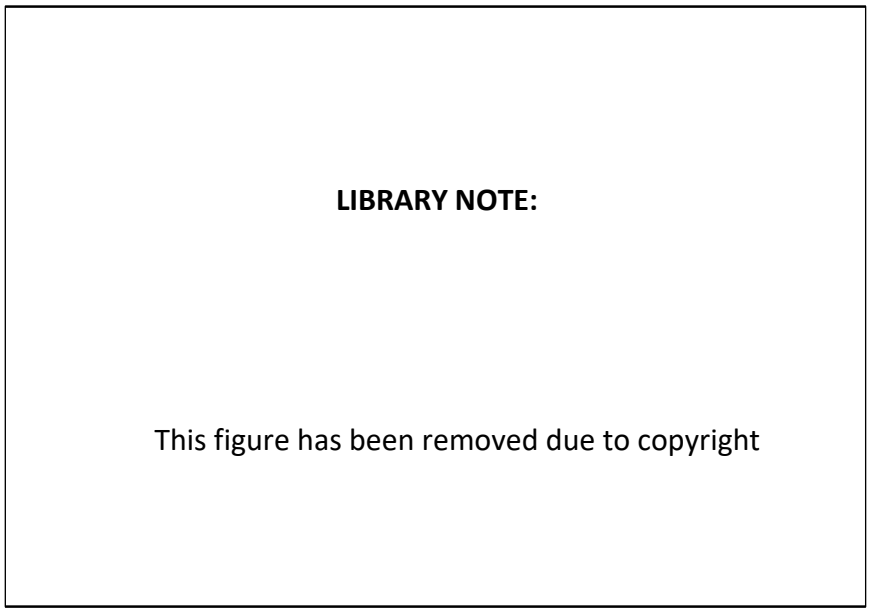

(b)

Figure 8.3: Photographs of (a) prevapourised and (b) ultrasonic spray biofuel-blended H_2/N_2 flames. The photographs have been combined from Chapters 4 and 5 with 3.5 and 4 mol% toluene/H_2 flames to better illustrate soot distribution and flame appearance.

Flame luminosity

The prevapourised and ultrasonically atomised biofuel surrogate/hydrogen flames are non-sooting and their luminosity is dominated by the gaseous species. In contrast, sooting biofuel/hydrogen flames are achieved by adding gas-assist atomised additives and the luminosity enhancement is primarily from the soot particulates [6]. Figure 8.5 shows the quantitative comparison of the effectiveness of luminosity (Figure 8.5a) and radiant fraction enhancement (Figure 8.5b) from adding 0.2 mol% eucalyptol (HE0.2), D-limonene (HL0.2), and anisole (HA0.2) via prevapourisation, ultrasonic spray, and

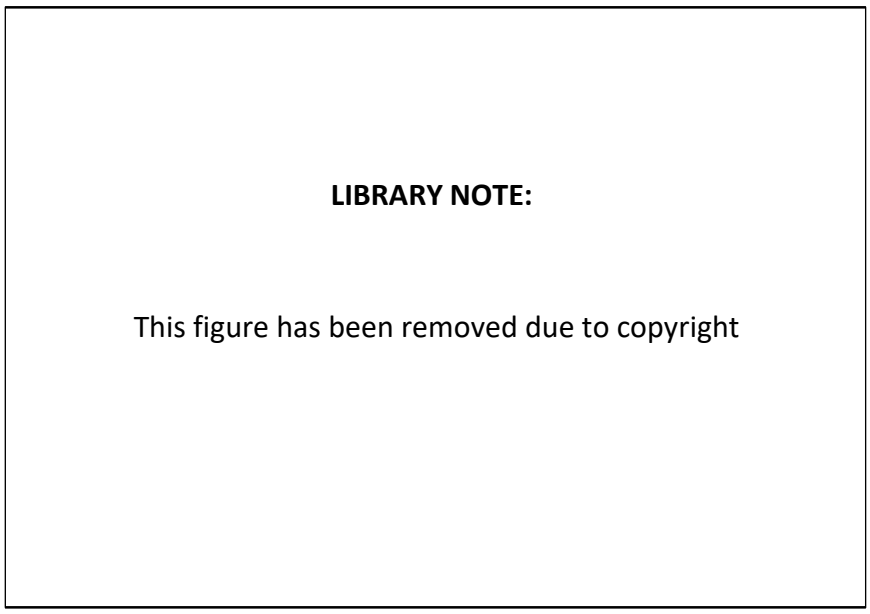

(b)

Figure 8.4: Photographs of gas-assist atomised (a) bio-oil blended and (b) essential oil blended H_2 flames reproduced from Chapter 7.

gas-assist atomisation. The illuminance and radiant heat flux of the laminar biofuel surrogates flames on a wick burner are shown in Figure 8.6 to illustrate the effect of biofuels' chemistry on flame luminosity and radiant heat flux. Figure 8.5a shows that the luminosity enhancement of an unblended hydrogen-based flame by the addition of prevapourised and ultrasonically atomised 0.2 mol% anisole is 200% and 30%, respectively. In comparison, adding 0.2 mol% anisole by gas-assist atomisation increases the luminosity of the unblended hydrogen flame by 400%, more effective than the introduction method of prevapourisation and ultrasonic spray. It is noticed that the effectiveness of various biofuel surrogates on the flame luminosity of blended hydrogen flames is not consistent with the flame illuminance trend of the laminar biofuel surrogate flames. For example, laminar eucalyptol flames exhibit the highest illuminance, whereas adding eucalyptol appears to be the least effective for the luminosity enhancement of a turbulent hydrogen flame. In addition to the impact caused by distinct flame conditions, this phenomenon may be also ascribed to the flame luminosity enhancement of the turbulent hydrogen flame is inferred from the photographs taken by

DSLR cameras while the flame illuminance of the laminar biofuel surrogate flames are directly measured with a lux meter.

Radiant heat flux

Similar trends are found in the effectiveness of the radiant heat flux enhancement from the introduction methods of prevapourisation, ultrasonic spray, and gas-assist atomisation shown in Figure 8.5b. Adding the biofuel surrogates by gas-assist atomisation leads to a larger radiant fraction enhancement. The promoted soot formation and elevated soot loading in the gas-assist atomised biofuel surrogate/hydrogen flames enhance the radiant heat flux via blackbody radiation from the soot particulates. Dissimilar to the inconsistent luminosity trends in laminar biofuel surrogate flames and blended hydrogen flames (refer to Chapter 4), the effectiveness of radiant fraction enhancement of biofuel-blended hydrogen flames follows the same trend of the radiant heat flux of the laminar biofuel flames. This observation suggests that adding biofuel surrogates to turbulent hydrogen-based flames does not significantly alter the pyrolysis, dissociation, and subsequent reactions of these biofuel surrogates to form PAHs and soot, hence, the sooting propensities of the biofuels may be appropriate to be used to predict the effectiveness of radiant intensity enhancement of hydrogen-based flames.

Flame temperature

As for the centreline flame temperature, adding prevapourised biofuel surrogates typically varies the centreline flame temperature within $\pm 85\,\mathrm{K}$, whereas adding ultrasonic atomised biofuel surrogates generally reduces the centreline flame temperature due to the enthalpy of vapourisation from the liquid droplets. The flame temperature reduction is up to 3% in 1 mol% spray eucalyptol blends at $x/L_f = 0.4$ (refer to Chapter 5). A more evident reduction in centreline flame temperature at 6% is found in the 0.3 mol% gas-assist atomised eucalyptol/hydrogen flames due to the enhanced radiative heat loss from the promoted sooting loading in the flame. Based on the comparison amongst the introduction methods of prevapourisation, ultrasonic atomisation, and gas-assist atomisation, it is concluded that adding biofuel surrogates by gas-assist atomisation is more beneficial for the flame luminosity and radiant heat flux enhancement of hydrogen-based flames than prevapourisation and ultrasonic atomisation.

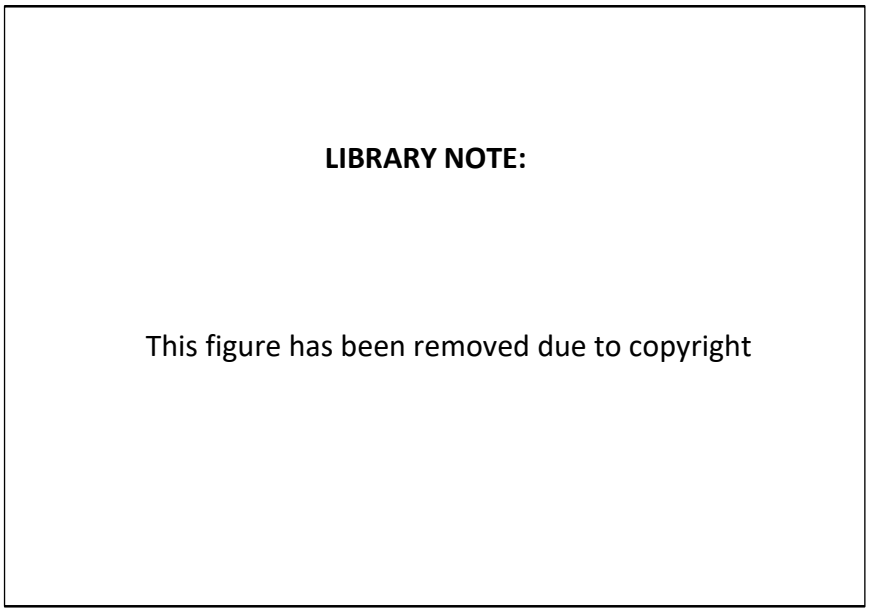

Figure 8.6: Illuminance and radiant heat flux of laminar nonpremixed flames on a wick-fed burner at extended wick length 1, 3, and 5 mm reproduced from Chapter 4. (a) Flame illuminance. (b) Flame radiant heat flux.

8.2.3 Analysis of influencing factors

Adding biofuel surrogates by ultrasonic or gas-assist atomisation is more effective than prevapourisation because the liquid droplets create local fuel-rich conditions, which are beneficial for soot formation. The analyses of the near-field spray characteristics of the gas-assist atomised biofuel surrogate/hydrogen flames reveal that the major difference between the gas-assist atomisation and the ultrasonic atomisation is that larger spray objects are

created, including irregular shapes, ligaments, and droplets compared with the droplets generated by ultrasonic spray. The size of the droplet generated by the gas-assist spray mostly ranges from 0.15–0.34 mm, several times larger than the droplet size (about 0.03–0.04 mm) generated by ultrasonic spray [3, 7, 8]. In addition, the breakup length of the biofuel surrogate sprays and the lesser dispersion of the liquid droplets in gas-assist atomisation indicate that the mixing of hydrogen and additives is delayed and less homogeneous, compared with an earlier and more homogeneous mixing of liquid and hydrogen in ultrasonic atomisation as the finer liquid droplets are mixed and entrained by hydrogen prior to the jet exit. Therefore, the mixing of the reaction zone and the liquid fuel droplets is less homogeneous, which further enhances local fuel-rich conditions. It is concluded that these distinct spray characteristics induced by gas-assist atomisation further promote the local fuel-rich conditions and hence benefit soot formation.

Aside from the droplet size, another factor that affects soot formation and corresponding radiant heat flux is the higher strain rate at the jet exit observed in ultrasonic atomisation in contrast to gas-assist atomisation [9]. In the ultrasonic atomisation regime, the droplets are generated and mixed with hydrogen 300 mm upstream of the jet exit. In other words, the fine droplets are entrained by the carrier gas and have similar velocities when they reach the jet exit. In the gas-assist atomisation regime, the momentum of the liquid jet at the jet exit is minimum compared with the ambient carrier gas. The momentum of the objects increases with the breakup processes and eventually is close to the ambient gas [10–12]. This distinct characteristic may play an important role in the formation of PAH/soot formation as a high strain rate has been reported to significantly reduce soot formation [1, 13–16]. Chapter 5 reported a large increase in radiant fraction (115%) and soot formation as the exit strain rate of the prevapourised toluene/hydrogen flame is reduced from $20\,000\,s^{-1}$ to $12\,000\,s^{-1}$. The higher droplet momentum at the jet exit in the ultrasonic atomisation regime than that in the gas-assist atomisation regime leads to a higher exit strain rate and inhibits PAH formation. The difference in the initial momentum of the droplets may be another factor that impacts the effectiveness of introduction methods on radiant heat flux enhancement.

8.3 References

[1] X. Dong, G. J. Nathan, S. Mahmoud, P. J. Ashman, D. Gu, and B. B. Dally. "Global characteristics of non-premixed jet flames of hydrogen–hydrocarbon blended fuels". *Combust. Flame* 162 (2015), pp. 1326–1335.

[2] A. R. Choudhuri and S. Gollahalli. "Combustion characteristics of hydrogen–hydrocarbon hybrid fuels". *Int. J. Hydrog. Energy* 25 (2000), pp. 451–462.

[3] M. J. Evans, D. B. Proud, P. R. Medwell, H. Pitsch, and B. B. Dally. "Highly radiating hydrogen flames: effect of toluene concentration and phase". *Proc. Combust. Inst.* 38 (2021), pp. 1099–1106.

[4] Y. D. Wu and D. K. Lai. "A density functional study of substituent effects on the O- H and O- CH3 bond dissociation energies in phenol and anisole". *J. Org. Chem.* 61 (1996), pp. 7904–7910.

[5] M. Nowakowska, O. Herbinet, A. Dufour, and P.-A. Glaude. "Kinetic study of the pyrolysis and oxidation of guaiacol". *J. Phys. Chem. A* 122 (2018), pp. 7894–7909.

[6] K. Andersson, R. Johansson, and F. Johnsson. "Thermal radiation in oxy-fuel flames". *Int. J. Greenh. Gas Control* 5 (2011), S58–S65.

[7] R. J. Lang. "Ultrasonic atomization of liquids". *J. Acoust. Soc. Am.* 34 (1962), pp. 6–8.

[8] D. B. Proud, M. J. Evans, P. R. Medwell, and Q. N. Chan. "Experimental investigation of the flame structure of dilute sprays issuing into a hot and low-oxygen coflow". *Combust. Flame* 230 (2021), p. 111439.

[9] R. Rajan and A. B. Pandit. "Correlations to predict droplet size in ultrasonic atomisation". *Ultrasonics* 39 (2001), pp. 235–255.

[10] A. Sinha, R. S. Prakash, A. M. Mohan, and R. Ravikrishna. "Airblast spray in crossflow–structure, trajectory and droplet sizing". *Int. J. Multiph. Flow* 72 (2015), pp. 97–111.

[11] A. Kourmatzis, P. X. Pham, and A. R. Masri. "A two-angle far-field microscope imaging technique for spray flows". *Meas. Sci. Technol.* 28 (2017), p. 035302.

[12] A. Kourmatzis, P. X. Pham, and A. R. Masri. "Air assisted atomization and spray density characterization of ethanol and a range of biodiesels". *Fuel* 108 (2013), pp. 758–770.

[13] N. Qamar, G. Nathan, Z. Alwahabi, and K. King. "The effect of global mixing on soot volume fraction: measurements in simple jet, precessing jet, and bluff body flames". *Proc. Combust. Inst.* 30 (2005), pp. 1493–1500.

[14] S. R. Turns and F. H. Myhr. "Oxides of nitrogen emissions from turbulent jet flames: Part I-Fuel effects and flame radiation". *Combust. Flame* 87 (1991), pp. 319–335.

[15] G. Nathan, J. Mi, Z. Alwahabi, G. Newbold, and D. Nobes. "Impacts of a jet's exit flow pattern on mixing and combustion performance". *Prog. Energy Combust. Sci.* 32 (2006), pp. 496–538.

[16] Y. Sivathanu and J. Gore. "Total radiative heat loss in jet flames from single point radiative flux measurements". *Combust. Flame* 94 (1993), pp. 265–270.

Chapter 9

Conclusions and outlook

9.1 Conclusions

The research presented in this thesis established fundamental and further advanced understandings of the approach of adding sooting biofuel additives to turbulent nonpremixed hydrogen flames for radiant intensity enhancement by promoting soot formation within the flame, making hydrogen flames suitable for practical applications that rely on radiant heat transfer. Five liquid biofuels and their corresponding surrogates have been selected as soot-enhancing additives to analyse the effects of various physical and chemical properties on the combustion characteristics of biofuel/hydrogen flames. Toluene, anisole, and guaiacol were chosen as the surrogates for bio-oils, while eucalyptol and D-limonene were chosen as the surrogates for essential oils. Burners with complementary functions were designed to evaluate the effect of different introduction methods and influencing factors on hydrogen blending with biofuels. The combustion characteristics of the unblended and biofuel surrogate blended hydrogen-based flames have been investigated through combined experimental and numerical methods, namely flame appearance, luminosity, radiant heat flux, flame temperature, spray characteristics, and pollutant emissions.

The sooting propensity analyses of the biofuel surrogates enable the comparison between monoterpenes and aromatics to understand the effect of various chemical structures on soot formation, which has not been well documented in previous research. The sooting propensities of biofuel surrogates from high to low generally follow the order of aromatics $>$ monoterpenes $>$ alkenes $>$ alkanes $>$ aldehydes. The results suggest that biofuels possessing an aromatic structure generally exhibit a greater tendency for the formation

of polycyclic aromatic hydrocarbons (PAHs), thereby being more effective in luminosity and radiant fraction enhancement of hydrogen-based flames than cyclic monoterpenes.

The effectiveness of adding different biofuels for radiant intensity enhancement follows the decreasing trend as toluene > anisole > D-limonene > eucalyptol > guaiacol. Aromatic biofuels tend to have larger radiant intensity enhancement than monoterpenes in the context of hydrogen combustion because the higher unsaturation degree of aromatic structures favours the formation of PAHs. Bond dissociation enthalpy (BDE) is a critical index in assessing the effectiveness of biofuel addition on radiant intensity enhancement. The weak C-H bond in the allylic group in D-limonene is beneficial for hydrogen abstraction to take place via the HACA mechanism, thereby promoting PAHs formation. The efficacy of oxygenated fuels in enhancing radiant heat flux is lower compared with non-oxygenated fuels as the presence of oxygen content in oxygenated fuels facilitates the oxidation of PAHs. The dissimilar trend found in the radiant intensity of pure guaiacol flame and guaiacol/hydrogen flame demonstrates that the viscosity and surface tension is another influencing factor for radiation enhancement because the distinct physical properties affect the spray characteristics in the context of gas-assist atomisation, which in turn affects the effectiveness of radiation enhancement.

Apart from the chemical and physical properties of liquid biofuel, the method of biofuel introduction plays an important role in soot formation in biofuel/hydrogen flames. Adding biofuel surrogates (0.2–1 mol%) to hydrogen-based flames by prevapourisation and ultrasonically atomisation has limited impacts on the flame height, width, and colouration. The most noteworthy change is the enhanced blue coloration due to the promoted formation of carbonaceous radicals. The flame luminosity and radiant fraction were increased by 61–293% and 2–22%, respectively. In comparison, adding 0.1–0.3 mol% gas-assist atomised biofuel surrogates to hydrogen flames achieves radiating flames on the needle spray burner. A pronounced transition of flame colouration from red/blue to yellow is observed, indicating that soot formation is significantly promoted by the addition of gas-assist atomised biofuel surrogates. The flame luminosity and radiant fraction are increased by 30–500% and 2–15% by adding 0.1–0.3 mol% biofuel surrogates.

The mechanisms that dominate the effectiveness of introduction methods on soot formation are the local fuel-rich conditions created by droplets and the exit strain in different blending regimes. The ultrasonic spray bio-

fuel/hydrogen flames appear to have higher radiant intensity than prevapourised biofuel/hydrogen flames due to the local fuel-rich conditions created by liquid droplets (0.03 mm), which benefit PAH/soot formation. Larger droplets (0.15–0.34 mm) are formed by gas-assist atomisation than ultrasonic atomisation (0.03 mm), which further enhances local fuel-rich conditions, hence resulting in higher radiant intensity. The evaluation of spray characteristics and their influencing non-dimensional parameters reveals that the momentum flux ratio controls the macroscopic spray characteristics such as breakup length and area fraction, while the Weber number describes the microscopic spray characteristics such as droplet size, ligaments, and wave-like structures. These analyses indicate that the Weber number is the dominant non-dimensional parameter for PAH/soot formation in biofuel/hydrogen flames.

The exit strain rate is a critical non-dimensional parameter that affects the soot formation and radiant intensity enhancement of biofuel/hydrogen flames. Reducing the exit strain rate from 20 000 s^{-1} to 12 000 s^{-1} increases the soot formation and the corresponding radiant fraction by 115% in prevapourised toluene/hydrogen flames. The significantly higher radiant intensity found in toluene/hydrogen flames with half of the exit strain rate reveals that a lower strain rate promotes PAH/soot formation as the formation of PAH/soot requires time. The lower exit velocity of the liquid droplets in the gas-assist atomisation regime also contributes to its higher effectiveness in radiant intensity enhancement. The understanding of the dominant mechanisms and influencing factors provides insights into the application of biofuel/hydrogen flames, such as burner design.

One of the phenomena that comes with the biofuel addition to hydrogen flames for radiant intensity enhancement is the increased nitrogen oxides (NO_x) emissions. The numerical analysis of NO formation pathways reveals that the increased global NO_x emissions are mainly because the dominant subset of the thermal route: $OH + N \rightleftharpoons H + NO$ and prompt route: $CH + N_2 \rightleftharpoons H + NCN$ are enhanced by biofuel addition, with the HNO-intermediate route: $H + HNO \rightleftharpoons H_2 + NO$ also contributing. Given that the thermal route of NO formation dominates NO_x emissions from biofuel/hydrogen flames, the temperature drops in spray flames as a result of the enthalpy of droplet vapourisation, reducing NO_x emissions. As the soot formation in the biofuel/hydrogen flame is enhanced, an additional temperature drop is achieved by the promoted radiative heat loss, which in turn reduces NO_x emissions.

The findings of this research have established a fundamental understanding of the efficacy and effectiveness of blending turbulent nonpremixed hydrogen flames with renewable biofuels for radiant intensity enhancement and other potential impacts on flame appearance, luminosity, temperature, and pollutant emissions. The investigation of dominant influencing factors and underlying mechanisms through various introduction methods and chemical analyses contributes to the understanding of soot formation in blended flames and the design of the non-dimensional parameters.

9.2 Outlook

Soot evolution and its correlations with flame temperature, residence time, and mixing mechanism are extremely complex, hence require advanced and comprehensive diagnostic techniques. The experimental diagnostics employed in this study mainly focus on measuring the global combustion characteristics of the biofuel-blended hydrogen-based flames, e.g., global radiant heat flux and NO_x emissions. The PAH and soot evolution in different flames is inferred and predicted based on the global flame characteristic measurements and chemical analysis. The direct measurement of soot particulates is critical to understanding the microscopic and instantaneous soot formation within the flame. Combustion processes are easily perturbed by using physical probing, resulting in the alteration of the fundamental flame behaviour and flow disturbance. Laser diagnostic techniques provide the capability for non-intrusive, in-situ, spatially, and temporally well-resolved measurements of critical chemical parameters. Laser diagnostics acquire qualitative or quantitative data by resultant signals from the interactions between the laser beam and individual atoms, molecules, solid particles, and liquid droplets. They can be configured to obtain 0 to 4-dimensional data. Laser diagnostic techniques can be used for the quantitative and qualitative detection of soot particles and liquid droplet distribution, flame temperature, and species concentrations in the future investigation of biofuel/hydrogen flames.

As for the numerical approach, there is a lack of chemical analysis for the PAHs and NO_x formation in essential oil surrogates' blends (i.e. eucalyptol, D-limonene) via Chemkin simulation, as detailed chemical kinetic mechanisms, which include PAH and NO_x reactions are not available for these fuels. Developing comprehensive kinetic mechanisms for essential oils can advance the understanding of the effect of terpenoid structures on PAHs and NO_x formation. In addition, numerical modelling using Chemkin Pro is limited

to one-dimensional simulation and lacks important boundary conditions, making the model differ from the real situation. Using more comprehensive computational fluid dynamics (CFD) models such as large eddy simulation (LES) and direct numerical simulation (DNS) for soot modelling and the prediction of resultant radiant intensity can benefit the understanding of the effect of biofuel addition to hydrogen flames.

Appendix A

Toluene addition to turbulent hydrogen/natural gas flames in bluff-body burners

Statement of Authorship

Title of Paper	*Toluene addition to turbulent H_2/natural gas flames in bluff-body burners*
Publication Status	☒ Published ☐ Accepted for Publication ☐ Submitted for Publication ☐ Unpublished and Unsubmitted work written in manuscript style
Publication Details	A. J. Gee, Y. Yin, K.K. Foo, A. Chinnici, N. Smith and P. R. Medwell (2023). *"Toluene addition to turbulent H2/natural gas flames in bluff-body burners" International Journal of Hydrogen Energy*, vol. 47 (65), pp. 27733-27746.

Principal Author

Name of Principal Author (Candidate)	Adam Gee		
Contribution to the Paper	I led the conceptualisation of the paper, with assistance from Paul Medwell, Neil Smith and Alfonso Chinnici. I led the development of the experiment campaign. With guidance from Paul Medwell and Kae Ken Foo, I selected the experimental cases, laboratory equipment and diagnostic techniques in order to address the specific goals of the experimental campaign. I completed the experiments with assistance from Yilong Yin, including set up, data collection and pack up. I led the running and data collection of the computational model in Chemkin. With guidance from Alfonso Chinnici, I selected the computational model, boundary conditions and flame cases used to generate numerical data. I processed, analysed and interpreted the experimental and numerical data, and wrote the entirety of the manuscript including generation of any figures or tables. I also acted as corresponding author, addressing the editor/reviewer comments.		
Overall percentage (%)	75%		
Certification:	This paper reports on original research I conducted during the period of my Higher Degree by Research candidature and is not subject to any obligations or contractual agreements with a third party that would constrain its inclusion in this thesis. I am the primary author of this paper.		
Signature	Digitally signed by Adam Gee Date: 2023.10.31 16:38:37 +10'30'	Date	31 October 2023

Co-Author Contributions

By signing the Statement of Authorship, each author certifies that:

i. the candidate's stated contribution to the publication is accurate (as detailed above);

ii. permission is granted for the candidate in include the publication in the thesis; and

iii. the sum of all co-author contributions is equal to 100% less the candidate's stated contribution.

Name of Co-Author	Yilong Yin		
Contribution to the Paper	This co-author assisted with experimental set up and data collection. This co-author helped to evaluate the experimental data.		
Signature	2023.11.02 10:42:20 +10'30'	Date	

Name of Co-Author	Kae Ken Foo		
Contribution to the Paper	This co-author provided assistance in the design and data collection of the experimental portion of this work. This co-author helped to evaluate the experimental data and provided assistance in the initial drafting of the paper.		
Signature	Digitally signed by Kae Ken Foo DN: C=AU, E=kaekenfoo@gmail.com, CN=Kae Ken Foo Date: 2023.11.01 16:12:51+10'30'	Date	1/11/2023

Name of Co-Author	Alfonso Chinnici		
Contribution to the Paper	This co-author provided guidance for the Chemkin component on the paper, helping generate and analyse computation data. This co-author contributed to the final stages of drafting of the paper.		
Signature		Date	01/11/2023

Name of Co-Author	Neil Smith		
Contribution to the Paper	This co-author contributed to the conception of the paper. This co-author contributed to the analysis and presentation of experimental results.		
Signature	Digitally signed by Neil Smith Date: 2023.11.01 11:06:53 +10'30'	Date	

Name of Co-Author	Paul Medwell		
Contribution to the Paper	This co-author contributed to conceptualising the paper, designing the experiments and analysing experimental and computational data. This co-author contributed to the drafting of the paper.		
Signature	Paul Medwell 2023.10.31 16:47:55 +10'30'	Date	31-OCT-2023

INTERNATIONAL JOURNAL OF HYDROGEN ENERGY 47 (2022) 27733–27746

Available online at www.sciencedirect.com

ScienceDirect

journal homepage: www.elsevier.com/locate/he

Toluene addition to turbulent H_2/natural gas flames in bluff-body burners

Adam J. Gee [a,*], *Yilong Yin* [a], *Kae Ken Foo* [a], *Alfonso Chinnici* [a], *Neil Smith* [b], *Paul R. Medwell* [a]

[a] School of Mechanical Engineering, The University of Adelaide, Adelaide, SA 5005, Australia
[b] School of Chemical Engineering and Advanced Materials, The University of Adelaide, Adelaide, SA 5005, Australia

HIGHLIGHTS

- Complete replacement of natural gas with H_2 causes an 80% reduction in heat flux.
- Positive non-linear effect on heat flux and illuminance for toluene doped H_2 flame.
- 2–3% toluene required for H_2 flame to exhibit equivalent illuminance to a natural gas.
- 4% toluene required for H_2 flame to exhibit equivalent heat flux to natural gas.
- H_2 addition beneficial to heat flux in high strain rate environments.

GRAPHICAL ABSTRACT

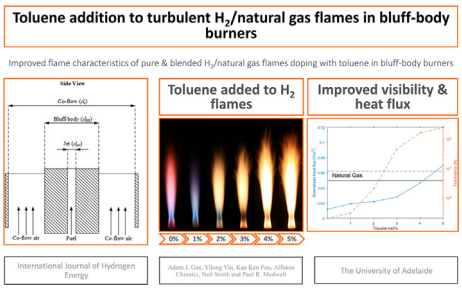

ARTICLE INFO

Article history:
Received 11 April 2022
Received in revised form
31 May 2022
Accepted 16 June 2022
Available online 10 July 2022

Keywords:
Hydrogen
Toluene
Radiation
Bluff-body
Doping

ABSTRACT

A key challenge in the transition towards using hydrogen as an alternative carbon-free fuel is the reduced thermal radiation due to the absence of soot. A novel solution to this may be doping with highly sooting bio-oils. This study investigates the efficacy of toluene as a prevapourised dopant in turbulent pure hydrogen and blended hydrogen/natural gas flames as a means of improving soot loading and radiant heat transfer. All flames are stabilised on bluff-body burners to emulate the recirculation component of many industrial combustors. Total heat flux and illuminance increase non-linearly with toluene concentration for fuel blends and bluff-body diameters. By reducing the bluff-body diameter from 64 mm to 50 mm, a 20/80 (vol%) H_2/natural gas mixture produces a more radiative flame than a 10/90H_2/natural gas mixture in the smaller bluff-body. Opposed-flow flame simulations of soot precursors indicate that as strain rate increases, although overall soot precursor concentration decreases, a 20 vol% hydrogen mixture will produce more soot than a 10 vol% mixture. This suggests the addition of hydrogen up to 20 vol% may be beneficial for soot production in high strain environments.

* *Corresponding author.*
E-mail address: adam.gee@adelaide.edu.au (A.J. Gee).
https://doi.org/10.1016/j.ijhydene.2022.06.154

Introduction

As the world shifts towards renewable sources of energy, the importance of combustion has become apparent for applications that cannot readily be replaced by electrification [1]. Interest in hydrogen (H_2) as an alternative to natural gas (NG) to fuel the combustion needs of industrial heating has grown considerably in recent years [2,3]. The characteristics of hydrogen flames have been studied extensively and the benefits of hydrogen combustion are widely documented. The main benefits of hydrogen are a potentially 100% renewable production process [4] with carbon-free emission. A hydrogen flame has increased stability due to its increased flame speed and wider flammability limits [5,6]. Although currently not a cost-effective alternative, it is expected that green hydrogen, via water electrolysis from renewable electricity, will soon become cost-competitive and become a more attractive carbon-free heat energy source for industrial processes [7]. In this way, hydrogen can be used as an energy storage medium by generating it when there is excess renewable electricity supply. The potential role for hydrogen in energy networks is well established, with the focus now shifting towards solutions to the variety of challenges associated with the integration of a new fuel in existing gas and energy infrastructure.

The challenges associated with the integration of hydrogen in industry applications are not only economic but also related to its performance. The challenges associated with the complete replacement of all current fuels for hydrogen are perhaps too great, but there is a growing interest in understanding the feasibility of blending hydrogen with existing fuels in various applications. When the fuel composition is changed, so too are the resulting flame characteristics, which can have a significant effect on performance and safety. The design and use of a burner assumes the use of a fuel with specific properties, such as natural gas. The addition of a new reacting species in hydrogen has a significant effect on differential diffusivity, reaction kinetics and, combined with factors affected by varying burner geometries, makes predicting the consequences of hydrogen blending difficult [8]. The reduced radiant heat transfer of hydrogen due to lack of soot is of particular concern with regard to burner thermal efficiencies and although the reduced thermal radiation of hydrogen flames is well documented [9–14] there is still a gap in the knowledge about the extent to which the content of hydrogen in a particular fuel blend will affect performance parameters such as radiant heat transfer in different burner systems. This is especially relevant for adoption strategies, which may follow a gradual integration of hydrogen as a growing component of an existing fuel mixture where sooting fuels are 'diluted' and the resulting magnitude of radiative heat transfer becomes affected to an unknown degree [15].

In hydrocarbon-based fuels, the major contributor to radiative heat transfer is the reradiating of thermal energy from soot particles, with gases such as water molecules (H_2O) and carbon dioxide (CO_2) also contributing [16]. The notion to increase soot is counterintuitive from a health and environmental standpoint and certainly soot poses a risk to those areas but its role in radiant heat transfer is critical to many combustion applications [16,17]. Soot particles are more efficient emitters than gaseous species and are responsible for the majority of thermal radiation in most hydrocarbon flames [17–19]. The concentration of soot particles is closely coupled to radiant heat losses of a flame [20]. In the combustion of hydrogen flames, there is no carbon present and hence, no soot production. The presence of hydrogen therefore affects a flame's thermal radiation, since soot particles are important heat carriers [13,21]. Thermal radiation is the primary mode of heat transfer for many large-scale burner systems [22,23] thus a lack of soot production and subsequent reduction in thermal radiation would be detrimental to their operation with hydrogen. Direct-fired industrial processes that operate at very high temperatures, such as rotary and glass kilns, boilers and process heaters are particularly reliant on radiation. Additionally, many industry burner systems utilize highly turbulent combustion regimes, the analysis of which with respect to sooting flames is far less prevalent than for laminar flames [24]. Soot is also responsible for much of the visible emissions in hydrocarbon flames due to the blackbody radiation from soot [16,25]. Consequently, hydrogen flames are often reported as having very poor visibility [26]. The need for solutions to improve the visibility of hydrogen flames is often mentioned as part of a safe adoption strategy of hydrogen for both industrial and domestic use [27]. For cases where hydrogen is blended with a hydrocarbon fuel, the thermal radiation is affected by more than simple dilution of carbon-based species: competing chemical and thermal effects have also been reported [28]. Studies comparing the addition of hydrogen with the addition of inert species for laminar [29,30] and turbulent [31] flames report that, despite global reductions in soot volume fractions, hydrogen is less effective than inert species at suppressing soot formation, suggesting a chemical promoting effect. Other operating parameters such as the oxygen (O_2) concentration [32], and the recirculation rate [33] are known to affect the physical and chemical interactions of blended fuels. The degree to which these interactions affect burner performance for various amounts of hydrogen is a risk faced by industry. Reduced radiative heat transfer [30,31,34], lower flame visibility [26], reduced air requirements [35], increased flue gas moisture content and increased NOx emissions [36–40] are some of the key points of concern associated with hydrogen integration to fossil fuel processes.

Extensive efforts have been made to characterise the effect of hydrogen addition in a variety of burners and propose solutions to typical challenges of hydrogen. Kumar and Mishra [13] showed that for hydrogen addition to an LPG diffusion flame there is a negligible effect on flame length for up to 20 vol% hydrogen but a noticeable effect beyond this point. Hydrogen addition up to 40 vol% increased the soot-free-length by approximately 61%, and consequently a negative effect on radiant heat transfer fraction is reported. Kashir et al. [21,41] has previously investigated the accuracy of model prediction both for the characteristics of methane/hydrogen bluff-body swirl flames [41] and the impact of hydrogen enrichment and bluff-body diameter for propane flames [21]. The authors report the increasing effects of reducing bluff-body diameter on flame length, attributed to the lower recirculation intensity and subsequent reduction in mixing of reactants. In this work the authors considered fractions of

hydrogen ranging from 10 to 70 vol% [41] and 30–90 vol% [21], respectively. In the former case [41] key features reported were an increase in OH mass fraction and subsequent reaction zone thickness with hydrogen addition. Due to conservation of total volumetric flow rate a penalty is paid on mass flow and thermal input, subsequently the flame temperature was reported to reduce with hydrogen addition — the peak flame temperature was also shifted downstream. In the latter case [21] hydrogen addition decreased radiant heat transfer, consistent with previous experimental data [13] — this was stated to be primarily a consequence of sooting-containing fuels. Adding a dopant to poorly radiating flames has been discussed as a potential solution to improve radiant heat transfer [19]. By doping the flame with particles that emulate the radiant properties of soot, it might be possible to supplement lost radiant heat transfer. The addition of non-combusting metal oxide particles has been proposed as a solution to improve thermal radiation in low sooting flames, [42,43]. Combustible particles such as pulverised coal and some waste-fuels have also been used as a soot surrogate to improve radiative heat transfer [19,44]. The recent investigation by Evans et al. [45] on the use of liquid dopants in hydrogen flames has shown merit for toluene, as a representative for the broad family of bio-oils. Toluene is an aromatic compound that is present in the chemical structure of most bio-oils with a high sooting propensity, which is greater than that of petroleum-derived fuels [45–47]. Toluene was added at 1–5 mol% of fuel in 1:1H_2:N_2 turbulent (Re = 5000) simple jet flames [45]. The results showed a positive non-linear relationship between the dopant concentration and soot formation. The method of toluene injection, either as a spray or prevapourised, was also found to be an important factor. Computational analysis via OPPDIF models of the sooting characteristics of toluene showed competing chemical pathways for oxidation via formaldehyde (CH_2O) or soot formation via acetylene (C_2H_2), identified by A2 rate of production. It was noted that oxidation was the preferred pathway for concentrations of toluene below 5 mol% of the fuel due to higher availability of OH and H from the reaction zone which promotes the oxidation [45,48]. This effect is reported to change at larger concentrations, consequently it was suggested that doping and blending should be considered different regimes with respect to soot loading. It was concluded that toluene is a promising candidate for doping in hydrogen flames to improve the radiative heat transfer [45]. The efficacy of toluene in a binary n-heptane or iso-octane dopant mixture has also been considered previously, where a positive non-linear correlation between toluene-containing fuels and soot production is reported [49,50]. Russo et al. [51] investigated the sooting effects of prevapourised toluene in premixed methane flames and found similarly that toluene doped flames yielded higher soot concentrations.

The potential for toluene as a fuel additive to improve thermal radiation has been well established in previous work but there is still a need for further investigation to assess its efficacy under more industry-representative conditions. The study by Evans et al. considered only simple jet flames with relatively low turbulence intensity [45]. Additionally, by only considering pure hydrogen blended with nitrogen, there was a penalty on flame temperature, and consequently, a strong effect on the overall reaction kinetics. Since the integration of hydrogen may happen gradually with low concentrations blended into current fuel blends, further investigation on the effects of blends of hydrogen in natural gas without inert diluents should be undertaken to build a more realistic picture. A significant novelty of this work is the study of toluene as a dopant in flames which are indicative of a transitional approach to hydrogen. That is, ensuring sufficient turbulence and recirculation to mimic industry combustors and considering realistic fuel blends including 10, 20 and 100 vol% hydrogen addition with specific reference to the properties of natural gas in the same burner system. This research combines experimental flame imaging techniques and heat flux data with computational modelling of soot precursors to report the efficacy of toluene as a soot surrogate for improving radiant heat transfer and visibility in turbulent hydrogen/natural gas flames stabilised on bluff-body burners to emulate the recirculation component of industry burners.

Methods

Experimental setup

The geometric complexities of full-scale industrial burners are difficult to replicate with lab-scale experiments, and likewise, characterisation of the governing chemistry and physics is challenging in large-scale systems. A common feature of industrial burner design is recirculation, most commonly achieved with modifications to the jet geometry or redirection of hot exhaust gases [52]. Recirculation, and its absence, can have a large effect on fuel/air mixing, residence time and overall stability [52,53]. Bluff-body experimental burners were popularised by Masri et al. [54] and Dally et al. [55] and have since been used elsewhere in literature [53,56–59] because they capture the key physics of recirculated flow in a controllable and characterisable way. A bluff-body burner creates recirculation and provides increased stability, which is useful in turbulent flames. The combustion conditions created by bluff-body burners are similar to practical combustors used in many industry applications. This geometry is therefore a useful tool in studying industry-representative flames while preserving relatively simple and well-defined boundary conditions [60]. It is due to their ability to emulate industry burner physics and help stabilise highly turbulent flames that bluff-body burners are used in this investigation.

In this investigation, the experimental results are collected using the burner apparatus presented in Fig. 1 and described previously [33,61]. The burner consists of a cylinder with a central 4.6-mm-diameter jet (d_{jet}), from which the fuel is issued. Two burners with external diameters (d_{BB}) of 50 mm and 64 mm are used. A 4.6 mm central jet is chosen as it is commonly used in literature [62,63] and frequently used with these bluff-body diameters [33,61]. The burner is positioned in the centre of a co-flowing air stream and raised 10 mm above the annular flow constrictor for visibility. Co-flowing air produces a recirculation of hot gases, allowing the flame to stabilise [60]. This design enables the control of recirculation by adjusting the jet and co-flow inlet conditions independently to simulate various operating conditions. An annular contractor

with a diameter (d_c) of 190-mm, with honeycomb mesh around the bluff-body burner, delivering uniform co-flow air to the flame. The co-flow velocity is maintained at 11 m/s and 20 m/s for the hydrogen and natural gas/hydrogen flames, respectively. It should be noted that the momentum flux ratio ($\rho_{jet}U_{jet}$:$\rho_{coflow}U_{coflow}$) between these cases varies by no more than 8% across all cases. This ratio has been shown to be the dictating parameter for the vortical structure and the length of the recirculation zone [33,55].

Liquid toluene (assay: 99.5%) is vapourised at 150 °C using a Bronkhorst Controlled Evaporator and Mixer (CEM). Toluene, at 1–5 mol%, is added to 10, 20 and 100 vol% hydrogen (assay: 99.999%) in natural gas fuel blends. A bulk mean jet Reynolds number of 10,000 is kept constant for all cases to ensure sufficiently turbulent conditions. The gas density, viscosity and velocity used to calculate Reynolds number are recorded in Table S1 of the supplementary data, the characteristic length is chosen as d_{jet}. Gas mixture data is calculated using previously established methods [64]. Composition of natural gas is also presented in the supplementary material (Table S2).

The heat transfer properties of the flames are primarily characterised by data collected from heat flux sensors (Medtherm 92241/2), to compare the radiative properties of flames with different fractions of hydrogen. Thermocouples measuring the temperature differential between the sensor surface and an internal heat sink form an electromotive force at the output which is directly proportional to the heat transfer rate. A conversion factor calibrated to the specific sensor is used to convert the measured voltage to heat flux. Voltage samples are taken at a frequency of 1000Hz for 30 s and a mean value is presented for each flame with corresponding uncertainty derived from the average variance between samples. To compare the flame structure and visibility for different burners and fuel blends, a DSLR camera (Canon EOS 6D) with a 50 mm lens is used for the flame photographs. Imaging is through a 594-nm (23-nm full-width at half maximum) notch filter to eliminate the orange colour—this particular colour has been reported previously [65,66] and attributed to sodium impurity corresponding to 589-nm, despite the use of high purity fuels. In this instance, the spectrometry data and comparison photos with and without the filter are used to highlight the presence of sodium. Flame photographs are helpful when presenting the effects on flame structure and colour, but can be misleading when discussing visibility and brightness to the naked eye due to any manipulation of the aperture and exposure times. A Lux meter (Protech QM1584) is used to measure flame brightness, or more specifically, flame illuminance (lumen/m^2), to further characterise and quantify the visibility of the flame cases.

Computational analysis

Numerical simulations of opposed-flow diffusion (OPPDIF) flames in Chemkin Pro v19.2 are used in combination with the experimental data to describe the flame behaviour and underlying chemistry. An opposed-flow configuration is chosen because it enables the study of soot formation and oxidation under idealised flow fields, which, in turn, enables a focus on the chemistry effects. The OPPDIF model has been used previously to study flame phenomena in jet flame burners, including bluff-bodies [67,68]. The OPPDIF model allows for analysis of homogeneous, gas-phase kinetics and sensitivity

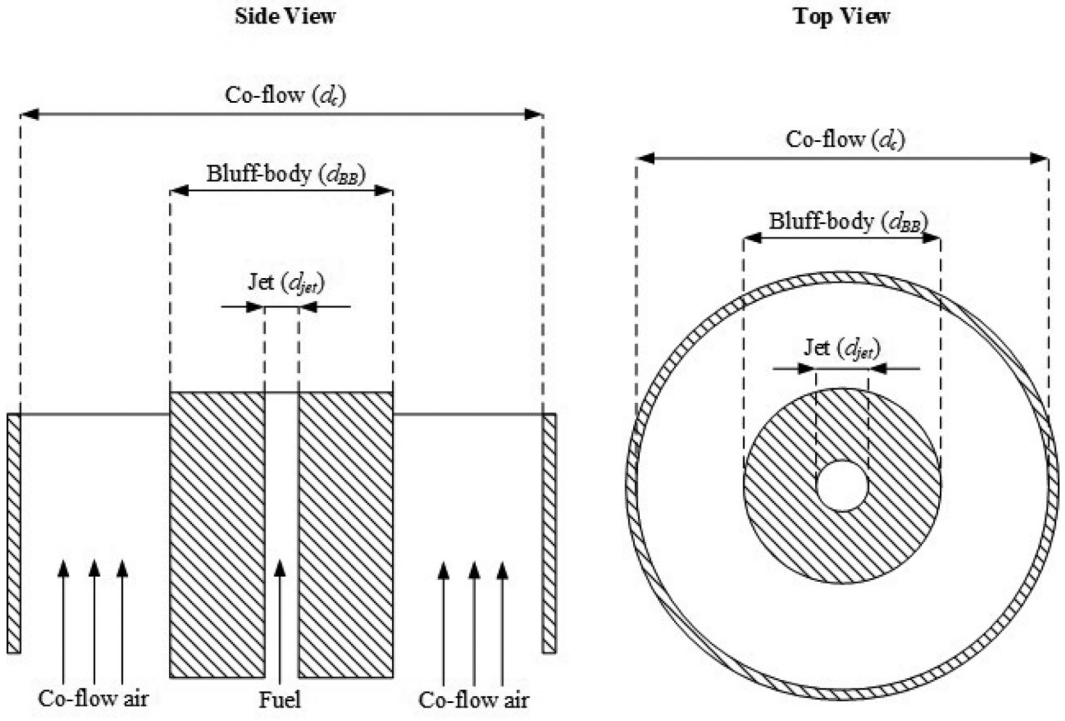

Fig. 1 – Diagram of the bluff-body burner and annular air contractor arrangement where d_{jet} = 4.6 mm, d_{BB} = 50 or 64 mm and d_c = 190 mm.

of a wide range of species or operating conditions. Sensitivity to the strain rate is considered, as it is an important parameter related to the burner design and operation, and affects the formation of species such as soot [69,70]. Strain is defined as the velocity difference normalised to the axial distance between the fuel and the oxidant jets, 50 mm in this case. Variations in the strain rate are achieved by adjusting fuel and oxidant stream velocities, ensuring similar momentum, to position the stagnation plane in the middle of the domain. Gas velocities used in each case are summarised in Table S3 in the supplementary material.

A chemical mechanism developed by Cai and Pitsch [71] is used for modelling the PAH formation, up to and including pyrene (A4). The mechanism includes thermodynamic and transport data for 335 species and 1610 gas-phase reactions. The behaviour of soot precursors, namely naphthalene (A2), will be used as a predictor of overall soot production and corresponding thermal radiation. A2 is often used as a soot indicator species in numerical studies because it is the rate-limiting step in the formation of large PAHs [24,45,72]. Additionally, A2 is the closest PAH in size to toluene, focussing the analysis of the chemical pathways. Unless specified otherwise, A2 is described by the summation of individual A2-variant species, of which $A2XC_{10}H_8$ is the dominant variant. Simulations of various H_2/CH_4 fuel blends in air are considered across a range of strain rates to study the effects of different fuel blends under a variety of operating conditions.

Results and discussion

Flame photographs and illuminance

Turbulent flames of hydrogen and blended hydrogen/natural gas were stabilised on two bluff-body burners with different diameters, and prevapourised toluene was added to the fuel stream at 1–5 mol%. Photographs for the hydrogen flames and hydrogen/natural gas flames (with 10 vol% hydrogen) at various levels of toluene addition are presented in Fig. 2 and Fig. 3, respectively. For each combination of base fuel and level of toluene addition, the presented image is a composite of two photos, corresponding to the two bluff-body diameters, namely 64 mm and 50 mm-diameter on the left and right side of the centreline, respectively.

The general structure of all flames is comparable to other bluff-body flames seen in literature [33,55,58,61,73] with three distinct zones present for each flame case — an initial recirculation zone followed by a high-strain neck zone and finally the jet-like downstream region [74]. Blends at 10 and 20 vol% hydrogen in natural gas flames are very similar to the reference natural gas flame for both bluff-body diameters without the addition of toluene. In these cases, the addition of hydrogen to natural gas has no observable effect on flame structure or visibility, with the exception of the 50 mm burner, which became brighter with the addition of hydrogen. This is consistent with previous investigations highlighting hydrogen addition up to 20 vol% having a negligible effect on flame length or overall structure [13]. Where the effect of hydrogen compared to methane is investigated in the literature, this result builds on existing work which describes a similarly

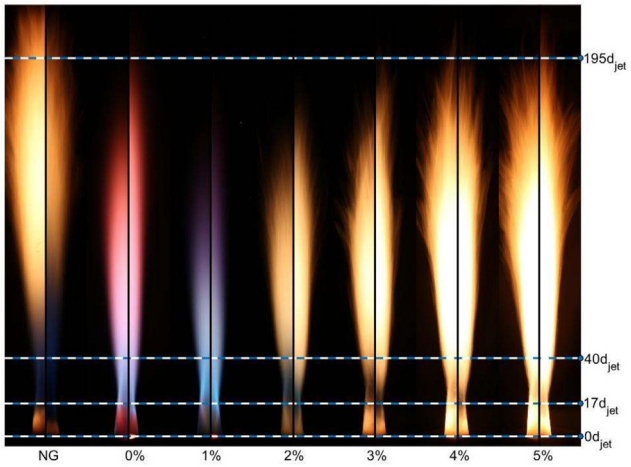

Fig. 2 – Split photographs natural gas flames with 100 vol% hydrogen, with the addition of 1–5 mol% toluene and stabilised on the 64 mm (left-half) and 50 mm (right-half) bluff-body burner. Reference natural gas (NG) flame photos also included. All flames are operated at Re = 10,000. Aperture and exposure settings from left to right: f/22 2s, f/1.8 4s, f/22 30s, 2s, 1/5s, 1/5s, 1/5s.

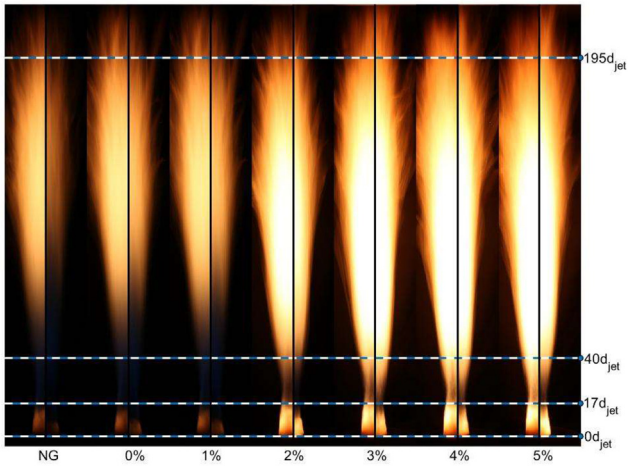

Fig. 3 – Split photographs of natural gas flames with 10 vol % hydrogen, with the addition of 1–5 mol% toluene and stabilised on the 64 mm (left-half) and 50 mm (right-half) bluff-body burner. Reference natural gas (NG) flame photos photo also included. All flames are operated at Re = 10,000. Aperture and exposure settings from left to right: f/22 1s, 1s, 1/2s, 1/2s, 1/2s, 1/2s, 1/2s.

unremarkable effect on the velocity contour plots in bluff-body burners [57]. A stronger contrast is observed between the reference natural gas and 100 vol% hydrogen flame cases. In this case, the 100 vol% hydrogen flames' recirculation zones became longer than the pure natural gas, consistent with previous investigations [21]. A consequence of hydrogen addition is that as the hydrogen content in the fuel grows the stoichiometric mixture fraction decreases. A table of stoichiometric mixture fractions for all fuel blends is included in the supplementary material (Table S3). The stoichiometric

mixture fraction for hydrogen is almost 50% lower than for natural gas. This causes the location of stoichiometric combustion, referred to as the stoichiometric contour line [75], to shrink inward towards the jet centreline. This contributes to the shorter and thinner flames in comparison to natural gas, as seen in Fig. 2. The flames overall became shorter and were significantly less visible than the reference natural gas flames, with photographs for the 100 vol% hydrogen (0 mol% toluene) taken at double the exposure time and with an aperture allowing 12 times more light than that of the natural gas flame photographs—thus the image intensity of the hydrogen flame is 24 times less bright than the equivalent natural gas photograph. The reduction in flame length due to hydrogen addition is commonly reported in literature [11,13,14] however, the effects of toluene on flame height in bluff-body burners for these fuel blends has not previously been reported. The notch-filtered photographs of the 100 vol% hydrogen flames show a pale blue/red compared to the yellow of the natural gas flames and are otherwise invisible to the naked eye. Toluene addition causes a noticeable increase in brightness for the 10, 20 and 100 vol% hydrogen flames. These flames are brighter and begin to take on a yellow colour typical of sooting flames with increasing toluene concentrations, which is consistent with previous investigations of toluene addition to a hydrogen-based flame [45], however this work provides a new insight into the effect of toluene on visibility for blended and bluff-body stabilised hydrogen/natural gas flames — compared to previous literature which only considered simple jet hydrogen/nitrogen flames at a lower turbulence regime. Incremental increases in toluene concentration result in a visibly more luminous yellow flame, most notably in the recirculation and jet regions of the bluff-body flame. As toluene concentrations increased, the recirculation zone length increases while the high-strain neck zone length decreases. The flames also become fractionally taller and wider with increasing toluene concentration for the 100 vol% hydrogen fuel and, albeit to a lesser extent, the 10 or 20 vol% hydrogen flames. The trends observed for base fuel and toluene addition are seen consistently in both bluff-body diameters. Reducing the bluff-body diameter from 64 mm to 50 mm causes a visible reduction in the recirculation zone brightness, width and length, and a visible increase in the total flame length, consistent with previous investigations [21]. This is due to a smaller recirculation zone in the 50 mm burner, allowing more fuel to be burnt further downstream [33]. Reducing the bluff-body diameter appears to reduce the visibility of the reference natural gas flame significantly, but this trend is not seen consistently for the fuels containing hydrogen.

Fig. 4 presents the flame illuminance data as a supplement to flame photographs (Figs. 2 and 3). Illuminance measurements are a way of capturing and quantifying the brightness in a way that enables a direct comparison of flame photographs with the heat flux measurements. The illuminance data supports the trends implied from the photographs, with illuminance increasing for each level of toluene addition. It is noteworthy that 2–3 mol% toluene is required for the pure hydrogen flames to emit equivalent illuminance to that of the natural gas reference case, as shown in Fig. 4. This is significant due to the safety concerns regarding the low visibility of hydrogen and flame detection [27]. The blended hydrogen/natural gas flame cases, with both 10 and 20 vol% hydrogen, exhibit a similar increase in illuminance with toluene addition. The flame illuminance in Fig. 4 does not decrease notably from that of pure natural gas for the addition of 20 vol% hydrogen (without toluene). This suggests that for natural gas fuel blends containing up to 20 vol% hydrogen, toluene is not required to improve flame illuminance. Previous investigations have shown a similarly unremarkable effect of hydrogen addition up to 20 vol% in hydrocarbon flames concerning reduced visibility [13,76] — however, quantification of the effect of hydrogen addition to natural gas with respect to toluene addition to improve visibility via soot loading is a novel contribution of this paper. The differences between 10 and 20 vol% hydrogen are also minor. Comparing both bluff-body diameters, a similar trend is observed with no significant effects on flame visibility between the 50 mm and 64 mm burners; apart from the natural gas reference cases, where the 64 mm burner is notably brighter than the 50 mm. It is interesting to note, however, that this trend is not observed for the pure and blended hydrogen cases. The discrepancy between cases with and without hydrogen is most likely the result of competing factors extending the residence time. In the 64 mm-bluff-body case, the flame has a recirculation zone that is larger than that observed in the 50 mm-bluff-body case, which helps promote the soot formation with its relatively long residence time. In contrast, the 50 mm-bluff-body flame has a longer flame length, which indicates a longer global residence time than the 64 mm-bluff-body flame. The proximity of the data points makes conjectures about the trends between burners difficult but, nevertheless, they can be used to supplement visual observations and trends in the heat flux data and soot precursor concentrations.

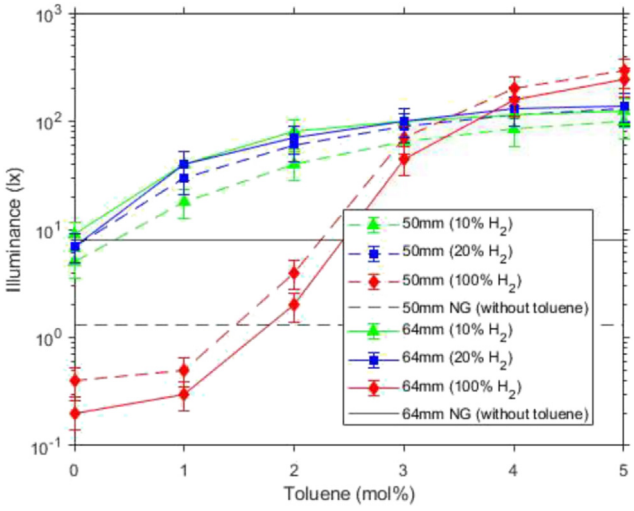

Fig. 4 – Illuminance (lx) measurements of turbulent pure and blended H_2 in natural gas (NG) (vol%) for the addition of 1–5 mol% toluene, and reference natural gas cases (without toluene addition) in a 50 mm and 64 mm bluff-body burner.

Flame heat flux

Thermal radiation heat flux measurements for all flames are presented in Fig. 5 and Fig. 6, for the 64 mm and 50 mm bluff-bodies, respectively. The heat flux data is normalised by the heat input from the fuel. It is logical that since both flame heat flux and flame illuminance are strongly dependant on toluene or soot concentration that a correlation may be seen in the two data sets. Fig. S2 in the supplementary material combines Figs. 4 and 5 to highlight the shared dependence on toluene concentration and resulting soot formation. In bluff-body flames soot accumulation and oxidation can be considered in the three distinct zones of a bluff-body flame, consequently changes to the characteristics of these zones affects how soot is produced and oxidised within them. Previous work by Rowhani et al. [61] has shown that in bluff-body flames soot volume fraction peaks first in the recirculation zone and in the downstream jet-like region, with almost no soot being produced in the neck zone due to high strain rates. It was also shown that the soot accumulation in the recirculation zone almost doubles by increasing the bluff-body diameter from 38 mm to 50 mm and then to 64 mm while the neck zone remains fairly consistent. Soot accumulation in the downstream region tends to increase with decreasing bluff-body diameter since this reduces the recirculation zone size and intensity allowing for more fuel to be burnt downstream. It has been previously established that decreasing the fuel to air ratio, perhaps by increased recirculation of air, also leads to reduced accumulation of soot in a recirculation due to increased oxidation [77]. Data in Figs. 4, Figs. 5 and 6 shows evidence of this via a larger total illuminance and heat flux, respectively, in the 50 mm bluff-body compared with the 64 mm. This suggests a larger content of fuel being burnt downstream and less being accumulated and burnt in the recirculation zone.

The normalised heat flux increases with increasing toluene concentration in all cases. The trends in the heat flux data are

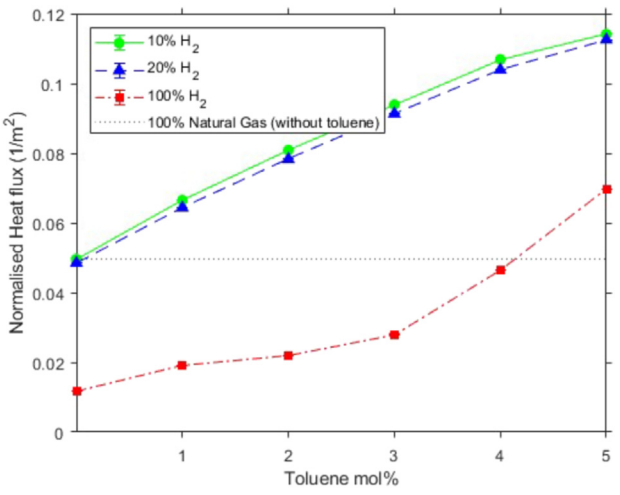

Fig. 5 – Heat flux data (normalised by heat input) for addition of 1–5 mol% toluene to pure and blended hydrogen/natural gas turbulent flames in a 64 mm bluff-body burner.

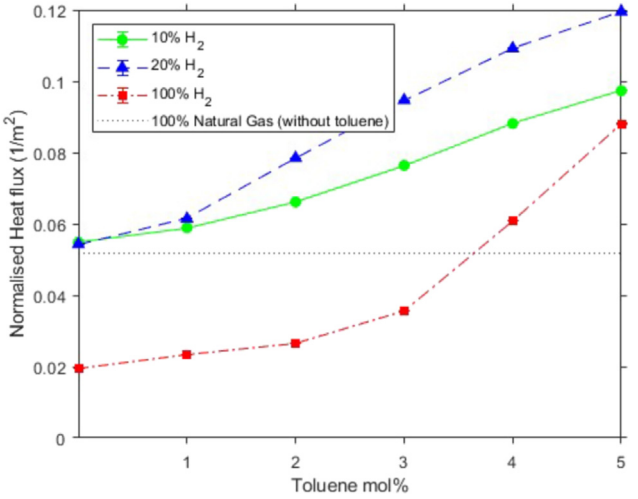

Fig. 6 – Heat flux data (normalised by heat input) for addition of 1–5 mol% toluene to pure and blended hydrogen/natural gas turbulent flames in a 50 mm bluff-body burner.

similar to that of illuminance, with the exception of the natural gas cases. The illuminance for natural gas in the 64 mm burner is almost 10 times greater than in the 50 mm burner. A discrepancy this large is not observed in the heat flux data. Additionally, a 10 vol% hydrogen blend (without toluene) significantly improves flame illuminance compared with the natural gas case in the 50 mm bluff-body. Otherwise, no significant reduction in heat flux is recorded for hydrogen addition of 10–20 vol% in natural gas, and thus, the addition of toluene does not appear to be required for these concentrations; however, the heat flux can be significantly improved by the addition of toluene. The pure hydrogen flame heat flux is approximately 80% lower than the pure natural gas case. To account for this reduction, a dopant concentration of 4 mol% toluene is required for the heat flux of the pure hydrogen flames to be equivalent to a natural gas flame. It should be noted that for toluene, the addition of 4 mol% in a pure hydrogen flame equates to 65% by mass, and 38% by energy input. This significant contribution of mass and enthalpy from the dopant is a limitation of the use of toluene as a means of supplementing reduced radiative heat transfer in hydrogen flames. This is most likely the cause of the more significant effects of toluene on flame structure and visibility in the pure cases compared with the blended cases, since its contribution to enthalpy and mass by toluene becomes much greater in the 100 vol% hydrogen cases as a result of the increased volumetric flow to maintain a Reynolds number of 10,000.

Computational analysis

To validate that the measured variations in heat flux are a consequence of increased soot formation due to toluene addition, the contribution of temperature and other radiant gases such as CO_2 and H_2O are considered. An approach adapted from previous work [78,79] using numerical data from an OPPDIF simulation of the aforementioned flame cases at two different strain rates are presented in Fig. 7. Here it can be

seen that toluene addition has a negligible effect on flame temperature. In this case, radiative heat losses are a function of the temperature, soot volume fraction and an absorption coefficient (the Planck mean) [78,79]. The variation in temperature with respect to toluene addition, as shown in Fig. 7, is not only too small to cause the experimentally measured variation in heat flux, since a 25K peak temperature variation would only result in a 13% change in radiant losses – but toluene addition has a reducing effect on the peak flame temperature. The experimentally measured variation in heat flux is much greater than this and therefore, given the contribution to the radiant heat loss from the soot volume fraction is much greater than the absorption coefficient, it can be assumed that the large variations in the experimental heat flux are primarily a consequence of increased soot loading due to toluene addition.

Comparing the heat flux trends in Figs. 5 and 6, that is, between the bluff-body diameters, it can be seen that both bluff-body diameters broadly exhibit similar trends. The 50 mm bluff-body diameter yields a consistently higher normalised heat flux than the 64 mm bluff-body diameter for toluene addition to the pure hydrogen fuel, whereas the 64 mm bluff-body burner produces a higher heat flux for toluene addition to the 10 vol% hydrogen-natural gas blend. Assuming changes in the soot volume fraction are the primary cause for variations in the normalised heat flux, then a link may be established between bluff-body diameter, and its effect on flame structure and resulting particle residence time and soot formation.

Typically, increased recirculation results in increased residence time, which promotes soot formation [53,80,81]. It has been reported previously that increasing the bluff-body diameter from 38-mm to 50 mm and 64 mm can double the recirculation zone length leading to increased particle residence time, which can increase the amount of soot formation [53]. It is also noteworthy that flame images presented in this paper show that a reduced bluff-body diameter causes a subsequent reduction in recirculation zone size but an increase in overall flame length by as much as 22% in some cases. This would also extend particle residence time and promote increased soot formation. This is also supported in literature with similar investigations of soot in bluff-body burners reporting a global decrease in the soot volume fraction of flames despite seeing local increases in regions of high recirculation [33]. Experimental data presented in Figs. 5 and 6 both show evidence of increased residence time via a combination of increased flame length and increased recirculation zone size. Comparison of visual luminosity of flame images (Figs. 2 and 3) provides an insight into local soot behaviour, where a more luminous region suggests a higher concentration of soot. For example, toluene addition to the pure hydrogen flames in the 50 mm bluff-body burner appear consistently brighter in their downstream region compared to the 64 mm burner (Fig. 2). This observation is also reflected in the illuminance data (Fig. 4). Similarly, the more luminous recirculation zones up to twice the length in the 64 mm burner compared with the 50 mm burner suggests a higher concentration of soot within the recirculation zone. It is also important to mention the effects of differential diffusion on soot formation, shown previously to be an important factor in the formation of soot as it relates to species' transport phenomena, especially for fuel mixtures containing hydrogen, which is highly diffusive [82,83]. The impact of hydrogen addition, and subsequent change in differential diffusivity, have been previously reported to affect factors such as flame length [84]—which, as mentioned previously, can affect residence time and soot formation.

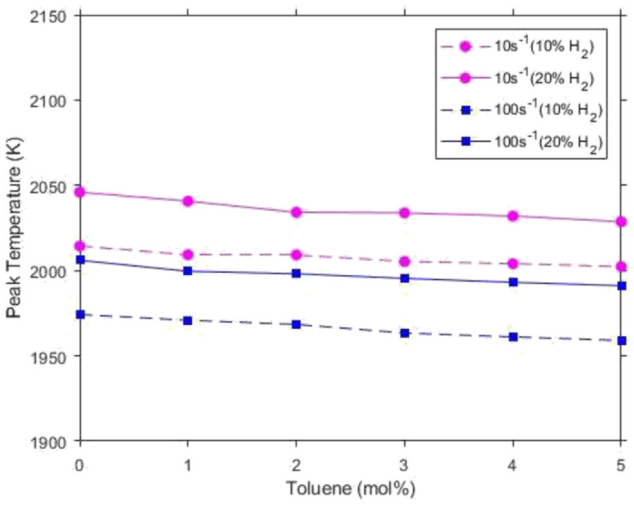

Fig. 7 – Calculated peak flame temperature from opposed-flow simulations with H_2/CH_4 fuel blends, doped with 1–5 mol% toluene at two different strain rates.

Another noteworthy observation is the shape of the curves in Figs. 5 and 6 for the blended hydrogen/natural gas cases in the 50 mm burner compared with the 64 mm burner. The 64 mm data plotted in Fig. 5 follow a consistent curve for both the 10 and 20 vol% hydrogen cases, with the 10 vol% hydrogen resulting in slightly higher heat flux at each increment of toluene addition. However, this trend is not seen in the 50 mm data presented in Fig. 6. Here, the data diverges as the toluene concentration increases, and, perhaps most interestingly, the 20 vol% hydrogen cases result in a higher heat flux compared to the 10 vol%. It is not appropriate to assume that, because heat flux measurements were normalised to thermal input, this is not a consequence of increased flame temperature, since radiation does not respond linearly with temperature ($Q_{rad} \propto T^4$). However, given the discrepancy is between burners and not fuel mixtures, and since the fuel blends for both burners are the same, this is unlikely to be a consequence of increased temperature due to hydrogen addition. Thermal and chemical-promoting effects of soot are well documented for the addition of hydrogen to a hydrocarbon mixture compared with an inert diluent [29–31,85] with various explanations given as to why. It is worth noting that to preserve Reynolds number in flames with varying compositions of fuels each with significantly different densities, jet velocity cannot be conserved between cases. This means for cases with relatively higher jet exit velocities, an increase in the fuel to air co-flow momentum flux ratio entrains less fuel into the recirculation zone near the bluff body surface. This leaner recirculation zone, in combination with a reduced residence time may result in an inhibition of soot nucleation and surface growth while soot oxidation is promoted. This effect was

shown previously for bluff-body stabilised ethylene/hydrogen flames by Deng et al. [74] where a leaner recirculation zone inhibited soot formation due to changes in jet velocity. This may explain the discrepancy between bluff-body diameters (Figs. 5 and 6) where the 20 vol% hydrogen fraction increases the fuel to air momentum flux ratio compared to the 10 vol% mixture, allowing for a leaner recirculation zone and a more dispersed soot concentration. This may not have occurred in the 64 mm bluff-body diameter due to a stronger recirculation zone compared to the 50 mm.

An alternative or additional cause may be increased strain rate in the 50 mm burner compared with the 64 mm. Reducing the bluff-body diameter and resulting recirculation zone size will increase the strain rate at the jet exit [33,86,87]. Too high a strain rate will restrict the combustion and push the system closer to its extinction strain rate [86,87]. A fuel mixture with a much higher extinction strain rate, such as one with a higher hydrogen content [88], may allow for more soot formation than a less resilient mixture through increased reactivity. Numerical simulations of an OPPDIF flame are used to test this hypothesis and examine the effects of the strain rate more closely. An OPPDIF model considers a one-dimensional (1D) flame created using opposed-flow fuel and oxidant streams. This 1D flame is representative of a local flame-front embedded within the larger, more complex bluff-body flame. In practice, these 1D flames encompass the flame and strain rate as a product of interactions between the fuel and the air streams. In this way, the governing reaction kinetics can be studied without the need to consider turbulent chemistry interactions, which are computationally more demanding and can be difficult to isolate in terms of specific variables. In this instance, the base fuel blends and toluene concentrations have been considered in the OPPDIF model for different strain rates.

The numerical modelling of the soot precursors in the flame cases in an OPPDIF configuration considered in this paper appear to support the hypothesis that increases in strain rate from a reduction in the bluff-body diameter caused the larger hydrogen blend to yield a higher heat flux. In the supplementary material provided, Fig. S1 shows the relationship between A2 rate of production (ROP) and the strain rate as a function of the axial distance. It can be seen that the peak A2 formation primarily occurs for low strain regions of the flame. The inverse relationship between soot formation and strain rate has been seen previously in literature [24,89]. In particular this has been shown for instantaneous soot volume fraction measurements in bluff-body flames [61]. This work further contributes to this well-established relationship by considering it with respect to soot precursors descended from toluene doped into hydrogen/natural gas flames. The numerical results presented in Fig. 8 show the effect of the strain rate on the fuel mixtures considered in the experimental cases. A similar trend to the experimental data is observed, where at higher strain rates the fuel blend with more hydrogen results in a higher A2 ROP. In this case, the distinction between 10 and 20 vol% hydrogen is very minor but a consistent trend is observed, nevertheless.

An analysis of chemical reaction pathways shows two main pathways are possible: either oxidation via formaldehyde (CH_2O) or soot formation via acetylene (C_2H_2). The strain rate has the strongest influence on reaction pathway preferences. The reaction pathway diagrams are given for a 5 mol% toluene addition to 10 vol% hydrogen at strain rates of $10s^{-1}$ and $200s^{-1}$ in Fig. 9 and Fig. 10, respectively. The effect of the hydrogen content (up to 20 vol%) and toluene addition (up to 5 mol%) did not significantly affect the reaction pathways when compared with the strain rate. While the toluene addition did not significantly impact the chemical pathways, its presence does shift the reaction away from the oxidative pathway and towards the formation of A2 and, subsequently, soot. Previous investigations have noted the competing formation of soot via A2 and oxidation via formaldehyde [45]. The effect of toluene on the ROP ratio between formaldehyde and A2 is presented in Fig. 11. A similar trend is seen here where at low toluene concentrations (<1 mol%) the oxidative tendencies of a hydrogen flame create a large discrepancy between the 10 and 20 vol% fuel blends—but as toluene concentration increases these become negligible.

Fig. 12 considers these strain rates at a wider selection of hydrogen concentrations to examine how this phenomenon behaves as the hydrogen content increases beyond 20 vol%. As the hydrogen concentration increases to 50 vol%, the effects of the strain rate become negligible with respect to A2 ROP, as this tends to zero when the hydrogen fraction approaches 100 vol%. As expected, based on the experimental data and trends in Fig. 8, at strain rates close to the extinction limit, the negative effects of hydrogen blending with A2 ROP are lessened, with an apparent improvement seen of up to 20 vol% hydrogen for the 200 s^{-1} case. This implicates that more hydrogen results in less soot and/or radiation may not apply to every burner, mode of operation or even every region within a flame.

It is worth noting that previous work by Evans et al. [45] reported a preference for oxidation (as opposed to soot formation) for concentrations of toluene <5 mol%. This was linked to a higher availability of OH and H species but no data was presented which compares the effect of strain rate or residence time. A change in strain rate has also been shown to

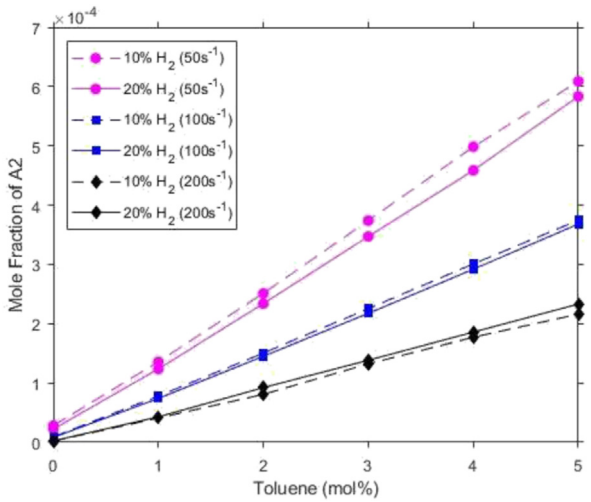

Fig. 8 – Calculated A2 mole fraction from opposed-flow simulations with H_2/CH_4 fuel blends, doped with 1–5 mol% toluene at three different strain rates.

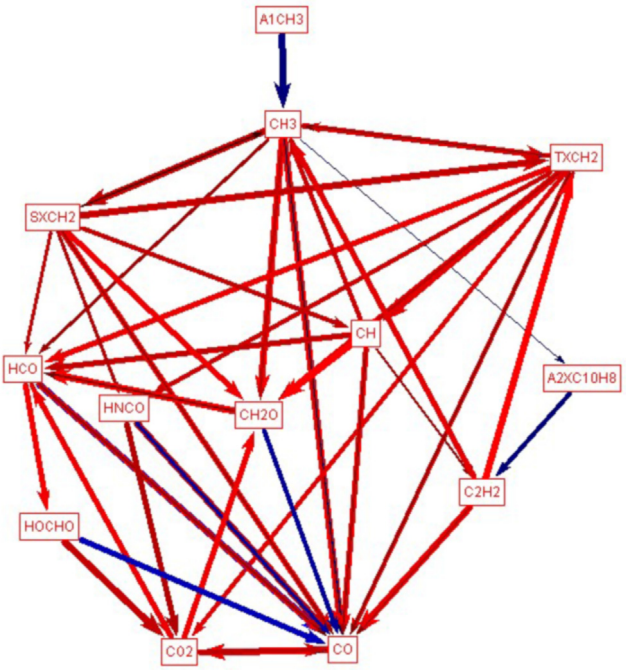

Fig. 9 – Reaction pathway diagram for toluene ($A1CH_3$) conversion to $A2XC_{10}H_8$ for 5 mol% toluene to a 10 vol% hydrogen in a methane fuel mixture at a strain rate of 10 s^{-1}. Line thickness and colour correspond to the relative rates of production and exo- (red)/endo (blue)-thermic reactions, respectively.

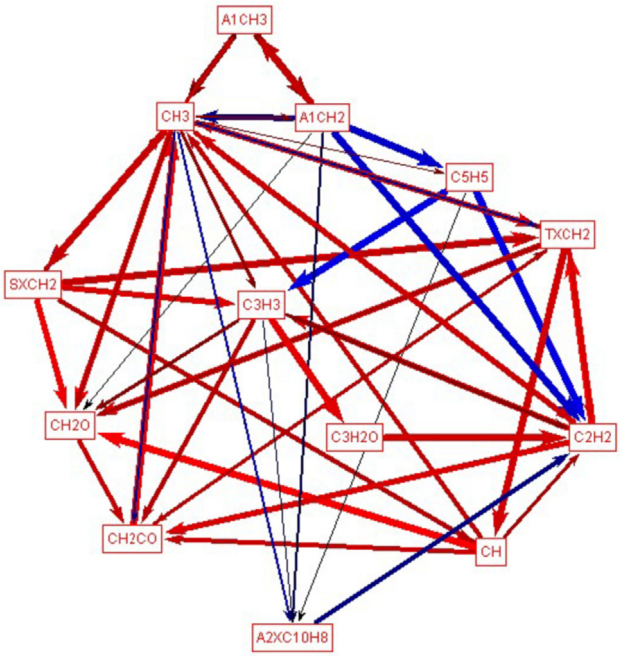

Fig. 10 – Reaction pathway diagram for toluene ($A1CH_3$) conversion to $A2XC_{10}H_8$ for 5 mol% toluene to a 10 vol% hydrogen in a methane fuel mixture at a strain rate of 200 s^{-1}. Line thickness and colour correspond to the relative rates of production and exo- (red)/endo (blue)-thermic reactions, respectively.

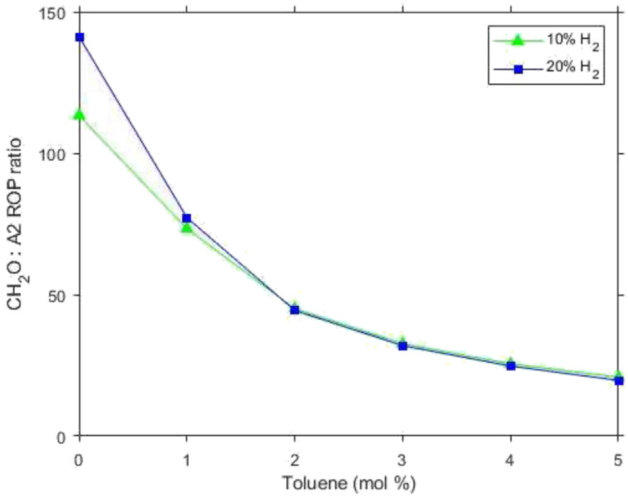

Fig. 11 – Calculated ROP ratio between formaldehyde (CH_2O) and naphthalene (A2) in opposed-flow fuel/air simulation for toluene addition to a 10 and 20 vol% H_2 in a CH_4 flame with a strain rate of 10 s^{-1}.

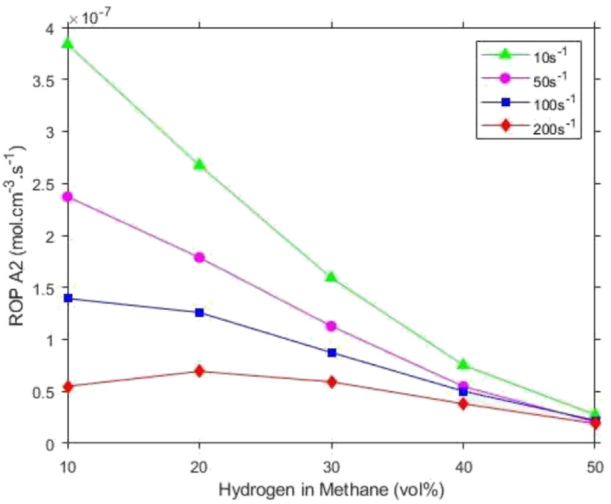

Fig. 12 – Calculated A2 rate of production (ROP) in opposed-flow simulations with H_2/CH_4 fuel blends at different strain rates.

affect these species [90]. The implication from the data presented in this paper that strain rate is a key parameter with regard to soot formation in the presence of hydrogen/natural gas flames is an important addition to the knowledge contributed by Evans et al. [45].

Conclusions

The efficacy of toluene addition to pure and blended hydrogen/natural gas flames on soot formation and the resulting radiative heat transfer, flame visibility and structure have been studied using a combination of experimental and computation methods. The experimental cases consisted of a series of turbulent diffusion flames stabilised on a 50 mm and

a 64 mm bluff-body burner, while the computational work was simulated in an opposed-flow diffusion flame model at various strain rates. This work builds on previous investigations regarding the use of toluene as a dopant by assessing its efficacy on highly turbulent pure and blended hydrogen/natural gas flames stabilised on bluff-body burners.

1. Supplementing flames containing hydrogen with pre-vapourised toluene improves the colour, illuminance and overall visibility of bluff-body stabilised flames-both for pure hydrogen flames and blended hydrogen/natural gas flames. Approximately 2 mol% toluene is required in the pure hydrogen flames to achieve the equivalent illuminance of a natural gas flame.
2. Toluene addition has a positive effect on the normalised heat flux data in both bluff-body burners. Hydrogen addition up to 20 vol% does not have a measurable impact on the normalised heat flux, while a complete substitution of natural gas for hydrogen results in an 80% reduction in the normalised heat flux. Approximately 4 mol% toluene is required to bring the pure hydrogen flames output equal to that of a pure natural gas flame. In this case, however, the significant contribution of mass and enthalpy from the dopant is a limitation on the use of toluene as a means of supplementing the reduced radiative heat transfer in hydrogen flames. This is a significant contribution to previous work which did not consider toluene's efficacy with respect to pure natural gas and its limitations for use as a dopant in large quantities.
3. Reducing the bluff-body diameter has a notable effect on the outcomes of hydrogen addition. In the smaller 50 mm bluff-body burner, hydrogen addition of 20 vol% resulted in a higher normalised heat flux than the 10 vol% cases, while the opposite effect was observed in the larger 64 mm bluff-body. This suggests that not only may the negative effects of hydrogen addition on thermal radiation be negated under some conditions, but that hydrogen addition may be beneficial to radiation.
4. The findings from the fuel/air OPPDIF simulations show a strong improvement in soot precursor rates of production via the acetylene pathway with the addition of toluene. The impact of hydrogen addition is strongly dependent on operating strain rate but it should be noted that hydrogen addition is negligible, if not mildly beneficial up to 20 vol% at high strain rates to soot precursor production.

Declaration of Competing Interest

The authors declare that they have no known competing financial interests or personal relationships that could have appeared to influence the work reported in this paper.

Acknowledgements

The authors would like to acknowledge the support from The Australian Research Council, The University of Adelaide and the Future Fuels CRC (RP1.4-03). The authors also thank Douglas Proud for his assistance with this work.

Appendix A. Supplementary data

Supplementary data to this article can be found online at https://doi.org/10.1016/j.ijhydene.2022.06.154.

REFERENCES

[1] Dreizler A, Pitsch H, Scherer V, Schulz C, Janicka J. The role of combustion science and technology in low and zero impact energy transformation processes. Appl Energy Comb Sci 2021;7:100040. https://doi.org/10.1016/j.jaecs.2021.100040.
[2] Pangborn J, Scott M, Sharer J. Technical prospects for commercial and residential distribution and utilization of hydrogen. Int J Hydrogen Energy 1977;2(4):431–45. https://doi.org/10.1016/0360-3199(77)90050-7.
[3] Scott M, Powells G. Sensing hydrogen transitions in homes through social practices: cooking, heating, and the decomposition of demand. Int J Hydrogen Energy 2020;45(7):3870–82. https://doi.org/10.1016/j.ijhydene.2019.12.025.
[4] Connolly D, Lund H, Mathiesen BV, Leahy M. The first step towards a 100% renewable energy-system for Ireland. Appl Energy 2011;88(2):502–7. https://doi.org/10.1016/j.apenergy.2010.03.006.
[5] Yilmaz İ, Ratner A, Ilbas M, Huang Y. Experimental investigation of thermoacoustic coupling using blended hydrogen–methane fuels in a low swirl burner. Int J Hydrogen Energy 2010;35(1):329–36. https://doi.org/10.1016/j.ijhydene.2009.10.018.
[6] Emadi M, Karkow D, Salameh T, Gohil A, Ratner A. Flame structure changes resulting from hydrogen-enrichment and pressurization for low-swirl premixed methane–air flames. Int J Hydrogen Energy 2012;37(13):10397–404. https://doi.org/10.1016/j.ijhydene.2012.04.017.
[7] Australia's National. Hydrogen strategy. In: Council of Australian governments (COAG) energy Council. Canberra: Department of Industry, Science and Energy Resources; 2019.
[8] Weber R, Mancini M. On scaling and mathematical modelling of large scale industrial flames. J Energy Inst 2020;93(1):43–51. https://doi.org/10.1016/j.joei.2019.04.010.
[9] Dong X, Nathan GJ, Mahmoud S, Ashman PJ, Gu D, Dally BB. Global characteristics of non-premixed jet flames of hydrogen–hydrocarbon blended fuels. Combust Flame 2015;162(4):1326–35. https://doi.org/10.1016/j.combustflame.2014.11.001.
[10] Kalbhor A, van Oijen J. Effects of hydrogen enrichment and water vapour dilution on soot formation in laminar ethylene counterflow flames. Int J Hydrogen Energy 2020;45(43):23653–73. https://doi.org/10.1016/j.ijhydene.2020.06.183.
[11] Choudhuri AR, Gollahalli SR. Combustion characteristics of hydrogen–hydrocarbon hybrid fuels. Int J Hydrogen Energy 2000;25(5):451–62. https://doi.org/10.1016/S0360-3199(99)00027-0.
[12] Wu L, Kobayashi N, Li Z, Huang H, Li J. Emission and heat transfer characteristics of methane–hydrogen hybrid fuel laminar diffusion flame. Int J Hydrogen Energy 2015;40(30):9579–89. https://doi.org/10.1016/j.ijhydene.2015.05.096.
[13] Kumar P, Mishra DP. Experimental investigation of laminar LPG–H2 jet diffusion flame. Int J Hydrogen Energy

2008;33(1):225–31. https://doi.org/10.1016/j.ijhydene.2007.09.023.
[14] Choudhuri AR, Gollahalli SR. Characteristics of hydrogen–hydrocarbon composite fuel turbulent jet flames. Int J Hydrogen Energy 2003;28(4):445–54. https://doi.org/10.1016/S0360-3199(02)00063-0.
[15] Gondal IA, Sahir MH. Prospects of natural gas pipeline infrastructure in hydrogen transportation. Int J Energy Res 2012;36(15):1338–45. https://doi.org/10.1002/er.1915.
[16] Sen S, Puri I. Thermal radiation modeling in flames and fires. Transport Phenonema in Fires; 2008. p. 301.
[17] Pessoa-Filho JB. Thermal radiation in combustion systems. J Braz Soc Mech Sci 1999;21(3):537–47.
[18] Hamadi MB, Vervisch P, Coppalle A. Radiation properties of soot from premixed flat flame. Combust Flame 1987;68(1):57–67. https://doi.org/10.1016/0010-2180(87)90065-4.
[19] Hutny WP, Lee GK. Improved radiative heat transfer from hydrogen flames. Int J Hydrogen Energy 1991;16(1):47–53. https://doi.org/10.1016/0360-3199(91)90059-R.
[20] Brookes SJ, Moss JB. Predictions of soot and thermal radiation properties in confined turbulent jet diffusion flames. Combust Flame 1999;116(4):486–503. https://doi.org/10.1016/S0010-2180(98)00056-X.
[21] Kashir B, Tabejamaat S, Jalalatian N. The impact of hydrogen enrichment and bluff-body lip thickness on characteristics of blended propane/hydrogen bluff-body stabilized turbulent diffusion flames. Energy Convers Manag 2015;103:1–13. https://doi.org/10.1016/j.enconman.2015.06.028.
[22] Hottel HC, Sarofim AF. Radiative transfer. McGraw-Hill; 1967.
[23] Viskanta R, Mengüç MP. Radiation heat transfer in combustion systems. Prog Energy Combust Sci 1987;13(2):97–160. https://doi.org/10.1016/0360-1285(87)90008-6.
[24] Bisetti F, Blanquart G, Mueller ME, Pitsch H. On the formation and early evolution of soot in turbulent nonpremixed flames. Combust Flame 2012;159(1):317–35. https://doi.org/10.1016/j.combustflame.2011.05.021.
[25] Saito K, Williams FA, Gordon AS. Effects of oxygen on soot formation in methane diffusion flames. Combust Sci Technol 1986;47(3–4):117–38. https://doi.org/10.1080/00102208608923869.
[26] Schiro F, Stoppato A, Benato A. Modelling and analyzing the impact of hydrogen enriched natural gas on domestic gas boilers in a decarbonization perspective. Carbon Res Con 2020;3:122–9. https://doi.org/10.1016/j.crcon.2020.08.001.
[27] Hord J. Is hydrogen a safe fuel? Int J Hydrogen Energy 1978;3(2):157–76. https://doi.org/10.1016/0360-3199(78)90016-2.
[28] Liu F, Liu Z, Sang Z, He X, Liu F, Liu C, Xu Y. Kinetic study of the effects of hydrogen blending to toluene reference fuel (TRF)/air mixtures on laminar burning velocity and flame structure. Fuel 2020;274:117850. https://doi.org/10.1016/j.fuel.2020.117850.
[29] Liu F, Ai Y, Kong W. Effect of hydrogen and helium addition to fuel on soot formation in an axisymmetric coflow laminar methane/air diffusion flame. Int J Hydrogen Energy 2014;39(8):3936–46. https://doi.org/10.1016/j.ijhydene.2013.12.151.
[30] Wang Y, Gu M, Chao L, Wu J, Lin Y, Huang X. Different chemical effect of hydrogen addition on soot formation in laminar coflow methane and ethylene diffusion flames. Int J Hydrogen Energy 2021;46(29):16063–74. https://doi.org/10.1016/j.ijhydene.2021.02.014.
[31] Boyette WR, Steinmetz SA, Guiberti TF, Dunn MJ, Roberts WL, Masri AR. Soot formation in turbulent flames of ethylene/hydrogen/ammonia. Combust Flame 2021;226:315–24. https://doi.org/10.1016/j.combustflame.2020.12.019.
[32] Xu L, Yan F, Wang Y, Chung SH. Chemical effects of hydrogen addition on soot formation in counterflow diffusion flames: dependence on fuel type and oxidizer composition. Combust Flame 2020;213:14–25. https://doi.org/10.1016/j.combustflame.2019.11.011.
[33] Rowhani A, Sun ZW, Medwell PR, Alwahabi ZT, Nathan GJ, Dally BB. Effects of the bluff-body diameter on the flow-field characteristics of non-premixed turbulent highly-sooting flames. Combust Sci Technol 2019:1–19. https://doi.org/10.1080/00102202.2019.1680508.
[34] Wu L, Kobayashi N, Li Z, Huang H. Experimental study on the effects of hydrogen addition on the emission and heat transfer characteristics of laminar methane diffusion flames with oxygen-enriched air. Int J Hydrogen Energy 2016;41(3):2023–36. https://doi.org/10.1016/j.ijhydene.2015.10.132.
[35] Hansen OR. Hydrogen infrastructure—efficient risk assessment and design optimization approach to ensure safe and practical solutions. Process Saf Environ Protect 2020;143:164–76. https://doi.org/10.1016/j.psep.2020.06.028.
[36] Cellek MS, Pınarbaşı A. Investigations on performance and emission characteristics of an industrial low swirl burner while burning natural gas, methane, hydrogen-enriched natural gas and hydrogen as fuels. Int J Hydrogen Energy 2018;43(2):1194–207. https://doi.org/10.1016/j.ijhydene.2017.05.107.
[37] Cho E-S, Chung SH. Improvement of flame stability and NOx reduction in hydrogen-added ultra lean premixed combustion. J Mech Sci Technol 2009;23(3):650–8. https://doi.org/10.1007/s12206-008-1223-x.
[38] Rajpara P, Shah R, Banerjee J. Effect of hydrogen addition on combustion and emission characteristics of methane fuelled upward swirl can combustor. Int J Hydrogen Energy 2018;43(36):17505–19. https://doi.org/10.1016/j.ijhydene.2018.07.111.
[39] Guo H, Smallwood GJ, Liu F, Ju Y, Gülder ÖL. The effect of hydrogen addition on flammability limit and NOx emission in ultra-lean counterflow CH4/air premixed flames. Proc Combust Inst 2005;30(1):303–11. https://doi.org/10.1016/j.proci.2004.08.177.
[40] Cano Ardila FE, Obando Arbeláez JE, Amell Arrieta AA. Emissions and dynamic stability of the flameless combustion regime using hydrogen blends with natural gas. Int J Hydrogen Energy 2020;46(1). https://doi.org/10.1016/j.ijhydene.2020.09.236.
[41] Kashir B, Tabejamaat S, Jalalatian N. A numerical study on combustion characteristics of blended methane-hydrogen bluff-body stabilized swirl diffusion flames. Int J Hydrogen Energy 2015;40(18):6243–58. https://doi.org/10.1016/j.ijhydene.2015.03.023.
[42] Baek SW, Ju Kim J, Kim HS, Kang SH. Effects of addition of solid particles on thermal characteristics in hydrogen-air flame. Combust Sci Technol 2002;174(8):99–116. https://doi.org/10.1080/00102200290021263.
[43] Waheed K, Baek SW, Javed I, Kristiyanto Y. Investigations on thermal radiative characteristics of LPG combustion: effect of alumina nanoparticles addition. Combust Sci Technol 2015;187(6):827–42. https://doi.org/10.1080/00102202.2014.973952.
[44] Schumacher G, Juniper L. Coal utilisation in the cement and concrete industries. In: Osborne D, editor. The coal handbook: towards cleaner production. Woodhead Publishing; 2013. p. 387–426.
[45] Evans MJ, Proud DB, Medwell PR, Pitsch H, Dally BB. Highly radiating hydrogen flames: effect of toluene concentration and phase. Proc Combust Inst 2020;38(1). https://doi.org/10.1016/j.proci.2020.07.005.

[46] Dooley S, Won SH, Chaos M, Heyne J, Ju Y, Dryer FL, Kumar K, Sung C-J, Wang H, Oehlschlaeger MA, Santoro RJ, Litzinger TA. A jet fuel surrogate formulated by real fuel properties. Combust Flame 2010;157(12):2333–9. https://doi.org/10.1016/j.combustflame.2010.07.001.
[47] Pepiot-Desjardins P, Pitsch H, Malhotra R, Kirby SR, Boehman AL. Structural group analysis for soot reduction tendency of oxygenated fuels. Combust Flame 2008;154(1):191–205. https://doi.org/10.1016/j.combustflame.2008.03.017.
[48] Katta VR, Stouffer S, Roquemore WM. Stability of lifted flames in centerbody burner. Combust Flame 2011;158(6):1149–59. https://doi.org/10.1016/j.combustflame.2010.10.022.
[49] Kashif M, Bonnety J, Matynia A, Da Costa P, Legros G. Sooting propensities of some gasoline surrogate fuels: combined effects of fuel blending and air vitiation. Combust Flame 2015;162(5):1840–7. https://doi.org/10.1016/j.combustflame.2014.12.005.
[50] Consalvi J-L, Liu F, Kashif M, Legros G. Numerical study of soot formation in laminar coflow methane/air diffusion flames doped by n-heptane/toluene and iso-octane/toluene blends. Combust Flame 2017;180:167–74. https://doi.org/10.1016/j.combustflame.2017.03.002.
[51] Russo C, Giarracca L, Stanzione F, Apicella B, Tregrossi A, Ciajolo A. Sooting structure of a premixed toluene-doped methane flame. Combust Flame 2018;190:252–9. https://doi.org/10.1016/j.combustflame.2017.12.004.
[52] Mullinger P, Jenkins B. Chapter 5 - flames and burners for furnaces. In: Mullinger P, Jenkins B, editors. Industrial and process furnaces. 2nd ed. Oxford: Butterworth-Heinemann; 2013. p. 139–207.
[53] Rowhani A, Chinnici A, Evans M, Medwell P, Nathan G, Dally B. Variation of residence time in non-premixed turbulent bluff-body ethylene flames as a function of burner diameter. In: 21st australasian fluid mechanics conference; December. 2018. Adelaide, Australia.
[54] Masri A, Kelman J, Dally B. The instantaneous spatial structure of the recirculation zone in bluff-body stabilized flames. In: Symposium (international) on combustion. Elsevier; 1998. https://doi.org/10.1016/S0082-0784(98)80503-1.
[55] Dally B, Masri A, Barlow R, Fiechtner G. Instantaneous and mean compositional structure of bluff-body stabilized nonpremixed flames. Combust Flame 1998;114(1–2):119–48. https://doi.org/10.1016/S0010-2180(97)00280-0.
[56] Dally BB, Masri AR, Barlow RS, Fiechtner GJ, Fletcher DF. Measurements of no in turbulent non-premixed flames stabilized on a bluff body. Symp (Int) Combust 1996;26(2):2191–7. https://doi.org/10.1016/S0082-0784(96)80045-2.
[57] Dutka M, Ditaranto M, Løvås T. NOx emissions and turbulent flow field in a partially premixed bluff body burner with CH4 and H2 fuels. Int J Hydrogen Energy 2016;41(28):12397–410. https://doi.org/10.1016/j.ijhydene.2016.05.154.
[58] Mueller ME, Chan QN, Qamar NH, Dally BB, Pitsch H, Alwahabi ZT, Nathan GJ. Experimental and computational study of soot evolution in a turbulent nonpremixed bluff body ethylene flame. Combust Flame 2013;160(7):1298–309. https://doi.org/10.1016/j.combustflame.2013.02.010.
[59] Qamar NH, Nathan GJ, Alwahabi ZT, King KD. The effect of global mixing on soot volume fraction: measurements in simple jet, precessing jet, and bluff body flames. Proc Combust Inst 2005;30(1):1493–500. https://doi.org/10.1016/j.proci.2004.08.102.
[60] AMME. Bluff-body flows and flames. 2018. Available from, https://web.aeromech.usyd.edu.au/thermofluids/bluff.php.
[61] Rowhani A, Sun Z, Medwell PR, Nathan GJ, Dally BB. Soot-flowfield interactions in turbulent non-premixed bluff-body flames of ethylene/nitrogen. Proc Combust Inst 2021;38(1):1125–32. https://doi.org/10.1016/j.proci.2020.06.148.
[62] Masri AR, Dibble RW, Barlow RS. Raman-Rayleigh measurements in bluff-body stabilised flames of hydrocarbon fuels. Symp (Int) Combust 1992;24(1):317–24. https://doi.org/10.1016/S0082-0784(06)80042-1.
[63] Liu C, Zhang J, Yang T, Ma Y. Bluff-body flames in hot and diluted environments. In: ASME power conference. American Society of Mechanical Engineers; 2018. https://doi.org/10.1115/POWER2018-7179.
[64] Jarungthammachote S. Simplified model for estimations of combustion products, adiabatic flame temperature and properties of burned gas. Therm Sci Eng Prog 2020;17:100393. https://doi.org/10.1016/j.tsep.2019.100393.
[65] Robinson JW, Smith V. Emission spectra of organic liquids in oxy-hydrogen flames. Anal Chim Acta 1966;36:489–98. https://doi.org/10.1016/0003-2670(66)80084-3.
[66] Arens EE, Youngquist RC, Starr SO. Intensity calibrated hydrogen flame spectrum. Int J Hydrogen Energy 2014;39(17):9545–51. https://doi.org/10.1016/j.ijhydene.2014.04.043.
[67] Lieuwen T, Shanbhogue S, Khosla S, Smith C. Dynamics of bluff body flames near blowoff. In: Collection of technical papers - 45th AIAA aerospace sciences meeting. vol. 3; 2007. https://doi.org/10.2514/6.2007-169.
[68] Morales AJ, Lasky IM, Geikie MK, Engelmann CA, Ahmed KA. Mechanisms of flame extinction and lean blowout of bluff body stabilized flames. Combust Flame 2019;203:31–45. https://doi.org/10.1016/j.combustflame.2019.02.002.
[69] Kim S-H, Kim M, Yoon Y, Jeung I-S. The effect of flame radiation on the scaling of nitrogen oxide emissions in turbulent hydrogen non-premixed flames. Proc Combust Inst 2002;29(2):1951–6. https://doi.org/10.1016/S1540-7489(02)80237-1.
[70] Kim S-H, Yoon Y, Jeung I-S. Nitrogen oxides emissions in turbulent hydrogen jet non-premixed flames: effects of coaxial air and flame radiation. Proc Combust Inst 2000;28(1):463–71. https://doi.org/10.1016/S0082-0784(00)80244-1.
[71] Cai L, Pitsch H. Optimized chemical mechanism for combustion of gasoline surrogate fuels. Combust Flame 2015;162(5):1623–37. https://doi.org/10.1016/j.combustflame.2014.11.018.
[72] Violi A, D'Anna A, D'Alessio A. Modeling of particulate formation in combustion and pyrolysis. Chem Eng Sci 1999;54(15–16):3433–42.
[73] Dally B, Fletcher D, Masri A. Flow and mixing fields of turbulent bluff-body jets and flames. Combust Theor Model 1998;2(2):193.
[74] Deng S, Mueller ME, Chan QN, Qamar NH, Dally BB, Alwahabi ZT, Nathan GJ. Hydrodynamic and chemical effects of hydrogen addition on soot evolution in turbulent nonpremixed bluff body ethylene flames. Proc Combust Inst 2017;36(1):807–14. https://doi.org/10.1016/j.proci.2016.09.004.
[75] Kang Y-H, Wang Q-H, Lu X-F, Ji X-Y, Miao S-S, Wang H, Guo Q, He H-H, Xu J. Experimental and theoretical study on the flow, mixing, and combustion characteristics of dimethyl ether, methane, and LPG jet diffusion flames. Fuel Process Technol 2015;129:98–112. https://doi.org/10.1016/j.fuproc.2014.09.004.
[76] Gülder ÖL, Snelling DR, Sawchuk RA. Influence of hydrogen addition to fuel on temperature field and soot formation in diffusion flames. Symp (Int) Combust 1996;26(2):2351–8. https://doi.org/10.1016/S0082-0784(96)80064-6.
[77] Mueller ME, Pitsch H. Large eddy simulation of soot evolution in an aircraft combustor. Phys Fluids 2013;25(11):110812. https://doi.org/10.1063/1.4819347.

[78] Evans MJ, Medwell PR, Sun Z, Chinnici A, Ye J, Chan QN, Dally BB. Downstream evolution of n-heptane/toluene flames in hot and vitiated coflows. Combust Flame 2019;202:78–89. https://doi.org/10.1016/j.combustflame.2019.01.008.
[79] Liu F, Guo H, Smallwood GJ, Gülder ÖL. Effects of gas and soot radiation on soot formation in a coflow laminar ethylene diffusion flame. J Quant Spectrosc Radiat Transf 2002;73(2):409–21. https://doi.org/10.1016/S0022-4073(01)00205-9.
[80] Wang X, Jin Q, Zhang J, Li Y, Li S, Mikulčić H, Vujanović M, Tan H, Duić N. Soot formation during polyurethane (PU) plastic pyrolysis: the effects of temperature and volatile residence time. Energy Convers Manag 2018;164:353–62. https://doi.org/10.1016/j.enconman.2018.02.082.
[81] Smooke MD, Long MB, Connelly BC, Colket MB, Hall RJ. Soot formation in laminar diffusion flames. Combust Flame 2005;143(4):613–28. https://doi.org/10.1016/j.combustflame.2005.08.028.
[82] Kronenburg A, Bilger RW, Kent JH. Modeling soot formation in turbulent methane–air jet diffusion flames. Combust Flame 2000;121(1):24–40. https://doi.org/10.1016/S0010-2180(99)00146-7.
[83] Sutherland JC, Smith PJ, Chen JH. Quantification of differential diffusion in nonpremixed systems. Combust Theor Model 2005;9(2):365–83. https://doi.org/10.1080/17455030500150009.
[84] Yen M, Magi V, Abraham J. Modeling the effects of hydrogen and nitrogen addition on soot formation in laminar ethylene jet diffusion flames. Chem Eng Sci 2019;196:116–29. https://doi.org/10.1016/j.ces.2018.07.061.
[85] Migliorini F. Study of combustion process of hydrogen-hydrocarbon mixtures. Politecnico di Milano; 2008.
[86] Ji W, Yang T, Ren Z, Deng S. Dependence of kinetic sensitivity direction in premixed flames. Combust Flame 2020;220:16–22. https://doi.org/10.1016/j.combustflame.2020.06.027.
[87] Xie S, Lu Z, Chen Z. Effects of strain rate and Lewis number on forced ignition of laminar counterflow diffusion flames. Combust Flame 2021;226:302–14. https://doi.org/10.1016/j.combustflame.2020.12.027.
[88] Vagelopoulos C, Egolfopoulos F. Laminar flame speeds and extinction strain rates of mixtures of carbon monoxide with hydrogen, methane, and air. Symp (Int) Combust 1994;25(1):1317–23. https://doi.org/10.1016/S0082-0784(06)80773-3.
[89] Kent JH, Bastin SJ. Parametric effects on sooting in turbulent acetylene diffusion flames. Combust Flame 1984;56(1):29–42. https://doi.org/10.1016/0010-2180(84)90003-8.
[90] Coriton B, Smooke MD, Gomez A. Effect of the composition of the hot product stream in the quasi-steady extinction of strained premixed flames. Combust Flame 2010;157(11):2155–64. https://doi.org/10.1016/j.combustflame.2010.05.002.

Appendix B

Radiation correction for thermocouples

This appendix contains the processes and equations used in this research to correct the radiative heat loss from the thermocouple in flame temperature measurements. To estimate the correction for radiative heat loss of thermocouples, a radiation and convection energy balance around the thermocouple bead is shown below:

$$h(T_g - T_{tc}) = \varepsilon_{tc}\sigma(T_{tc}^4 - T_w^4) \tag{B.1}$$

where h is the convective heat transfer coefficient, ε_{tc} is the bare-bead thermocouple emissivity, T_g is gas temperature, T_{tc} is the thermocouple temperature, T_w is the temperature of the characteristic radiant surroundings, and σ is the Stephen Boltzmann constant. The convective heat transfer coefficient h between the bead and gas flow can be estimated using Whitaker's correlation, given as:

$$Nu = 2 + (0.4Re^{0.5} + 0.06Re^{2/3})Pr^{0.4} \tag{B.2}$$

where the equations for the Nusselt number, Reynolds number and Prandtl number are shown below:

$$Nu = \frac{hd_b}{k_g} \tag{B.3}$$

$$Re = \frac{\rho_g U_g D_b}{\mu_g} \tag{B.4}$$

$$Pr = \frac{c_{p,g}\mu_g}{k_g} \tag{B.5}$$

where k_g, $c_{p,g}$, μ_g, ρ_g are the thermal conductivity, heat capacity, viscosity and density of gas respectively, D_b the diameter of the bead, and U_g the local gas velocity.